

VISUAL, RED AND INFRARED PHOTOGRAPHIC SURFACE
PHOTOMETRY OF NGC 55 AND NGC 253

By

GREGORY L. FITZGIBBONS

A DISSERTATION PRESENTED TO THE GRADUATE SCHOOL
OF THE UNIVERSITY OF FLORIDA IN PARTIAL FULFILLMENT
OF THE REQUIREMENTS FOR THE DEGREE OF
DOCTOR OF PHILOSOPHY

UNIVERSITY OF FLORIDA

1990

UNIVERSITY OF FLORIDA LIBRARIES

This work is dedicated to my mother and father, Virginia R. Fitzgibbons and William E. Fitzgibbons, who believed for so long.

ACKNOWLEDGMENTS

This work could not have been done without the help of the many individuals who contributed time, resources and support. I extend heartfelt thanks to my committee members, Drs. Stephen T. Gottesman, John P. Oliver, Pierre Ramond, Alex G. Smith and Haywood C. Smith, for their work. In particular, my gratitude goes to Steve for his interest and suggestions, especially in the early stages of the project, and to Alex for providing me support as a research assistant.

Drs. Daniel Klinglesmith III and Christopher Harvel taught me the rudiments of microdensitometry and answered many of my questions in the beginning of my work. I am thankful for their time and contributions.

The generous financial and material assistance of Kitt Peak National Observatory and Cerro Tololo Inter-American Observatory, and their former directors, Drs. Geoffrey Burbidge and Patrick Osmer, is much appreciated. The support of the National Science Foundation through grant 80LA/R-5 is gratefully acknowledged, as is support from the Department of Sponsored Research of the University of Florida.

Many people at Cerro El Roble gave much of their time to make this project a success, Drs. Jorge May, Carlos Torres, José Maza, and especially Edgardo Costa, who took many of the

plates. His help was indispensable in obtaining the necessary photographic images, in particular the troublesome IV - Ns. Señor Gonzalez also is to be thanked for his telescope work.

Appreciation is extended to the U. S. Naval Observatory Time Service Alternate Station at Miami for use of their microdensitometer, and to the former directors, Don Monger and Jim Martin. The program SCFTZ which operated the microdensitometer was written by Jim and his help was always kindly given.

I am grateful to William Pence for his comments regarding the "spur" of NGC 253.

Much of the data reduction was performed at the Northeast Regional Data Center (NERDC) and their assistance is appreciated.

My sincere thanks goes to my fellow graduate students and friends for the good times we enjoyed, and especially to Joe Pollock, Glenn Schneider and Roger Ball, who shared so many times, good and bad, with me.

Finally, I wish to thank the three people who gave so much of themselves toward helping me along: my mother, Virginia Fitzgibbons, my father, William Fitzgibbons, and my wife, Berna Lowenstein. Their patience and encouragement are deeply appreciated, and I know they are as happy as I am to see this labor come to a successful conclusion.

TABLE OF CONTENTS

	PAGE
ACKNOWLEDGMENTS.	iii
LIST OF TABLES	vii
LIST OF FIGURES.	ix
ABSTRACT	xiii
 CHAPTERS	
I. INTRODUCTION	1
Objective.	1
Previous Studies	4
NGC 55.	4
NGC 253	8
Adopted Distances.	16
II. PHOTOGRAPHIC MATERIAL AND REDUCTION	
METHODS	18
Observations	18
The Telescope	18
Plates and Filters.	18
Photographic Techniques	22
Calibration	24
Plate Digitization	25
Equipment	25
Technique	26
Data Reduction	29
Numerical Mapping Technique and	
Reduction of the Outer Field	29
Reduction of the Inner Field.	36
Density to Intensity Conversion	37
Star and Blemish Removal.	38
Photoelectric Calibration	41
Plate Addition.	49
Image Smoothing	50
III. PHOTOMETRIC DATA FOR NGC 55.	52
General Description.	52

	PAGE
Isophotal Contour Maps	54
Luminosity Profiles.	63
Major Axis.	63
Minor Axis.	69
Size of NGC 55.	71
Asymmetry Profiles	72
Major Axis.	72
Minor Axis.	76
Color Profiles	76
Major Axis.	80
Minor Axis.	84
Integrated Parameters and Colors	88
IV. PHOTOMETRIC DATA FOR NGC 253	106
General Description.	106
Isophotal Contour Maps	108
Luminosity Profiles.	118
Major Axis.	118
Minor Axis.	123
Size of NGC 253	123
Mean Axis Profiles	124
Ellipticity	132
Color Profiles	136
Major Axis.	136
Minor Axis.	141
Integrated Parameters and Colors	145
Decomposition of the Observed Profiles.	160
V. SUMMARY AND CONCLUSIONS.	172
REFERENCES	180
BIOGRAPHICAL SKETCH.	185

LIST OF TABLES

TABLE		PAGE
1.	DISTANCE TO NGC 55	16
2.	DISTANCE TO NGC 253.	17
3.	PLATE MATERIAL NGC 55.	20
4.	PLATE MATERIAL NGC 253	21
5.	APERTURE PHOTOMETRY OF NGC 55.	42
6.	NGC 55 PLATE CALIBRATION	44
7.	APERTURE PHOTOMETRY OF NGC 253	45
8.	NGC 253 PLATE CALIBRATION.	47
9.	ELEMENTS OF NGC 55	54
10.	NGC 55 MAJOR AXIS LUMINOSITY GRADIENTS	68
11.	NGC 55 MAJOR AXIS SCALE LENGTHS IN KPC.	69
12.	NGC 55 MINOR AXIS LUMINOSITY GRADIENTS	70
13.	NGC 55 MINOR AXIS SCALE LENGTHS IN KPC.	70
14.	SIZE OF NGC 55	71
15.	MEAN V LUMINOSITY DISTRIBUTION IN NGC 55	93
16.	MEAN R LUMINOSITY DISTRIBUTION IN NGC 55	94
17.	MEAN I LUMINOSITY DISTRIBUTION IN NGC 55	95
18.	PHOTOMETRIC PARAMETERS OF NGC 55 V	103

TABLE		PAGE
19.	PHOTOMETRIC PARAMETERS OF NGC 55 R	104
20.	PHOTOMETRIC PARAMETERS OF NGC 55 I	105
21.	ELEMENTS OF NGC 253.	108
22.	SIZE OF NGC 253.	124
23.	MEAN V LUMINOSITY DISTRIBUTION IN NGC 253.	150
24.	MEAN R LUMINOSITY DISTRIBUTION IN NGC 253.	151
25.	MEAN I LUMINOSITY DISTRIBUTION IN NGC 253.	152
26.	PHOTOMETRIC PARAMETERS OF NGC 253 V. . . .	161
27.	PHOTOMETRIC PARAMETERS OF NGC 253 R. . . .	162
28.	PHOTOMETRIC PARAMETERS OF NGC 253 I. . . .	163

LIST OF FIGURES

FIGURE		PAGE
1.	Density contour map of plate 9309.	35
2.	Photograph of NGC 55	53
3.	Short exposure V isophote map of NGC 55	55
4.	Short exposure R isophote map of NGC 55	56
5.	Short exposure I isophote map of NGC 55	57
6.	Visual isophote map made from added long exposure plates.	59
7.	Red isophote map made from added long exposure plates.	60
8.	Infrared isophote map made from added long exposure plates.	61
9.	Visual major and minor axis profiles of NGC 55.	64
10.	Red major and minor axis profiles of NGC 55	65
11.	Infrared major and minor axis profiles of NGC 55.	66
12.	Asymmetry profile for NGC 55 V data: major axis.	73
13.	Asymmetry profile for NGC 55 R data: major axis.	74
14.	Asymmetry profile for NGC 55 I data: major axis.	75
15.	Asymmetry profile for NGC 55 V data: minor axis.	77

FIGURE		PAGE
16.	Asymmetry profile for NGC 55 R data: minor axis.	78
17.	Asymmetry profile for NGC 55 I data: minor axis.	79
18.	Major axis (V - R) color profile for NGC 55.	81
19.	Major axis (R - I) color profile for NGC 55.	82
20.	Major axis (V - I) color profile for NGC 55.	83
21.	Minor axis (V - R) color profile for NGC 55.	85
22.	Minor axis (R - I) color profile for NGC 55.	86
23.	Minor axis (V - I) color profile for NGC 55.	87
24.	Equivalent mean V luminosity profile for NGC 55.	89
25.	Equivalent mean R luminosity profile for NGC 55.	90
26.	Equivalent mean I luminosity profile for NGC 55.	91
27.	Relative V integrated luminosity curves for NGC 55	97
28.	Relative R integrated luminosity curves for NGC 55	98
29.	Relative I integrated luminosity curves for NGC 55	99
30.	Photograph of NGC 253.	107
31.	Short exposure V isophote map of NGC 253.	109
32.	Short exposure R isophote map of NGC 253.	110

FIGURE		PAGE
33.	Short exposure I isophote map of NGC 253.	111
34.	Visual isophote map made from added long exposure plates.	114
35.	Red isophote map made from the long exposure plate 5394.	115
36.	Infrared isophote map made from added long exposure plates.	116
37.	Visual major and minor axis profiles of NGC 253	119
38.	Red major and minor axis profiles of NGC 253	120
39.	Infrared major and minor axis profiles of NGC 253	121
40.	Mean V semi-major axis profile for NGC 253	126
41.	Mean R semi-major axis profile for NGC 253	127
42.	Mean I semi-major axis profile for NGC 253	128
43.	Mean V semi-minor axis profile for NGC 253	129
44.	Mean R semi-minor axis profile for NGC 253	130
45.	Mean I semi-minor axis profile for NGC 253	131
46.	Ellipticity curve for NGC 253 V data . . .	133
47.	Ellipticity curve for NGC 253 R data . . .	134
48.	Ellipticity curve for NGC 253 I data . . .	135
49.	Major axis (V - R) color profile for NGC 253	137

FIGURE		PAGE
50.	Major axis (R - I) color profile for NGC 253	138
51.	Major axis (V - I) color profile for NGC 253	139
52.	Minor axis (V - R) color profile for NGC 253	142
53.	Minor axis (R - I) color profile for NGC 253	143
54.	Minor axis (V - I) color profile for NGC 253	144
55.	Equivalent mean V luminosity profile for NGC 253	146
56.	Equivalent mean R luminosity profile for NGC 253	147
57.	Equivalent mean I luminosity profile for NGC 253	148
58.	Relative V integrated luminosity curves for NGC 253.	154
59.	Relative R integrated luminosity curves for NGC 253.	155
60.	Relative I integrated luminosity curves for NGC 253.	156
61.	Decomposition of the V mean minor axis.	167
62.	Decomposition of the V mean major axis.	168
63.	Decomposition of the I mean minor axis.	169
64.	Decomposition of the I mean major axis.	170

Abstract of Dissertation Presented to the Graduate School
of the University of Florida in Partial Fulfillment of the
Requirements for the Degree of Doctor of Philosophy

VISUAL, RED AND INFRARED PHOTOGRAPHIC SURFACE
PHOTOMETRY OF NGC 55 AND NGC 253

By

Gregory L. Fitzgibbons

August 1990

Chairman: Stephen T. Gottesman
Major Department: Astronomy

Detailed photographic surface photometry is presented for the Sculptor Group galaxies NGC 55 and NGC 253. Observations in visual, red and infrared light from long and short exposure plates are used to produce isophote maps as well as major and minor axis profiles. The standard photometric parameters are derived and V-R, R-I and V-I colors are presented for the major and minor axes.

The integrated magnitude of NGC 55 is: $V_T = 8.17$, $R_T = 7.94$ and $I_T = 7.30$. A thickening of the disk is detected that increases with increasing wavelength, indicating the presence of a faint, red halo. At the detection limits of $V = 27.6$ magnitude per square arc second, $R = 27.8$ magnitude per square arc second, and $I = 27.0$ magnitude per square arc second, the size of NGC 55 is $35'.9 \times 9'.5$ (18.6 kpc \times 4.9 kpc), $42'.6 \times 10'.2$ (22.1 kpc \times 5.3 kpc) and $35'.8 \times 12'.8$ (18.5 kpc \times 6.6

kpc) at the assumed distance of 1.78 Mpc. The asymmetry of the galaxy is discussed.

The integrated magnitude of NGC 253 is: $V_T = 7.35$, $R_T = 6.41$ and $I_T = 5.75$. The disk appears to thicken with increasing wavelength, again indicating the presence of a red halo. At limits of $V = 26.9$ magnitude per square arc second, $R = 25.9$ magnitude per square arc second, and $I = 26.4$ magnitude per square arc second, the size of NGC 253 is $36'.3 \times 16'.4$ (30.1 kpc \times 13.6 kpc), $35'.0 \times 12'.3$ (29.0 \times 10.2 kpc), and $42'.8 \times 24'.2$ (35.5 kpc \times 20.1 kpc) at the assumed distance of 2.85 Mpc. A large spur is detected to the south that is most obvious in the infrared image. It increases the size to $42'.8 \times 31'.4$.

A three component model of the visual and infrared luminosity of NGC 253 is discussed. The relative contributions of a $r^{0.25}$ spheroid, an exponential disk, and a spiral arm component are determined.

CHAPTER I INTRODUCTION

Objective

The last ten years have witnessed an almost explosive growth in surface photometry of galaxies. Photographic plates, photoelectric photometers, and solid state charge-coupled devices (CCDs) have all been used as detectors. And yet, the luminosity, luminosity profiles, colors, and size are unmeasured quantities for most bright galaxies. In addition, an examination of published surface photometry (Davoust and Pence 1982; Pence and Davoust 1985) shows that most of the published observational material is in the B and V passbands, although a trend toward longer wavelengths can be discerned. It is desirable to supplement the blue and yellow data with longer wavelength measurements for a variety of reasons: (1) red and infrared passbands allow better penetration of obscuring dust (Elmegreen 1981), (2) an underlying old stellar component may be revealed (Schweizer 1976), (3) a halo or extended spheroidal component may be detected (see, e.g., Spinrad et al. 1978), and (4) color indices such as (V-I) can give information regarding the stellar constituents of a galaxy and be of particular value when given as a function of position.

Even for nearby galaxies much work remains to be done before we can hope to understand their structure and evolution. Their closeness causes them to have large angular sizes, and this makes CCD or photoelectric photometry difficult because these techniques are currently better suited to making brightness measurements of objects of small angular extent. On the other hand, photographic surface photometry can be done for almost any galaxy accessible to a CCD, and especially nearby objects because of the availability of wide field cameras. Also, the use of hypersensitizing techniques (Schoening 1978; Smith and Hoag 1979) allows the red and near infrared spectral region (600 - 900 nm) to be photographed with reasonably short exposure times. Thus, it is possible to conduct a multicolor investigation of the structure of galaxies with a particular emphasis on those longer wavelengths which trace the cooler stellar component that comprises the bulk of the luminous matter.

In this work we present detailed photographic surface photometry of the nearby galaxies NGC 55 and NGC 253, in V, R, and I passbands. The main objective is to provide a set of photometric data that can be used to determine the properties of the disk and halo components that comprise these galaxies, and measure their contributions to the overall luminosity. The result is a more complete picture of the structure of these galaxies, which will in turn improve our understanding

of other galaxies. A photograph of each galaxy appears in Chapter III and Chapter IV.

The observational material and reduction methods are discussed in Chapter II. In Chapter III the standard photometric parameters, as described by de Vaucouleurs (1962), are determined for NGC 55. The size and shape of this galaxy are discussed and compared to earlier work. Color indices and integrated magnitudes are presented and corrections for absorption are made. In Chapter IV, the standard photometric parameters are determined for NGC 253. As for NGC 55, the size, shape and colors are discussed and compared to previous studies, and integrated magnitudes and colors are presented and corrected for absorption. In addition, the luminosity profiles are decomposed into a disk, spheroid and spiral arm model. The results are summarized in Chapter V.

The choice of these two galaxies was based on several criteria: the galaxies should be free from interacting neighbors, they should be viewed at high inclinations so their halos can be studied, previous B band photometry should exist for comparison purposes, and kinematic data in the form of rotation curves should be available. The first criterion was the most difficult to satisfy. Both galaxies are members of the Sculptor group, a loose collection of galaxies about 2.4 Mpc distant, with NGC 247, NGC 300 and NGC 7793 as additional members (Puche and Carignan 1988). Neither NGC 55 nor NGC 253 has a close companion. Hummel, Dettmar and Wielebinski (1986)

place NGC 300 and an anonymous dwarf galaxy at projected distances of 320 and 180 kpc, respectively, from NGC 55. Puche and Carignan put the dwarf more than one Mpc away, but have NGC 253 and NGC 247 about 250 kpc apart. Lewis (1969) found displaced HI centroids in NGC 247 and NGC 253 and took this to indicate that these galaxies form a "stable pair." And Pritchett et al. (1987) in a study of the mean magnitudes of carbon stars in NGC 55 derived a distance that supports it forming a pair with NGC 300. Based on optical appearances, there are no compelling reasons to believe recent interactions have occurred. However, NGC 253 does show an optical "tail" or "spur" (Beck, Hutschenreiter and Wielebinski 1982) which is also detected in radio continuum observations (Beck et al. 1979), and it shows evidence of recent starburst activity. Consequently, the possibility of past interactions cannot be ruled out.

Previous Studies

NGC 55

Photographic surface photometry of NGC 55 was first done by de Vaucouleurs (1961) in the photographic (pg) passband (a Kodak 103a-0 plate and no filter). He found the maximum dimensions to be about $1^\circ \times 0.2^\circ$, but reliable measurements stopped at $45' \times 9'$, corresponding to about 26 magnitude per square arc second, hereafter written as $\mu_{pg} = 26$. The total integrated magnitude is given as 7.9, which, for his assumed distance of 2.3 Mpc, corresponds to an absolute magnitude of

$M_T = -19.1$. Attention is called to the pronounced asymmetry present in the galaxy's appearance. He found the luminosity distribution to be approximately exponential in the outer regions, but with the gradient increasing near the nucleus, and the west side showing the largest change. Based on the asymmetrical structure of NGC 55, de Vaucouleurs proposed that it is similar to the Large Magellanic Cloud (LMC) and is seen looking down the bar. Higher resolution surface photometry in blue light is given by Sersic (1968) but it does not go to as faint a level as that of de Vaucouleurs.

Spectroscopic observations of HII regions by de Vaucouleurs yielded three velocity measurements which he used to calculate a mass of $2 - 4 \times 10^{10}$ solar masses (M_\odot), and a M/L of $3.3 - 6.6 M_\odot/L_\odot$ ($L_\odot = 1$ solar luminosity). The inclination was assumed to be 90° (edge-on) and the position angle of the major axis was taken to be 105° .

The rotation velocities of the inner region of NGC 55 were measured by Seielstad and Whiteoak (1965) using the 21 cm emission line of HI and an assumed inclination of 79° . Robinson and van Damme (1966), also observing HI, measured velocities out to about $40'$ on the southeast side of the galaxy, possibly indicating a turnover in the velocity curve. The inclination was assumed to be 90° . Both sets of measurements show the center of rotational symmetry displaced about $2.5'$ southeast of the optical nucleus. For an adopted distance of 1.74 Mpc, Robinson and van Damme found the total

neutral hydrogen mass $M_{\text{HI}} = 2 \times 10^9 M_{\odot}$, the total mass of NGC 55 to be $2.5 \times 10^{10} M_{\odot}$, and a $M/L = 7.2$.

De Vaucouleurs (1981), with more extensive optical data than previously used, mapped the velocity field and found curious distortions of the velocity contours in the disk, indicative of motion more complicated than purely circular rotation.

Observing at 843 MHz, Harnett and Reynolds (1985) found the peak emission offset $1.3'$ southeast of the nucleus. The scale height of the radio continuum emission was $35'' \pm 7''$.

Using the surface photometry of de Vaucouleurs (1961), and the rotation data of Seielstad and Whiteoak (1965) and that of Robinson and van Damme (1966), Comte (1985) calculated a simple two-component mass model of a constant M/L disk and a spherical halo. For a disk $M/L = 1$, the derived total mass is $3.9 \times 10^{10} M_{\odot}$ and the ratio of disk mass to halo mass is 0.03.

Hummel, Dettmar and Wielebinski (1986) observed NGC 55 at 6 cm and 21 cm. For an assumed distance of 2.0 Mpc, they derived a total HI mass of $1.5 \times 10^9 M_{\odot}$ and a total galaxy mass of $2 \times 10^{10} M_{\odot}$. The HI extent is comparable to the optical dimensions and is not centered on the bar. Also, the HI distribution looks disturbed. The continuum emission is mainly concentrated on the bar and dominated by a slightly offset triple source, strongly suggesting ongoing star formation. They, too, find an asymmetry between the mass and

light distributions. Almost 80% of the total mass resides in the disk, the remainder in the off-centered bar component. The centers of the two components are 3.5' apart. About 30% of the blue light is in the bar region. The centroids of total light and neutral hydrogen emission are 2.7' and 2.1' southeast of the bar, respectively. The continuum emission is also displaced about 1' southeast of the bar. They find an inclination of about 80° , a position angle of 109° from their HI data, and a $M/L = 3.4$. Additional continuum information is available from Condon (1987) in the form of a map of 1.49 Ghz observations.

From HI studies of the Sculptor group galaxies, Puche and Carignan (1988) calculate the dynamical M/L for the group to be 83 ± 10 . For NGC 55 they find $M/L = 3.6$.

Graham (1982) was able to resolve old red giants in NGC 55 and placed an upper limit of 1.9 Mpc on its distance. Da Costa and Graham (1982) found three globular clusters, including a young cluster similar to those found in the LMC, and, assuming the distance given above, found an absolute magnitude of -9.1. This is comparable to the young clusters NGC 1818, NGC 1866 and NGC 2004 in the LMC. A distance modulus of 26.57 ($= 2.06$ Mpc) is given by de Vaucouleurs (1986) based on the brightest blue stars, the brightest superassociation, and the brightest cluster. A much smaller distance of 1.34 ± 0.08 Mpc was derived by Pritchett et al.

(1987) using the mean magnitude of carbon stars found in NGC 55.

The apparent distribution of stars perpendicular to the major axis was investigated by Kiszkurko-Koziej (1988). A difference between the north and south sides led to the conclusion that the inclination is between 80.8° and 81.7° , with the north side being closer to us. For a distance of 1.5 Mpc, Kiszkurko-Koziej determined the scale height of the young disk to be between 0.10 and 0.14 kpc, and scale height of the old disk to be between 0.18 and 0.21 kpc.

NGC 253

Unlike the case of NGC 55, an extensive body of literature exists for NGC 253. Pence (1978) gives a listing of publications through 1978. Here, rather than referencing all published papers, only those which have some bearing to the photometry or kinematics of NGC 253 will be mentioned. Attention will be confined for the most part to results published after 1978; the interested reader is referred to Pence's listing for earlier material.

Sersic (1968) presented photographic photometry in the B band of the bright inner region of NGC 253. Much deeper photometry was done by Freeman, Carrick and Craft (1975) in their photographic search for a corona to the galaxy. For an assumed distance of 3.0 Mpc they found no clear evidence for a corona at radii greater than 15 kpc along the minor axis, down to $\mu_b = 29.2$. Pence (1978) did detailed photographic

photometry of NGC 253 down to $\mu_b = 29$ and photoelectric drift scans in U, B and V. The maximum detected dimensions were $60' \times 26'$. The standard photometric parameters were derived, including a total magnitude $B_T = 8.05$ and a total luminosity $L_T = 2.65 \times 10^{10} L_\odot$ for an assumed distance of 2.5 Mpc. A three-component luminosity model consisting of spheroid, disk and spiral arm components was derived from the luminosity profiles. Spinrad et al. (1978) looked for a halo in red (r) and near infrared (i) light using photographic and photoelectric photometry. Their profiles indicate an extensive, faint spheroidal component that rapidly fades in brightness with increasing radius, and has an almost constant $r - i = 0.7$. The total spheroidal luminosity was found to be greater than or comparable to the disk luminosity. In a qualitative study of the optical halo around NGC 253, Beck, Hutschenreiter and Wielebinski (1982) examined enhanced images of deep plates taken in blue light, along with red and near infrared images. They found an extended halo that was more pronounced on the reddest plates, and that roughly coincided with the radio spur detected earlier by Beck et al. (1979). The minor axis could be followed out $10'$ from the nucleus and they concluded, in agreement with Spinrad et al. that any color gradient, if present, was small.

Telesco and Harper (1980) examined the infrared emission of NGC 253 between 1 and $300 \mu\text{m}$ over the inner $30''$ and calculated an integrated luminosity of $2.8 \times 10^{10} L_\odot$.

Photographic and photoelectric observations in the near infrared were published by Uyama, Matsumoto and Thomas (1984). The central regions of NGC 253 were examined at 0.7 - 0.9 μm , 1.25 μm and 2.2 μm . The color index (0.8 μm - 2.2 μm) of the disk ranged from 2.0 to 2.8, corresponding to colors of M0 III and M4 III stars. They found a color gradient increasing toward the galaxy's center where the visual absorption also increases. The inner disk was also observed in the near infrared in the J (1.27 μm), H (1.65 μm) and K (2.2 μm) bands and at the 2.6 mm line of CO emission by Scoville et al. (1985). Their major axis profiles show two components: a nuclear peak of diameter $\approx 20''$ and an extended, inner disk of diameter $\approx 360''$. The 2.2 μm distribution is dominated by a barlike feature at position angle 17° east of the major axis and extending $120''$ on either side of the nucleus. The nucleus itself is extremely red with respect to the disk. Both the nucleus and the inner disk show excess 2.2 μm radiation, probably caused by hot dust.

Young et al. (1989) used IRAS data to derive the global properties of NGC 253 including infrared luminosities at 12, 25, 60, and 100 μm , and total masses of gas and dust. For an assumed distance of 3.4 Mpc, the infrared luminosity (1 - 500 μm) is $\log L_{\text{IR}} = 10.42 L_\odot$, the total dust mass is $\log M_{\text{dust}} = 6.54 M_\odot$, $\log M_{\text{HI}} = 9.65 M_\odot$, and $\log M_{\text{H}_2} = 9.37 M_\odot$. The integrated fluxes at 12, 25, 60, and 100 μm are, respectively, 62.04, 147.34, 1157.2, and 1760.2 Jy.

The neutral hydrogen in NGC 253 was mapped by Huchtmeier (1972, 1975) who found a total HI mass of $4.1 \times 10^9 M_{\odot}$ for an assumed distance of 3 Mpc. Combes, Gottesman and Weliachew (1977), unlike Huchtmeier, found a centrally peaked HI distribution and a total HI mass of $4.9 \times 10^9 M_{\odot}$, using an assumed distance of 3.4 Mpc. Whiteoak and Gardner (1977), assuming the same distance, found a total HI mass of $3.8 \times 10^9 M_{\odot}$.

Radio continuum observations made at 8.7 GHz by Beck et al. (1979) detected emission 6' south and 5' north of the plane of the galaxy. They found the emission to be nearly constant between 2.5 and 4.5 kpc from the plane for an assumed distance of 3.4 Mpc and detected the "spur" extending toward the southwest, as mentioned earlier. Hummel, Smith and van der Hulst (1984) made continuum observations at 4.9 GHz. They divided the emission into three main components: a central source ($\approx 50\%$ of the total emission), an inner disk containing a bar ($\approx 30\%$) and an outer disk ($\approx 20\%$). The inner disk has a half power diameter of ≈ 5 kpc (for an assumed distance of 2.2 Mpc) and has a ridge of radio emission coinciding with the optical bar. The outer disk has a total extent of ≈ 15 kpc. There is some suggestion of the presence of a radio spiral arm. Other continuum observations of NGC 253 were made by Harnett and Reynolds (1985), at 843 MHz, and Condon (1983, 1987) at 1.465 and 1.49 GHz.

Fabbiano (1988) found the inner disk of NGC 253 to be quite bright in X-rays (0.2 - 10.2 keV), and noted extended X-ray emission with no optical or radio counterpart in the northern side. The major axis X-ray surface brightness profile can be traced out to $\approx 10'$ and is steeper than the optical (blue) profile. The minor axis profile can be traced out to $\approx 5'$ toward the southeast and $\approx 10'$ toward the northwest. For an assumed distance of 3.4 Mpc the X-ray luminosity $L_x = 1.1 \times 10^{40}$ erg/sec and 2.5×10^{40} erg/sec corresponding to the 0.2 - 3.5 keV and 1.2 - 10.2 keV ranges, respectively.

The large infrared flux from the nucleus of NGC 253 has led various investigators to classify this galaxy as a starburst galaxy (Rieke and Low 1975; Rieke et al. 1980; Donas and Deharveng 1984; Rieke, Lebofsky and Walker 1988). Examination of the nuclear region at 1.413 and 4.885 GHz (Condon et al. 1982) and at 1.490 and 4.860 GHz (Antonucci and Ulvestad 1988) showed numerous bright, compact sources, believed to be associated with the starburst activity. Turner and Ho (1983), observing at 2 and 6 cm, confirmed the presence of large numbers of HII regions and young stars. They proposed the existence of 4.7×10^4 OB stars in the nucleus to account for the observed flux. Hummel, Smith and van der Hulst (1984) measured the power at 4.9 GHz to be about 10^{21} W/Hz in a beam half power size of approximately $0.2' \times 0.1'$. From a compilation of measurements extending from 85.6 MHz to

10.7 GHz they calculated a spectral index of $\alpha = -0.43 \pm 0.07$ for the nuclear region, which they attribute to a starburst. Keel (1984), in a spectrophotometric study of the nuclei of strong radio sources, found evidence of both nonthermal activity and recent star formation in NGC 253. He proposed it as a LINER (Low Ionization Narrow Emission-line Region), a low ionization nucleus with a weak Seyfert core. Scoville *et al.* (1985) calculated a minimum star formation rate of OBA stars to be $2.3 M_{\odot}/\text{yr}$ assuming the observed far-infrared luminosity within a radius of 0.5 kpc is produced by young stars. And McCarty, Heckman and van Breugel (1987) found spectroscopic evidence for large-scale winds near the center of NGC 253, probably from starburst activity, and extensive regions of ionized gas along the minor axis. They also noted that the high latitude ionized gas southeast of the nucleus appears to coexist with the diffuse soft X-ray emission.

Numerous kinematic studies have been made of NGC 253. Burbidge, Burbidge and Prendergast (1962) obtained a rotation curve out to $290''$ from optical spectra and noted non-circular motions in the nuclear region. Demoulin and Burbidge (1970) also made spectroscopic observations of the central region but with a higher dispersion and found material blue-shifted up to 120 km/sec. Turbulent velocities were noted southeast of the nucleus, up to 150 km/sec. They proposed a violent event in the center some $1 - 2 \times 10^7$ years ago, ejecting a cone or column of gas. Huchtmeier (1975) published HI rotation

measurements out to 17.5'. The maximum velocity was 205 km/sec at a radius of 8' from which he derived a total mass of $1.4 \times 10^{11} M_{\odot}$ using a Brandt curve and a distance of 3 Mpc. Gottesman et al. (1976) observed the central region of NGC 253 in the 21 cm absorption line and found an excess of blue-shifted gas, indicating an outflow. Combes, Gottesman and Weliachew (1977) also found evidence for noncircular motions in the central region and noted faster rotation of HII than HI about 4.5' northeast of the center. Using optical spectra, Ulrich (1978) studied the gas flowing out of the nucleus and put it at 0.01 M_{\odot} /yr. She hypothesized a population of 10^3 10^6 stars could account for the flow. Pence (1978) used 25 H α interferograms of the entire bright disk to measure velocities, extending from the nucleus out to a maximum distance of 650" and derived a total mass of $1.42 \times 10^{11} M_{\odot}$, in agreement with Huchtmeier. He also noted noncircular motions in excess of 50 km/sec in several areas, and pointed out that the streaming motions within 200" of the nucleus are similar to that predicted by a simple kinematic model of gas flow near a bar. Scoville et al. (1985), assuming a distance of 3.4 Mpc, estimated the total mass of the H $_2$ inside a radius of 4 kpc to be approximately $2 \times 10^9 M_{\odot}$, 7% of the dynamical mass within the same radius. A plume extending northward about 1.5 kpc from the nucleus (for an assumed distance of 3.1 Mpc) and moving at 168 km/sec was detected by Turner (1985) observing the OH line at 1667 MHz, and may be related to the starburst

nature of this galaxy. Finally, Canzian, Mundy and Scoville (1988) observed the molecular gas in the bar of NGC 253 in the CO emission line. They found it to have an angular extent of $39'' \times 12''$ at position angle 64° and, at an assumed distance of 3.4 Mpc, a mass in molecular clouds of $4.8 \times 10^8 M_\odot$, 0.4 times the dynamical mass of the region; hence, the gas is a significant contributor to the potential. The gas appears to rotate as a rigid body with a steep rotation curve, although the gradient is not as steep as that found by Gottesman et al. Canzian and co-workers concluded that models of barred spirals may not apply to galaxies with so much gas.

Lewis and Robinson (1973) give the total mass of the Sculptor group of galaxies as $(4.4 \pm 1.5 \text{ p.e.}) \times 10^{11} M_\odot$, almost all of which was determined from 21 cm rotation curves. Their virial mass, excluding NGC 24 and NGC 45, is $6.1 \times 10^{12} M_\odot$. From HI studies of the Sculptor group, Puche and Carignan (1988) find the total mass to total blue luminosity, M/L_B , for NGC 253 to be 12.0, and for the dynamical M/L_B for the group, $83 \pm 10 M_\odot/L_\odot$.

There have been two recent determinations of the distance to NGC 253, both using different indicators. Blecha (1986), in a search for globular clusters, detected 25 reliable candidates within $13'$ of the center, with a $r^{0.25}$ spatial distribution. Matching the luminosity function to our galaxy's globulars yielded a distance of 2.88 ± 0.5 Mpc. De Vaucouleurs (1986) gives a distance modulus of 27.42

(= 3.05 Mpc) based on the HI line width (B and H bands) Tully-Fisher relation. Pence (1978) gives eight previous determinations of the distance to NGC 253 or the Sculptor group, the mean of which is 2.9 ± 0.67 Mpc.

Adopted Distances

Recent distance determinations for NGC 55 are listed in Table 1. Sandage and Tammann used blue and red supergiants; Graham used old red giants; de Vaucouleurs used the brightest blue stars, super associations and the brightest clusters; and Pritchett et al. used carbon stars. The value from Puche and Carignan is the mean of two values they list based on tertiary indicators (de Vaucouleurs 1979a,b) which they derived using the relations given by de Vaucouleurs and Davoust (1980) and Bottinelli et al. (1983). Giving a weight of two to the value of Puche and Carignan yields a mean distance of 1.78 ± 0.34 Mpc which will be adopted for this work. At this distance, one arc second is 8.6 pc; one arc minute is 518 pc. This corresponds to 0.85 kpc/mm on the photographic plates used in this study.

TABLE 1
DISTANCE TO NGC 55

Source	Distance (Mpc)
Sandage and Tammann (1981)	2.3
Graham (1982)	1.9
de Vaucouleurs (1986)	2.06
Pritchett <u>et al.</u> (1987)	1.34
Puche and Carignan (1988)	1.56

Table 2 lists recent distance determinations for NGC 253.

TABLE 2
DISTANCE TO NGC 253

Source	Distance (Mpc)
Sandage and Tammann (1981)	4.0
Blecha (1986)	2.88
de Vaucouleurs (1986)	3.05
Puche and Carignan (1988)	2.59

The Sandage and Tammann value is again based on blue and red supergiants. The values of Blecha and de Vaucouleurs are based on globular clusters and the Tully-Fisher relation and have already been described. Four values listed by Puche and Carignan, based on tertiary indicators, were combined and the mean used. As for their NGC 55 values, these are based on the work of de Vaucouleurs, de Vaucouleurs and Davoust, and Bottinelli et al. A weight of four is given to this value of the distance. The resulting mean value of all the distances, 2.85 ± 0.54 Mpc will be adopted for this work. At this distance, one arc second is 13.8 pc and one arc minute is 829 pc. This corresponds to 1.35 kpc/mm on the photographic plates used in this study.

CHAPTER II PHOTOGRAPHIC MATERIAL AND REDUCTION METHODS

Observations

The Telescope

Photographic surface photometry of NGC 55 and NGC 253, which have angular sizes of more than one-half degree, required the use of a telescope with a field of view of at least several degrees. The 70/100 cm Maksutov Astrograph at Cerro el Roble (Capilla de Caleu), operated by the University of Chile, was used for all the observations. The telescope had a 210 cm focal length and a plate scale of 98.2"/mm. The field of view was 25 square degrees on 18 cm x 18 cm plates. From geometrical considerations (Dawe 1984) the unvignetted field had a radius of about 2° and therefore did not affect the galaxy images. Located at latitude $-32^\circ 58' 54''$, west longitude $71^\circ 01' 10.5''$, and an elevation of 2220 meters, the observatory was in the coastal range of mountains. The site had good seeing (typically one arc second) and moderately dark skies.

Plates and Filters

Observations were begun in late 1980 and continued through late 1984. Of the many plates taken during this period, those judged to be the best by visual examination were

selected for analysis. The plates used and other relevant information are listed in Table 3 for NGC 55 and in Table 4 for NGC 253. The passbands used were defined as follows: the visual (V) was a Kodak IIa-D emulsion behind a 2mm Schott GG 495 filter; the red (R) was a Kodak IIIa-F emulsion behind a 2mm Schott RG 610 filter; and the infrared (I) was a Kodak IV-N emulsion behind a 2mm Schott RG 695 filter. The wavelength intervals of each passband were approximately 500 - 650 nm, 610 - 700 nm, and 700 - 900 nm. The effective wavelength λ_{eff} was calculated using

$$\lambda_{eff} = \frac{\int_0^{\infty} S(\lambda) \lambda d\lambda}{\int_0^{\infty} S(\lambda) d\lambda} \quad (1)$$

where $S(\lambda)$ is the product of the emulsion sensitivity and the filter transmission at each λ . For the V, R and I passbands used here the effective wavelengths were 572.3 nm, 656.0 nm, and 794.1 nm, the last value being that of Koo (1985). The RG 610 filter was broken in August 1982 and a filter known simply as the "Russian" filter was substituted for it. This "new" filter was 1.5 mm thick glass with a transmission curve that closely matched that of a 2 mm Schott OG 590, although it did not have as high a transmittance. It was used for the short exposure plates and the matching of these observations with those taken with the RG 610 filter is discussed later. The resulting bandpass was about 590 - 700 nm and $\lambda_{eff} = 645.9$ nm.

TABLE 3

PLATE MATERIAL NGC 55

Plate #	Date	Observer	Exposure	Emulsion	Filter	Size	Developer
6467	11/17-18/81	Fitzgibbons	115 ^a	IIIIa-F ^a	RG 610	18x18 cm ²	MWP-2 9 ^a
6473	11/19-20/81	Fitzgibbons	120 ^a	IIIIa-F ^a	RG 610	18x18 cm ²	MWP-2 9 ^a
6487	11/24-25/81	Fitzgibbons	60 ^a	IIa-D	GG 495	18x18 cm ²	D-19 5 ^a
6488	11/24-25/81	Fitzgibbons	150 ^a	IIIIa-F ^a	RG 610	18x18 cm ²	MWP-2 9 ^a
8544	11/3-4/83	Costa	20 ^a	IIIIa-F	Russian	18x18 cm ²	D-19 5 ^a
9232	8/28-29/84	Costa ^b	60 ^a	IIa-D	GG 495	18x18 cm ²	D-19 5 ^a
9241	8/30-31/84	Costa ^b	15 ^a	IIa-D	GG 495	18x18 cm ²	D-19 5 ^a
9281	9/26-27/84	Costa ^b	60 ^a	IV-N ^c	RG 695	18x18 cm ²	D-19 7 ^a
9403	11/18-19/84	Costa ^b	60 ^a	IV-N ^c	RG 695	18x18 cm ²	D-19 5 ^a
9416	11/19-20/84	Costa ^b	70 ^a	IV-N ^c	RG 695	18x18 cm ²	D-19 5 ^a
9440	11/21-22/84	Costa ^b	20 ^a	IV-N ^c	RG 695	18x18 cm ²	D-19 5 ^a

Notes: ^a Plate was baked in 4% H₂ forming gas at 65° C.

^b Observers were Costa and Gonzalez.

^c Plate was bathed in 0.001M AgNO₃ for 4^a.

TABLE 4

PLATE MATERIAL NGC 253

Plate #	Date	Observer	Exposure	Emulsion	Filter	Size	Developer
5394	1/2-3/81	Fitzgibbons	60 ^m	IIIa-F ^a	RG 610	18x18 cm ²	MWP-2 9 ^m
5396	1/2-3/81	Fitzgibbons	20 ^m	IIa-D ^a	GG 495	4 x 5 in ²	D-19 5 ^m
5410	1/3-4/81	Fitzgibbons	30 ^m	IIa-D ^a	GG 495	4 x 5 in ²	D-19 5 ^m
8545	11/3-4/83	Costa	20 ^m	IIIa-F	Russian	18x18 cm ²	D-19 5 ^m
9243	8/30-31/84	Costa ^b	10 ^m	IIa-D	GG 495	18x18 cm ²	D-19 5 ^m
9301	9/27-28/84	Costa ^b	60 ^m	IV-N ^c	RG 695	18x18 cm ²	D-19 5 ^m
9302	9/27-28/84	Costa ^b	15 ^m	IV-N ^c	RG 695	18x18 cm ²	D-19 5 ^m
9309	9/28-29/84	Costa ^b	60 ^m	IV-N ^c	RG 695	18x18 cm ²	D-19 5 ^m
9404	11/18-19/84	Costa ^b	60 ^m	IV-N ^c	RG 695	18x18 cm ²	D-19 5 ^m
9417	11/19-20/84	Costa ^b	70 ^m	IV-N ^c	RG 695	18x18 cm ²	D-19 5 ^m

Notes: ^a Plate was baked in 4% H₂ forming gas at 65° C.

^b Observers were Costa and Gonzalez.

^c Plate was bathed in 0.001M AgNO₃ for 4^m.

The choice of plate and filter combinations was largely determined by the purpose of the investigation. The outer regions of galaxies are faint and the light received is only a small fraction of the contribution from the background. Hence, to enhance detection of these faint features, emulsions with good contrast and relatively high signal-to-noise ratios were used (Latham 1978; Furenlid 1978). In addition, noise introduced during scanning with the microdensitometer, caused by granularity, was reduced by the choice of fine-grained emulsions. The filters, with the emulsions, approximate standard photometric passbands and allow for photoelectric calibration of the data. Early type stars and dust will be most evident in the V exposures, HII regions in the R, and underlying disk stars and old, cool stars will dominate the I exposures.

Photographic Techniques

Many of the plates were hypersensitized. The IIa-D and IIIa-F plates were baked in 4% H₂ forming gas at 65° C and stored in dry nitrogen until used. Each IV-N plate was bathed for four minutes in a 0.001M AgNO₃ solution while being agitated on a Mount Wilson type rocker. This was followed by hand agitation for two minutes in a bath of isopropanol. The back of the plate was dried with a paper towel and the plate was then placed emulsion up and rapidly dried under a stream of cool air on a rotating turntable, following a procedure similar to that described by Schoening (1978). Because IV-N

plates experience a rapid growth of fog level within hours of silver nitrate bathing, each plate was used immediately after being prepared. Also, the isopropanol dissolved the anti-halation backing. This caused an increase in the sizes of stellar images arising from light reflecting off the interface between the emulsion and the glass substrate, but did not appear to have any other adverse effects. Although hypersensitization caused an increase in fog level and a decrease in signal-to noise ratio (Hoag, Furenlid and Schoening 1978), this loss was more than offset by the increase in speed of the emulsion.

The V and R exposures were done with no moon in the sky. At least two of the I exposures were taken with the moon above the horizon (plates 6461 and 9309). This was not a problem with the IV-N emulsion and RG 695 filter (Schoening 1978) because the scattered moonlight is primarily smaller wavelengths than the filter passes. In no instance was the moon near the object being photographed.

The nucleus of each galaxy was considerably brighter than the outermost regions; as a result, an exposure deep enough to record the outer disk and halo overexposed the nucleus. This necessitated the taking of both long and short exposures of each galaxy with each emulsion. Each color had at least one short and one long exposure.

In the beginning the IIIa-F and IV-N plates were developed for nine minutes in MWP-2 (Diffley 1968) on a Mount

Wilson type rocker, but this practice was abandoned when less than satisfactory development seemed to be the usual result. Subsequently all plates were hung vertically in a large tank of D-19 for five minutes with nitrogen burst agitation every 30 seconds. Plate 9281 was in the developer for about seven minutes because of a timer problem, but suffered no adverse effects. Following development, the plates were stopped, fixed, washed and given a rinse in Photo-Flo solution. All treatments were done at approximately 20° C.

Calibration

All of the plates were calibrated using a sixteen-hole tube sensitometer described elsewhere (Fitzgibbons 1981). The light source had a color temperature of about 3100 K. A set of Schott filters matching those used in the telescope plateholder was available for the sensitometer. The resulting set of spots was used to construct the characteristic curve for each plate.

Errors due to the photometric calibration are discussed by de Vaucouleurs (1948). These can arise from the calibration device itself and the exposure conditions, as well as the history of the emulsion before exposure and during development. To minimize the calibration errors, whenever possible the plate in the telescope and the plate in the sensitometer were cut from the same original 20 cm x 25 cm plate. Both pieces were hypersensitized together, given almost simultaneous exposures of the same duration, and

developed together immediately afterward. The sensitometer was kept in a closet on the observing floor so the temperature and humidity of it and the telescope were closely matched. In some cases only smaller plates were available, either 18 cm x 18 cm or 4 in x 5 in. For these, plates from the same box were hypersensitized together with one being used in the telescope and another in the sensitometer. In all cases, both the object plate and the calibration plate received identical exposures and were developed together.

Plate Digitization

Equipment

The plates were digitized with the Boller and Chivens PDS 1010A microdensitometer at the U. S. Naval Observatory Time Service Alternate Station at Miami, Florida. It was equipped with a computer-controlled x-y stage that could accomodate plates up to 25 cm x 25 cm. A program called SCFTZ controlled the machine and performed a raster scan. The x and y limits of the scans, scanning speed, distance between samples, and the spacing in y between scans were entered as input data. The output densities were recorded on magnetic tape after each scan row.

At some time the machine caused density measurements in excess of about 2.5 to become compressed and therefore no longer linear (J. Martin, private communication). When this occurred is not known. However, this should not have had an adverse effect on the measurements since the calibration

plates would also have been affected, and few, if any regions of interest in this study had densities as high as 2.5. Another, more serious problem was the appearance of bands in the digitized images of four plates. These are believed to have been caused by drops in voltage to the microdensitometer at semi-regular intervals. Later, a regulated power supply was used to run the microdensitometer and these bands were either absent or much reduced on the output images.

Technique

Before a plate was digitized, a coordinate system was chosen to define the orientation of the field. This coordinate system served to ensure that as many plates as possible were oriented the same way so identical areas were scanned on each. This facilitated the adding or subtracting of images by preventing any shifts or rotations that might otherwise be introduced. The coordinate system was defined by selecting two widely spaced stars near an edge of a plate that were at approximately the same right ascension or declination. The object plate was then positioned such that these stars defined the x-axis of a scan. The calibration plate was then placed on the stage near the object plate and positioned such that the x scan direction passed through each row of spots. Although the coordinate system defined in this way was used for many of the plates, other systems using different pairs of stars had to be used, too. These were required when the plates didn't have the same two stars used previously, either

because they were smaller plates, or because the telescope was not pointed at the same position.

Digitization was done in a three-step process: first, the calibration plate was scanned and then two scans were made of the object plate. The microdensitometer was zeroed at the level of the fog on the calibration plate, and a $50\text{ }\mu\text{m} \times 50\text{ }\mu\text{m}$ aperture used to scan the calibration spots, with two scans being made through each row of eight spots. The step size in x was $50\text{ }\mu\text{m}$ as was the offset in y between scans.

The plate with the object was divided into two overlapping regions; an inner, or object field containing the galaxy, and an outer, or background field covering most of the plate and containing the inner field. The outer field, which extends far beyond the visible object, was measured with the same aperture as was used for the calibration plate. The area chosen was typically $15\text{ cm} \times 15\text{ cm}$, although the small plates and short exposure plates had smaller areas. Because of the large area of the outer field, widely spaced samples were taken to keep the number of data small. Pairs of scans were made in the x -direction with a sampling interval of $50\text{ }\mu\text{m}$ and a shift in y of $50\text{ }\mu\text{m}$ between each scan. Each pair of scans was separated in the y -direction by either 5 or 10 mm.

The inner field contained both the galaxy and sky background. The area was chosen to extend about twice as far as the galaxy could be seen; on deep $18\text{ cm} \times 18\text{ cm}$ plates this was $5\text{ cm} \times 5\text{ cm}$. On smaller plates a smaller area had to be

chosen but one which still enclosed the galaxy. A star near the nucleus of the galaxy was used to center the area so each plate would have matching inner fields. In all cases the sides of the inner field are parallel to the sides of the outer field. The inner field scans were done with an aperture of $12.5\ \mu\text{m} \times 12.5\ \mu\text{m}$ or $25\ \mu\text{m} \times 25\ \mu\text{m}$, the choice being determined by the diameter of the smallest stellar images. Scans were done with a step size of $12\ \mu\text{m}$ or $25\ \mu\text{m}$, and the spacing between scans was the same as the step size.

As a check on the photometry, for most plates density readings were made of the same position on the plate, before and after the inner field scans. In general, those scans showing drifts larger than a few percent in density were not used in the analysis. Exceptions to this occurred for two of the short exposure plates which had large drifts in the density readings caused by changes in the alignment of the diaphragms in the microdensitometer during scanning. These occurred at or near the end of a scan, and the affected regions were discarded. For the plates for which before and after density readings could not be directly compared, the appearance of the background of the inner region was visually examined on the digitized images. In the one or two cases where the background showed large variations that looked like photometer drift, the images were discarded. The removal of variations caused by probable photometer drift is discussed later in this chapter.

Data Reduction

Numerical Mapping Technique and Reduction of the Outer Field

The data from the microdensitometer scans of the inner field consist of measurements of the galaxy and the surrounding sky. The galaxy image has a component due to the sky brightness which is small in the central regions where a bright nucleus dominates, but which in turn becomes dominant as the outermost extent of the galaxy is reached. Because the contribution to the total luminosity of a galaxy arising from its faintest parts can be large, the sky background must be carefully removed so that only light from the galaxy remains. Fluctuations in the sky level are the major source of error and care must be taken to remove them. Various means have been developed to do this sky subtraction although many are over-simplified and do not adequately allow for variations in sky brightness or plate response over the area considered.

The Numerical Mapping Technique described by Jones et al. (1967) was used for the determination and elimination of the sky background. As they point out, (1) it allows exhaustive use of the information in a photograph of an extended object rather than the narrow sampling along selected cross-sections widely used previously; (2) it permits much more rigorous allowance for the photometric "local errors" of the photographic emulsion and sky background irregularities of various origins which are the main limitations to accurate photometry of faint objects, such as the outer regions of

galaxies; and (3) it is designed for data in digitized form from a scanning microdensitometer. The method has been successfully used in other photometric studies (Barbon, Benacchio and Capaccioli 1976; Tsikoudi 1977; Pence 1978) and only a brief description of it will be given here. Much of the original computer code has been rewritten to enable it to handle larger arrays and to make the density to intensity conversion. The algorithm for fitting the polynomial to the background densities was left unchanged. The reductions were done on the IBM 3090/400 computer of the NERDC at the University of Florida.

Over the inner field of the plate the measurements are composed of contributions from both the galaxy and the sky, I_{G+S} . The outer field has only the sky, I_s , contributing to it. In the Numerical Mapping Technique orthogonal functions are used to analyze the measurements in the outer field and to determine the best approximation to the sky background over the whole plate by least squares techniques. The result is a polynomial in x and y expressing the density at each point. The sky values in the region of the galaxy are calculated by interpolation over the "hole" caused by the inner field. The contribution due to the galaxy alone, relative to the sky is then given by

$$I_G = \frac{I_{G+S} - I_s}{I_s} . \quad (2)$$

Plots of the scans of the outer field were examined for each plate before any analysis was performed. Any scans or pixels that showed obvious irregularities were not included in the background sample. These were caused by scans that were too close to the edge of a plate or that included a defect in the emulsion. The remaining data were then used to map the background.

The background sky measurements of the outer field are composed of two distinct components: (1) a slowly varying continuous component caused by real differences in sky brightness, emulsion sensitivity, etc., and (2) a discrete component due to point sources of light and defects in the emulsion. The two components are treated separately and by different methods.

The discrete component was removed before fitting the continuous component. This was accomplished by fitting a low order polynomial $D(x,y)$, where

$$D(x,y) = D(1) + D(2)x + D(3)y + D(4)x^2 + D(5)xy + \dots \\ \dots + D(10)y^3 \quad (3)$$

by least squares to the density readings $d(x,y)$ of the outer field. Readings which had residual $R(x,y) = d(x,y) - D(x,y)$ greater in magnitude than a specific rejection level, 3σ , were discarded and the process was repeated on the reduced data set until no more residuals were rejected or the distribution was Gaussian, which is to be expected in the ideal case. The

value of β used was between 2 and 3, depending on the analysis cycle, and σ is the standard deviation of the residuals. For an unbiased estimate of the standard deviation of residuals σ , Jones et al. used

$$e_k = \sqrt{\left(\frac{E_k}{N_2 - k} \right)} \quad (4)$$

where $k = 10$ denotes the number of coefficients used to define $D(x,y)$, N_2 is the number of data points and $N_2 - k$ is the number of degrees of freedom remaining after subtracting one for each coefficient $D(k)$ in equation (2) and

$$E_k = \sum_{n=1}^{N_2} (d_n(x,y) - D_n(x,y))^2. \quad (5)$$

With the discrete component of the background removed the continuous component can be mapped. This mapping is complicated by two factors: (1) the remaining outer field data are affected by small random fluctuations (noise), and a certain amount of smoothing is necessary to avoid a rough and physically unrealistic representation; and (2) the distribution of the data points has a large hole in the central region corresponding to the inner field, and this will produce instability over the inner field if a polynomial of too high a degree is used to fit the data.

If the wavelength (shortest distance between two relative maxima or two relative minima) of the approximating polynomial is smaller than the width of the hole, it may oscillate unrealistically over the inner field where there are no data. To guard against this, an upper limit is placed on the degree of the polynomial to keep the wavelength sufficiently large to control instability. The highest permissible degrees in x and y are determined by normalizing the coordinates by a linear transformation so that the limits of the outer field extend from -1 to $+1$ in both x and y . Then the shortest permissible wavelength in normalized coordinates will be the length of the transformed side of the rectangular hole. With the value of the shortest wavelength determined, a standard orthogonal system, Chebychev polynomials, is applied to find the highest permissible degree of the polynomial, using Table 4 on page 41 of Jones et al.

For most of the plates used here, the continuous component of the sky background is represented with a polynomial

$$Y(x,y) = D(1) + D(2)x + D(3)y + D(4)x^2 + D(5)xy + \dots \\ \dots + D(43)xy^7 + D(44)x^8 + D(45)y^8 \quad (6)$$

of degree eight in both x and y . The only exception was plate 5410 which used a polynomial of degree seven. The polynomial may be truncated at some term to effect the desired smoothing of the data mentioned above. The terms of the polynomial are calculated such that they are mutually independent in the

sense that if any term is terminated, the remaining series is still a least squares fit (see Jones et al. p. 42). The criterion for defining the cutoff is to minimize the standard deviation of the residuals as given by equation (4) with k equal to 36 or 45, depending on the degree of the polynomial. By examining how the standard deviation of residuals changes as the number of terms included in the polynomial is changed, and by including terms that make a significant contribution to decreasing the residuals an upper limit on the number of terms is determined.

With the cutoff of terms in the polynomial determined, the remaining background data of the outer field are fitted again by least squares with the adopted number of terms. The polynomial is used to produce a density contour map of the sky over both the outer and the inner fields as shown in Figure 1 (plate 9309) which also shows the relative sizes of the inner and outer fields for a typical plate.

Before approximating the variations in density of the sky background, the number of data in the outer field were reduced by taking samples every 2.5 mm in x and at either 5 mm or 10 mm in y , depending on what was used for the scan. Because the background scans are in pairs with each scan having width 50 μm , an effective aperture of 100 μm x 100 μm was formed by taking a mean of four pixels for each sample. This has the beneficial effect of reducing the noise caused by granulation.

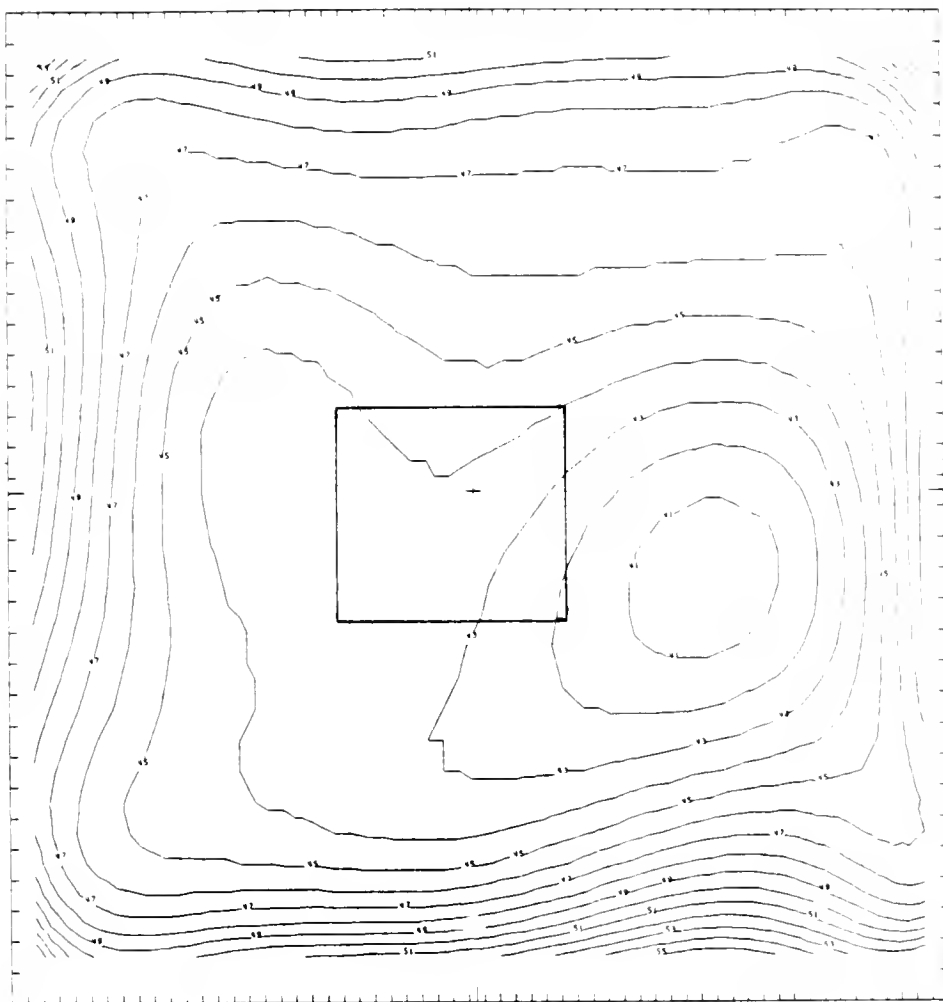


Figure 1. Density contour map of plate 9309. The contours are every 0.01D with the circular area having the lowest value, -0.41. For this plate, $k = 45$. The x-axis is 142.5 mm in length; the y-axis is 145 mm. The small square shows the inner field for this plate.

The result was a set on the order of 500 to 1000 background samples depending on the size of the plate.

The outer field was at least several times as large as the inner field, so that after removing the latter, there was still enough area to use for sky background fitting. Tests were run on plate 9416 to determine the effect of first, having the background sampled at intervals of 5 mm and 10 mm spacing in y , and second, on changing the size of the inner field from 37.5 mm x 35 mm to 25 mm x 30 mm. In the first case, although the number of data samples was reduced by a factor of two, there was little difference in the contour maps of the background and the interpolated inner field for the two spacings. The final contour map of the galaxy image was only slightly affected, with the image being slightly noisier for the larger spacing test. The difference was negligible. In the second case, the smaller inner field did not seem to have a significant affect on the results: the contours of the galaxy images were almost identical to the original ones, and only the faintest contour levels showed a small, occasional change. Thus, it appeared that the fitting of the background was not adversely affected by the choices selected for the inner and outer field measurements.

Reduction of the Inner Field

The inner fields were chosen to satisfy two criteria: (1) they had to be large enough to completely contain the faintest detectable light level of the galaxy on each plate, and (2)

the inner field boundaries should overlap the background scans whenever possible. The first criterion was satisfied by selecting areas considerably larger than the size of the image on the plates and that contained the isophotes measured in previous studies. The second criterion was important because the inner and outer fields were scanned with different size apertures. The data were put on a common system by taking the mean of the readings along the common boundary measured through both apertures, inner and outer, M_i and M_o , and then multiplying the outer field values by their ratio M_i/M_o .

Because the inner fields were measured with small apertures, either $12.5 \mu\text{m}$ or $25 \mu\text{m}$ on a side, averages were formed of 6×6 or 3×3 sets of pixels, respectively, to reduce the number of pixels and improve the signal to noise ratio. This reduction in the number of pixels was necessitated by the constraints on getting plots of the data. The resulting resolution was $7.1''$ and $7.4''$, respectively. This loss of resolution is not important, especially in the outer regions of the galaxies where no fine structure is expected.

Density to Intensity Conversion

Before the background sky was subtracted from the inner field data, photographic densities were converted to intensities using calibration plate data. This was accomplished using a polynomial of the form (de Vaucouleurs 1968; Wevers 1984)

$$\log E = \sum_{i=0}^n a_i (\log \omega)^i \quad (7)$$

to represent the characteristic curve, where E was the relative exposure ($=It$) and ω the opacitance ($=10^{\Delta D}-1$) of each calibration spot, ΔD was the density above fog, and n was usually 3 but sometimes 4. The values of the coefficients, a_i , were then determined by a least squares fit to the calibration plate data. The advantages of this formulation were that it was a relatively simple mathematical representation of the data and it avoided the errors that would have resulted from using the usual characteristic curve near the threshold where the curve asymptotically approaches the $\log E$ axis.

The values of the coefficients a_i were read into the subroutine which converted the density measurements of the inner field to intensities, $I_{G+S}(x,y)$. The value of the sky background at each position, $I_s(x,y)$ was also calculated using the computed sky density $Y(x,y)$ from equation (6) and the a_i above. Then the intensity of the galaxy alone, I_G , was calculated from equation (2) giving

$$I_G(x,y) = \frac{I_{G+S}(x,y) - I_s(x,y)}{I_s(x,y)}. \quad (8)$$

Star and Blemish Removal

The inner field area surrounding each galaxy contained on the order of 1000 stars and background galaxies. In addition, the hypersensitization procedure sometimes produced blemishes, especially on the IV-N emulsion. These unwanted features were removed before any further processing was done to the image. Because of the variety of sizes, shapes, intensities, and

local background values, an automatic rejection procedure was not found to be successful. Consequently, for objects judged to be well away from the galaxy, the size and position of each object was specified and the affected pixels replaced by a mean value formed from the surrounding pixels. For objects near the galaxy image, a different procedure had to be used, especially for those objects that were superimposed on regions of the galaxy with a large intensity gradient. These objects were removed a pixel row at a time, interpolating over the affected pixels using pixels on either side of the affected ones. Contour maps were then made of each image and were used to judge the smoothness of the procedure and to make corrections where necessary. The only significant problem was in the southeast area of NGC 253 where a large, low surface brightness region had two bright stars superimposed on it. Detailed structure in this region was lost as a result of removing the stellar images.

One of the plates, 8544, had a satellite trail cutting through the galaxy image running north-northwest and south-southeast and passing north of the nucleus. The trail was removed by interpolating over the affected pixels and the resulting contours are quite smooth.

After the stars and blemishes were removed from an image, the mean intensities of each row and column were plotted. Ideally, out away from the galaxy, these should have an average value of zero, but this was usually not the case.

This nonzero level was noted by other photometrists (Jones et al. 1967; Tsikoudi 1977) and Pence (1978) who hypothesized its origin in a small drift in the response of the microphotometer during the scan of the plate. In all cases where the mean intensities of the rows and columns were not zero, a correction was applied by fitting a plane to the mean values of the outer rows and columns and subtracting it from the image. Because the sky densities were so low, the short exposure plates showed the largest effects of photometer drift, up to 8% of the sky intensity for plate 8545. However, the data more than about one magnitude below sky were not used, and the drift effect was subtracted out, so this was not a problem.

As mentioned earlier, four of the images had low-intensity bands of noise in them: those of plates 5394, 6487, 6488, and 9417. These bands were parallel to the scan direction and quasi-periodic in nature. After any linear corrections were made to the background as described above, a sine function with period and amplitude approximately matching that of the noise was subtracted from each column of the image. Although it was not possible to completely remove all of the noise in some cases, the level that remained was less than 1% of the sky background. And because most of these plates were combined with other plates of similar passbands to form composite images later, the overall level of the noise was further reduced.

Photoelectric Calibration

The zero-point calibration of each plate was done using either photoelectric photometry measurements through one or more apertures centered on the galaxy's nucleus (Jones et al. 1967) or photoelectric drift scans through the nucleus. Since the plate measurements were normalized to the sky intensity, the zero-point of each plate was just the sky magnitude.

For NGC 55, Longo and de Vaucouleurs (1983) listed eight measurements in the Johnson V system, hereafter V_J , taken through seven apertures. The measurements through the four or five largest apertures were used for the calibration. These apertures ranged from 22.2" to 131" radius for the long exposure plates, and down to 10.4" for the short exposure plate. Three measurements in the Cousins system were made with an aperture of 131" radius and were provided by de Vaucouleurs (private communication), two in R_c and one in I_c . The pertinent data are listed in Table 5. Where more than one measurement through a given aperture was available, the mean of the measured magnitudes was used in the calibration. Because many of the V_J measurements were made through small apertures, annuli were formed by taking the difference between the largest and smaller aperture values. This served two purposes: it minimized the errors caused by problems in centering a small aperture on the nucleus of a galaxy where luminosity gradients are usually largest, and it reduced or eliminated the effect of an overexposed nucleus.

TABLE 5
APERTURE PHOTOMETRY OF NGC 55

Aperture Radius	Passband	Magnitude	Source ^a
10.4"	V _J	13.31	1
22.2	"	12.33	"
44.4	"	11.18	"
67.2	"	10.24	"
131	"	9.38	"
"	"	9.32	"
"	R _c	8.99:	2
"	"	9.06	"
"	I _c	8.60:	"

Note: ^a (1) Longo and de Vaucouleurs (1983); (2) de Vaucouleurs (private communication).

In the case of a single aperture measurement, the sky magnitude is computed in a straightforward manner. If m_a is the measured magnitude through an aperture of radius a , and L_a is the integrated luminosity within the same radius derived from the photographic plate, then

$$m_a = k - 2.5 \log L_a \quad (9)$$

where

$$L_a = \int_0^{2\pi} \int_0^a I(r, \theta) r dr d\theta. \quad (10)$$

$I(r, \theta)$ is measured in terms of the sky background, and the constant term, k , in equation (9) is the magnitude of the sky. The integrated luminosity is calculated by a program based on

one given by Jones et al. that sums up all the values of $I(r, \theta)$ in the digitized image in the area of interest.

For annuli, let F_1 , F_2 , m_1 , and m_2 be the photoelectrically measured fluxes and their corresponding magnitudes for two apertures, and let $F_a = F_2 - F_1$ be the flux corresponding to the annulus. Then

$$F_a = 10^{-0.4m_2} - 10^{-0.4m_1} \quad (11)$$

and

$$m_a = -2.5 \log(10^{-0.4m_2} - 10^{-0.4m_1}). \quad (12)$$

Using equation (10) to get $L_a = L_2 - L_1$, the sky value is then given by equation (9).

Two of the plates, 6473 and 6488, were quite deep, and since only one aperture size was used for the photoelectric measurements, annuli could not be formed to avoid any effects of a heavily exposed nucleus. Instead, the magnitude scale, and therefore the sky value, for each of these plates was determined by a method similar to that used by Tsikoudi (1977) to calibrate galaxy photometry. The luminosity profile along the major axis was plotted on an arbitrary magnitude scale and placed over the already calibrated profile for plate 6467. The uncalibrated profile was then shifted along the magnitude scale until the two profiles matched as best as could be

judged by eye. Table 6 lists the calculated sky magnitudes for the NGC 55 plate material.

TABLE 6
NGC 55 PLATE CALIBRATION

Plate #	Emulsion	Exposure	$\langle k \rangle^a$	N ^b
6467	IIIa-F	115 ^m	20.83±0.05	2
6473	IIIa-F	120 ^m	20.64±0.05 ^c	-
6487	IIa-D	60 ^m	21.03±0.05	4
6488	IIIa-F	150 ^m	20.84±0.05 ^c	-
8544	IIIa-F	20 ^m	20.86±0.05	2
9232	IIa-D	60 ^m	21.05±0.07	4
9241	IIa-D	15 ^m	20.76±0.04	5
9281	IV-N	60 ^m	19.55±0.02 ^d	1
9403	IV-N	60 ^m	19.44±0.02 ^d	1
9416	IV-N	70 ^m	19.56±0.02 ^d	1
9440	IV-N	20 ^m	19.33±0.02 ^d	1

Notes: ^a The mean zero point in magnitudes per square arc second derived from the aperture measurements and corrected to a common color system.

^b The number of measurements used to determine $\langle k \rangle$.

^c The sky value as determined from plate 6467 as explained in the text. The error is that of plate 6467.

^d Estimated uncertainty based on internal plate error. See Chapter III.

For NGC 253, Longo and de Vaucouleurs gave fourteen measurements taken through thirteen apertures in the V_J passband. Two of these were based on B magnitudes and were omitted from consideration. Of the eleven measurements that remained, the eight taken through apertures 10.4" to 80.7" radius were used to form annuli as described above. One measurement, listed as having $V_J = 12.65$ and aperture size 16.9" was not used because

it was much fainter than the values listed for apertures of 10.4" and 14.7". The apertures and magnitudes that were used for the calibration are listed in Table 7. The calculation of the sky magnitude for each plate proceeded as for NGC 55.

TABLE 7
APERTURE PHOTOMETRY OF NGC 253

Aperture Radius	Passband	Magnitude
10.4"	V _J	12.32
14.7	"	12.06
22.2	"	11.32
32.9	"	10.76
44.4	"	10.20
57.2	"	9.72
72.0	"	9.40
80.7	"	9.19

Source: Longo and de Vaucouleurs (1983).

As a check on the accuracy of the aperture photometry, photoelectric photometry drift scans were used to compute sky values. Using the photoelectrically measured magnitudes of the galaxy through a given aperture at different positions, the sky value was calculated at the same positions from the integrated photographic data, just as for the aperture photometry. Since the drift scans were measured through a larger aperture than the digitized pixel size, the digitized image was convolved with a Gaussian beam to degrade the resolution to match the photoelectric data before proceeding. The photoelectric drift scans were in the V_J passband and were kindly made available by Dr. W. D. Pence. The observations were made using the 92 cm reflector at Mc Donald Observatory

with a 32.48" diameter aperture, each scan being in an east-west direction and passing through the nucleus. Four or five determinations were made for each of plates 5396, 5410, and 9243, giving sky values of $\mu_v = 19.88 \pm 0.14$, 19.99 ± 0.11 and 19.74 ± 0.19 , respectively. These compare well with the aperture photometry values of $\mu_v = 19.94 \pm 0.07$, 19.88 ± 0.08 and 19.72 ± 0.03 .

No aperture photometry data were available for the red and infrared passbands for NGC 253. However, Spinrad et al. (1978) made east-west drift scan measurements of NGC 253 in r and i passbands centered at wavelengths 604.0 and 746.0 nm, respectively, using a 67 arc second square aperture. The red and infrared digitized images were convolved with a Gaussian beam to degrade them to their resolution and integrated magnitudes were calculated at five or six locations corresponding to the same positions in the drift scan data. Sky magnitudes were determined as before using equations (9) and (10).

The calibration plate 8545 was lightly exposed and its characteristic curve did not extend to densities as high as those in the galaxy image. It did, however, extend up to the linear region where the relationship between density and intensity is well behaved. As a consequence, the sky value derived from drift scan measurements was not considered as reliable. Instead, the magnitude scale for this plate was determined by the method of matching the luminosity profile to

that of plate 5394 as discussed earlier for the NGC 55 plates 6467, 6473 and 6488. The uncertainty in the derived value of k , the sky magnitude, was estimated from the fitting procedure. All of the sky magnitudes for the NGC 253 plates are listed in Table 8.

TABLE 8
NGC 253 PLATE CALIBRATION

Plate #	Emulsion	Exposure	$\langle k \rangle^a$	N^b
5394	IIIa-F	60 ^m	20.06±0.08	5
5396	IIa-D	20 ^m	19.86±0.07	6
5410	IIa-D	30 ^m	19.80±0.07	8
8545	IIIa-F	20 ^m	19.93±0.15 ^c	-
9243	IIa-D	10 ^m	19.64±0.03	7
9301	IV-N	60 ^m	19.16±0.18	6
9302	IV-N	15 ^m	19.59±0.13	6
9309	IV-N	60 ^m	19.03±0.22	6
9404	IV-N	60 ^m	18.86±0.39	6
9417	IV-N	70 ^m	19.13±0.19	6

Notes: ^a The mean zero point in magnitudes per square arc second derived from the aperture measurements or drift scans and corrected to a common color system.

^b The number of measurements used to determine $\langle k \rangle$.

^c The sky value as determined from plate 5394 as explained in the text. The error is an estimate.

The magnitudes determined using equations (9) through (12) were not all on a common system. The photoelectric aperture measurements were in the Johnson V_J and the Cousins R_c and I_c passbands which had effective wavelengths of 550 nm (Walker 1987), 640 nm and 790 nm (Bessel 1979). The drift scans were in V_J and the Spinrad et al. (1978) r and i passbands mentioned earlier. Only the Cousins I_c and the I pass-

band used here were a close enough match to interchange. And, as mentioned early in this chapter, two plates were taken through a "Russian" red filter, hereafter R_r which, with the IIIa-F emulsion yielded an effective wavelength of 646 nm. Each of these points will now be addressed.

To convert the NGC 55 data, the V_j , R_c and I_c aperture photometry taken through a 262" diameter diaphragm centered on the nucleus was plotted versus effective wavelength. A smooth curve was drawn through the points and the magnitudes corresponding to the effective wavelengths of the system used here were read off the graph. The conversions were as follows:
 $V = V_j - 0.08$; $R_r = R_c - 0.02$; $R = R_c - 0.05$; and $I = I_c$.

NGC 253 has a strong color gradient near the nucleus so mean magnitudes in r and i were taken from Spinrad et al. at 2.68' and 4.9' east and west of the nucleus. As for the NGC 55 data, a plot was made of magnitude versus effective wavelength for each position. Since only two passbands were available only a straight line could be fit to the data, although this may not be a problem given that the plot of the NGC 55 data for three colors had only a small amount of curvature. The determination of the correction to be made to I involved a small extrapolation while that for R_r and R required interpolations. The means of the results were:
 $V = V_j - 0.08$; $R_r = r - 0.20$; $R = r - 0.24$; and $I = i - 0.28$.
 The value for V was taken from the NGC 55 fit. The difference between the two values used to get the mean I conversion

constant was 0.1 magnitude, the largest of all the differences.

It is difficult to estimate an error in these conversions but 0.1 magnitude is probably not unreasonable given the simple nature of the process used. All of the magnitudes given in Tables 6 and 8 were corrected using the above conversions.

Plate Addition

The long-exposure intensity maps, now calibrated and cleaned of stars and blemishes, were reduced in size by taking a 2×2 average of all the pixels. This served two purposes: it reduced the number of pixels in each image to the order of 256×256 , resulting in a large saving in time and money in the subsequent image processing, and it improved the signal to noise ratio of the data. Angular resolution was reduced to about 14" for the V and R plates, 15" for the NGC 253 I plates, and 20" for the NGC 55 I plates. The resulting intensity maps in each color were aligned and added together for each galaxy. Those portions that completely overlapped were used to form the final images. All of the individual images were given equal weight except that of plate 6487 which was given half weight because of residual noise in the background.

As a final check on the photoelectric calibrations, the added long exposure major axis profiles were compared to the short exposure profiles. The two profiles in each color were

overlaid and any offset on the magnitude scales was noted. All three colors of the NGC 55 data showed small discrepancies which can probably be traced to the small size of the apertures used for the photoelectric measurements and the heavy exposure of the nuclear regions on the plates. The long exposure profiles were judged to be most likely in error, and they were shifted in magnitude to bring them into agreement with the short exposure profiles. The adjustments amounted to -0.14, 0.25, and -0.13 magnitudes for the V, R, and I profiles, respectively. Only the V magnitude for NGC 253 showed a discrepancy between the long and short exposure profiles, amounting to 0.32 magnitudes. The final values of the sky magnitudes adopted for NGC 55 were: $\mu_v = 20.91 \pm 0.04$; $\mu_R = 21.02 \pm 0.03$; and $\mu_I = 19.39 \pm 0.01$. The last two values are more uncertain than their errors imply. For NGC 253 the sky values were: $\mu_v = 20.15 \pm 0.05$; $\mu_R = 20.06 \pm 0.08$; and, finally, $\mu_I = 19.10 \pm 0.11$.

Image Smoothing

The added deep images of both galaxies were smoothed to further reduce the effects of residual background noise and to diminish small scale irregularities in the outer contours. This was generally done in three steps similar to that described in Jones et al. First, light smoothing was done by convolving the images with a Gaussian beam whose full width at the 1% level was five pixels. Moderate smoothing was done by

convolving a Gaussian beam whose full width was seven pixels. Finally, heavy smoothing was done by first doing a 2×2 averaging of all the pixels and then convolving a Gaussian beam whose full width was five pixels. This final step was not performed on the NGC 253 red data because of the low quality of the data at the level where the smoothing would be done. The light and moderate smoothings were used for the intermediate areas of the galaxy and the heavy smoothing was used for the outermost regions where the signal was weak and the isophotes began to break up into islands. The result is a decrease in the high frequency component in the structure that diminishes the effects of small dust clouds, HII regions and noise in the outer regions. The major structural features are, however, preserved.

Smoothing was also done to the short exposure plates, not to improve the signal to noise so much as to remove clutter from the maps caused by resolved features such as individual HII regions. Here, the images were convolved with a Gaussian beam whose full width at the 1% level was five pixels. The size of the beam used for smoothing is indicated on the isophote maps.

CHAPTER III PHOTOMETRIC DATA FOR NGC 55

General Description

NGC 55 is classified as a Magellanic type barred spiral, SB(s)m sp (de Vaucouleurs, de Vaucouleurs and Corwin 1976, hereafter referred to as RC2), although the classification is marked as uncertain. Classification of this galaxy is difficult because it is viewed nearly edge-on and is seen looking along the bar from a "rear view" (de Vaucouleurs 1961). The appearance in blue light is shown in Figure 2, reproduced from a print in the Atlas of Galaxies (Sandage and Bedke 1988) where resolution into stars can just be discerned. North is at the top and east is to the left in the photograph. The scale of the print is shown by the bar in the northwest corner.

One immediately notices the asymmetry in this system. The optical nucleus is displaced from the center of the galaxy, and, as mentioned in Chapter I, the radio nucleus, mass center, and centroid of total light are all offset toward the southeast (see pages 5,6 and 7 for the positions). The western side appears to terminate rather abruptly and the northern and southern halves are of different thickness near the region of the bar. Numerous HII regions are readily seen



Figure 2. NGC 55 reproduced from the Atlas of Galaxies (Sandage and Bedke 1988).

as well as the presence of a considerable amount of dust, and the former seem to be almost exclusively found on the eastern side. Rotation is present with the east side of the galaxy receding (de Vaucouleurs 1961). Table 9 presents some observational parameters of NGC 55.

TABLE 9
ELEMENTS OF NGC 55

R. A. (1950) ^a	00 ^h 12 ^m .40
Dec. (1950) ^a	-39° 28'.0
Galactic l, b ^a	332°.90, -75°.74
Supergalactic L, B ^a	256°.3, -2°.4
Type ^a	SB(s)m sp? (t=9)
Observed velocity V ^a	+131 km/sec
Corrected velocity V ₀ ^a	+98 km/sec
Apparent distance modulus	26.48 ± 0.4:
Corrected distance modulus	26.25 ± 0.4:

Note: ^a RC2, 1976.

Isophotal Contour Maps

The short exposure V, R and I isophote maps of the inner region of NGC 55 are shown in Figures 3, 4 and 5. The contour interval is $\mu = 0.2$ and the scale is shown by the bar. Also shown is the full width at half maximum (FWHM) of the smoothing Gaussian beam. The R map appears larger than the other maps because it extends over a larger range of magnitudes. Three bright HII regions 0'.9, 1'.7 and 4'.0 east of the nucleus, and roughly on the major axis, are easily identified, especially on the V and R maps. In addition, the dark dust lane to the east of the nucleus and running northeast to southwest between the inner HII regions and the nucleus can

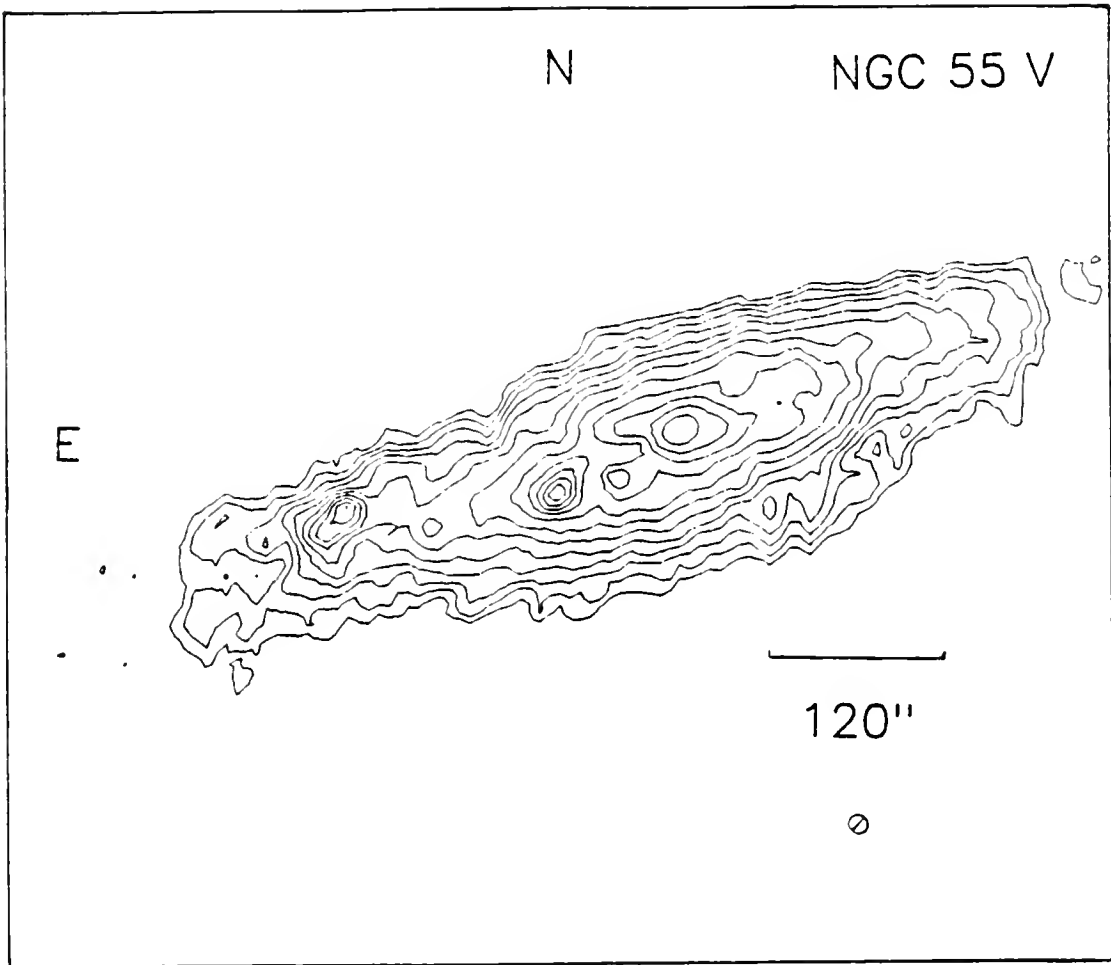


Figure 3. Short exposure V isophote map of NGC 55. The contour interval is 0.2 magnitude and the innermost isophote is at $\mu_v = 20.26$ and the outermost at 22.26. North is up and east is to the left. The bar shows the scale and the FWHM of the smoothing beam is shown by the circle.

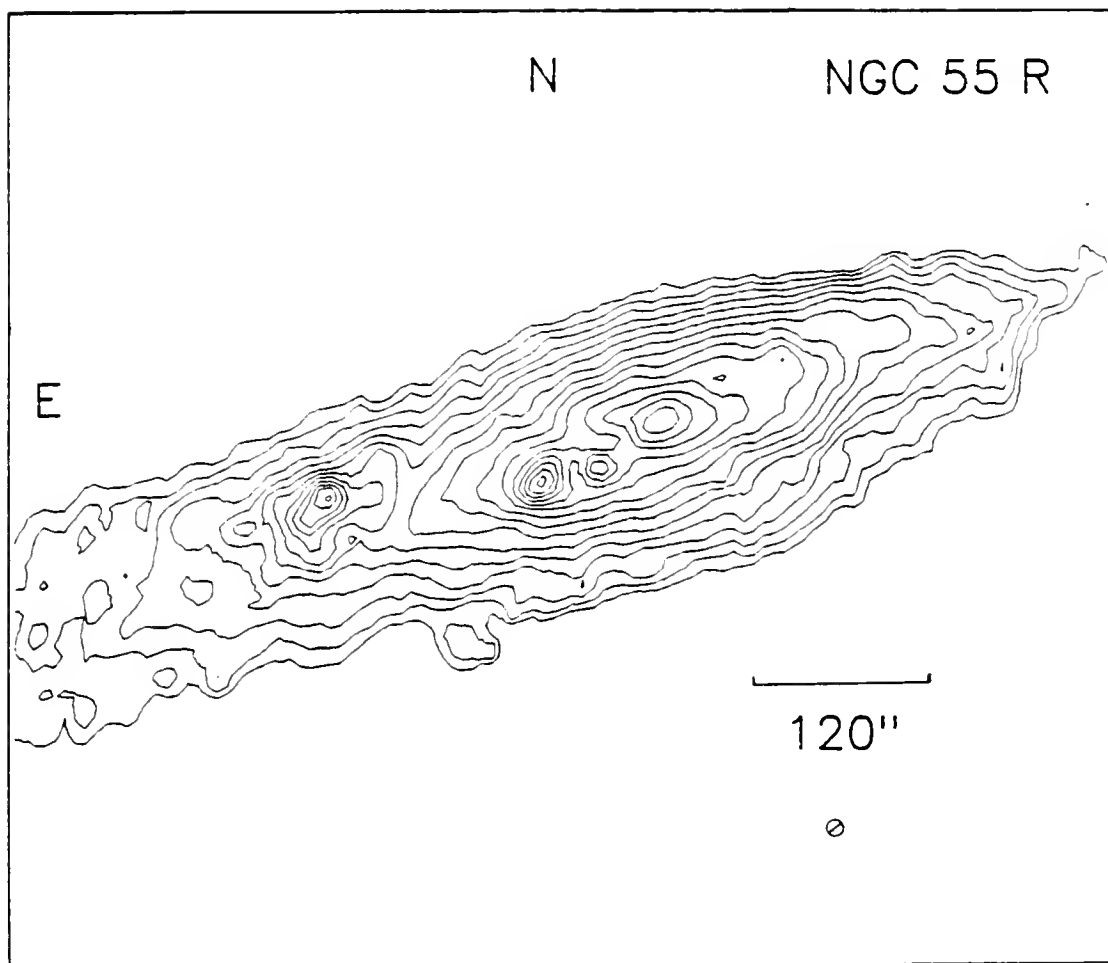


Figure 4. Short exposure R isophote map of NGC 55. The contour interval is 0.2 magnitude and the innermost isophote is at $\mu_r = 19.76$ and the outermost at 22.36. North is up and east is to the left. The bar shows the scale and the FWHM of the smoothing beam is shown by the circle.

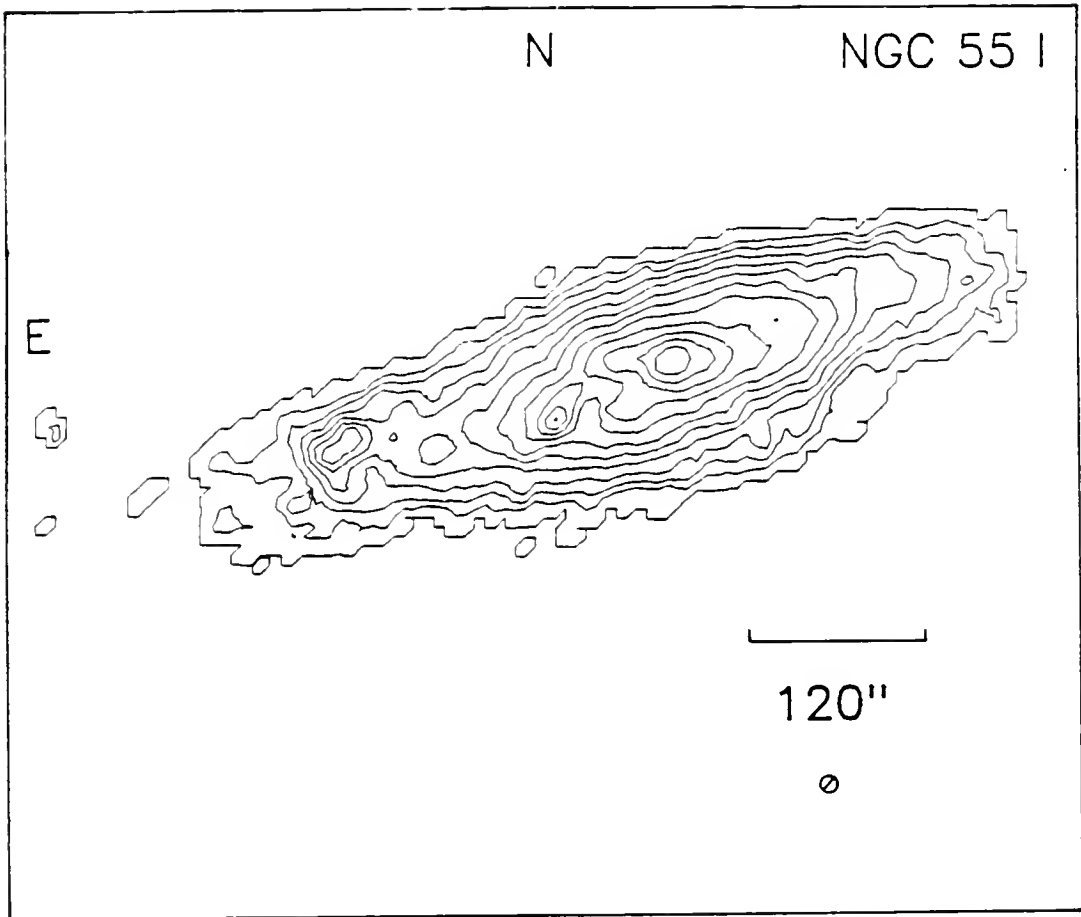


Figure 5. Short exposure I isophote map of NGC 55. The contour interval is 0.2 magnitude and the innermost isophote is at $\mu_I = 19.13$ and the outermost at 21.33. North is up and east is to the left. The bar shows the scale and the FWHM of the smoothing beam is shown by the circle.

also be seen. The nucleus itself appears almost circular or slightly elongated along the major axis. Isophotes surrounding the nucleus appear to be oriented at a smaller position angle ($93.^{\circ}8$) than the outer isophotes, although this shift in position angle is probably caused by the dust lanes to the east and west of the nucleus, as can be seen in Figure 2. A blue (pg) light isophote map (de Vaucouleurs 1961) shows much the same appearance.

Figures 6, 7 and 8 show the V, R and I isophote maps from the added long exposure plates. Again, the bar shows the scale of the map, and the circle the FWHM of the smoothing beam. Here the contour interval is $\mu = 0.5$. These maps do not show the total extent of the galaxy but go to a level where the contours start to break up into islands and the residual background noise begins to show. A lobe of increased brightness is visible on the east side about $10'$ from the nucleus: this is interpreted as an inner, asymmetrical arm by de Vaucouleurs. Also of interest is the tongue of material about $8'$ from the nucleus in position angle $\approx 265^{\circ}$ seen in the I map. This feature closely matches a similar feature in HI mapped by Hummel, Dettmar and Wielebinski (1986). The lobe at the west end of the galaxy and the slight bulge along the south side of the minor axis may be related to HI features, too, although no optical emission is seen in the northeast where they have HI extending in a tongue. They ascribe the HI features to warping and wobbling of the HI plane.

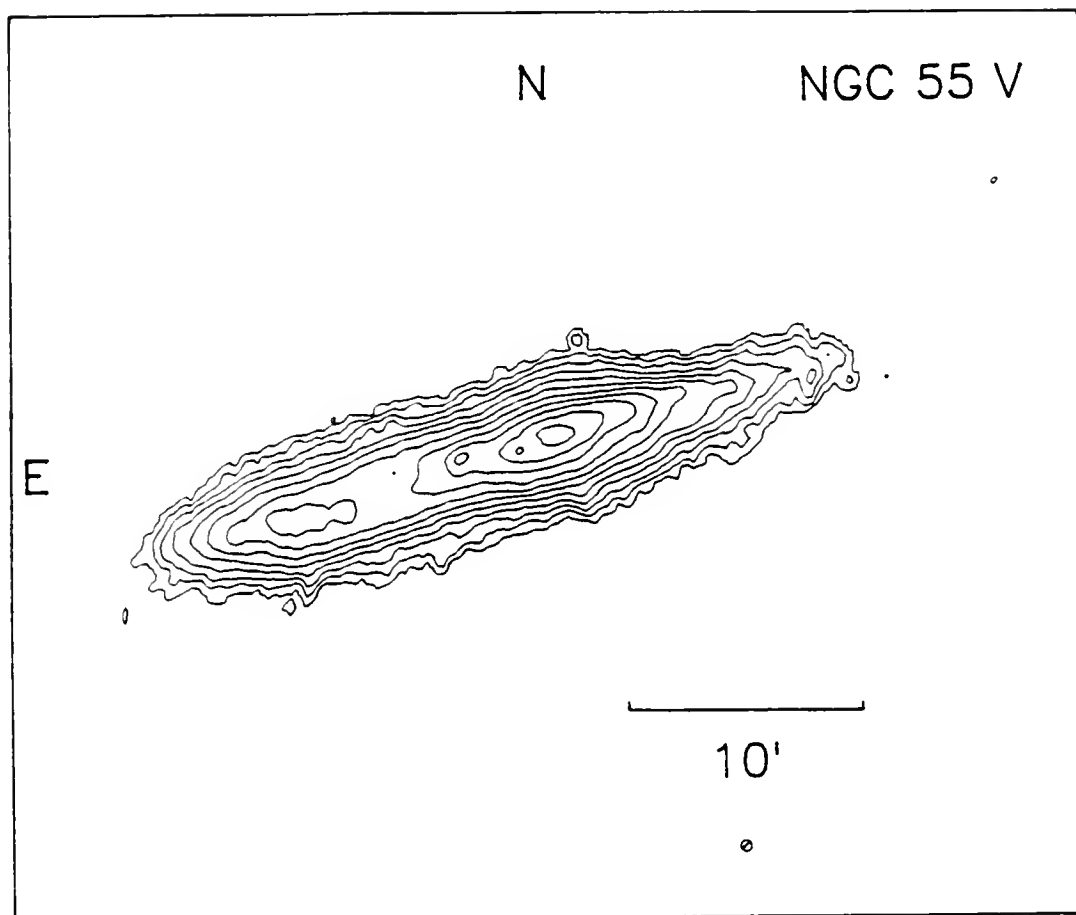


Figure 6. Visual isophote map made from added long exposure plates. The contour interval is 0.5 magnitude. The innermost isophote is at $\mu_v = 20.92$ and the outermost at 25.92. North is up and east is to the left. The bar shows the scale and the FWHM of the smoothing beam is shown by the circle.

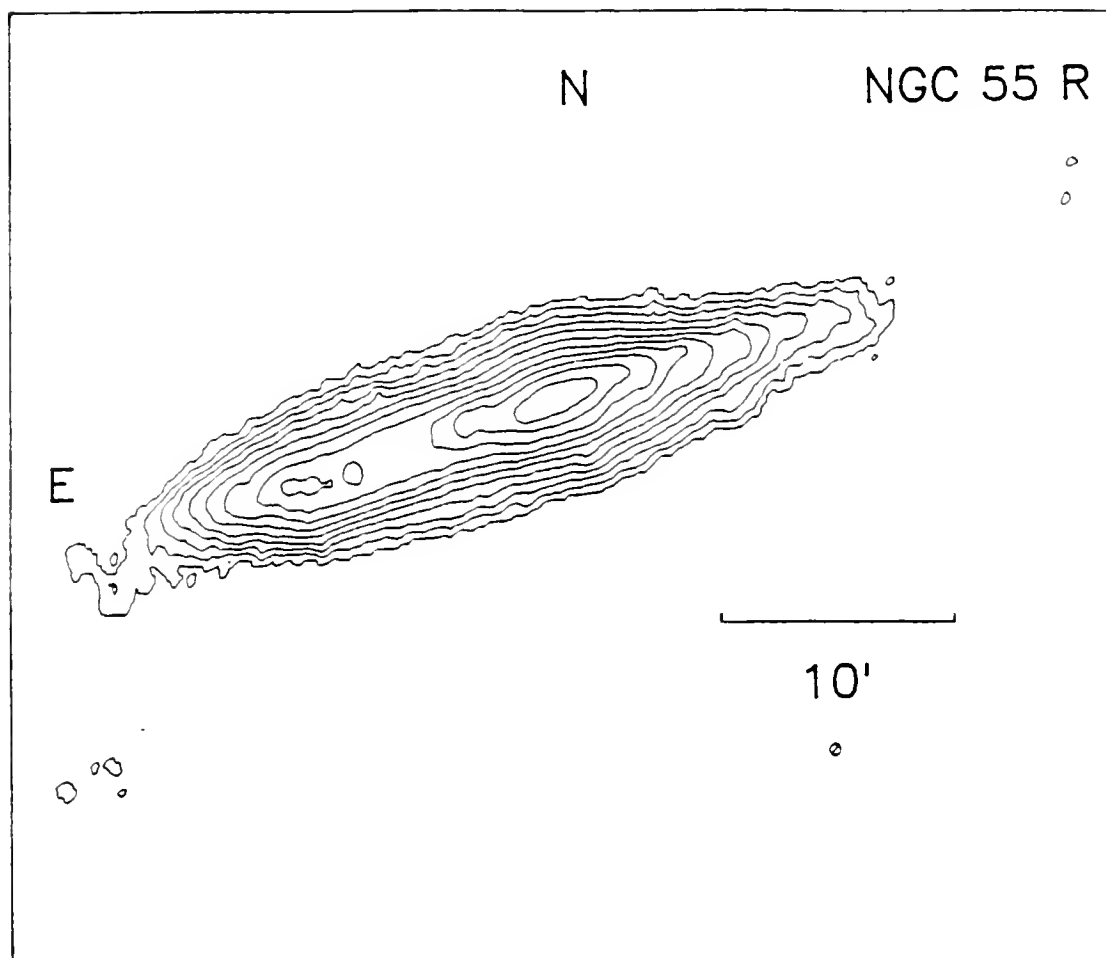


Figure 7. Red isophote map made from added long exposure plates. The contour interval is 0.5 magnitude. The innermost isophote is at $\mu_r = 21.02$ and the outermost at 26.02. North is up and east is to the left. The bar shows the scale and the FWHM of the smoothing beam is shown by the circle.

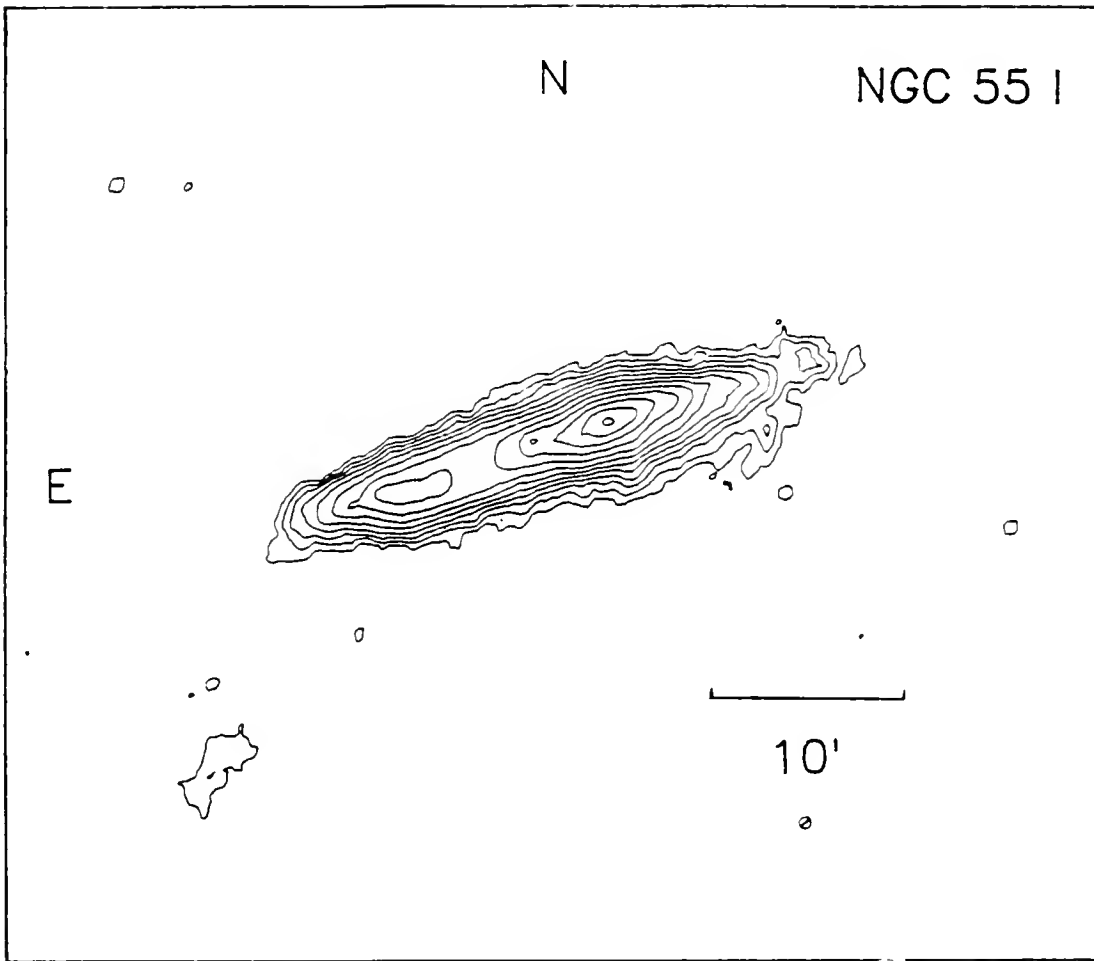


Figure 8. Infrared isophote map made from added long exposure plates. The contour interval is 0.5 magnitude. The innermost isophote is at $\mu_r = 19.39$ and the outermost at 24.89. North is up and east is to the left. The bar shows the scale and the FWHM of the smoothing beam is shown by the circle.

The position angle of the major axis is $107^\circ.8 \pm 0^\circ.5$ as estimated from the long exposure isophote maps. This compares well with determinations of 105° (de Vaucouleurs 1961) and 107° (Robinson and van Damme 1966) from optical data, and 109° (Hummel, Dettmar and Wielebinski 1986) from 21 cm data. The minor axis is taken as the line perpendicular to the major axis and passing through the nucleus, even though this line does not pass through the center of the image.

As mentioned in Chapter I, the published optical inclination values for NGC 55 range from 79° to 90° , and the HI yields an inclination of $\approx 80^\circ$. From the appearance of the galaxy in photographs, the lower value is probably ruled out since no indication of far side structure or an elongated bar is seen. The inclination, i , can be calculated using equation (13)

$$\cos^2 i = \frac{(q^2 - q_0^2)}{(1 - q_0^2)} \quad (13)$$

where q is the ratio of the apparent minor axis to the major axis, and q_0 is the ratio of the true minor axis to the major axis. Measurements of the axes at $\mu = 23, 24, 25$, and 26 in V, R and I yield mean values of q of 0.21 ± 0.02 , 0.22 ± 0.02 , and 0.25 ± 0.04 , respectively. The mean q from de Vaucouleurs (1961) at $\mu_{pg} = 23.7, 24.7$ and 25.85 is 0.20 ± 0.02 , the same as the value in the RC2. The mean value of the four flattest ($q \leq 0.25$) SBm galaxies in the RC2 (not including NGC 55) is

$\langle q \rangle = 0.25 \pm 0.005$. If late type galaxies that might be mistaken for SBm, or vice versa, are examined, the means are: $\langle q \rangle = 0.19 \pm 0.05$ (9 SBd); $\langle q \rangle = 0.22 \pm 0.04$ (2 SBdm); and $\langle q \rangle = 0.20 \pm 0.03$ (6 Im). Inclinations for NGC 55 greater than 80° result from the possible real solutions of equation (13) using the above estimates as q_0 . Only in the case of the smallest value of q , 0.11, for the SBd galaxy NGC 7412 A, can a value of i less than 80° be obtained. Hence, we conclude that $80^\circ < i < 90^\circ$, and a value of $i = 85^\circ$ will be adopted here.

Luminosity Profiles

Figures 9, 10 and 11 show slices along the major and minor axes in each color. The bright, inner regions are from the short exposure images, and the more heavily smoothed and added long exposure images are used for the fainter magnitudes. Representative internal errors are shown by the bars at the side of each figure for three brightness levels. Each displays the effect of a $\pm 1 \sigma$ error, and is the standard deviation of two to four sets of pixels from near the corners of the images used to form the profiles.

Major Axis

The major axis profiles all show the marked asymmetry of this galaxy. To the east of the nucleus bright HII regions are apparent at $1'.5$, $4'.0$ and $9'.5$, and obscuring dust is evident at $0'.7$ and $5'.0$. Dust on the east side also causes the depression in the luminosity profile between $5'$ and $9'$.

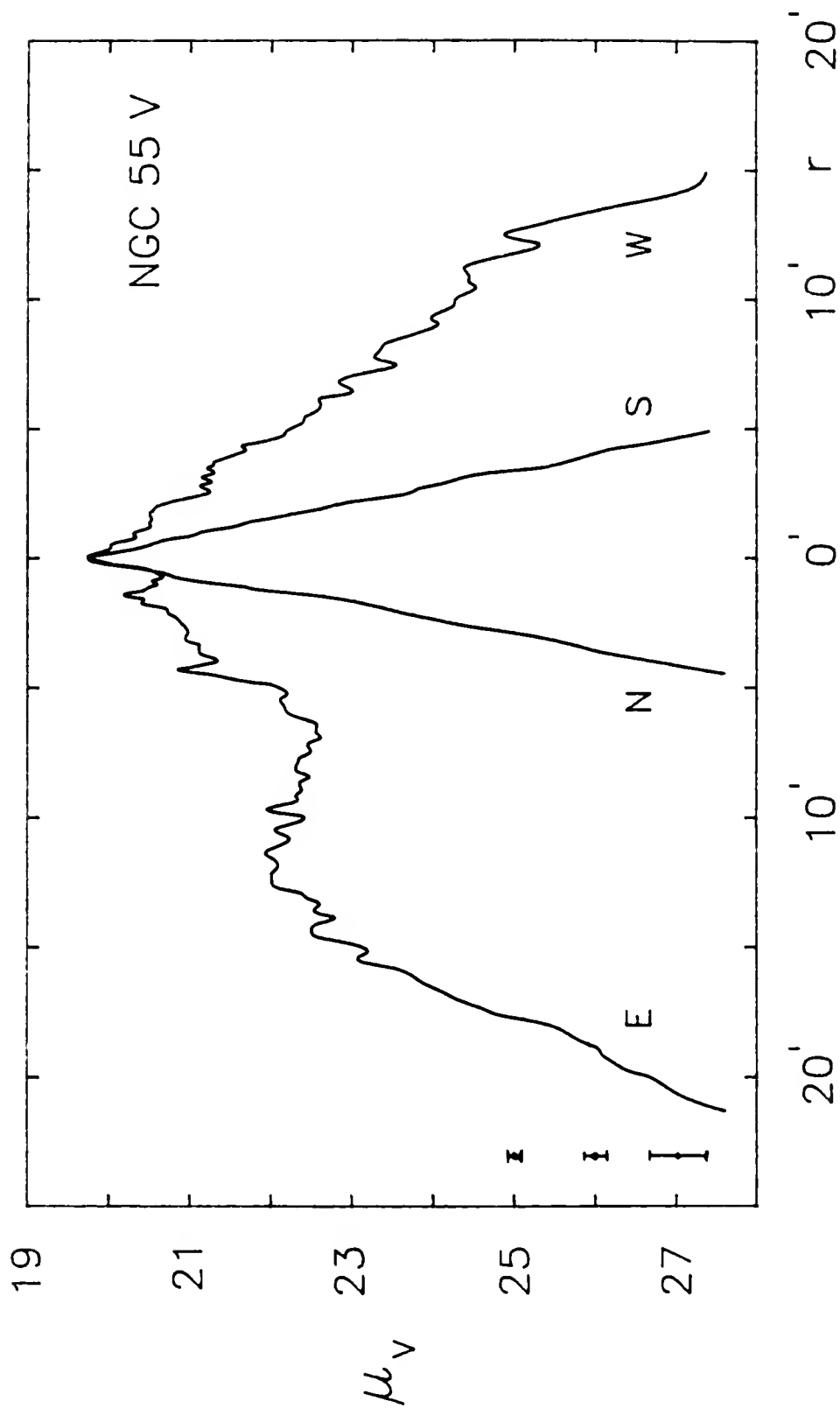


Figure 9. Visual major and minor axis profiles of NGC 55. For $\mu_V \leq 22$ the data are from the short exposure plate.

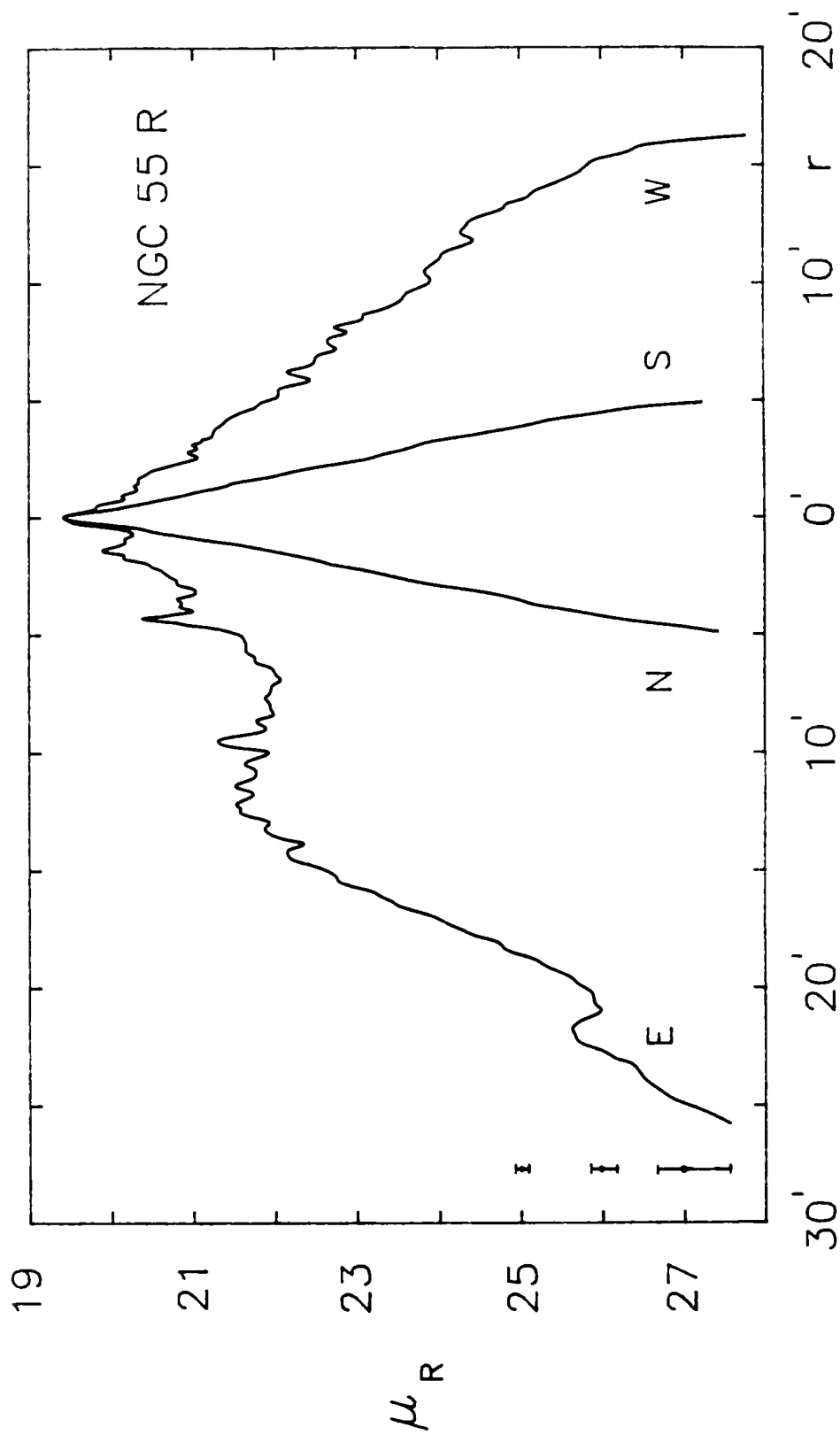


Figure 10. Red major and minor axis profiles of NGC 55. For $\mu_R \leq 21$ the data are from the short exposure plate.

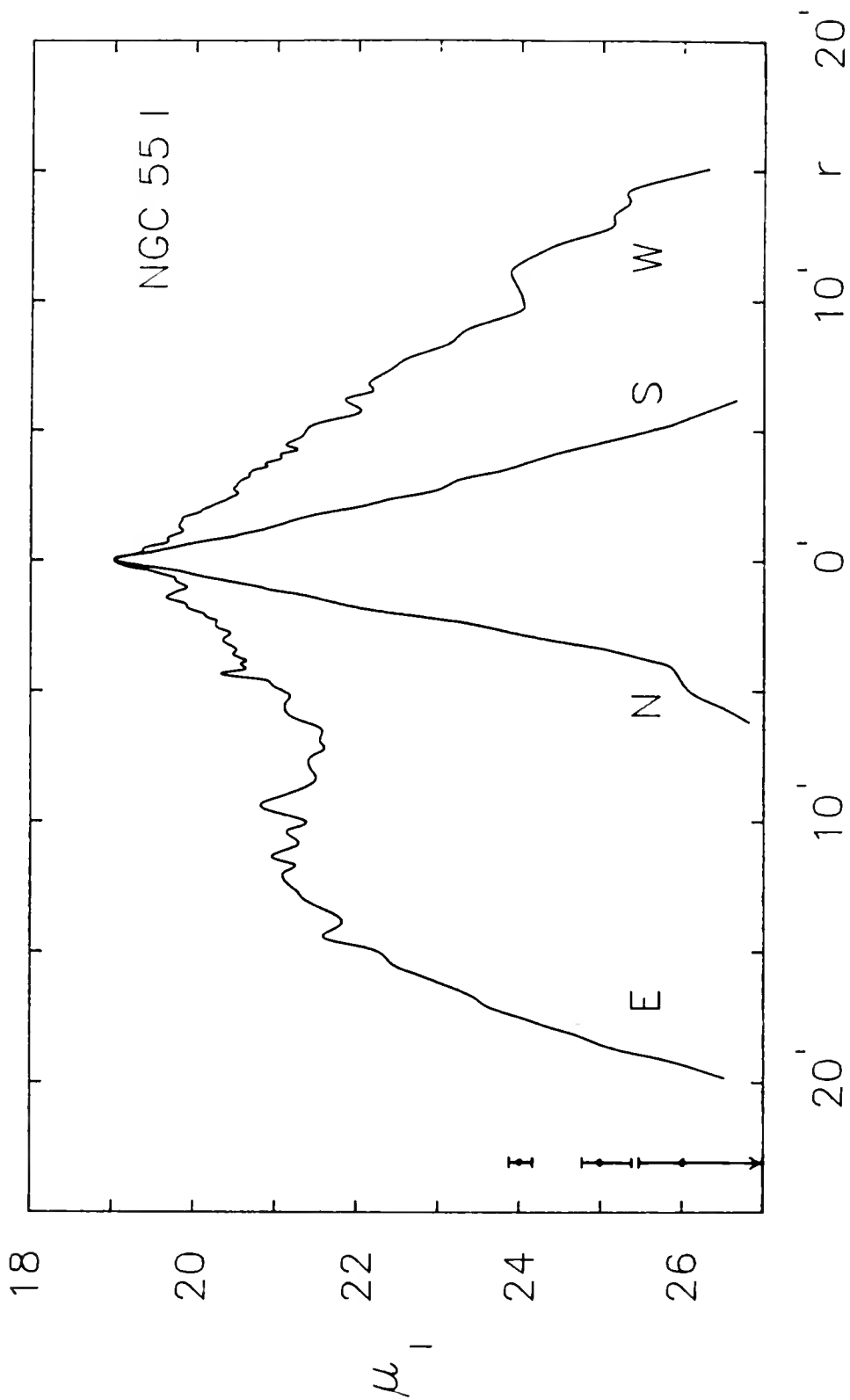


Figure 11. Infrared major and minor axis profiles of NGC 55. For $\mu_I \leq 21$ the data are from the short exposure plate.

On the west side, the drops in brightness at 2'.0 and 4'.5 are seen to correspond to dust (see Figure 2). No HII regions are cut by the major axis on this side. The large "bump" at 22' on the east side of the R profile is not real but an artifact caused by noise on one of the R plates.

All three colors show that the luminosity distribution is approximately exponential in the outer regions, in agreement with the pg ($\lambda_{eff} \approx 430$ nm) study of de Vaucouleurs (1961). This is especially noticeable for the west profile where the decline is easily seen to extend over at least five magnitudes. On the east side, the exponential decline can be followed nearly as far but only below about $\mu_V = 23$ and $\mu_R = \mu_I \geq 22$.

The gradients of these exponential regions, in units of magnitudes per arc minute, are given in Table 10. Column (1) gives the color, or passband, of the observation. The gradients of the east and west profiles of the major axis are given in columns (2) and (3), with the magnitude range used for the calculation in parentheses. The mean gradient of both sides is given in column (4), and column (5) gives the gradient of the entire west profile and the magnitude range. The pg mean gradient is from de Vaucouleurs and is included for comparison; the other pg values are the results of calculations made using his luminosity profile. In all cases the values are only approximate because of the uncertainties in the magnitudes at the fainter levels. It is the differences

between the gradients that are emphasized, not their actual values.

TABLE 10

NGC 55 MAJOR AXIS LUMINOSITY GRADIENTS

Color	East ^a	West ^a	Mean ^a	West ^a
pg	0.31 (23-27)	0.41 (23-27)	0.35 ^b	0.31: (20-27)
V	0.75 (24-28)	0.55 (24-28)	0.65	0.45 (19-28)
R	0.70 (23-25)	0.32 (23-25)	0.51	0.40 (19-28)
I	0.96 (23-27)	0.41 (23-27)	0.68	0.44 (19-27)

Notes: ^a All values are in magnitudes per arc minute.

^b Value from de Vaucouleurs (1961).

Examination of Table 10 shows that the east profile is substantially different from the west profile when compared at similar brightness levels. In general, the gradient increases with wavelength on the east side of the major axis, while no such trend is recognized for the corresponding sections of the west side. This implies that the relative contribution of blue objects to the luminosity at a given position in the east profile increases with increasing radial distance. With the exception of the pg data, the gradients on the east side are all larger than those on the west. Hence, the eastern part of the disk has a much different morphology than does the western part, more than can be explained by simply adding a contribution due to a small inner asymmetric arm. If one considers the appearance of the LMC on the side with its asymmetric arm, this is not to be unexpected.

The gradients can also be expressed in terms of a scale length. For an exponential luminosity distribution the intensity goes as $I(r) = I_0 \exp(-\alpha r)$, or, in terms of a magnitude, $m(r) = m(0) + 1.086(\alpha r)$. Table 11 lists the scale lengths $1/\alpha$ in kpc for the same data as in Table 10.

TABLE 11

NGC 55 MAJOR AXIS SCALE LENGTHS IN KPC

Color	$1/\alpha$ East	$1/\alpha$ West	$\langle 1/\alpha \rangle$	$1/\alpha$ West
pg	1.81	1.37	1.61	1.81:
V	0.75	1.02	0.87	1.25
R	0.80	1.76	1.10	1.41
I	0.59	1.37	0.83	1.28

Minor Axis

Unlike the major axis profile, the minor axis profile is almost uniform in its appearance: the "bump" visible on the north I profile at $\mu_1 = 26$ is due to background noise. All three colors are well approximated by an exponential decline in brightness, although the I profile may show a hint of the beginning of a $r^{0.25}$ shape. From this we conclude that NGC 55 shows little evidence of a spheroidal bulge component. This is in keeping with its classification as a late-type galaxy, which implies that it should exhibit little or no spheroidal bulge.

Gradients, in magnitudes per arc minute, are listed in Table 12. The numbers in parentheses are the magnitude intervals used in the calculations of the gradients. The corresponding scale lengths in kpc are given in Table 13.

TABLE 12

NGC 55 MINOR AXIS LUMINOSITY GRADIENTS

Color	North ^a	South ^a	Mean ^a
pg	1.05 (23-27) ^b	0.825 (23-27) ^b	0.938 (23-27)
V	1.81 (19-28)	1.56 (19-28)	1.68 (19-28)
R	1.56 (19-28)	1.47 (19-28)	1.52 (19-28)
I	1.72 (19-26)	1.27 (19-27)	1.50 (19-26)

Notes: ^a All values are in magnitudes per arc minute.

^b Value from de Vaucouleurs (1961).

TABLE 13

NGC 55 MINOR AXIS SCALE LENGTHS IN KPC

Color	1/ α North	1/ α South	<1/ α >
pg	0.54	0.68	0.61
V	0.31	0.36	0.33
R	0.36	0.38	0.37
I	0.33	0.44	0.37

All of the colors agree in that the gradient of the southern half of the minor axis is less than that of the northern half. This is most easily interpreted as the result of an asymmetric distribution of stars perpendicular to the plane of the galaxy. Direct evidence of this can be seen in Figure 2 where faint material is visible either in front of or to the south of the nucleus. As was noted for the east side of the major axis, the longer wavelength surface brightness decreases more rapidly than does the pg brightness. This implied increase in the relative contribution of blue sources with distance above and below the plane of the galaxy is difficult to understand. It is, therefore, worth considering that the pg photometry may be in error, especially since it

was done using techniques that have since been replaced by more sophisticated methods.

Size of NGC 55

The size of NGC 55 is determined from the maximum extent of the luminosity profiles. For each color the profiles are extended to reach the faintest level attained by any one part of a profile by extrapolating up to a few tenths of a magnitude. The dimensions are given in Table 14 where column (1) lists the passband, column (2) gives the surface brightness at the measured position, and columns (3) and (4) give the major and minor axis sizes in arc minutes and kpc. A colon marks uncertain values: these arise from those profiles with "bumps" on their lowest portions. As a result, the value of 2a for the red image and 2b for the infrared image are overestimates. De Vaucouleurs pg data are again included for comparison.

TABLE 14
SIZE OF NGC 55

Color	μ	2a	2b
pg	26:	45'	9'
		23.3 kpc	4.7 kpc
V	27.6	35'.9	9'.5
		18.6 kpc	4.9 kpc
R	27.8	42'.6:	10'.2
		22.1: kpc	5.3 kpc
I	27.0	35'.8	12'.8:
		18.5 kpc	6.6: kpc

Note: The pg data are from de Vaucouleurs (1961).

The large extent of NGC 55 in the pg is somewhat remarkable. De Vaucouleurs reported it could be traced out to an

unreliable $1^\circ \times 0^\circ.2$ (31.1 kpc \times 6.2 kpc). Apparently, this outermost part of NGC 55 must be very blue if it is real, especially on the west side, because it does not appear on the V, R and I profiles. This point will be considered further when the colors and integrated magnitudes of NGC 55 are discussed.

Measured at the 3σ level the V, R and I major axes are: $35'.4$ (18.3 kpc), $41'.2$ (21.3 kpc), and $37'.1$ (19.2 kpc). The corresponding minor axes are: $9'.1$ (4.7 kpc), $9'.5$ (4.9 kpc), and $9'.2$ (4.8 kpc).

Asymmetry Profiles

Major Axis

Asymmetry profiles, formed by taking the difference between the two sides of the major axis luminosity profiles, $\Delta m(N - S) = \mu(N) - \mu(S)$, are shown in Figures 12, 13 and 14. Each color shows the inner $7'$ of NGC 55 to be nearly symmetrical, the two sides differing in brightness by a factor of about 2 at most. However, beyond $7'$, the east profile starts rising while the west profile continues its exponential decline (see Figures 9, 10 and 11). It is here that the dissimilarity begins to show and it continues to grow for as far as the measurements extend. The visual asymmetry profile shows an almost steady increase in the difference between the east and west sides of the major axis beyond $7'$. The red and infrared profiles, however, show a small decrease in the growth rate of the asymmetry starting around $r > 11'$. This

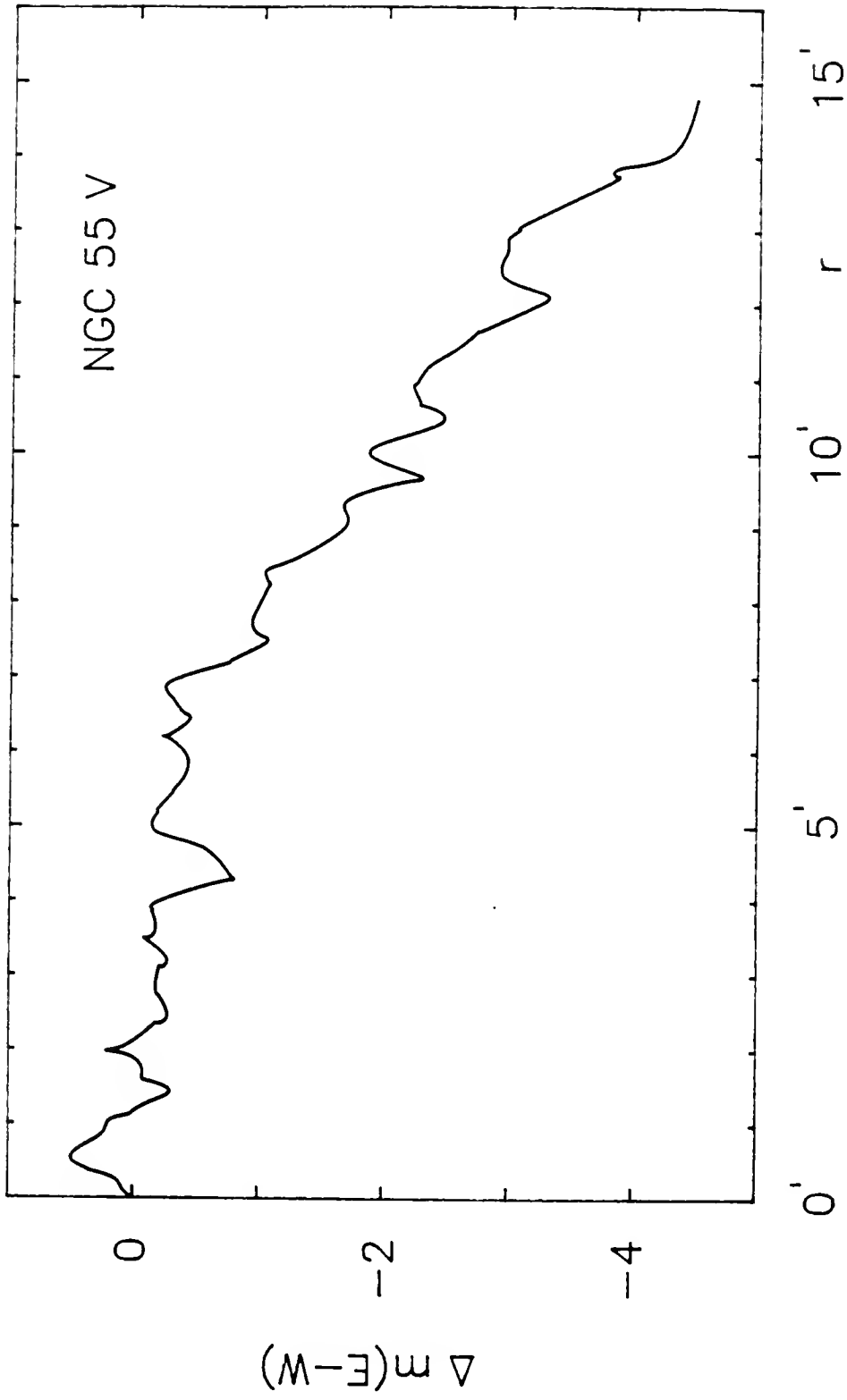


Figure 12. Asymmetry profile for NGC 55 V data. The ordinate is the magnitude difference between the east and west sides of the major axis.

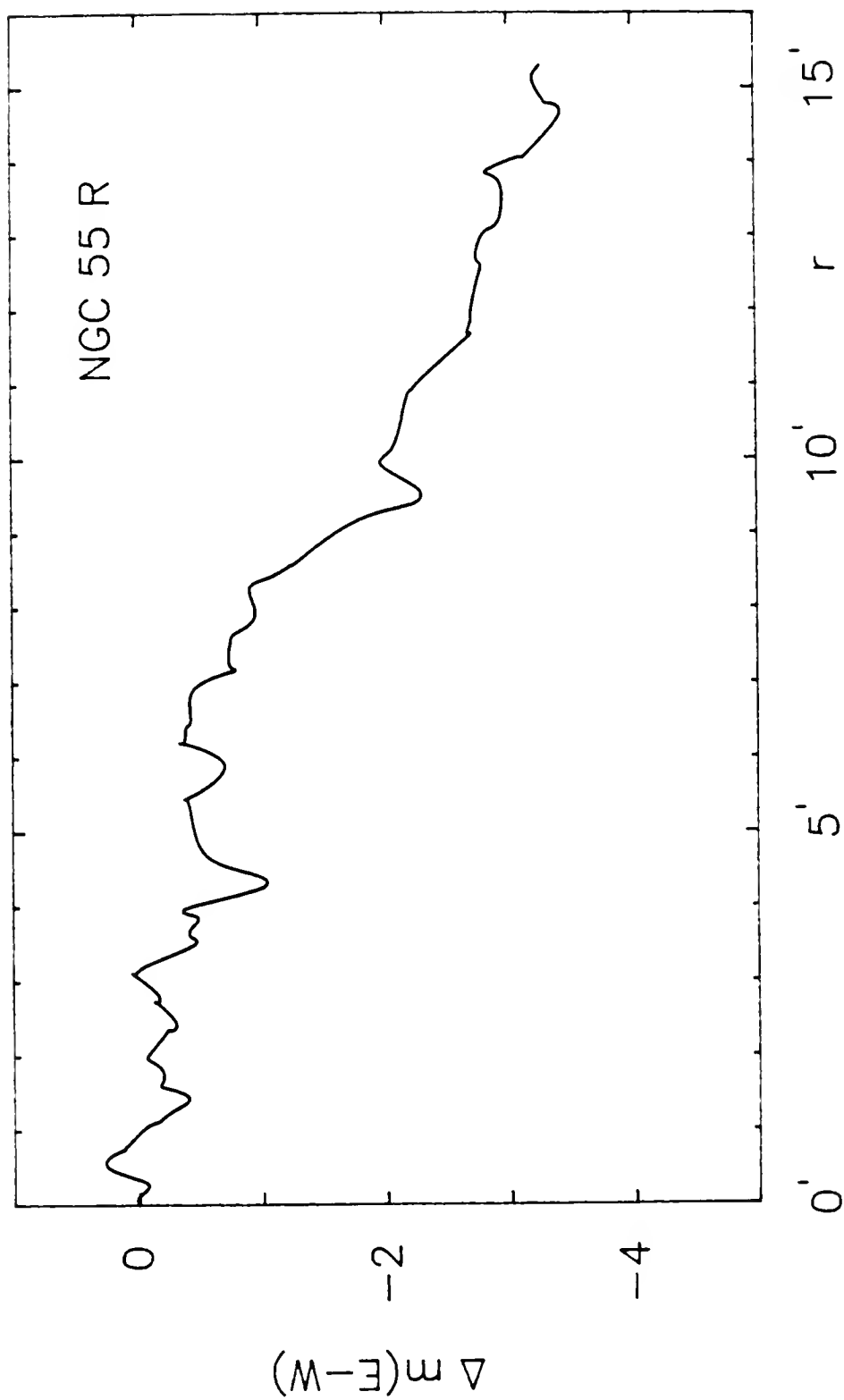


Figure 13. Asymmetry profile for NGC 55 R data. The ordinate is the magnitude difference between the east and west sides of the major axis.

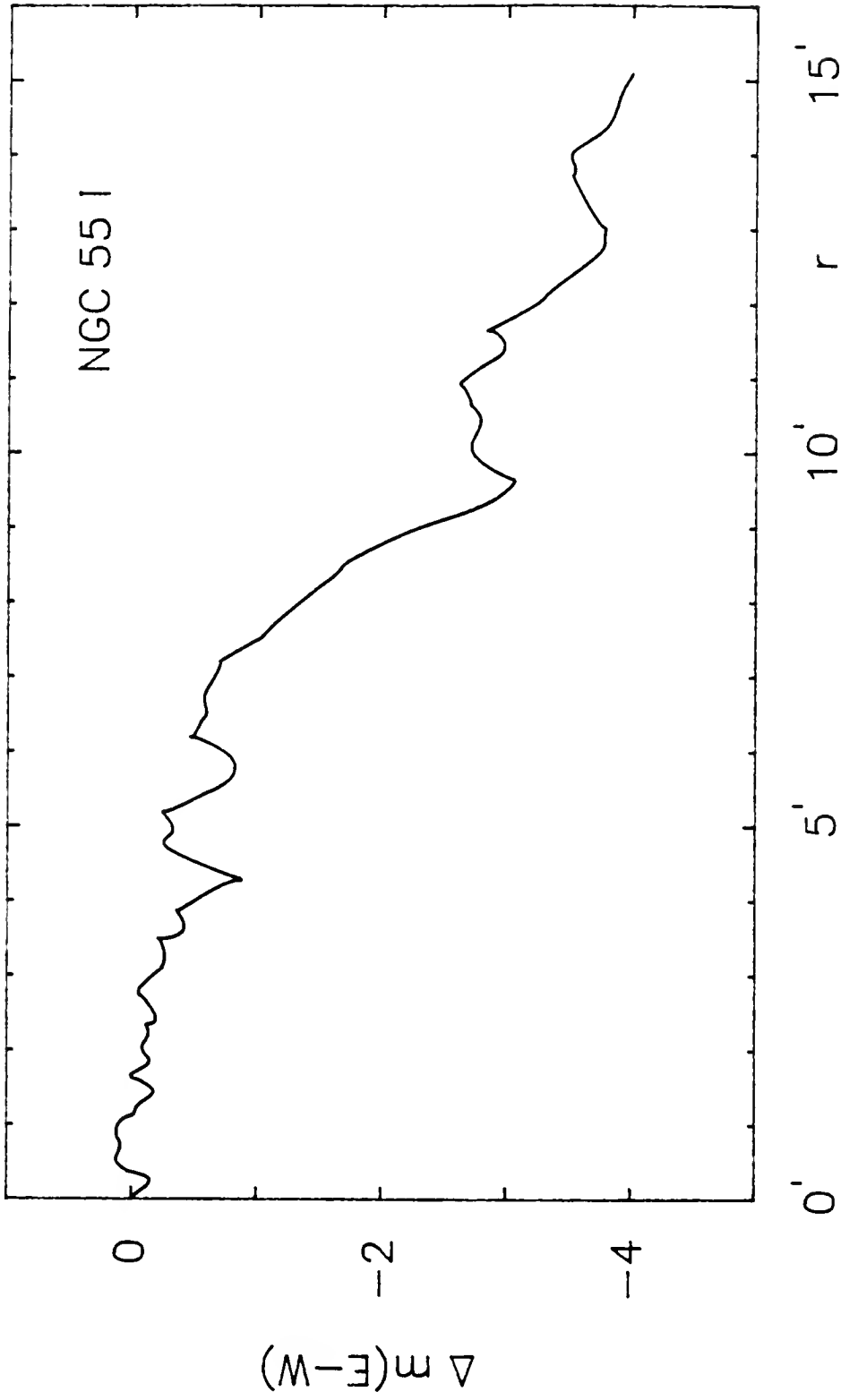


Figure 14. Asymmetry profile for NGC 55 I data. The ordinate is the magnitude difference between the east and west sides of the major axis.

coincides with the region where the east side of the luminosity profile begins its turnover toward an exponential decline.

Minor Axis

Figures 15, 16 and 17 show the asymmetry profiles for the minor axis data, $\Delta m(E - W) = \mu(E) - \mu(W)$. The inner arc minute in each color is quite uniform. A slight increase in asymmetry seen at $r \geq 1'$ is attributable to the luminous area south of the bar seen in Figure 2 and mentioned in the discussion of the minor axis gradients. All three colors show the asymmetry increases with increasing distance from the plane of the galaxy. In each case the southern half of the minor axis is brighter than the northern half. The large increase in the I asymmetry profile for $r \geq 3'$ may not be real but the result of photometric errors, and differences in the slopes of the curves for $r \geq 3'$ may not be significant. The sudden downturn in the I profile at $r \geq 4'$ is caused by the "bump" on the north luminosity profile at $\mu_r \geq 26$ where the photometric errors are large.

Color Profiles

Three color indices are formed for each axis: V-R, R-I and V-I. However, it should be kept in mind that because of the uncertainty in the photoelectric R and I calibrations, the possibility of (large) systematic errors in the color indices cannot be discounted.

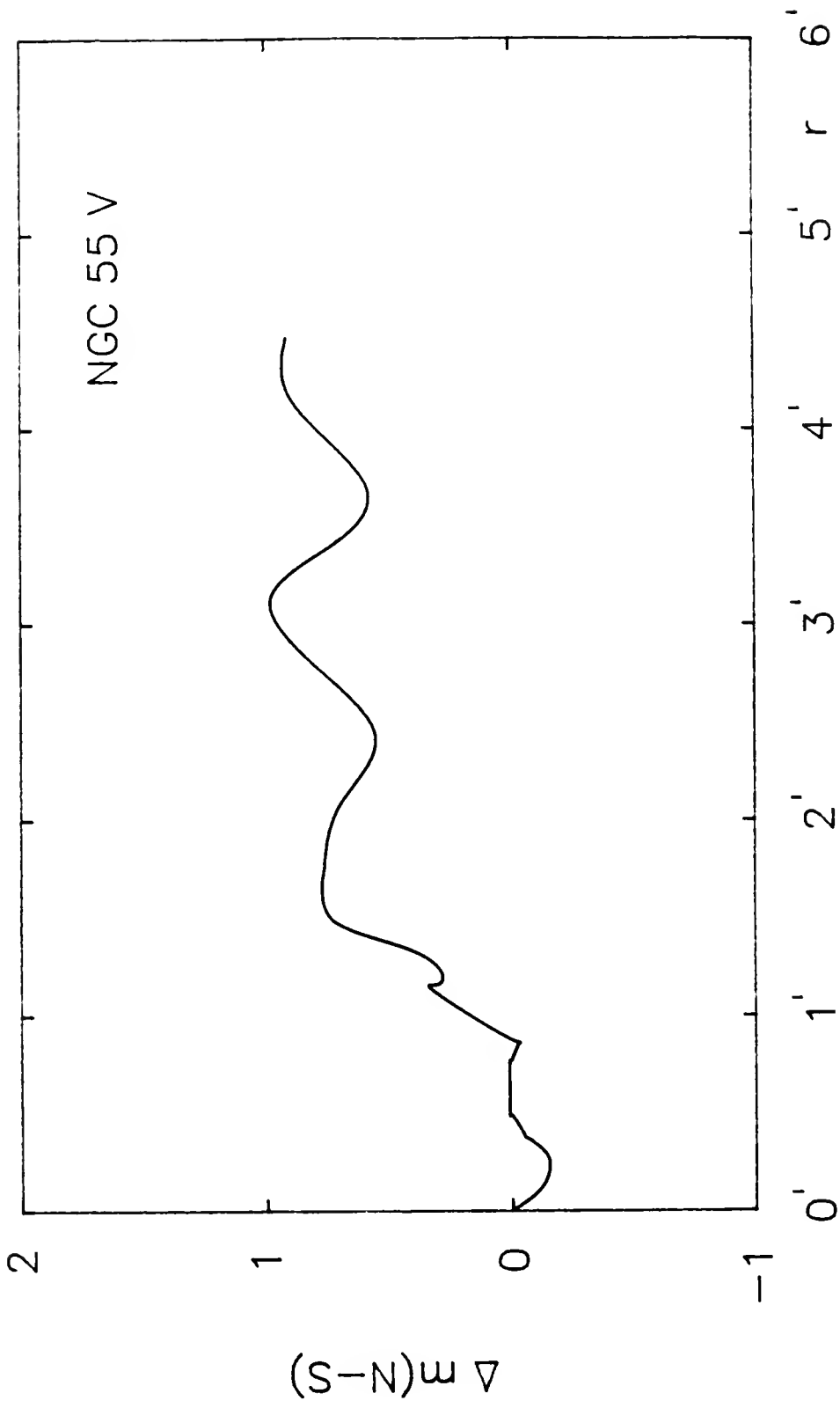


Figure 15. Asymmetry profile for NGC 55 V data. The ordinate is the magnitude difference between the north and south sides of the minor axis.

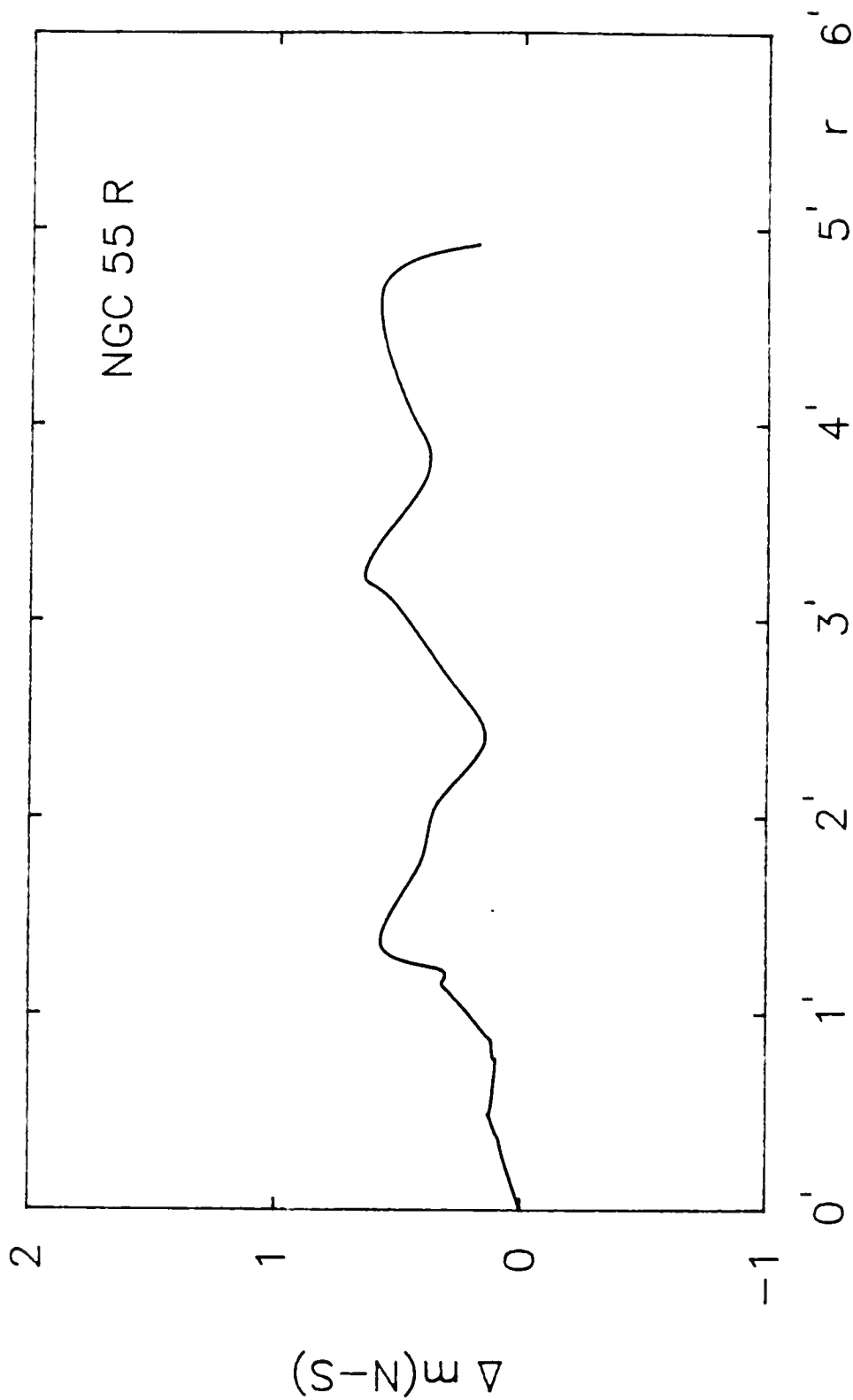


Figure 16. Asymmetry profile for NGC 55 R data. The ordinate is the magnitude difference between the north and south sides of the minor axis.

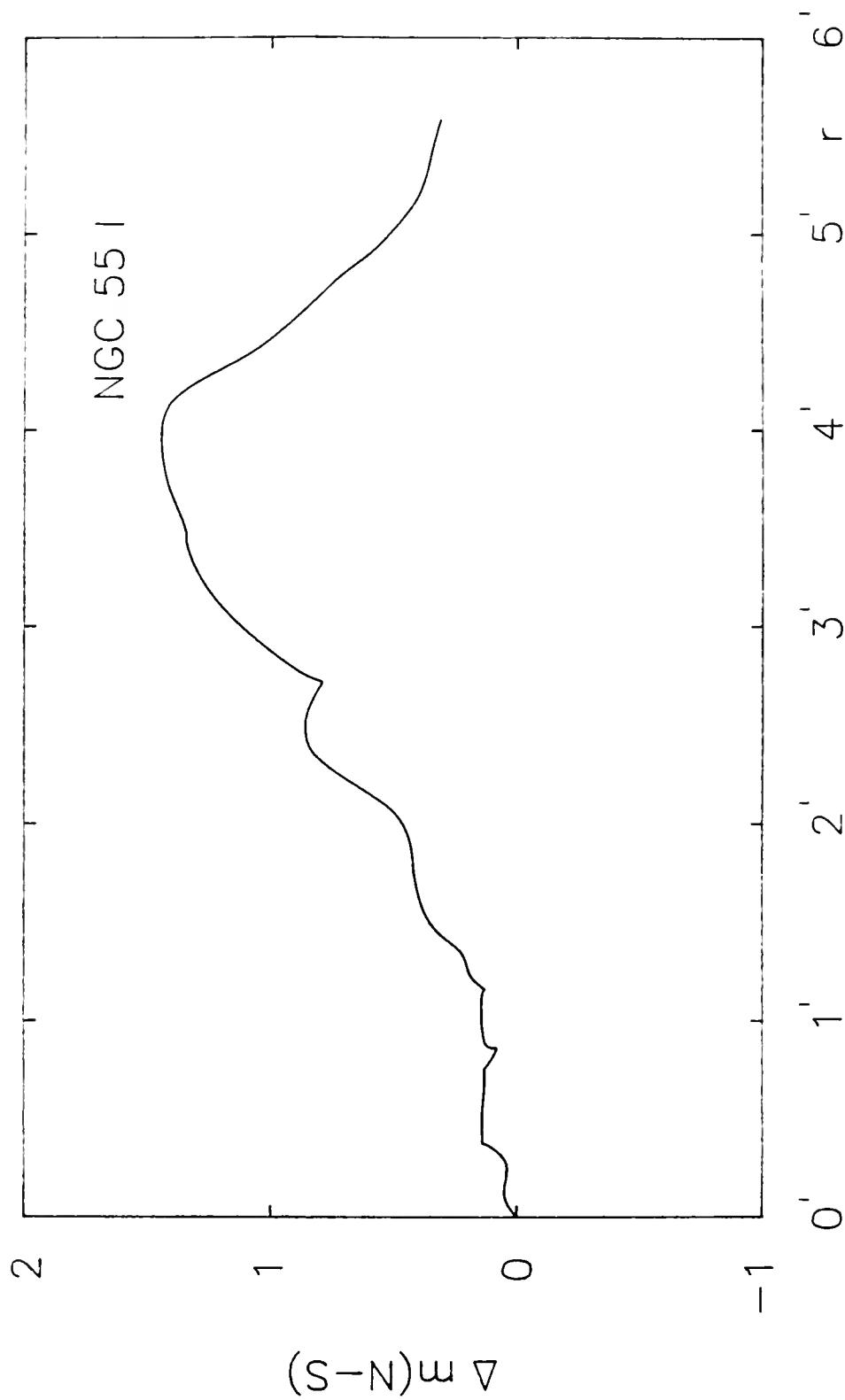


Figure 17. Asymmetry profile for NGC 55 I data. The ordinate is the magnitude difference between the north and south sides of the minor axis.

Major Axis

The major axis color profiles are shown in Figures 18, 19 and 20. As can be seen, the nucleus is not a feature distinguished by its color, which is about $V-R = 0.33$, $R-I = 0.40$, and $V-I = 0.73$. The region within about 5' of the nucleus is the bright inner disk and bar. It is somewhat bluer than the outer disk, having a nearly constant $V-R \approx 0.2$, $R-I \approx 0.4$, and $V-I \approx 0.6$. The prominent red peak to the east of the nucleus occurs at the edge of the dusty region about 1' across and clearly visible on the photograph, isophote maps and major axis luminosity profiles. A valley approximately 3' east of the nucleus in the $V-R$ profile is an artifact produced as a result of the removal of a satellite trail on the short exposure red image. This feature shows as a peak at the same location in the $R-I$ profile.

Beyond about 4' to 5' east and west of the nucleus, the outer disk of the galaxy is encountered. Errors in the photometry cause the color indices to be especially untrustworthy at distances in excess of about 15' on the east side and 10' on the west, so all discussion will be restricted to this range. Within these limits, the east profile is redder than the west, $V-I \approx 0.9$ versus 0.8. This is not surprising given the large amount of visible obscuration on the east side of the disk.

A prominent feature is seen at 9'.5 east of the nucleus. This red area is seen as a bright peak on the major axis lumi-

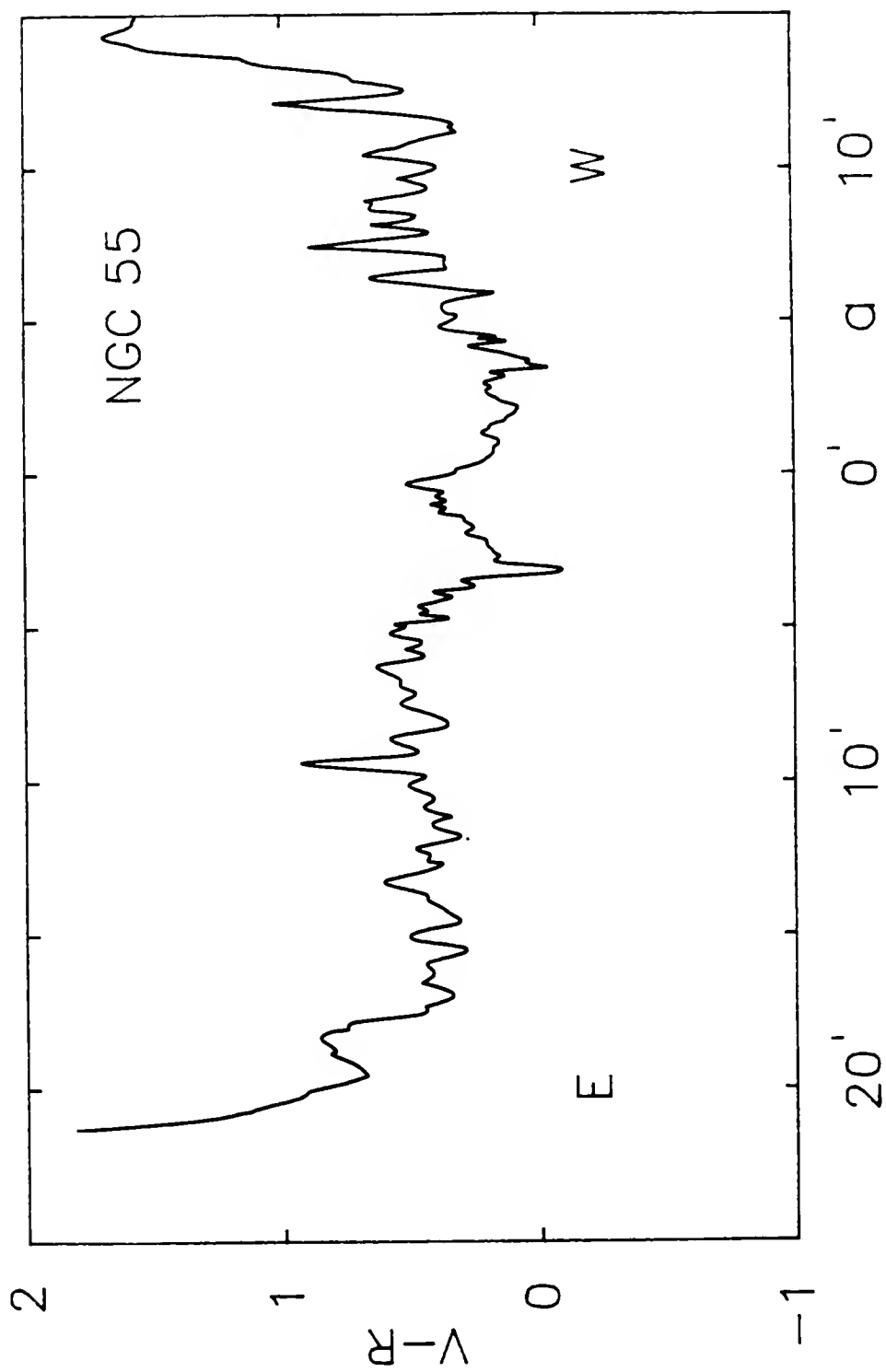


Figure 18. Major axis (V - R) color profile for NGC 55.

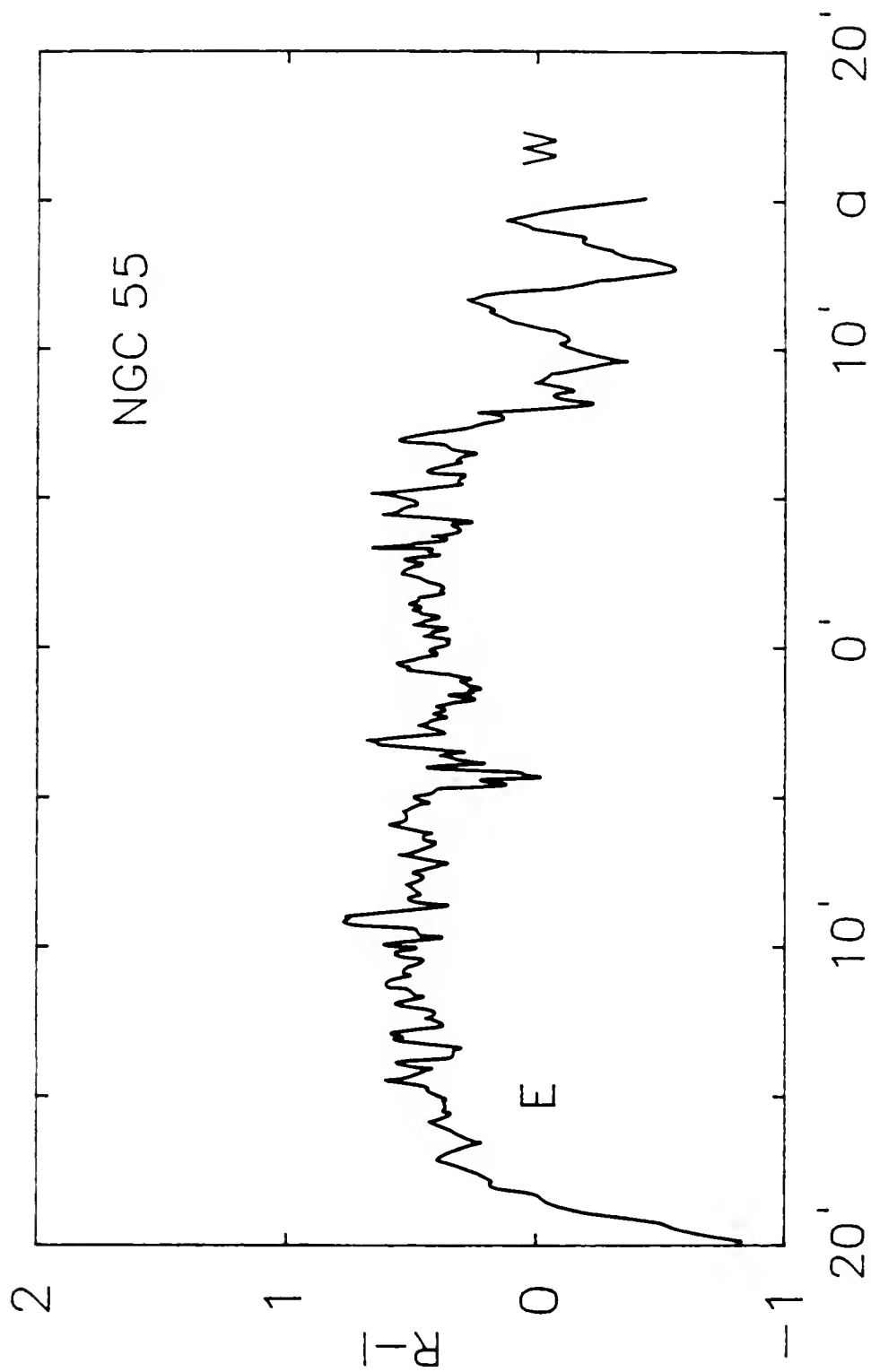


Figure 19. Major axis (R - I) color profile for NGC 55.

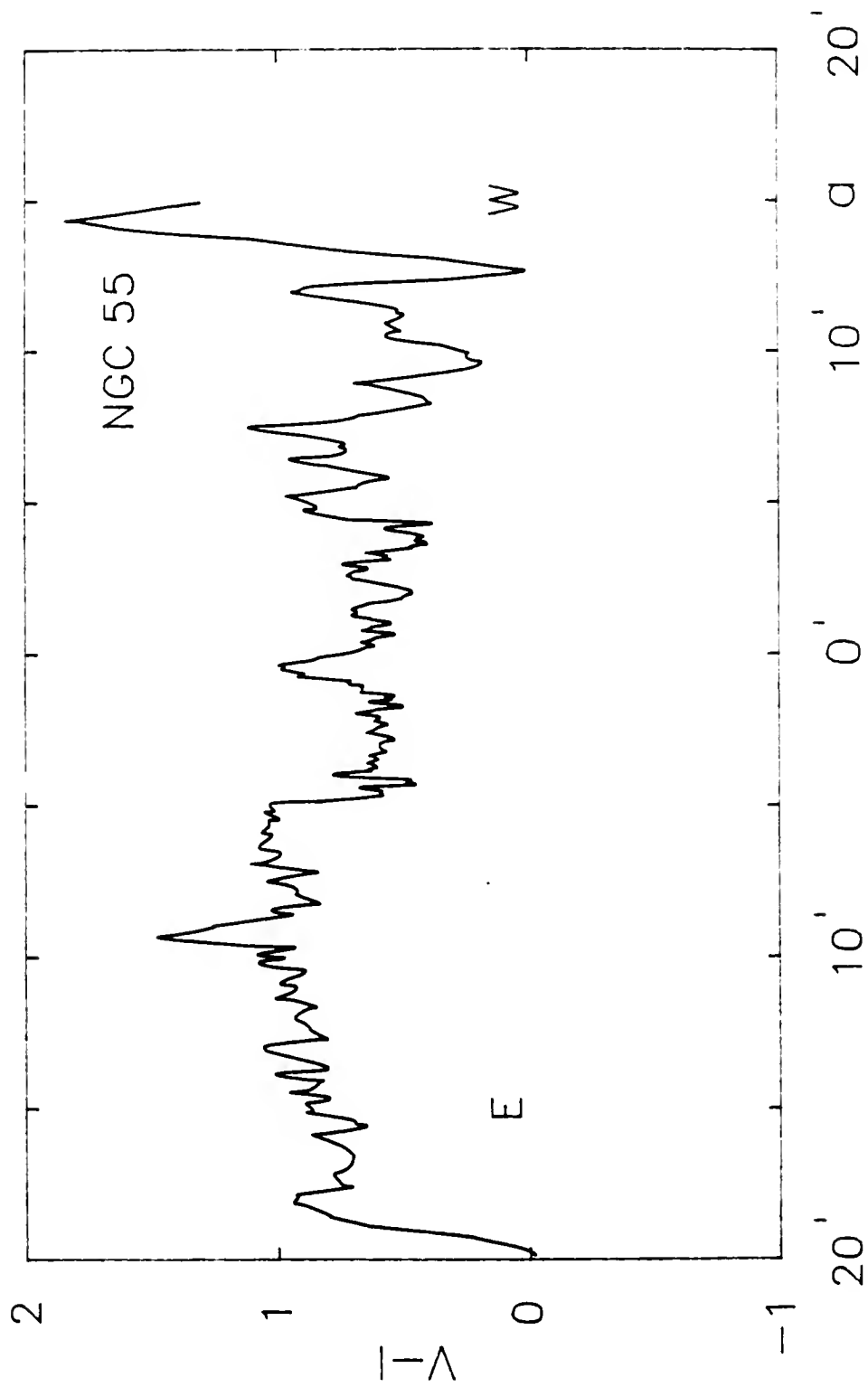


Figure 20. Major axis (V - I) color profile for NGC 55.

osity profiles. It is also visible on the isophote maps as the west edge of the bright island at about $10'$, and on the photograph where some details can be seen. An enhancement in star density occurs here and de Vaucouleurs (1961) lists two HII regions here. Color indices of $V-R \approx 0.9$, $R-I \approx 0.5$ and $V-I \approx 1.4$ indicate this feature is probably one or more heavily reddened young star clusters. The location would place it on the near side or the inside of the asymmetric arm.

Minor Axis

Figures 21, 22 and 23 show the minor axis color profiles. Photometric errors render color measurements unreliable at distances in excess of $\geq 3'$. In addition, a comparison of the long and short exposure I north profile shows variations up to a few tenths of a magnitude in the region of overlap. The two profiles were joined between $1'$ and $2'$ to form the composite profile and the transition is not as smooth as could be hoped for. Coupled with the large gradient in the north infrared profile, the $R-I$ and $V-I$ colors on this side are prone to be less reliable than their counterparts on the south side.

Within about $1'.2$ either side of the nucleus the color is approximately constant: $V-R \approx 0.2$, $R-I \approx 0.4$, $V-I \approx 0.6$. Again, the nucleus is not distinguished by its color. A slightly redder area is seen less than $0'.5$ due south, which appears to be related to the dust in this region.

In general, the south side of the minor axis has nearly constant or slowly increasing color indices with increasing

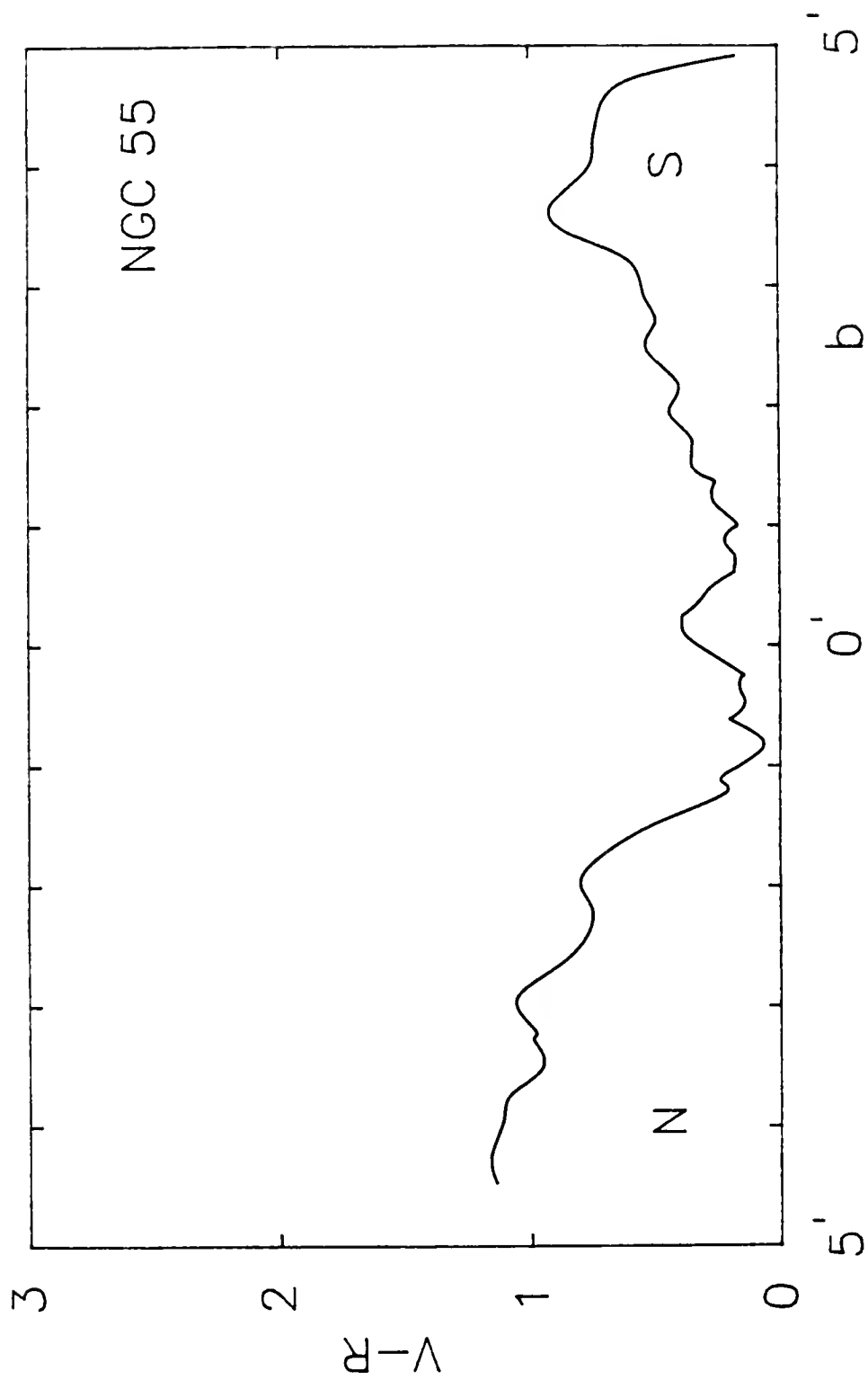


Figure 21. Minor axis (V - R) color profile for NGC 55.

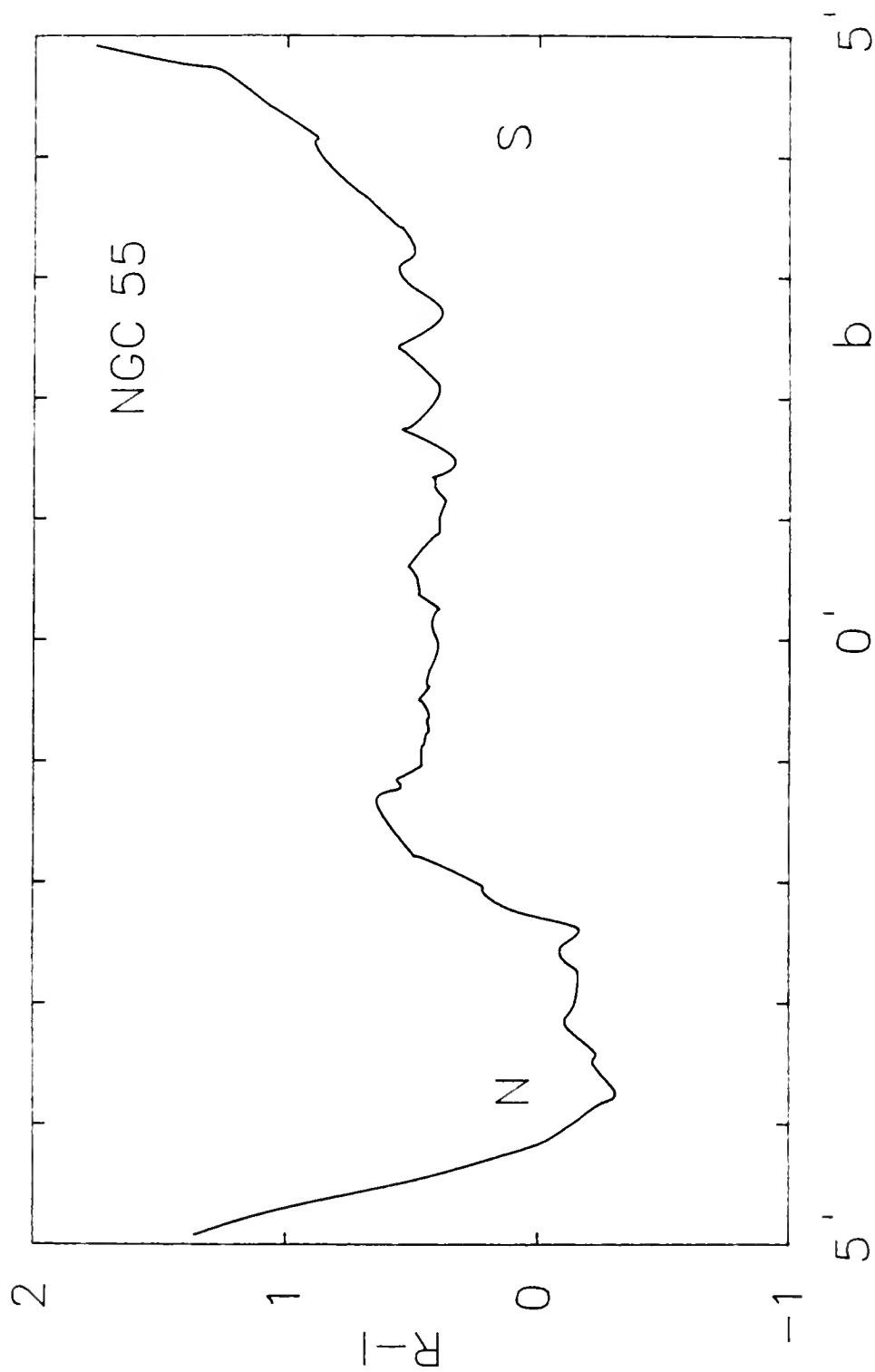


Figure 22. Minor axis (R - I) color profile for NGC 55.

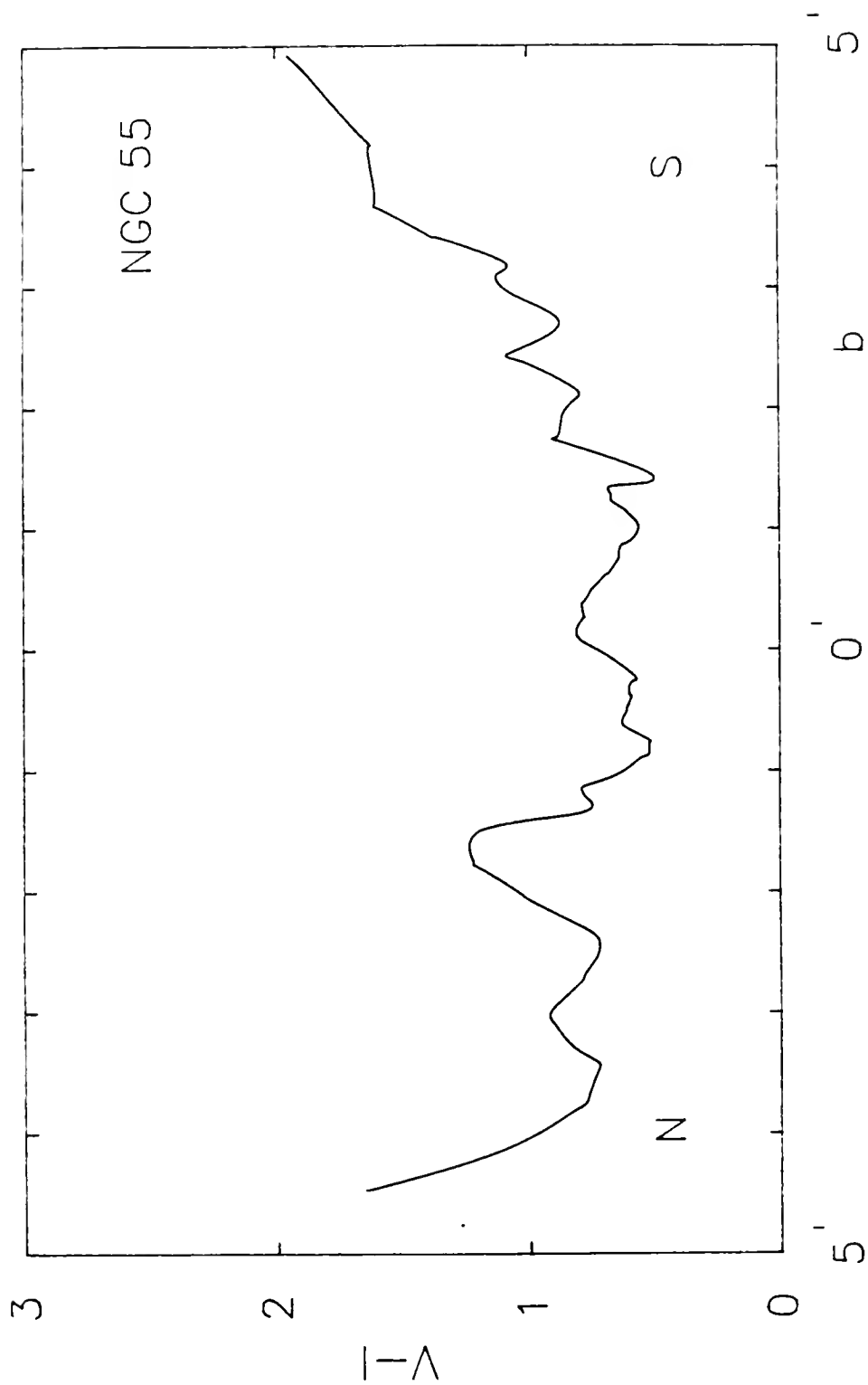


Figure 23. Minor axis (V - I) color profile for NGC 55.

distance. The luminous area 1'-2' south of the bar, mentioned in the discussion of the asymmetry profiles, does not consist of material significantly different from the rest of the bar as judged by its colors. In contrast, the north side of the minor axis exhibits peculiar behavior. The V-R color index increases beyond about 1' while the R-I color index becomes negative between 2' and 4'. The latter values are highly suspect, and an error of one or two tenths of a magnitude could change these to positive values. Lastly, the V-I color index shows a red hump at about 1'.5. There may be some dust at this location but nothing definite can be seen on the photograph.

Integrated Parameters and Colors

The standard photometric parameters as defined by de Vaucouleurs (1962) have been calculated. First, the array of intensities $I(x,y)$ in each color was numerically integrated within isophotes spaced at 0.10 in $\log I$. Then the equivalent radius $r^* = \sqrt{(A/\pi)}$ was computed for each intensity level by calculating the total area, A , in square arc minutes within a given isophote, including islands. The resulting equivalent luminosity profiles for V, R and I are shown in Figures 24, 25 and 26.

Comparison of the three profiles shows all are approximately exponential over about a six magnitude range. A small rise occurs in each profile at about $3' \leq r^* \leq 5'$, caused by the bright areas corresponding to the asymmetric arm. In

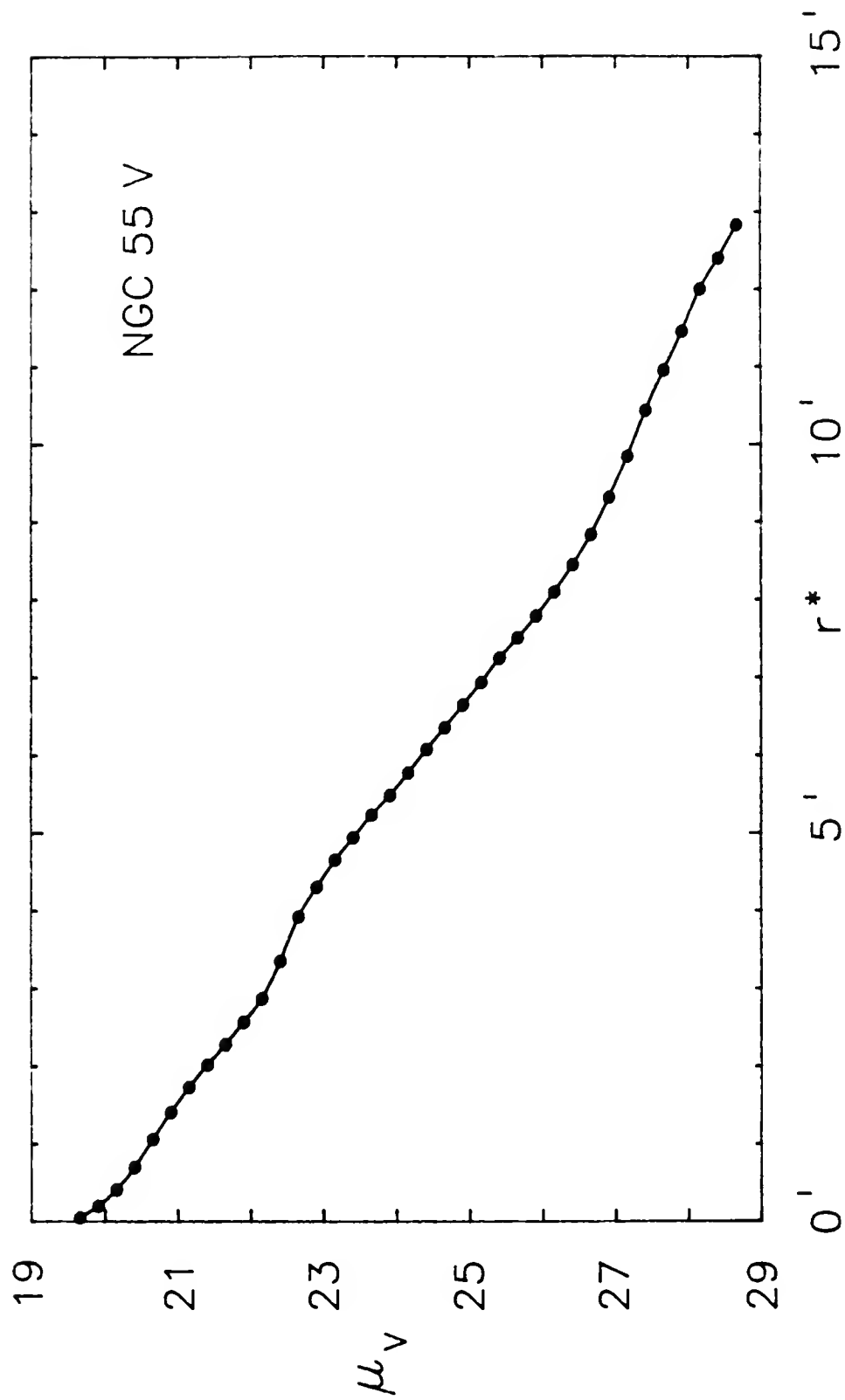


Figure 24. Equivalent mean V luminosity profile for NGC 55.

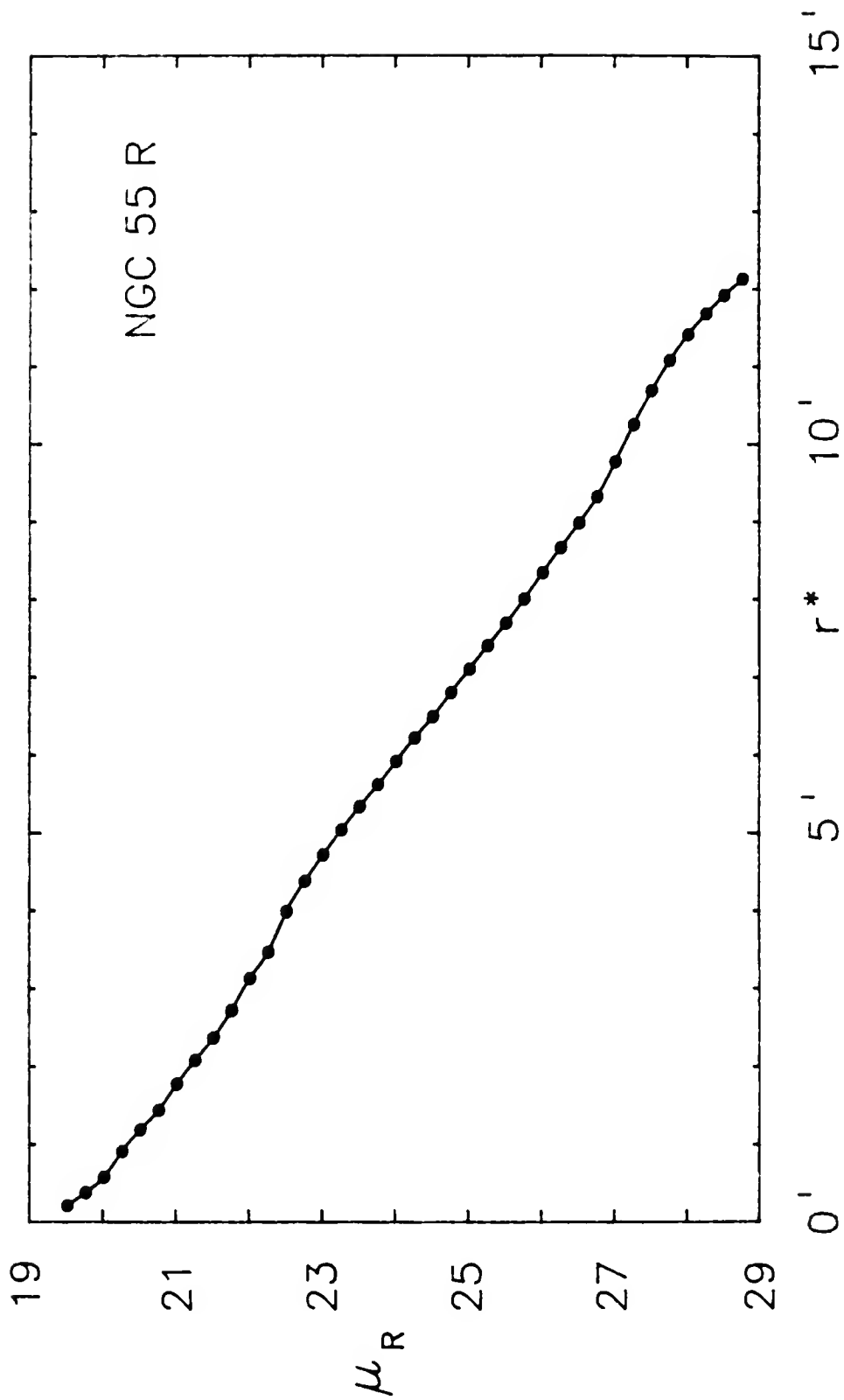


Figure 25. Equivalent mean R luminosity profile for NGC 55.

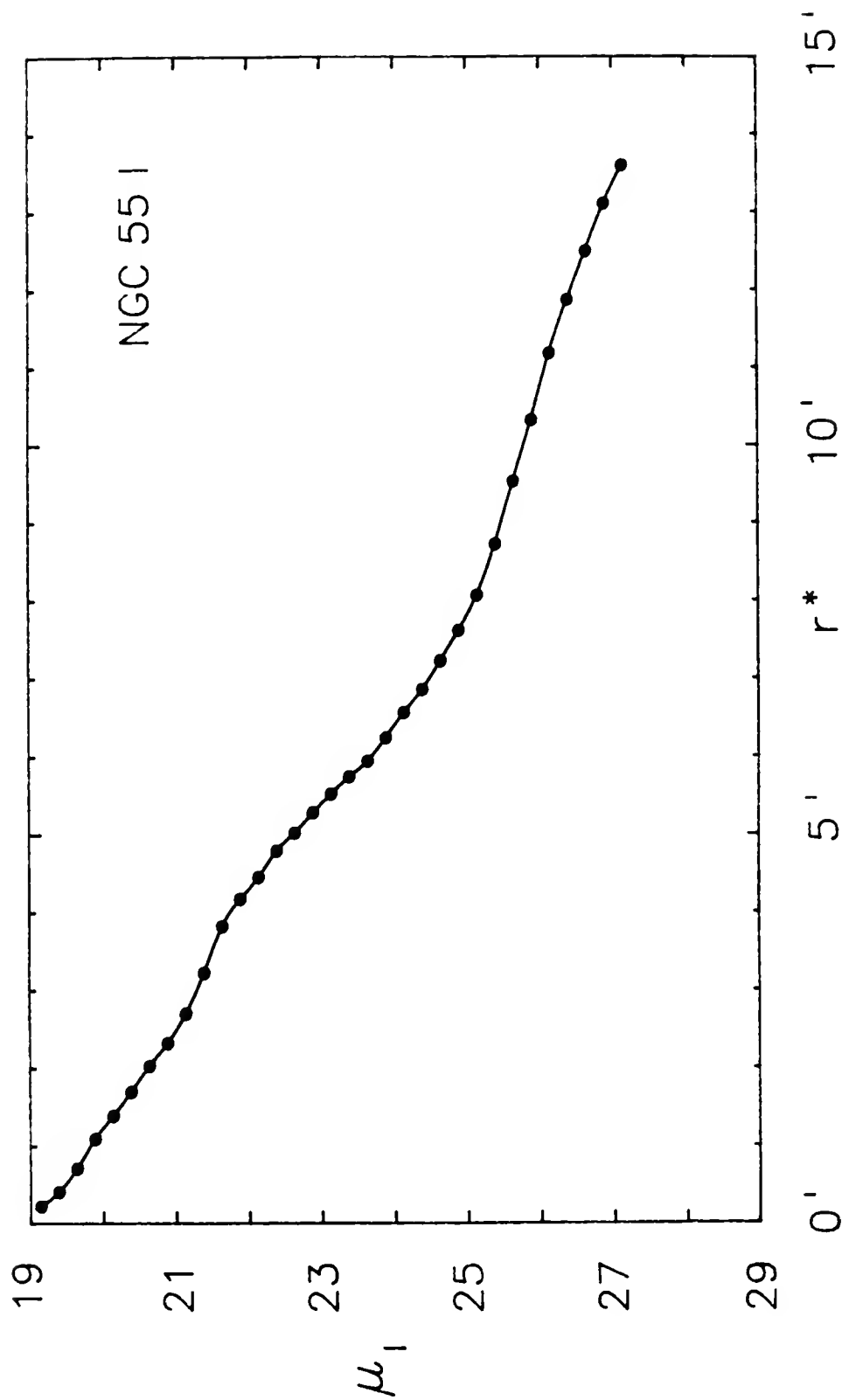


Figure 26. Equivalent mean I luminosity profile for NGC 55.

contrast, de Vaucouleurs (1961) pg data, when plotted, show little or no rise here. The V and R profiles are quite similar, the R profile being a few tenths of a magnitude brighter over almost its entire range. The I equivalent luminosity profile, however, is much brighter than either the V or R profile over its entire length, and the asymmetric arm contribution is more pronounced. Hence, much of the light of this feature must be obscured by dust. Additionally, the contribution of the faint, and presumably heavily reddened, outer regions pushes the profile up at large r' . It is also possible this profile shows evidence of a red halo to NGC 55, although the major and minor axis luminosity profiles do not lend this much support. The infrared results presented here should be verified by independent measurements to clarify this interesting possibility.

Tables 15, 16 and 17 give the mean luminosity distributions for the V, R and I data, based on the equivalent radius calculations. Column (1) lists the intensity level in each isophote step and column (2) gives the included area in square arc minutes. Column (3) gives the integrated luminosity $L(r') = 2\pi \int_0^{r'} I(r) r dr$ at each equivalent radius r' as the power ($= I \times \Delta A$) within each isophote level. Column (4) lists the integrated luminosity at each level as the sum of the power. To get the total luminosity $L_T = 2\pi \int_0^{\infty} I(r) r dr$, a small correction was added to the integrated luminosity within the last value of r' , calculated using a small extrapolation

TABLE 15

MEAN V LUMINOSITY DISTRIBUTION IN NGC 55

log I	Area	Power	Sum P	r*	k(r*)	2a	2b	Mag
0.5	0.008	0.026	0.026	0.05	0.001			19.66
0.4	.126	.295	.321	.20	.001			19.91
0.3	.528	.891	1.21	.41	.035	0.97	0.58	20.16
0.2	1.54	1.79	3.00	.70	.087	1.48:	.84	20.41
0.1	3.53	2.76	5.76	1.06	.166	4.00	1.29	20.66
0.0	6.25	3.09	8.85	1.41	.255	4.90:	1.61	20.91
-0.1	9.40	2.78	11.63	1.73	.335	6.97:	1.94	21.16
-0.2	12.82	2.43	14.06	2.02	.405	8.45	2.13	21.41
-0.3	16.33	1.98	16.04	2.28	.463	9.03:	2.45	21.66
-0.4	20.75	1.97	18.01	2.57	.519	9.42	2.77	21.91
-0.5	25.88	1.82	19.83	2.87	.572	9.94:	2.97	22.16
-0.6	35.29	2.64	22.47	3.35	.648	18.45:	3.16	22.41
-0.7	48.24	2.92	25.39	3.92	.732	20.90	3.42	22.66
-0.8	57.97	1.73	27.12	4.30	.782	21.87	3.74	22.91
-0.9	67.82	1.39	28.51	4.65	.822	22.77	4.00	23.16
-1.0	76.78	1.00	29.51	4.94	.851	24.00	4.32	23.41
-1.1	85.80	.804	30.31	5.23	.874	24.52	4.65	23.66
-1.2	94.48	.613	30.93	5.48	.892	25.29	5.03	23.91
-1.3	104.4	.559	31.49	5.77	.908	26.39	5.42	24.16
-1.4	115.8	.508	31.99	6.07	.922	28.39	5.81	24.41
-1.5	126.7	.386	32.38	6.35	.934	29.03	6.00	24.66
-1.6	138.6	.335	32.72	6.64	.943	29.29	6.26	24.91
-1.7	150.8	.272	32.99	6.93	.951	29.68:	6.39	25.16
-1.8	164.5	.243	33.23	7.24	.958	30.97	6.65	25.41
-1.9	176.6	.172	33.40	7.50	.963	31.48	7.03	25.66
-2.0	190.2	.151	33.55	7.78	.967	32.06	7.48	25.91
-2.1	205.6	.137	33.69	8.09	.971	32.77	7.87	26.16
-2.2	223.7	.128	33.82	8.44	.975	33.42	8.13	26.41
-2.3	245.0	.120	33.94	8.83	.979	33.81	8.39	26.66
-2.4	272.4	.121	34.06	9.31	.982	34.45	8.71	26.91
-2.5	304.3	.112	34.17	9.84	.985	35.10	8.97	27.16
-2.6	342.0	.106	34.28	10.43	.988	36.1	9.3	27.41
-2.7	376.5	.077	34.35	10.95	.990			27.66
-2.8	412.1	.065	34.42	11.45	.993			27.91
-2.9	452.2	.057	34.48	12.00	.994			28.16
-3.0	482.7	.035	34.52	12.40	.995			28.41
-3.1	516.9	.031	34.54	12.83	.996			28.66
			34.68:		(1)			

TABLE 16

MEAN R LUMINOSITY DISTRIBUTION IN NGC 55

log I	Area	Power	Sum P	r*	k(r*)	2a	2b	Mag
0.6	0.139	0.586	0.586	0.21	0.012			19.52
0.5	.454	1.09	1.68	.38	.036			19.77
0.4	1.06	1.66	3.34	.58	.071	1.08	0.65	20.02
0.3	2.60	3.38	6.72	.91	.142	3.06	0.90	20.27
0.2	4.45	3.26	9.98	1.19	.211	4.08	1.32	20.52
0.1	6.51	2.94	12.92	1.44	.273	4.92	1.68	20.77
0.0	9.95	3.83	16.75	1.78	.354	7.68:	2.04	21.02
-0.1	13.59	3.25	20.00	2.08	.423	8.52	2.28	21.27
-0.2	17.65	2.88	22.88	2.37	.484	9.36	2.64	21.52
-0.3	23.24	3.12	26.00	2.72	.550	17.52:	2.88	21.77
-0.4	30.78	3.36	29.36	3.13	.621	19.20	3.36	22.02
-0.5	37.89	2.54	31.90	3.47	.675	20.40	3.60	22.27
-0.6	50.01	3.43	35.33	3.99	.747	21.84	3.96	22.52
-0.7	60.19	2.28	37.61	4.38	.795	23.76	4.32	22.77
-0.8	69.87	1.72	39.33	4.72	.832	24.24	4.68	23.02
-0.9	79.72	1.40	40.73	5.04	.861	24.96	5.04	23.27
-1.0	89.56	1.11	41.84	5.34	.885	25.80	5.40	23.52
-1.1	99.24	0.864	42.70	5.62	.903	26.64	6.00	23.77
-1.2	110.1	.771	43.48	5.92	.920	28.44	6.24	24.02
-1.3	121.4	.626	44.10	6.22	.933	29.16	6.48	24.27
-1.4	132.2	.482	44.58	6.49	.943	30.72	6.72	24.52
-1.5	145.4	.467	45.05	6.80	.953	31.68	7.08	24.77
-1.6	158.3	.363	45.41	7.10	.960	32.28	7.44	25.02
-1.7	172.0	.309	45.72	7.40	.967	33.12	7.92	25.27
-1.8	185.8	.244	45.97	7.69	.972	33.84	8.16	25.52
-1.9	201.2	.219	46.18	8.00	.977	35.04:	8.40	25.77
-2.0	218.3	.192	46.38	8.34	.981	38.2	8.9	26.02
-2.1	235.7	.155	46.53	8.66	.984	38.6	9.0	26.27
-2.2	253.4	.125	46.66	8.98	.987	39.8	9.2	26.52
-2.3	272.9	.110	46.77	9.32	.989	40.4	9.4	26.77
-2.4	300.1	.121	46.89	9.77	.992	41.0	9.6	27.02
-2.5	329.8	.105	46.99	10.25	.994	41.5	9.7	27.27
-2.6	359.0	.083	47.08	10.69	.996			27.52
-2.7	385.7	.060	47.14	11.08	.997			27.77
-2.8	408.9	.041	47.18	11.41	.998			28.02
-2.9	428.4	.028	47.20	11.68	.998			28.27
-3.0	446.3	.020	47.22	11.92	.999			28.52
-3.1	462.4	.014	47.24	12.13	.999			28.77
			47.28:		(1)			

TABLE 17

MEAN I LUMINOSITY DISTRIBUTION IN NGC 55

log I	Area	Power	Sum P	r*	k(r*)	2a	2b	Mag
0.1	0.152	0.204	0.204	0.22	0.011			19.14
0.0	.534	.565	.769	.41	.040	0.97	0.49	19.39
-0.1	1.60	.945	1.71	.71	.090	1.30	0.81	19.64
-0.2	3.74	1.497	3.21	1.09	.168	3.57	1.14	19.89
-0.3	6.08	1.297	4.51	1.39	.237	4.22	1.46	20.14
-0.4	9.07	1.305	5.81	1.70	.305	5.03:	1.70	20.39
-0.5	12.91	1.397	7.21	2.03	.378	7.86	2.03	20.64
-0.6	16.86	1.130	8.34	2.32	.438	8.43	2.43	20.89
-0.7	22.84	1.337	9.68	2.70	.508	10.54:	2.76	21.14
-0.8	32.65	1.769	11.45	3.22	.601	18.24	3.08	21.39
-0.9	45.89	1.886	13.33	3.82	.699	18.81	3.41	21.64
-1.0	54.64	0.983	14.32	4.17	.751	20.27:	3.73	21.89
-1.1	62.32	.685	15.00	4.45	.787	21.41	4.05	22.14
-1.2	72.14	.701	15.70	4.79	.824	22.86	4.38	22.39
-1.3	79.07	.393	16.09	5.02	.844	23.68	4.62	22.64
-1.4	87.61	.384	16.48	5.28	.865	24.24	4.86	22.89
-1.5	95.61	.284	16.76	5.52	.879	24.81	5.27	23.14
-1.6	103.5	.221	16.98	5.74	.891	25.70	5.68	23.39
-1.7	111.0	.168	17.15	5.94	.900	26.43	6.00	23.64
-1.8	122.4	.204	17.36	6.24	.911	26.92	6.41	23.89
-1.9	135.1	.180	17.54	6.56	.920	29.35:	6.73	24.14
-2.0	147.6	.139	17.67	6.85	.927	30.00:	7.14	24.39
-2.1	163.7	.145	17.82	7.22	.935	30.57:	7.46	24.64
-2.2	182.2	.131	17.95	7.61	.942	31.05	7.78	24.89
-2.3	204.1	.124	18.07	8.06	.948	31.8	8.1	25.14
-2.4	239.0	.155	18.23	8.72	.956	33.2	8.5	25.39
-2.5	285.5	.165	18.39	9.53	.965	33.6	8.9	25.64
-2.6	334.9	.139	18.53	10.32	.972	34.1	9.7	25.89
-2.7	392.7	.130	18.66	11.18	.979	34.4	10.8	26.14
-2.8	442.5	.089	18.75	11.87	.984			26.39
-2.9	490.0	.068	18.82	12.49	.987			26.64
-3.0	539.0	.055	18.88	13.10	.990			26.89
-3.1	580.0	.037	18.91	13.59	.992			27.14
			19.06:		(1)			

from the last reliable data points to $I = 0$ (de Vaucouleurs 1960, Appendix). Column (5) gives the equivalent radius at each level and column (6) gives the fraction of the total luminosity contained in each successive level. Columns (7) and (8) list the sizes of the major and minor axes at each level and column (9) gives the surface brightness in magnitudes per square arc second. The total magnitudes are: $V_T = 8.17 \pm 0.04$, $R_T = 7.94 \pm 0.03$, and $I_T = 7.30 \pm 0.02$ where the errors are the errors in sky determination and the interpolation correction to the integrated magnitude. Errors in the values for R and I are underestimated because of the uncertainty in the sky values.

The relative integrated luminosity, $k(r') = L(r')/L_T$ is plotted in Figures 27, 28 and 29 for the V, R and I data, respectively. The quantities r_1' , r_0' , r_3' and μ_1 , μ_0 , and μ_3 , corresponding to $k = 1/4$, $1/2$ and $3/4$ are also shown. The equivalent effective radius, defined by $k(r_0') = 1/2$, is $r_0' = 2'.47$, $2'.45$ and $2'.66$ for V, R and I. These correspond to 1.28, 1.27 and 1.38 kpc at 1.78 Mpc. Quartiles are defined by $k(r_1') = 1/4$ and $k(r_3') = 3/4$. These are at $r_1' = 1'.39$, $1'.35$ and $1'.45$, corresponding to 0.72, 0.70 and 0.75 kpc, and $r_3' = 4'.05$, $4'.02$ and $4'.16$, or, 2.10, 2.08 and 2.15 kpc for V, R and I, respectively. By way of comparison, the pg values from de Vaucouleurs (1961, Figure 4) are $r_0' = 3'.3$, $r_1' = 1'.9$ and $r_3' = 5'.13$. His larger values reflect the smaller

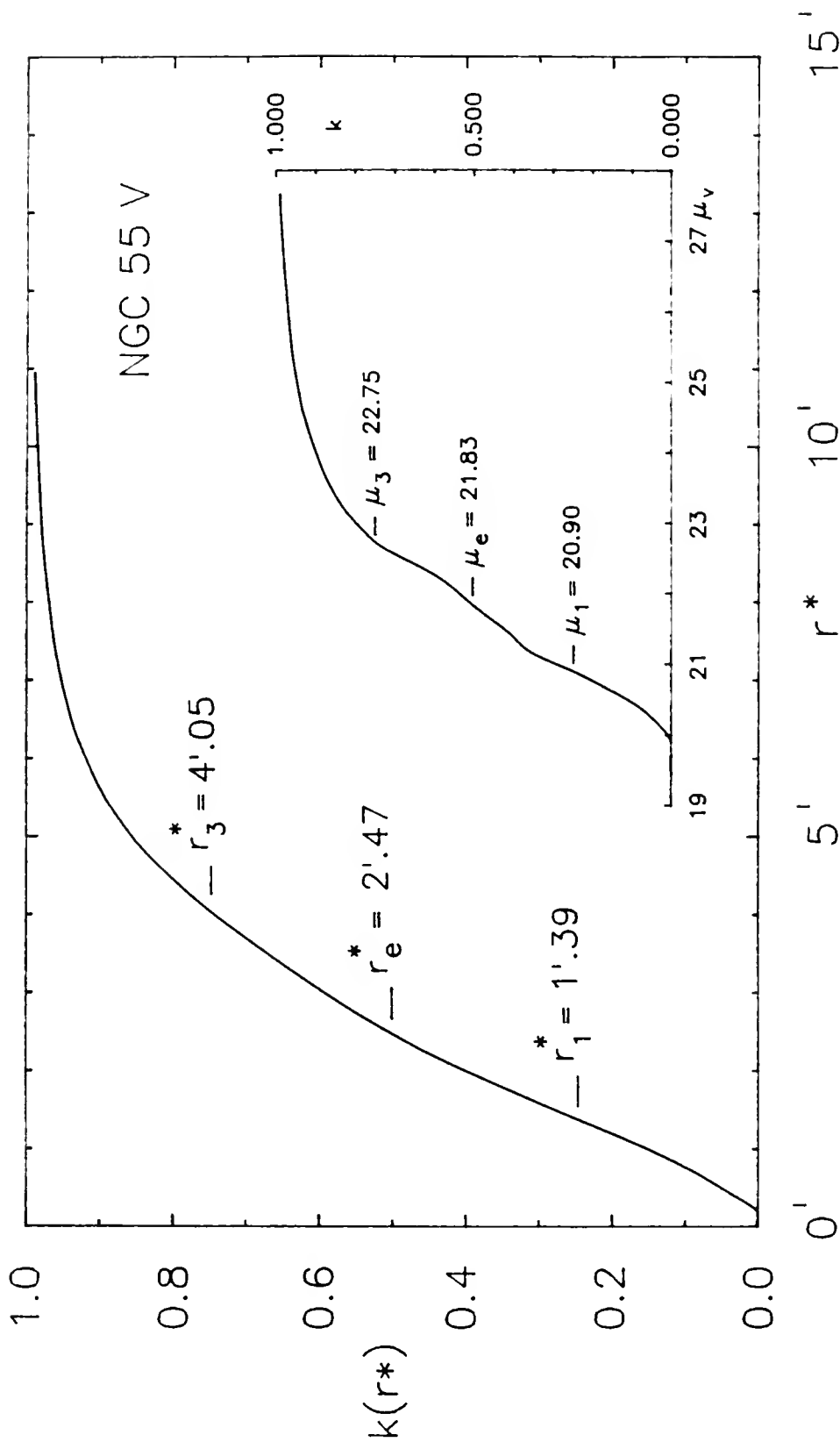


Figure 27. Relative V integrated luminosity curves for NGC 55 showing the fraction $k = L(r^*)/L_r$ of the total luminosity emitted within radius r^* . The insert shows the fraction of the total luminosity in regions brighter than μ_v .

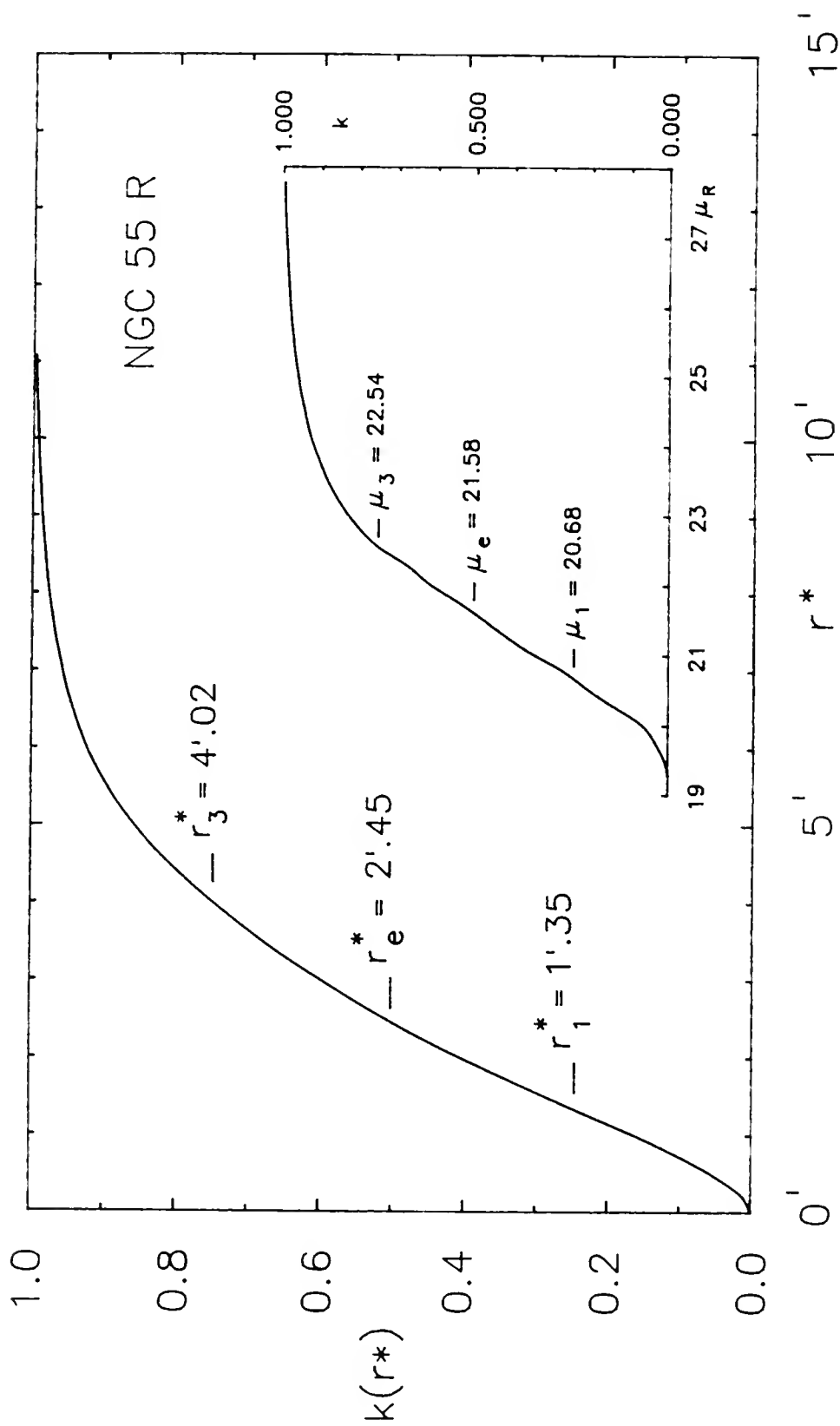


Figure 28. Relative R integrated luminosity curves for NGC 55 showing the fraction $k = L(r^*)/L_T$ of the total luminosity emitted within radius r^* . The insert shows the fraction of the total luminosity in regions brighter than μ_R .

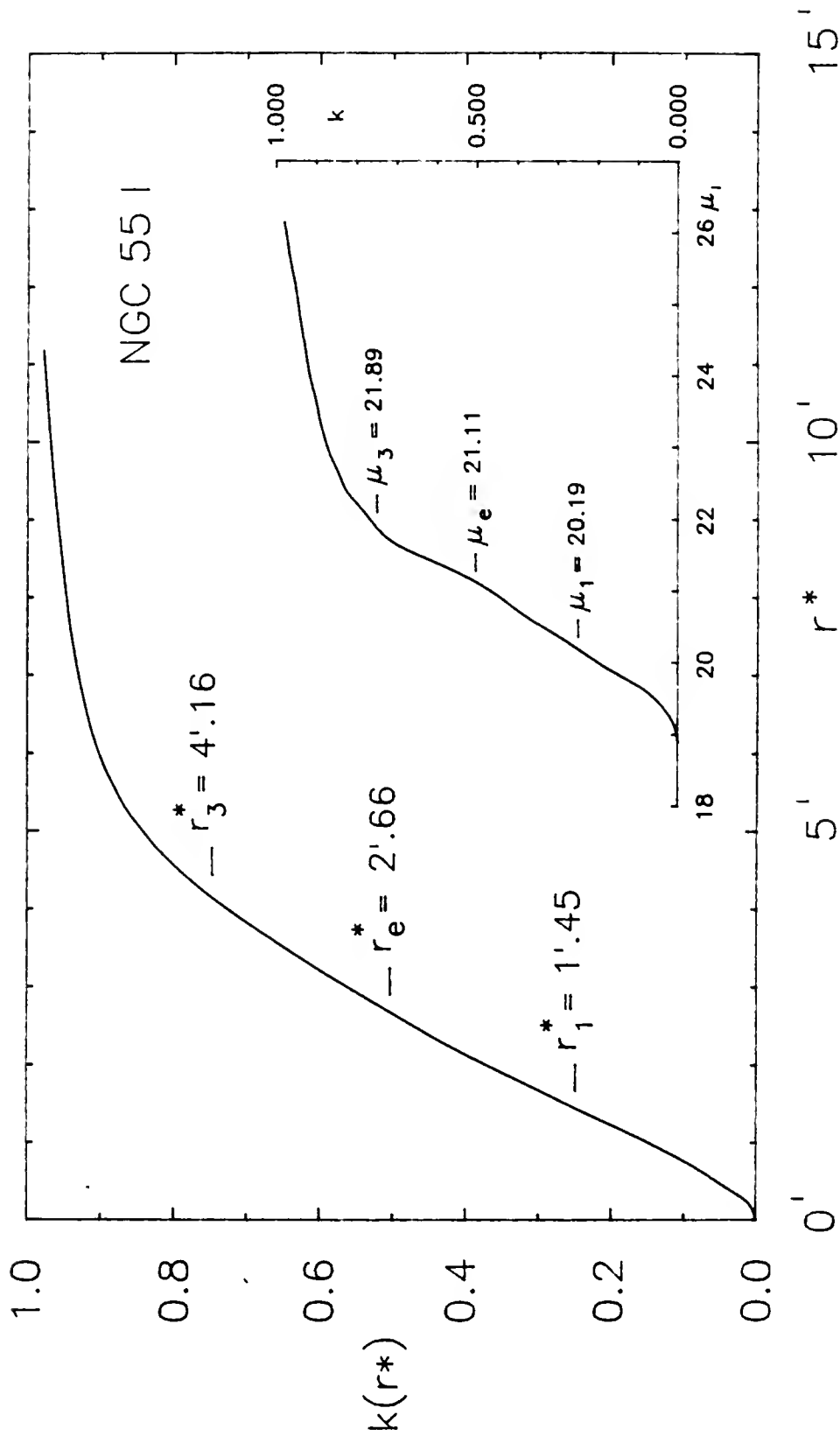


Figure 29. Relative I integrated luminosity curves for NGC 55 showing the fraction $k = L(r^*)/L_T$ of the total luminosity emitted within radius r^* . The insert shows the fraction of the total luminosity in regions brighter than μ_1 .

gradient he found in the exponential light distribution of this galaxy.

Concentration indices, defined by $C_{21} = r_0^*/r_1^*$ and $C_{32} = r_3^*/r_0^*$ have values of 1.78, 1.81, 1.83 and 1.64, 1.64 and 1.56, respectively, for V, R and I. De Vaucouleurs finds $C_{21} = 1.74$ and $C_{32} = 1.61$ in pg. These values are to be compared to the values expected for a pure exponential distribution, $C_{21} = 1.75$ and $C_{32} = 1.60$. The V, R and I C_{21} values indicate the light becomes more centrally concentrated with increasing wavelength than would be the case for an exponential distribution. The V and R C_{32} values continue to show that the light is mostly concentrated in the inner regions. However, the I C_{32} value indicates the luminosity in the region between r_0^* and r_3^* is less centrally concentrated than it would be for a purely exponential disk. The increased contribution to the I luminosity coming from the asymmetric arm in this range of r^* is mainly responsible for this change.

Corrections are usually made to the apparent magnitudes to account for galactic extinction, internal extinction and redshift. The correction for redshift, called the K correction, is less than 0.01 magnitude for NGC 55 (Pence 1976) and will be neglected. The correction for galactic extinction is estimated to be $A_g = 0.23$ in the RC2. Using the values of $A_\lambda/E(B-V)$ given by Savage and Mathis (1979) and interpolating to the effective wavelengths used here, values of $A_v = 0.17$, $A_R = 0.14$ and $A_I = 0.11$ are obtained. Internal extinction is

difficult to estimate. Based on RC2 data, the internal differential absorption $A_0(i) = 0.68$ for blue light. Subtracting this quantity gives the face-on magnitude, not the absorption-free magnitude which is unknown because it depends on the dust distribution in NGC 55. For the V, R and I passbands the estimated values of $A_0(i)$ are 0.49, 0.42 and 0.32. Applying the standard corrections given in the RC2 to the integrated magnitudes m_T using the above values of A_λ and $A_0(i)$ yields the total face-on magnitude corrected for galactic and internal absorption:

$$m_T^0 = m_T - A_\lambda - A_0(i). \quad (14)$$

For NGC 55 $V_T^0 = 7.51 \pm 0.06$, $R_T^0 = 7.38 \pm 0.05$, and $I_T^0 = 6.87 \pm 0.04$.

The RC2 gives values of $B_T = 7.9 \pm 0.3$ (m.e.) and $B_T^0 = 6.99$ which seem much too bright, and a zero point error is suspected in the earlier photometry. A mean zero point correction of -0.55 ± 0.1 is derived for Mount Stromlo photographic magnitudes (the source of the pg and B magnitudes given above) by de Vaucouleurs and Agüero (1973). If this correction is applied to the listed B_T , a new value of $B_T = 8.45$ is obtained. By way of comparison, de Vaucouleurs and Freeman (1972) list $B_T = 8.56$ for NGC 55 and Puche, Carignan and Wainscoat (1990) have $B_T = 8.41$. Here, the value $B_T = 8.56$ will be used. Then correcting for galactic and internal absorption using the values given above, $B_T^0 = 7.65$.

At the assumed distance of 1.78 Mpc, the distance modulus of NGC 55 is 26.25 and the corrected face-on absolute magnitudes are : $M_T^0(B) = -18.60$, $M_T^0(V) = -18.74$, $M_T^0(R) = -18.87$, and $M_T^0(I) = -19.38$, all with an uncertainty of about ± 0.4 . Thus, NGC 55 is brighter than the LMC which has $M_T^0(B) = -18.35$ assuming the RC2 values for $B_T = 0.14$ and a distance of 50 kpc (de Vaucouleurs and Freeman 1972).

The colors of NGC 55 are $(B_J - V)_T = 0.39$, $(V - R)_T = 0.23 \pm 0.05$, and $(V - I)_T = 0.87 \pm 0.04$. Converting the V magnitude here to the Johnson V_J gives $(B_J - V_J)_T = 0.31$, somewhat bluer than that given by de Vaucouleurs and Freeman, $(B_J - V_J)_T = 0.55$, or that of Puche, Carignan and Wainscoat of $(B_J - V_J)_T = 0.47$. Following the precepts given in the RC2, the corrected face-on value of $(B_J - V_J)_T^0 = 0.04$. Using RC2 data, a mean corrected face-on color of $\langle (B_J - V_J)_T^0 \rangle = 0.353 \pm 0.087$ was found by de Vaucouleurs (1977) for 20 SBm galaxies, after 8 cycles of 2σ rejection of large residuals (mainly to remove galaxies with line emission). The difference between the corrected face-on color and the mean face-on color, given by $(B_J - V_J)_T^0 - \langle (B_J - V_J)_T^0 \rangle = -0.31$, may be caused by line emission in NGC 55 (see discussion by de Vaucouleurs 1977), although there is no way to check this here. At any event, the colors are somewhat peculiar.

All of the basic photometric parameters for NGC 55 obtained from the V, R and I plate analyses are summarized in Tables 18, 19 and 20.

TABLE 18

PHOTOMETRIC PARAMETERS OF NGC 55 V

Apparent distance modulus	$26.42 \pm 0.4:$
Corrected distance modulus	$26.25 \pm 0.4:$
Distance	1.78 ± 0.34 Mpc
Inclination	85°
Major axis position angle	$107^\circ.8 \pm 0^\circ.5$
Mean axis ratio $\langle b/a \rangle$, $23 < \mu < 26$	0.21 ± 0.02
Total apparent magnitude	$V_T = 8.17 \pm 0.04$
Corrected magnitude	$V_T^0 = 7.51 \pm 0.04$
Absolute magnitude	$M_T^0 = -18.74 \pm 0.4:$
Threshold surface brightness	$\mu_v = 27.6$
Major axis at threshold	$2a = 35'.9, 18.6$ kpc
Minor axis at threshold	$2b = 9'.5, 4.9$ kpc
Major axis at $\mu_v = 25.0$	$2a = 30'.1, 15.6$ kpc
Minor axis at $\mu_v = 25.0$	$2b = 6'.4, 3.3$ kpc
Luminosity within $\mu_v = 25.0$	$k = 0.946$
Mean gradient of exponential component, mag/arc minute	$G(a) = 0.65$ $G(b) = 1.68$
Parameters at $k = 1/4$	
Surface brightness	$\mu_1 = 20.90$
Equivalent radius	$r_1^* = 1'.39, 0.72$ kpc
Semi-major axis	$a_1 = 2'.4, 1.2$ kpc
Axis ratio	$b_1/a_1 = 0.33:$
Parameters at $k = 1/2$	
Surface brightness	$\mu_2 = 21.83$
Equivalent radius	$r_2^* = 2'.47, 1.28$ kpc
Semi-major axis	$a_2 = 4'.64, 2.40$ kpc
Axis ratio	$b_2/a_2 = 0.28$
Parameters at $k = 3/4$	
Surface brightness	$\mu_3 = 22.75$
Equivalent radius	$r_3^* = 4'.05, 2.10$ kpc
Semi-major axis	$a_3 = 10'.48, 5.43$ kpc
Axis ratio	$b_3/a_3 = 0.17$
Concentration indices	
C_{21}	$r_3^*/r_1^* = 1.78$
C_{32}	$r_3^*/r_2^* = 1.64$
Theoretical C_{21}	1.75
Theoretical C_{32}	1.60

TABLE 19

PHOTOMETRIC PARAMETERS OF NGC 55 R

Apparent distance modulus	$26.39 \pm 0.4:$
Corrected distance modulus	$26.25 \pm 0.4:$
Distance	1.78 ± 0.34 Mpc
Inclination	85°
Major axis position angle	$107^\circ.8 \pm 0^\circ.5$
Mean axis ratio $\langle b/a \rangle$, $23 < \mu < 26$	0.22 ± 0.02
Total apparent magnitude	$R_T = 7.94 \pm 0.03$
Corrected magnitude	$R_T^0 = 7.38 \pm 0.03$
Absolute magnitude	$M_T^0 = -18.87 \pm 0.4:$
Threshold surface brightness	$\mu_R = 27.8$
Major axis at threshold	$2a = 42'.6, 22.1$ kpc
Minor axis at threshold	$2b = 10'.2, 5.3$ kpc
Major axis at $\mu_R = 25.0$	$2a = 32'.0, 16.6$ kpc
Minor axis at $\mu_R = 25.0$	$2b = 7'.4, 3.8$ kpc
Luminosity within $\mu_R = 25.0$	$k = 0.959$
Mean gradient of exponential component, mag/arc minute	$G(a) = 0.51$ $G(b) = 1.52$
Parameters at $k = 1/4$	
Surface brightness	$\mu_1 = 20.68$
Equivalent radius	$r_1^* = 1'.35, 0.70$ kpc
Semi-major axis	$a_1 = 2'.33, 1.21$ kpc
Axis ratio	$b_1/a_1 = 0.33$
Parameters at $k = 1/2$	
Surface brightness	$\mu_2 = 21.58$
Equivalent radius	$r_2^* = 2'.45, 1.27$ kpc
Semi-major axis	$a_2 = 4'.79, 2.48$ kpc
Axis ratio	$b_2/a_2 = 0.28$
Parameters at $k = 3/4$	
Surface brightness	$\mu_3 = 22.54$
Equivalent radius	$r_3^* = 4'.02, 2.08$ kpc
Semi-major axis	$a_3 = 10'.93, 5.66$ kpc
Axis ratio	$b_3/a_3 = 0.185$
Concentration indices	
C_{21}	$r_2^*/r_1^* = 1.74$
C_{32}	$r_3^*/r_2^* = 1.64$
Theoretical C_{21}	1.75
Theoretical C_{32}	1.60

TABLE 20

PHOTOMETRIC PARAMETERS OF NGC 55 I

Apparent distance modulus	$26.36 \pm 0.4:$
Corrected distance modulus	$26.25 \pm 0.4:$
Distance	1.78 ± 0.34 Mpc
Inclination	85°
Major axis position angle	$107^\circ.8 \pm 0^\circ.5$
Mean axis ratio $\langle b/a \rangle$, $23 < \mu < 26$	0.25 ± 0.04
Total apparent magnitude	$I_T = 7.30 \pm 0.02$
Corrected magnitude	$I_T^0 = 6.87 \pm 0.02$
Absolute magnitude	$M_T^0 = -19.38 \pm 0.4:$
Threshold surface brightness	$\mu_I = 27.0$
Major axis at threshold	$2a = 35'.8, 18.5$ kpc
Minor axis at threshold	$2b = 12'.8, 6.6$ kpc
Major axis at $\mu_I = 25.0$	$2a = 31'.2, 16.2$ kpc
Minor axis at $\mu_I = 25.0$	$2b = 8'.0, 4.1$ kpc
Luminosity within $\mu_I = 25.0$	$k = 0.945$
Mean gradient of exponential component, mag/arc minute	$G(a) = 0.68$ $G(b) = 1.50$
Parameters at $k = 1/4$	
Surface brightness	$\mu_1 = 20.19$
Equivalent radius	$r_1^* = 1'.45, 0.75$ kpc
Semi-major axis	$a_1 = 2'.15, 1.11$ kpc
Axis ratio	$b_1/a_1 = 0.34$
Parameters at $k = 1/2$	
Surface brightness	$\mu_* = 21.11$
Equivalent radius	$r_*^* = 2'.66, 1.38$ kpc
Semi-major axis	$a_* = 5'.0:, 2.6$ kpc
Axis ratio	$b_*/a_* = 0.27$
Parameters at $k = 3/4$	
Surface brightness	$\mu_3 = 21.89$
Equivalent radius	$r_3^* = 4'.16, 2.15$ kpc
Semi-major axis	$a_3 = 10'.38, 5.38$ kpc
Axis ratio	$b_3/a_3 = 0.18$
Concentration indices	
C_{21}	$r_*^*/r_1^* = 1.83$
C_{32}	$r_3^*/r_*^* = 1.56$
Theoretical C_{21}	1.75
Theoretical C_{32}	1.60

CHAPTER IV
PHOTOMETRIC DATA FOR NGC 253

General Description

NGC 253 is classified in the RC2 as an intermediate type spiral with a weak bar, SAB(s) c. The bar is not easy to see in photographs or isophote maps because of the large inclination of this system. Pence (1978) gives a rectified photograph and remarks that NGC 253 is strikingly similar to M 83 which is seen nearly face-on. The appearance of NGC 253 in blue light is shown in Figure 30, reproduced from a print in the Hubble Atlas (Sandage 1961). North is at the top and east is to the left. The scale of the print is shown by the bar in the northwest corner. A considerable amount of dust is present, obscuring much of the structure of this galaxy. The large amount of dust seen in projection along the northwest side of the disk is used to indicate this is the near side. Pence gives the northeast side as approaching us, so we are seeing NGC 253 from "below", looking under the disk. The nucleus is heavily obscured by thick dust and can only be seen at longer wavelengths. Hereafter, unless otherwise specified, the nucleus refers to the brightest part of the optical image. This position does not coincide with the nucleus as measured at longer wavelengths, but is about 7" east and 2" north of

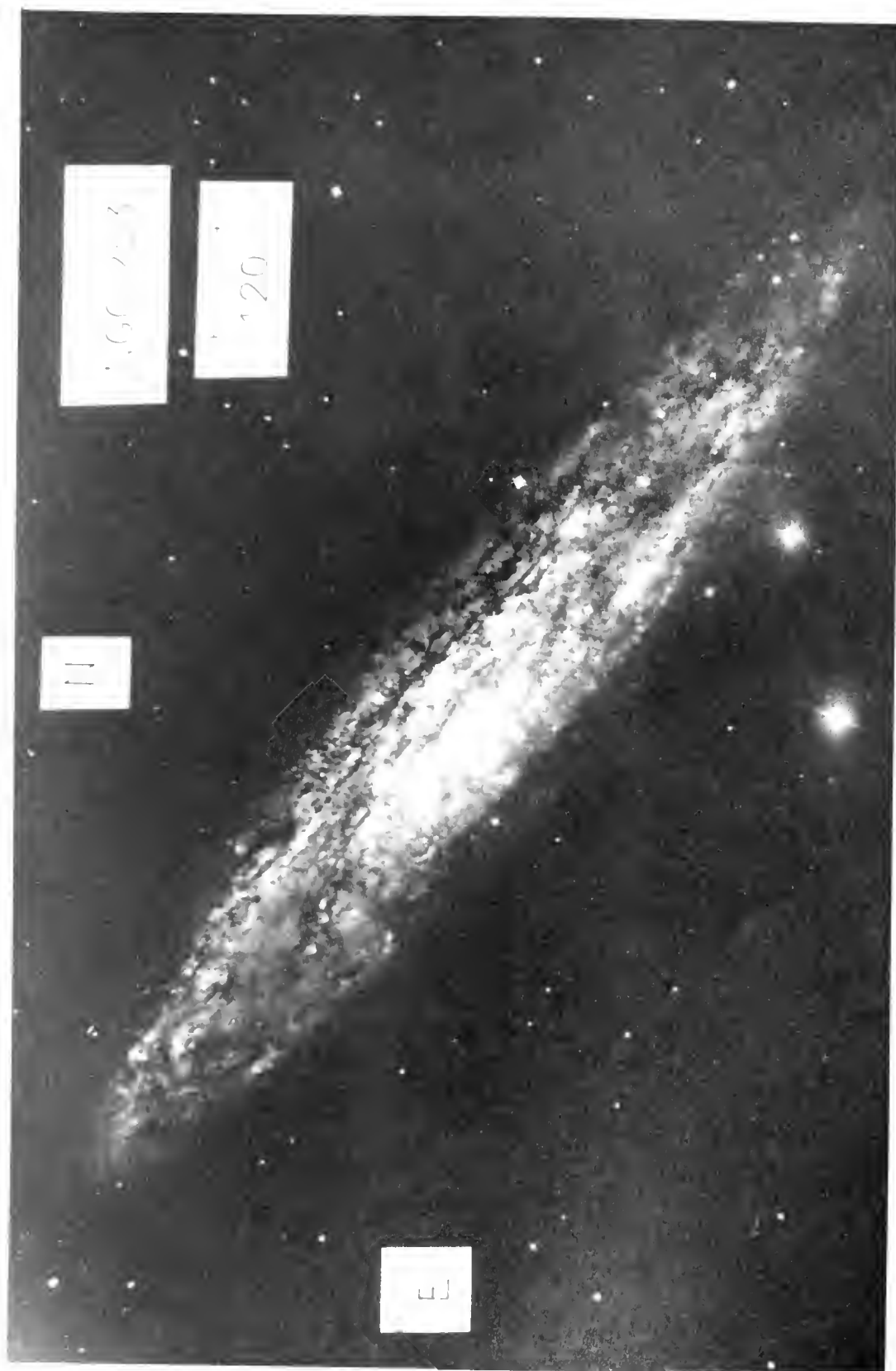


Figure 30. NGC 253 reproduced from the Hubble Atlas (Sandage 1961).

that location (Pence 1978). Table 21 presents some observational parameters of NGC 253.

TABLE 21
ELEMENTS OF NGC 253

R. A. (1950) ^a	00 ^h 45 ^m .13
Dec. (1950) ^a	-25° 33'.7
Galactic l, b ^a	99°.57, -87°.97
Supergalactic L, B ^a	271°.6, -5°.0
Type ^a	SAB(s)c (t=5)
Observed velocity V ^a	+249 km/sec
Corrected velocity V ₀ ^a	+259 km/sec
Apparent distance modulus	27.48 ± 0.4:
Corrected distance modulus	27.27 ± 0.4:

Note: ^a RC2, 1976.

Isophotal Contour Maps

Short exposure V, R and I isophote maps of the bright inner disk of NGC 253 are shown in Figures 31, 32 and 33. The maps show essentially what is visible on the photograph. The contour interval is $\mu = 0.25$ and the scale is shown by the bar. Also shown is the FWHM of the smoothing Gaussian beam. Dust lanes are noticeable on all three maps, but especially so on the near side of the galaxy and on the V map. The prominent lane seen about 1'.1 northeast of the nucleus lies about 4.6 kpc from the center of NGC 253 (for an assumed inclination of 78°.5) if it is in the plane of the disk. Absorption due to dust is somewhat minimized going to the infrared as can be seen by comparing the V and I maps, although the heavily obscured regions to the west and northwest of the nucleus remain well concealed. Comparison of the I map with the I'

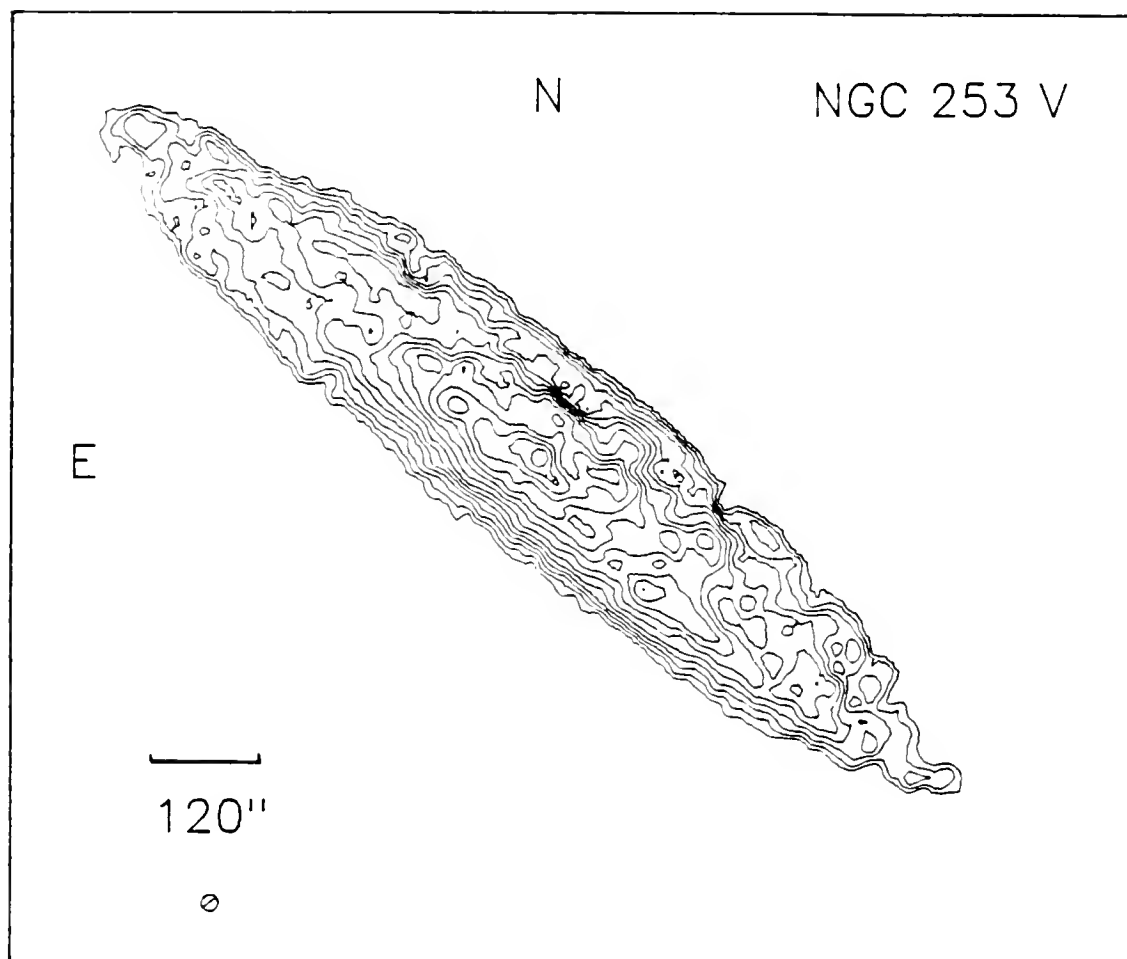


Figure 31. Short exposure V isophote map of NGC 253. The contour interval is 0.25 magnitude and the innermost isophote is at $\mu_v = 19.39$ and the outermost at 22.64. North is up and east is to the left. The bar shows the scale and the FWHM of the smoothing beam is shown by the circle.

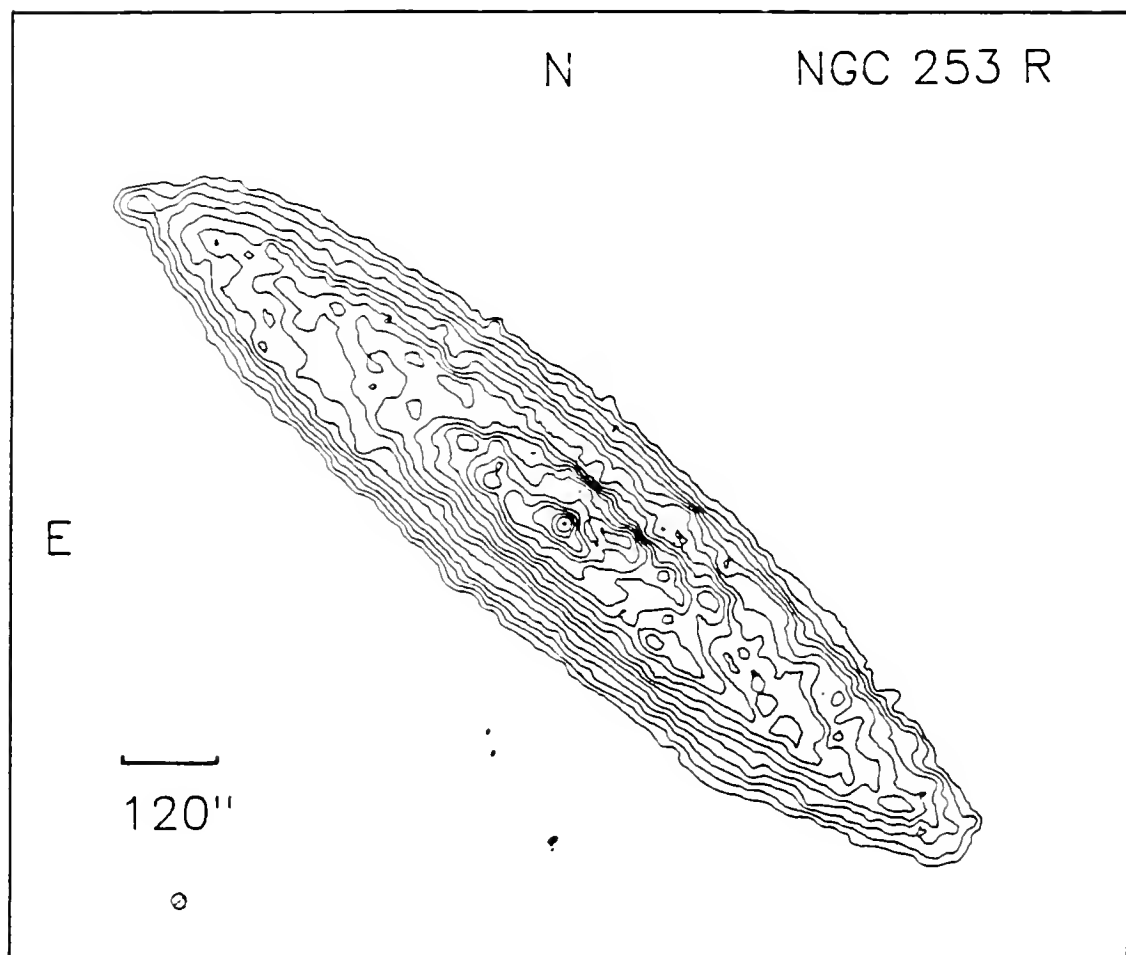


Figure 32. Short exposure R isophote map of NGC 253. The contour interval is 0.25 magnitude and the innermost isophote is at $\mu_R = 17.93$ and the outermost at 22.43. North is up and east is to the left. The bar shows the scale and the FWHM of the smoothing beam is shown by the circle.

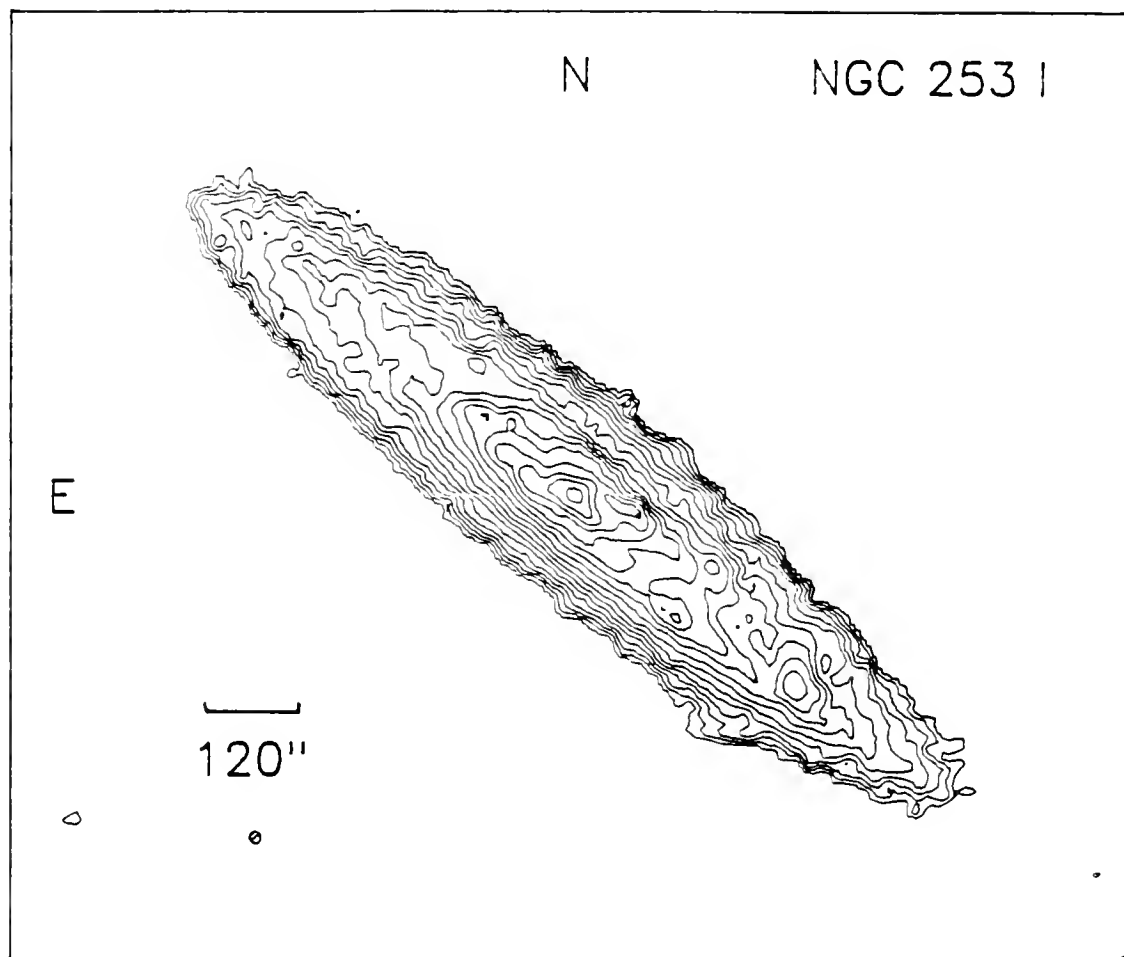


Figure 33. Short exposure I isophote map of NGC 253. The contour interval is 0.25 magnitude and the innermost isophote is at $\mu_1 = 17.59$ and the outermost at 21.59. North is up and east is to the left. The bar shows the scale and the FWHM of the smoothing beam is shown by the circle.

map in Uyama, Matsumoto and Thomas (1984) shows excellent agreement.

Although foreshortened by the inclination of NGC 253 and partially hidden by dust, the bar can be identified on the isophote maps. Its major axis is at position angle 76° on the V map, and 74° on the R and I maps, with an uncertainty of about $\pm 2^\circ$. In comparison, Pence (1978) estimates the position angle of the bar to be 80° from his blue photograph and rectified image, while Uyama, Matsumoto and Thomas place the position angle at 71° using an infrared plate. Based on $2.2\ \mu\text{m}$ data, Scoville et al. (1985) place the bar at position angle 68° . This decrease in position angle with increasing wavelength is probably related to better visibility of the bar at the longer wavelengths.

The apparent size of the bar is difficult to estimate from the isophote maps. Measurements indicate the approximate dimensions are $2'.9 \times 1'.0$ in V, $3'.0 \times 1'.1$ in R, and in I, $3'.0 \times 1'.2$. These correspond to face-on sizes of 5.6 kpc \times 3.8 kpc, 5.4 kpc \times 4.2 kpc, and 5.4 kpc \times 4.6 kpc, respectively. Pence found the size to be 5.8 kpc \times 3.8 kpc in blue light and Uyama, Matsumoto and Thomas found 6.5 kpc \times 3.9 kpc with their infrared plate, both measurements being corrected to 2.85 Mpc distance and face-on projection. The $2.2\ \mu\text{m}$ data of Scoville et al. give a face-on size of about 5.9 kpc in length when scaled to 2.85 Mpc, and a measurement on their Figure 6 yields a face-on width of about 4.4 kpc as a lower

limit. Considering the effects of dust, the infrared measurements are probably closer to the real size of the bar than are the other colors. The mean of the three infrared measurements yields $5.9 \text{ kpc} \times 4.3 \text{ kpc} \pm 0.4 \text{ kpc}$.

Figures 34, 35 and 36 show the V, R and I isophote maps from the long exposure plates. The contour interval is $\mu = 0.50$. Again, the scale is shown by the bar on each Figure and the small circle shows the FWHM of the beam used to smooth the data. The position angle is taken to be $51^\circ.0$ after Pence. This value fits the isophote maps well, cutting the outer contours at approximately right angles in all colors. The minor axis, deduced from this assumed position angle, also cuts the outer contours at right angles. The estimated error in this value for the data presented here is about $\pm 0^\circ.4$, which results from an uncertainty of ± 1 pixel in the positions of the best fitting lines at the edges of the maps.

Most of the details such as dust lanes and the bar are indistinct on the deep maps. However, the large size of NGC 253 begins to become apparent and the outermost isophotes indicate an increase in axial ratio, b/a , which will be discussed later.

An interesting large feature shows in the south beginning at $\mu_V = 24.65$, $\mu_R = 24.06$ and $\mu_I = 23.66$, and extending toward the southeast, although the R map does not go to a faint enough level to show anything but the brightest area. The beginning of this large extension can be seen in Pence's

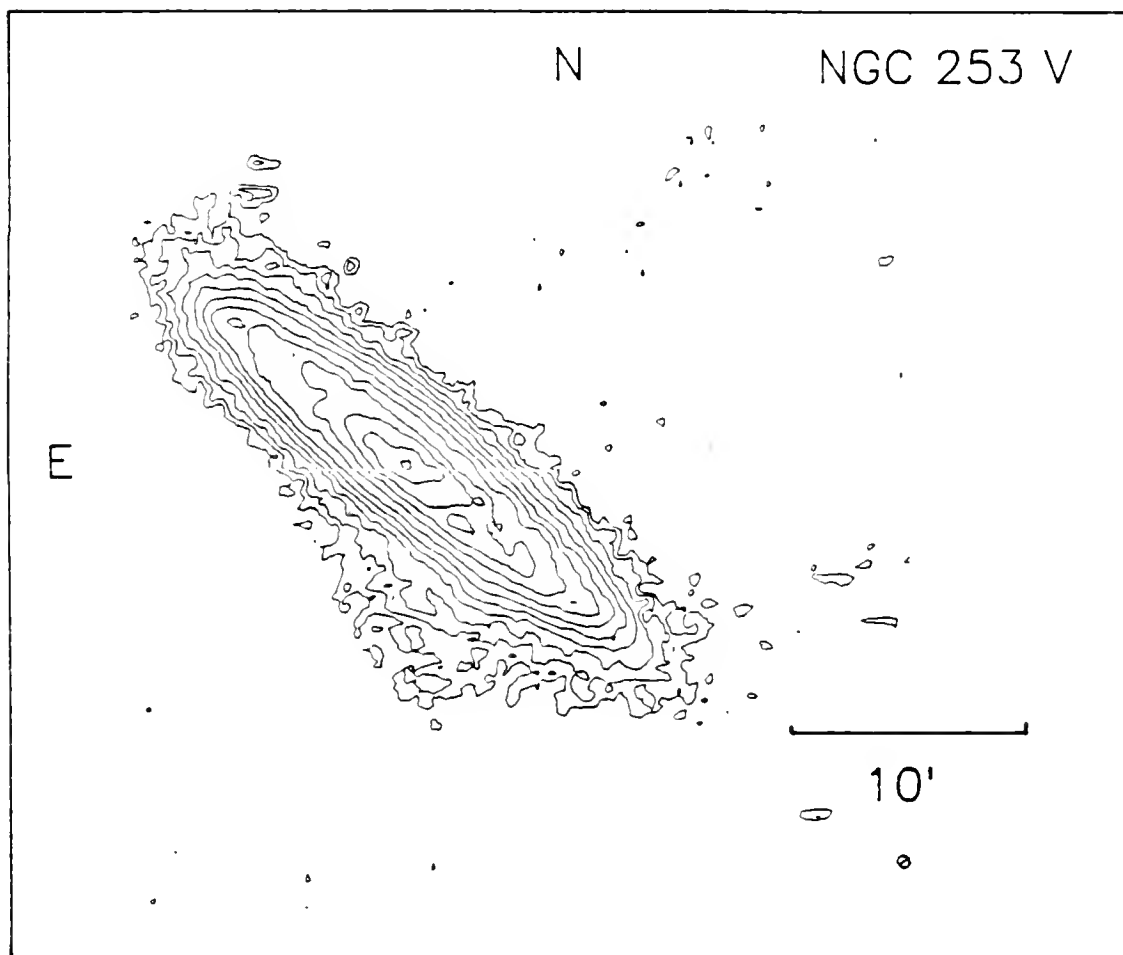


Figure 34. Visual isophote map made from added long exposure plates. The contour interval is 0.5 magnitude. The innermost isophote is at $\mu_v = 20.15$ and the outermost at 25.65. North is up and east is to the left. The bar shows the scale and the FWHM of the smoothing beam is shown by the circle.

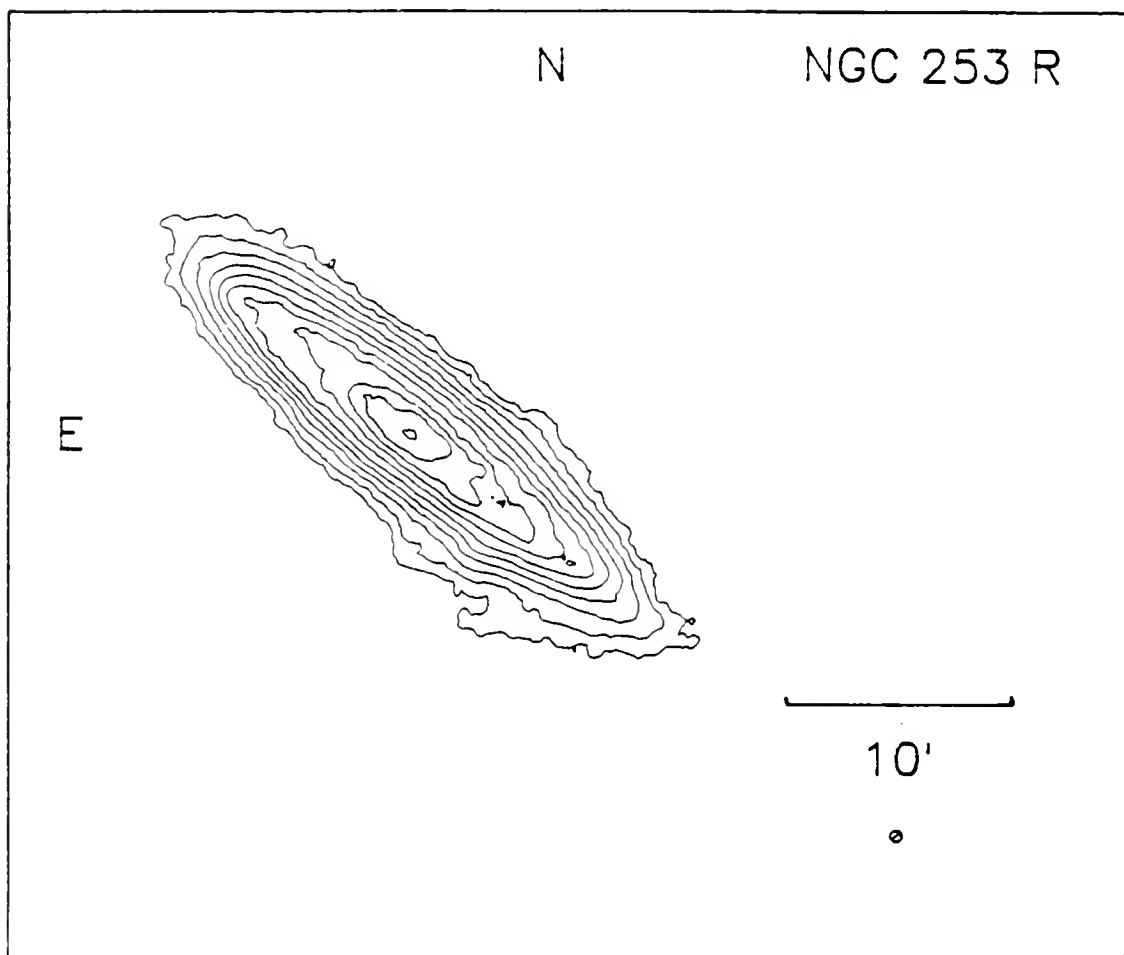


Figure 35. Red isophote map made from long exposure plate 5394. The contour interval is 0.5 magnitude. The innermost isophote is at $\mu_R = 19.06$ and the outermost at 24.06. North is up and east is to the left. The bar shows the scale and the FWHM of the smoothing beam is shown by the circle.

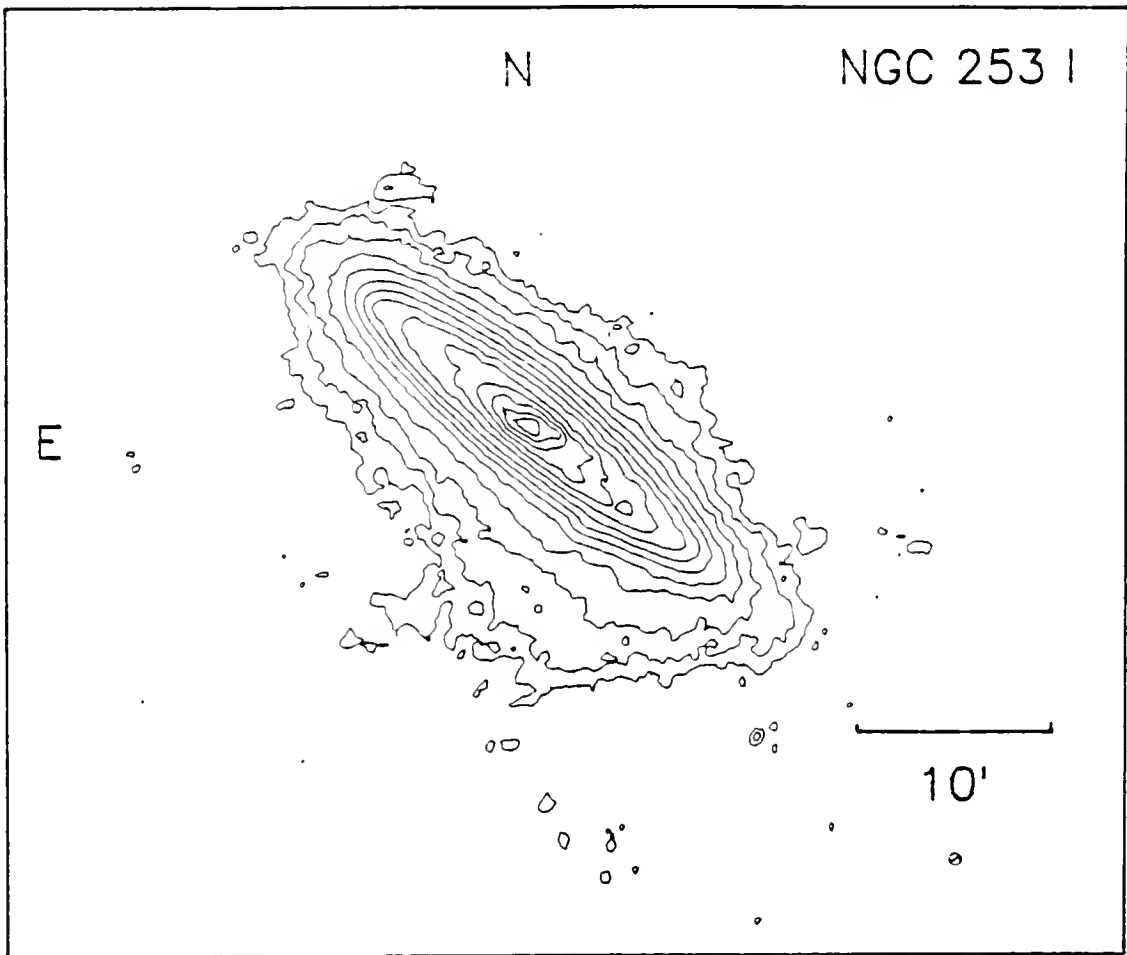


Figure 36. Infrared isophote map made from added long exposure plates. The contour interval is 0.5 magnitude. The innermost isophote is at $\mu_r = 18.10$ and the outermost at 24.60. North is up and east is to the left. The bar shows the scale and the FWHM of the smoothing beam is shown by the circle.

isophote map at about $\mu_b = 26$, but his map does not go faint enough to allow it to be followed to large distances as on the V and I maps. Careful examination of the brighter contours on the V, R and I maps shows a slight bulge in nearly the same direction and that may well be related, starting as bright as $\mu_v = 23.65$, $\mu_R = 21.56$ and $\mu_I \leq 21.66$. Beck, Hutschenreiter and Wielebinski (1982) noted this feature in their photographic photometry and its appearance in blue light is quite similar to the V and I maps presented here. They remarked that the extension is more easily seen at longer wavelengths, which is confirmed here. In an earlier paper, Beck et al. (1979), observing at 3.4 cm, noted a "spur" at nearly the same position. Although it encompasses the area in which two G5 stars are found (SAO 166575 $m_v = 8.9$, and SAO 166579 $m_v = 8.5$), the care taken to remove the images of the stars renders it unlikely that the feature is residual scattered light. The V-I color is $\approx 1.0 - 1.3$ between 7' and 10' south of the nucleus, but the errors are large in these outer isophotes. The nature of this feature is unknown. It may be a remnant of a previous interaction with another member of the Sculptor group and consist of material too old to contain many blue stars and unable to form new ones, but this is uncertain. A similar but smaller feature is seen in the north-northwest at position angle $\approx 28^\circ$ which is also present in the blue image of Beck et al.

The inclination calculated by Pence is $78^\circ.5$ from equation (13) with $q_0 = 0.154$, the mean value of b/a for the five flattest Sc galaxies in the RC2. Since q_0 is determined from B passband photometry at the $\mu_b = 25$ isophote, the value of q must be calculated at the same level. In the present case this is approximately equal to $\mu_v = 24.3$, $\mu_r = 23.4$ and $\mu_i = 22.8$ based on the color indices discussed later. Using the values of q at these levels, equation (13) yields inclinations of $77^\circ.3$, $77^\circ.7$ and $75^\circ.2$, respectively. Because NGC 253 shows a thickening of the disk with increasing wavelength, discussed in the next section, and because q_0 is not known for any color except blue, the inclinations computed using the V, R and I data will not be used, but Pence's value mentioned above will be adopted here.

Luminosity Profiles

Figures 37, 38 and 39 show slices along the major and minor axes in each color. The bright, inner regions are from the short exposure images, and the more heavily smoothed and added long exposure images are used for the fainter magnitudes. Representative internal errors are shown by the bars at the side of each figure, and are the standard deviations of two or four sets of pixels from near the corners of the images used to form the profiles.

Major Axis

The major axis profiles are characterized by a small, bright nuclear region, a nuclear bulge/bar, a bright inner

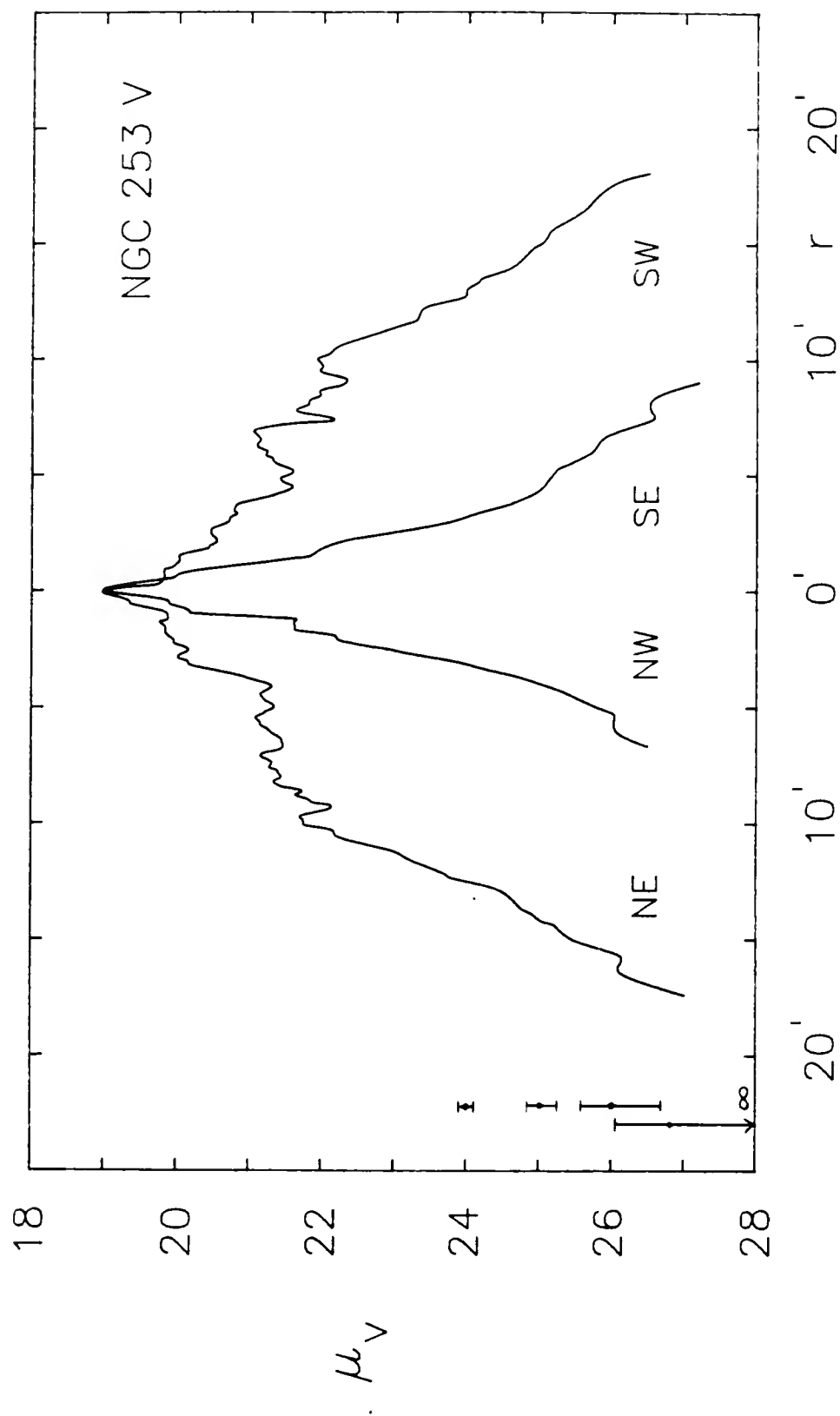


Figure 37. Visual major and minor axis profiles of NGC 253. For $\mu_V \leq 22$ the data are from the short exposure plate.

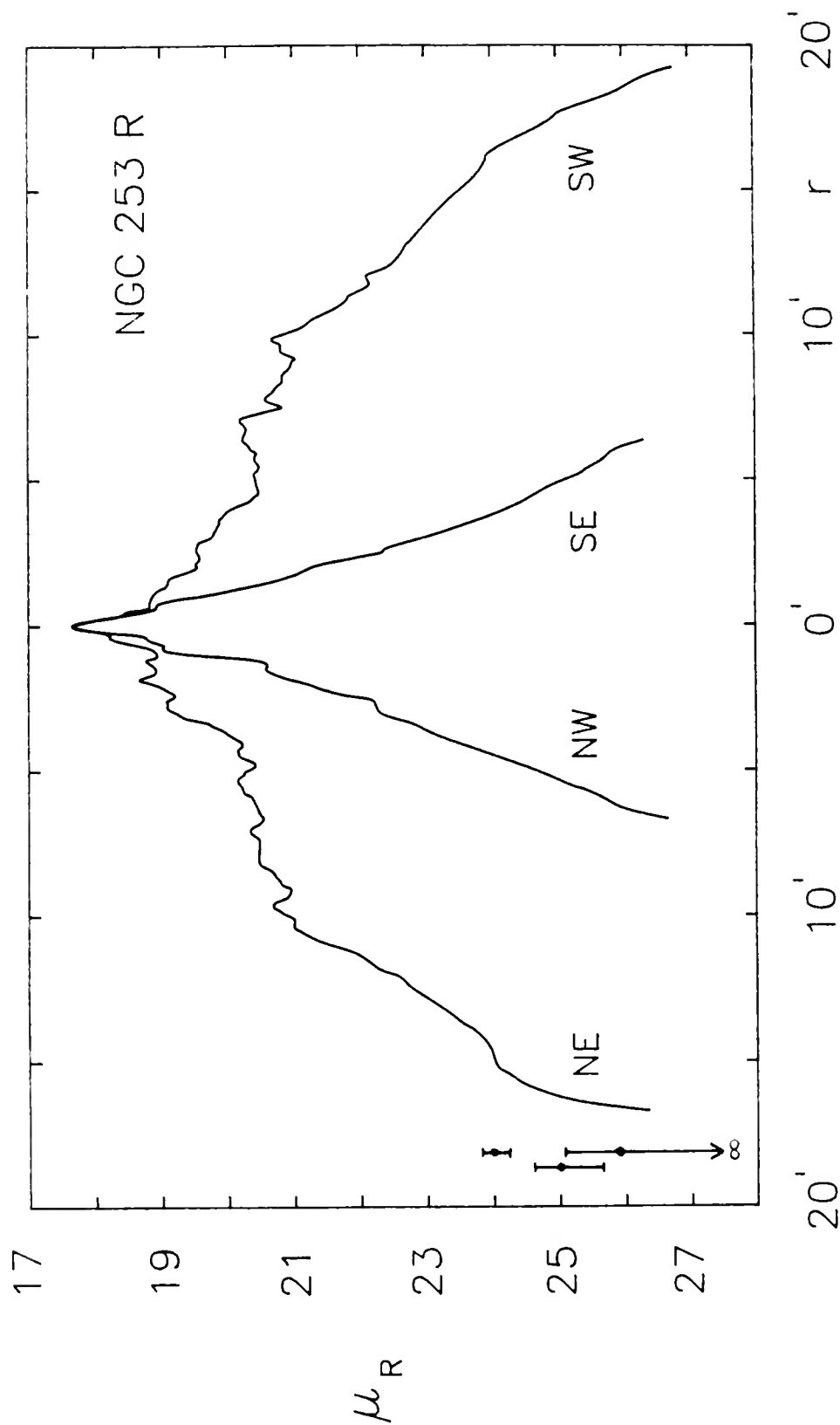


Figure 38. Red major and minor axis profiles of NGC 253. For $\mu_R \leq 22$ the data are from the short exposure plate.

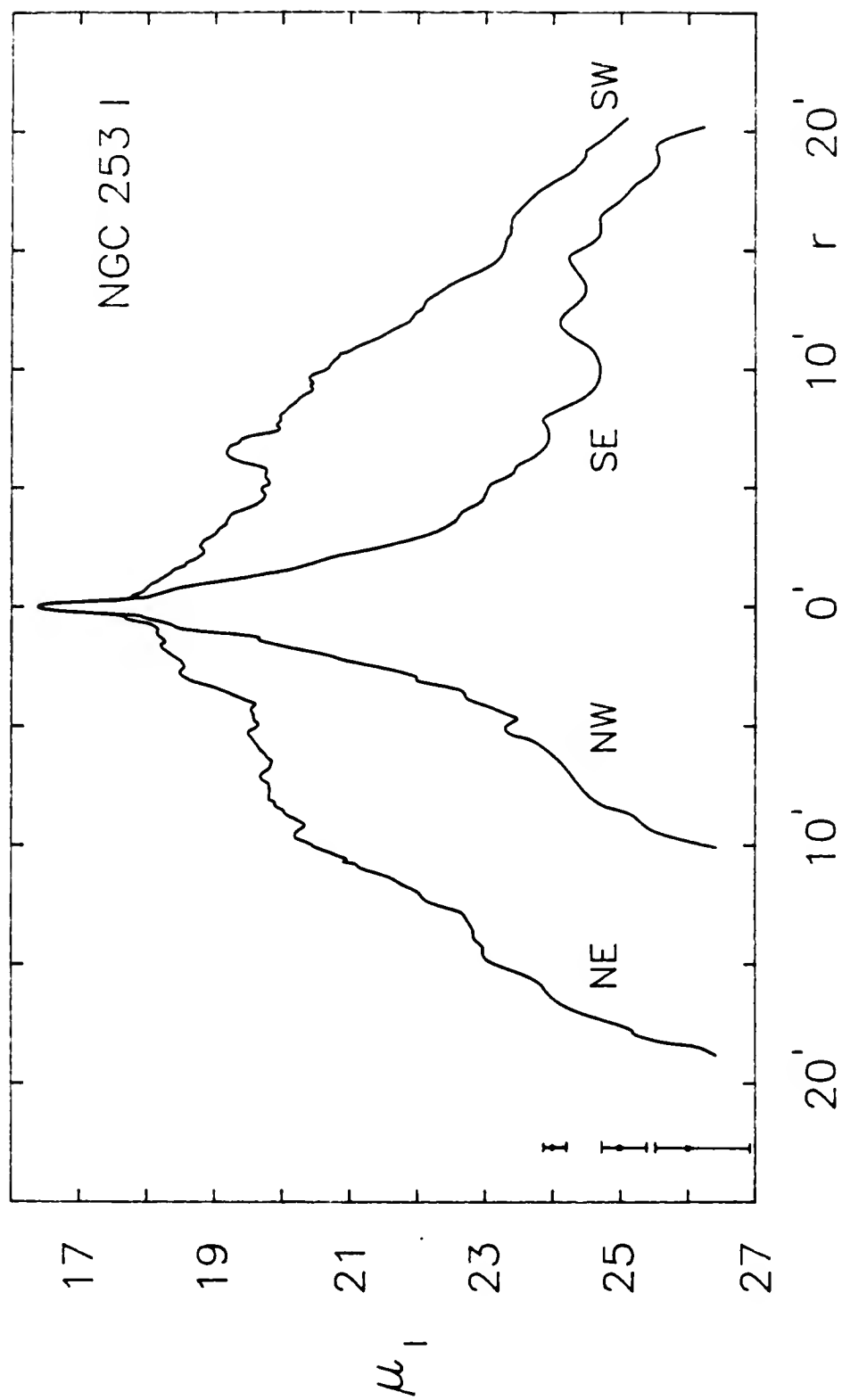


Figure 39. Infrared major and minor axis profiles of NGC 253. For $\mu_I \leq 21$ the data are from the short exposure plate.

disk, a plateau, and a rapidly fading exponential disk. A comparison of the profiles shows the nuclear region to be quite red. Little detail can be seen in this region because of the low resolution of the images. Extending about $1'$ either side of the nucleus is the bar which is seen to have an asymmetrical appearance in the V and R profiles due to the dust to the west of the nucleus. Beyond the bar, especially on the northeast side, is the bright inner disk, distinguished by its slowly decreasing brightness. It terminates rather abruptly at $r \approx 3'$ (2.5 kpc) and even closer to the nucleus on the southwest side. An examination of the photograph shows an end to the bright inner disk and the presence of large dust lanes at these locations. The two sides appear more symmetrical with increasing wavelength and Scoville et al. (1985) find the inner disk to be bright and quite symmetrical at $1.27 \mu\text{m}$ and $2.2 \mu\text{m}$. Between approximately $5'$ and $11'$ on either side of the nucleus, a kind of plateau is seen in the profiles where the surface brightness drops by only about 1 magnitude. Bright spiral arms are seen in the disk in this region, mixed with dust. The edge of this plateau coincides with the "edge" of the galaxy as seen on the photograph. The prominent "bump" on the southeast infrared profile at $r \approx 6'.5$ is a "star cloud" in the disk that must be heavily reddened. Outside of the plateau the surface brightness shows a sharp exponential decline. The southwest profiles are terminated at $r \approx 20'$ because of the presence of a bright star at $r \approx 23'$ in that

direction. The steep downturn in the northeast red profile beyond $r \approx 15'$, which is not seen in the V and I, is probably not real.

Minor Axis

The minor axis profiles all show a non-exponential decline. Absorbing dust causes the formation of "steps" on the bright portions of the profiles but these become less noticeable with increasing wavelength. The dust lanes are more obvious on the northwest profiles, as expected from the photographic appearance of this galaxy. As will be discussed later, these profiles can be fit with a de Vaucouleurs $r^{0.25}$ brightness model. For $r \geq 7'$ the V and I southeast profiles have reached the large spur discussed earlier, and its effect on the I profile is especially noteworthy. The last position corresponds to a length of 16.6 kpc, and if this feature lies in the plane of NGC 253, the galaxy can be traced out to about 5 times as far in this direction.

Size of NGC 253

The size of NGC 253 is determined using the maximum extent of the luminosity profiles. For each color the profiles are extrapolated to reach the faintest level attained by any one part of the profile, or to the noise limit, whichever was reached first. In the case of the infrared southeast minor axis, this is done first ignoring the extension beyond $r \approx 10'$ and then including it. The dimensions are given in Table 22 where column (1) lists the passband, column (2) lists

the surface brightness at the measured position, and columns (3) and (4) give the major and minor axis sizes in arc minutes and kiloparsecs. A colon is used to mark uncertain values.

TABLE 22
SIZE OF NGC 253

Color	μ	2a	2b
B	27.2	39'	13'.5
		32.3 kpc	11.2 kpc
V	26.9	36'.3	16'.4
		30.1 kpc	13.6 kpc
R	25.9	35'.0	12'.3:
		29.0 kpc	10.2: kpc
I	26.4	42'.8	24'.2:
		35.5 kpc	20.1: kpc
"	"	"	31'.4:
			26.0: kpc

Note: * The B data are from Pence (1978).

Measured at the 3σ level the V, R and I major axes are: 31'.8 (26.4 kpc), 33'.1 (27.4 kpc), and 39'.4 (32.7 kpc). The corresponding minor axes are: 10'.6 (8.8 kpc), 9'.61 (8.0 kpc), and 27'.4 (22.7 kpc) and 20'.9 (17.3 kpc), the last value not including the southeast spur. Pence (1978) found the total extent of NGC 253 at $\mu_b = 29$ to be 60' x 26' (49.7 kpc x 21.6 kpc at 2.85 Mpc), but these measurements are not very reliable.

Mean Axis Profiles

Mean luminosity profiles are formed by combining the data on either side of the nucleus. These profiles give a better sense of the major features that make up the luminosity

distribution because small random features are averaged out and symmetric features are preserved. Factors such as noise, plate blemishes and foreground stars have necessitated the use of only one side of a profile to form the outermost points of most of the mean profiles. Where this occurs the data are indicated by dots.

The semi-major axis profiles, Figures 40, 41 and 42, show the nuclear region and bar ($a < 1'$), the bright inner disk ($1' < a < 4'$), the plateau ($4' < a < 10'$) and the exponential disk ($a > 10'$). The bar is not obvious in these profiles, probably because the dust on the southwest side "cancels" the brightness on the northeast side. Dust is also responsible for the absorption at $a = 4'$ and $a = 9'$. At the edge of the plateau, around $a = 10'$, are the outer spiral arms. The prominence of this "edge" diminishes with increasing wavelength, and is quite noticeable in Pence's blue photometry.

The semi-minor axis profiles, Figures 43, 44 and 45, show the nuclear region ($a < 0'.5$), the bar ($a < 1'$), and the spiral arms ($a \approx 2'$). Dust is responsible for the absorption at $a = 0'.5$ and $1'.5$. Especially noticeable in these profiles is the non-exponential decline in the luminosity, particularly in the V and I profiles for $b \geq 3'$. The behavior of the R profile at $\mu_R \geq 24$ does not agree well with the V and I profiles. This is most likely a result of the poorer quality of the red photometric data for NGC 253. Spinrad et al. (1978), using red data along the minor axis calculate a

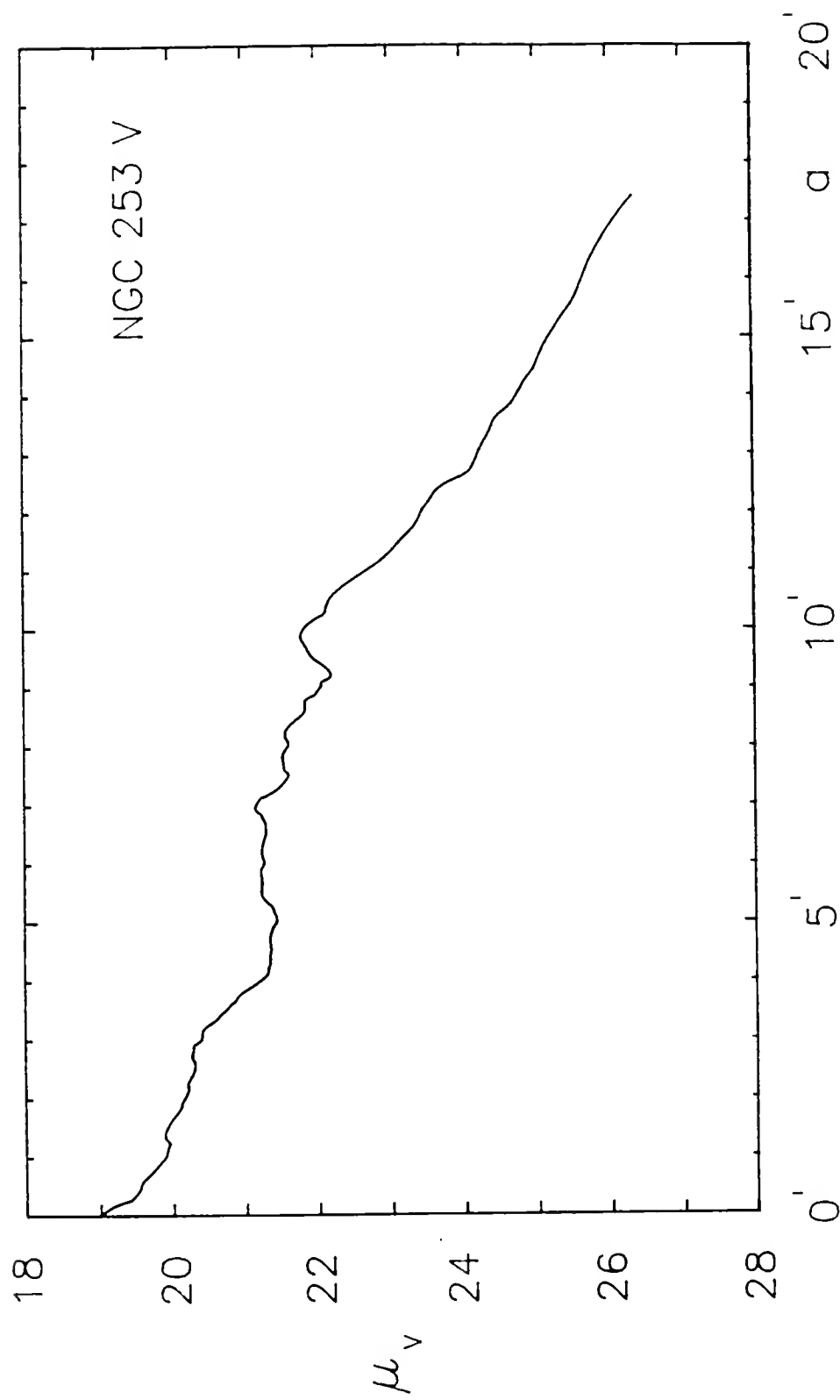


Figure 40. Mean V semi-major axis profile for NGC 253.

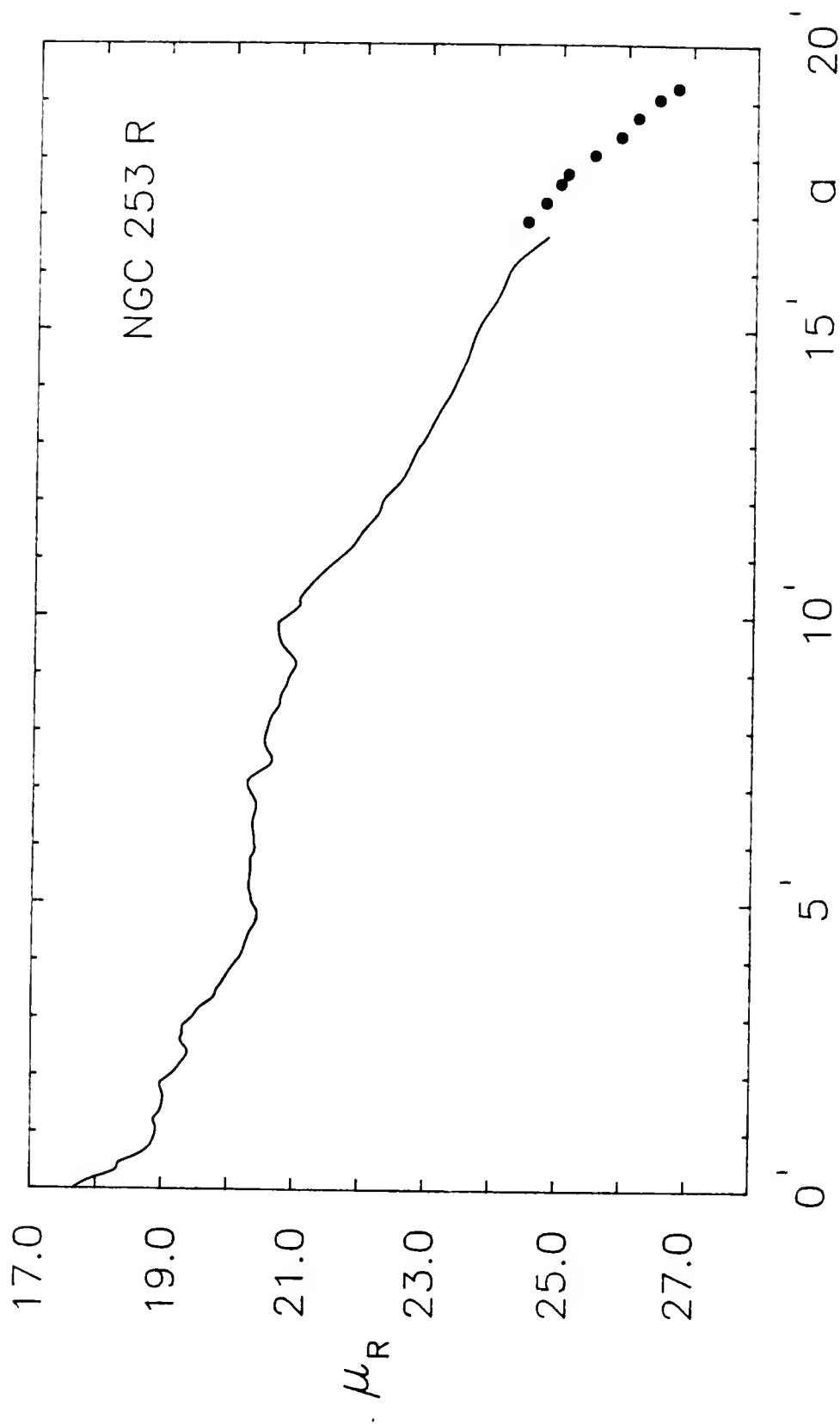


Figure 41. Mean R semi-major axis profile for NGC 253. The dots indicate data from only the southwest axis.

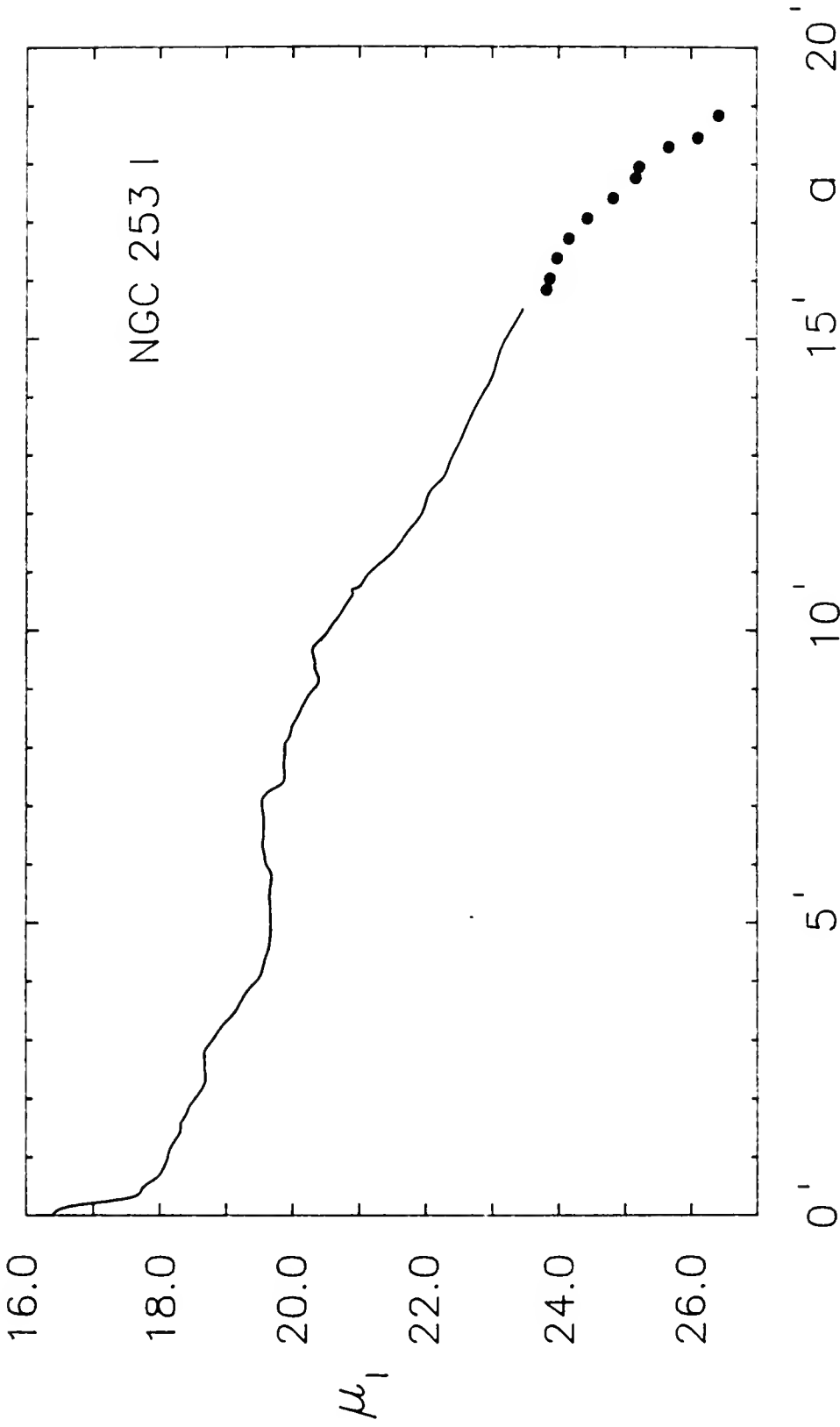


Figure 42. Mean I semi-major axis profile for NGC 253. The dots indicate data from only the northeast axis.

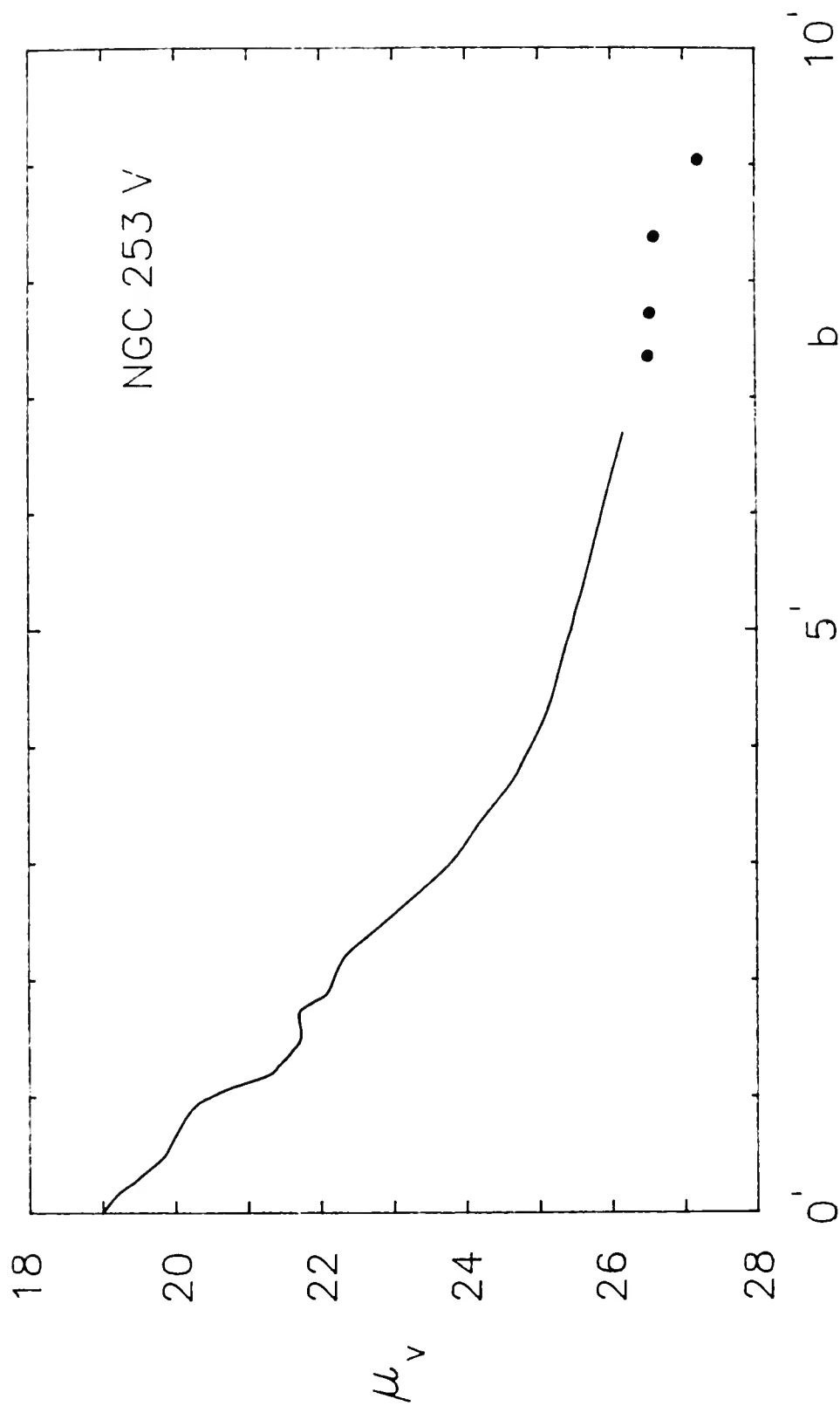


Figure 43. Mean V semi-minor axis profile for NGC 253. The dots indicate data from only the southeast axis.

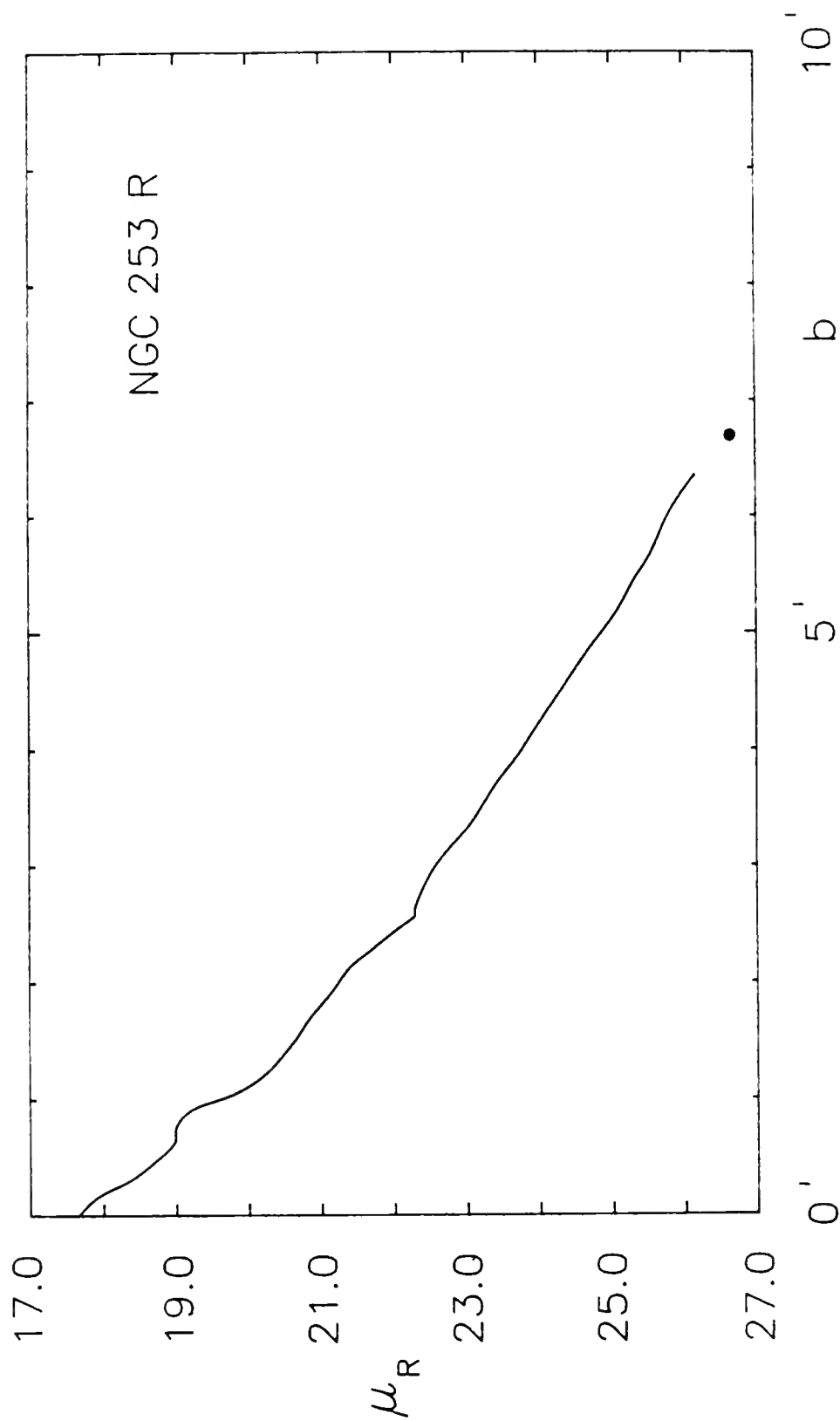


Figure 44. Mean R semi-minor axis profile for NGC 253. The dot indicates a value from only the northwest axis.

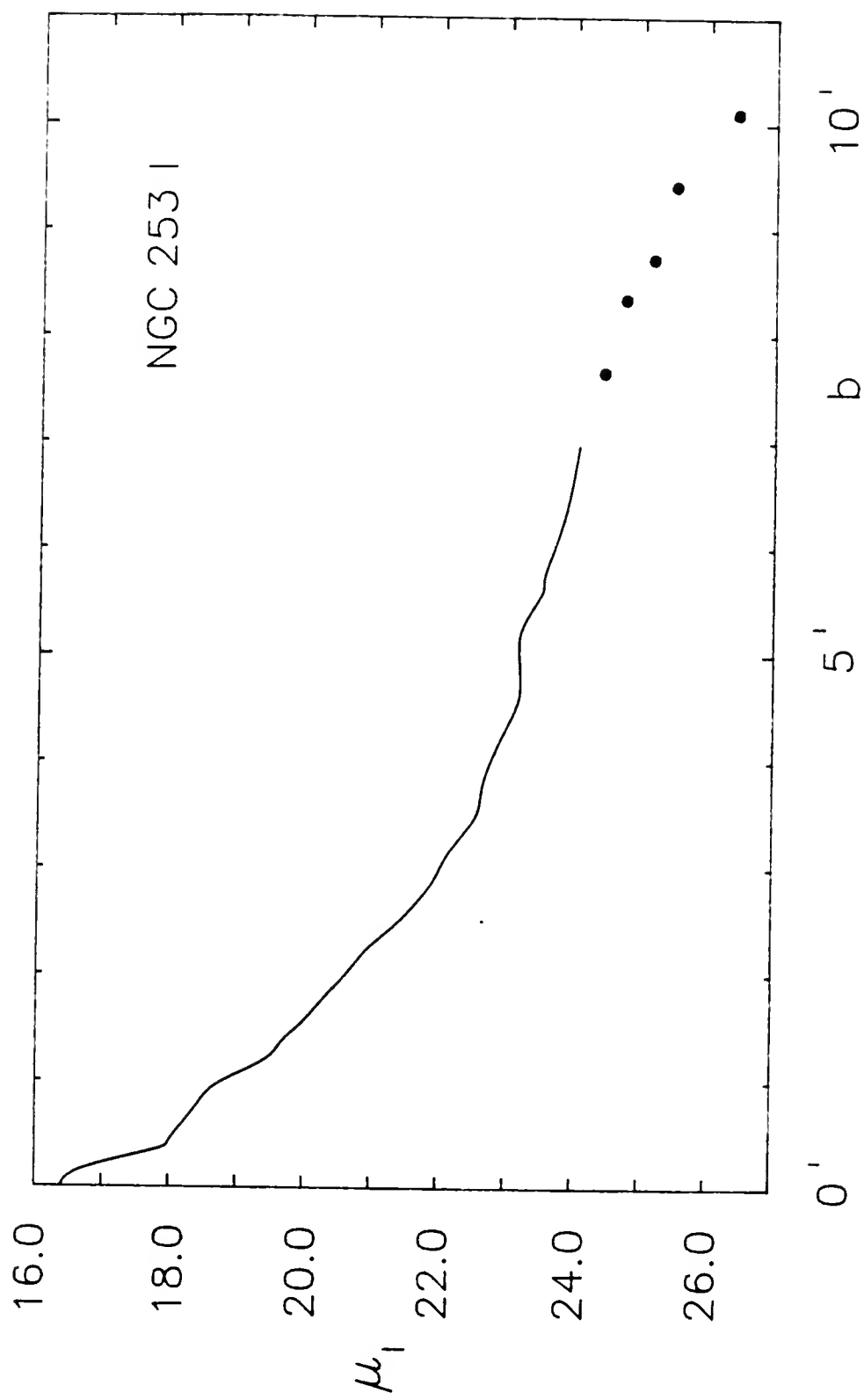


Figure 45. Mean I semi-minor axis profile for NGC 253. The dots indicate data from only the northwest axis.

surface brightness declining as $I \sim r^{-2.94}$ for $5' \leq r \leq 25'$. Although the R data in this work are not reliable in this range, the V and I mean minor axes indicate the surface brightness declines as $I \sim r^{-2.46}$ and $r^{-3.53}$ for $5' < r < 10'$, in agreement with their rapid decline for the halo.

Ellipticity

The ellipticity, defined as the ratio of the semi-minor axis to the semi-major axis, b/a , is shown for each color in Figures 46, 47 and 48. The points represent measurements made at 0.2 magnitude intervals using the mean axis profiles. A sixth-order polynomial was fit to the data and is shown by the solid curve.

Both the R and I values show the nuclear region to be elongated along the minor axis. For $b/a > 0.3$ and $a \leq 3'$ the decline in ellipticity is larger in V than in I. All three curves show a minimum value of $b/a \approx 0.18$ at $a \approx 10'$, where the spiral arms appear to end and the exponential decline in brightness begins. At large radii, the ellipticity increases, especially on the deeper V and I profiles, showing the effect of the rapidly growing minor axis. Note that this increase in ellipticity does not include the effect of the large south spur and therefore shows an actual halo or spheroidal component. The R data do not show as much of an expected rise in ellipticity, due to the steeply declining mean minor axis at faint light levels.

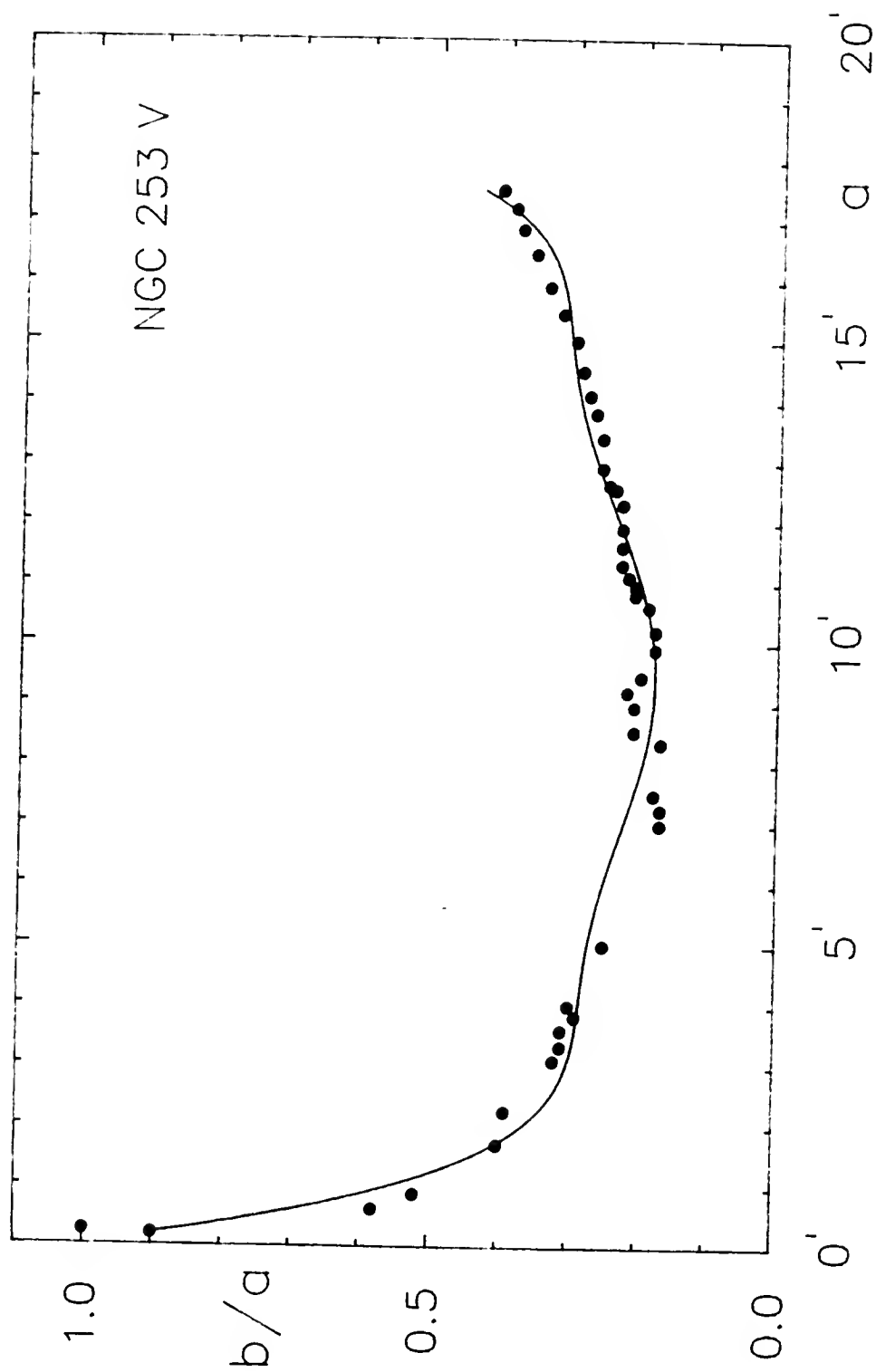


Figure 46. Ellipticity curve for the NGC 253 V data.

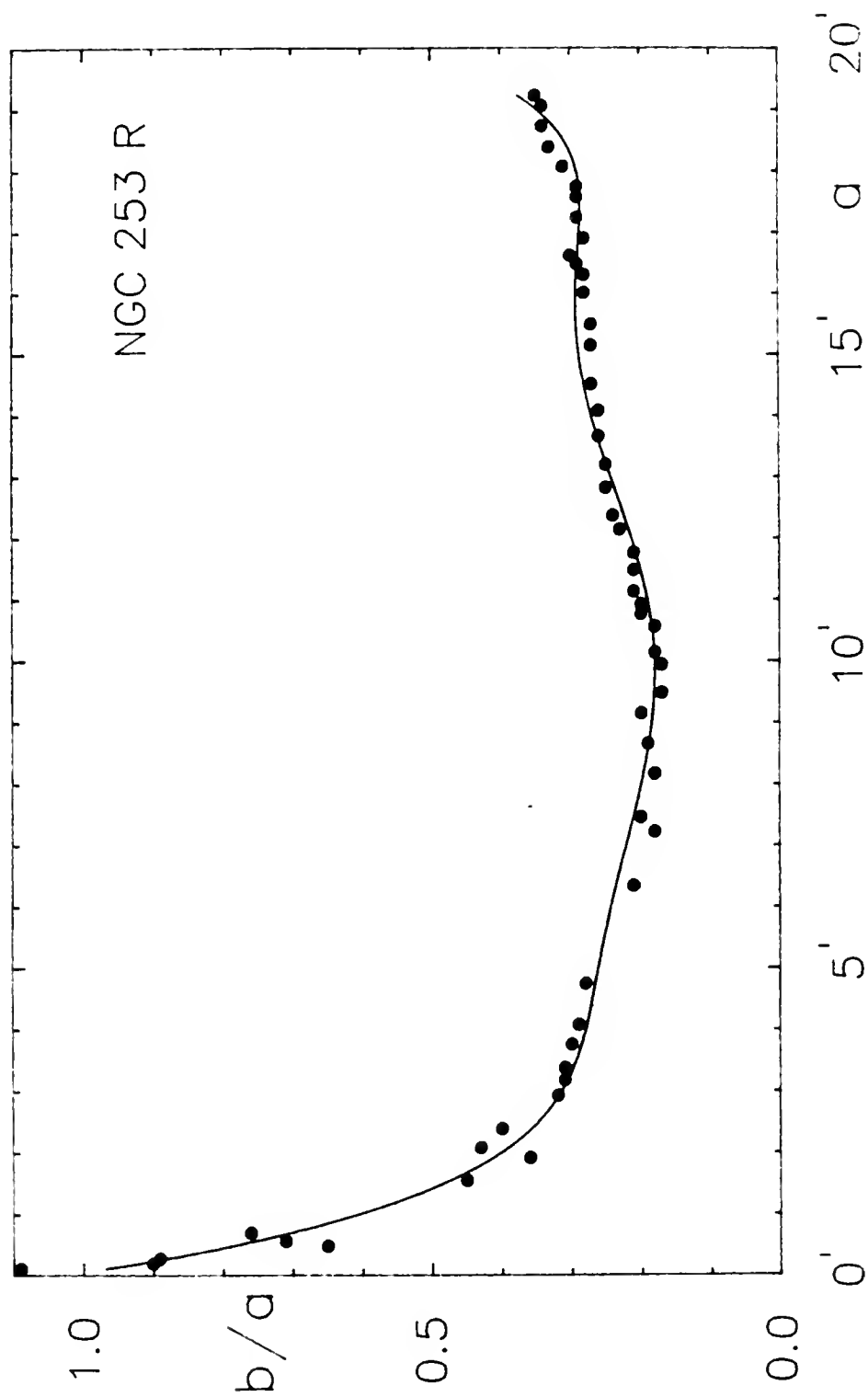


Figure 47. Ellipticity curve for the NGC 253 R data.

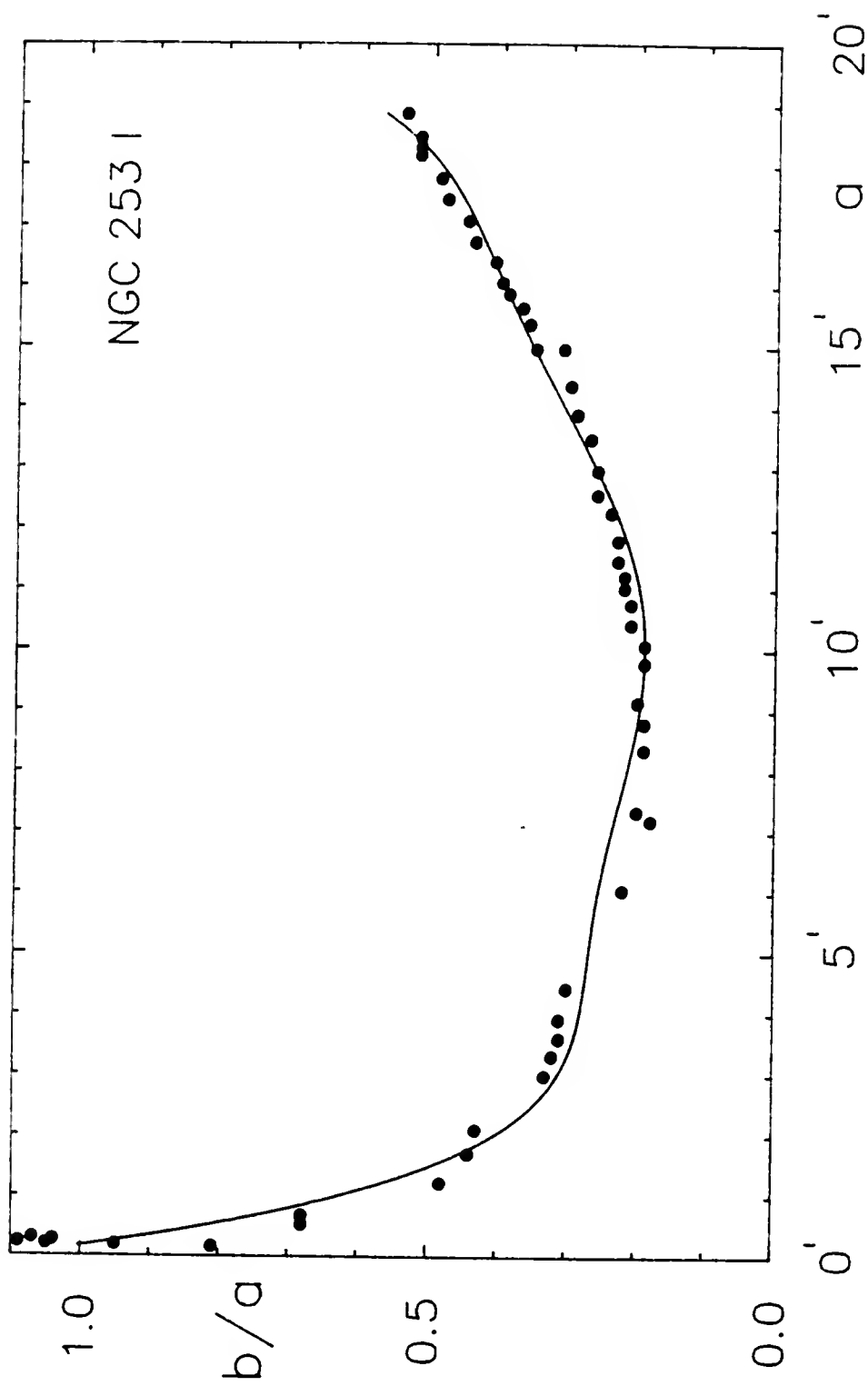


Figure 48. Ellipticity curve for the NGC 253 I data.

Between $23.7 < \mu_b < 26.2$ ($11'.7 < a < 18'.8$) Pence finds the ellipticity increases from 0.22 to 0.275. Spinrad et al. report a similar trend for their r data: for $25.5 \leq \mu_r \leq 27.0$ ($13' \leq a \leq 21'$) the ellipticity increases from 0.23 to 0.53. Over the same range as covered by Pence, the ellipticity in V, R and I also shows a similar trend: 0.22 to 0.42, 0.20 to 0.32, and 0.21 to 0.56, respectively. There is strong evidence of a thickening of the disk with decreasing brightness level, and, neglecting the poorer quality R values, with increasing wavelength. This can also be noticed in the luminosity profiles.

Color Profiles

Three color indices are formed for each axis: V-R, R-I and V-I. Photometric errors render the indices unreliable beyond about $a = 15'$ and $b = 4'$ for the V and I, and even less for the R data.

Major Axis

The major axis color profiles are shown in Figures 49, 50 and 51. They can be divided into three sections. First is a narrow spike with a base $1' - 2'$ wide containing the nucleus and the bar. Second is a plateau that is different from the plateau discussed above when describing the luminosity profile in that the former contains the latter but extends from the spike out to about $10'$. Third is a region corresponding to the exponential disk, extending from about $10'$ outward.

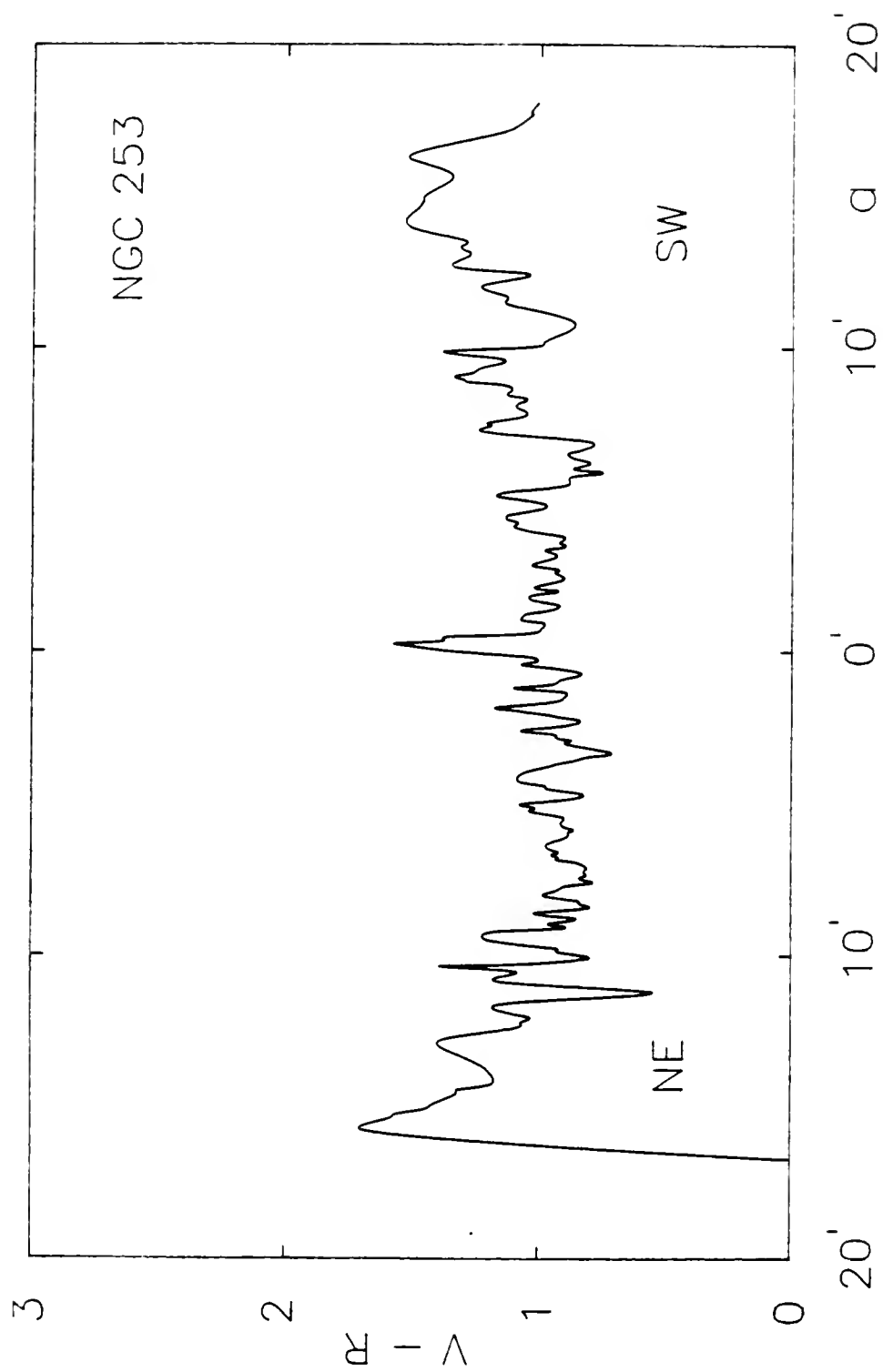


Figure 49. Major axis (V - R) color profile for NGC 253.

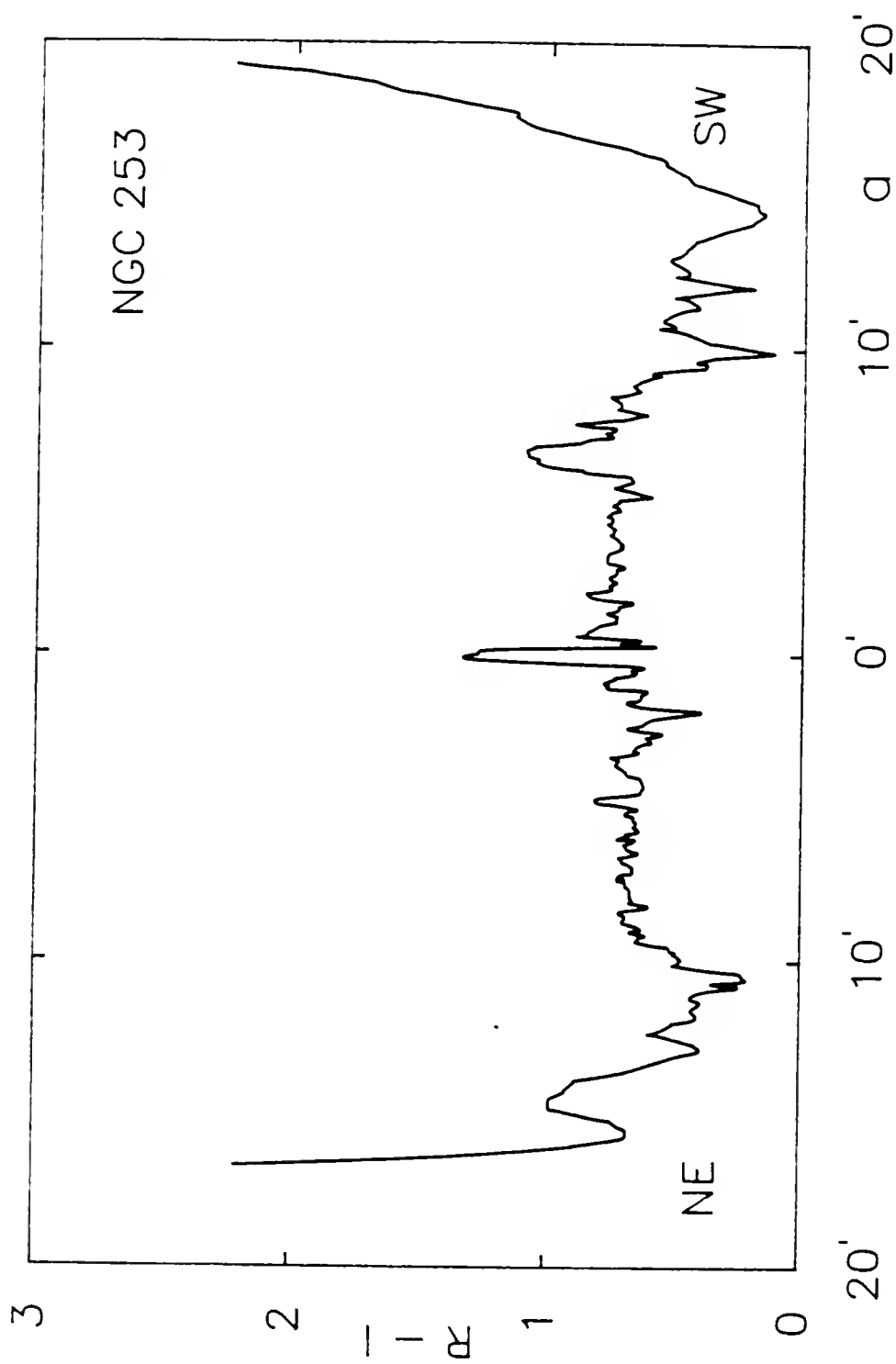


Figure 50. Major axis (R - I) color profile for NGC 253.

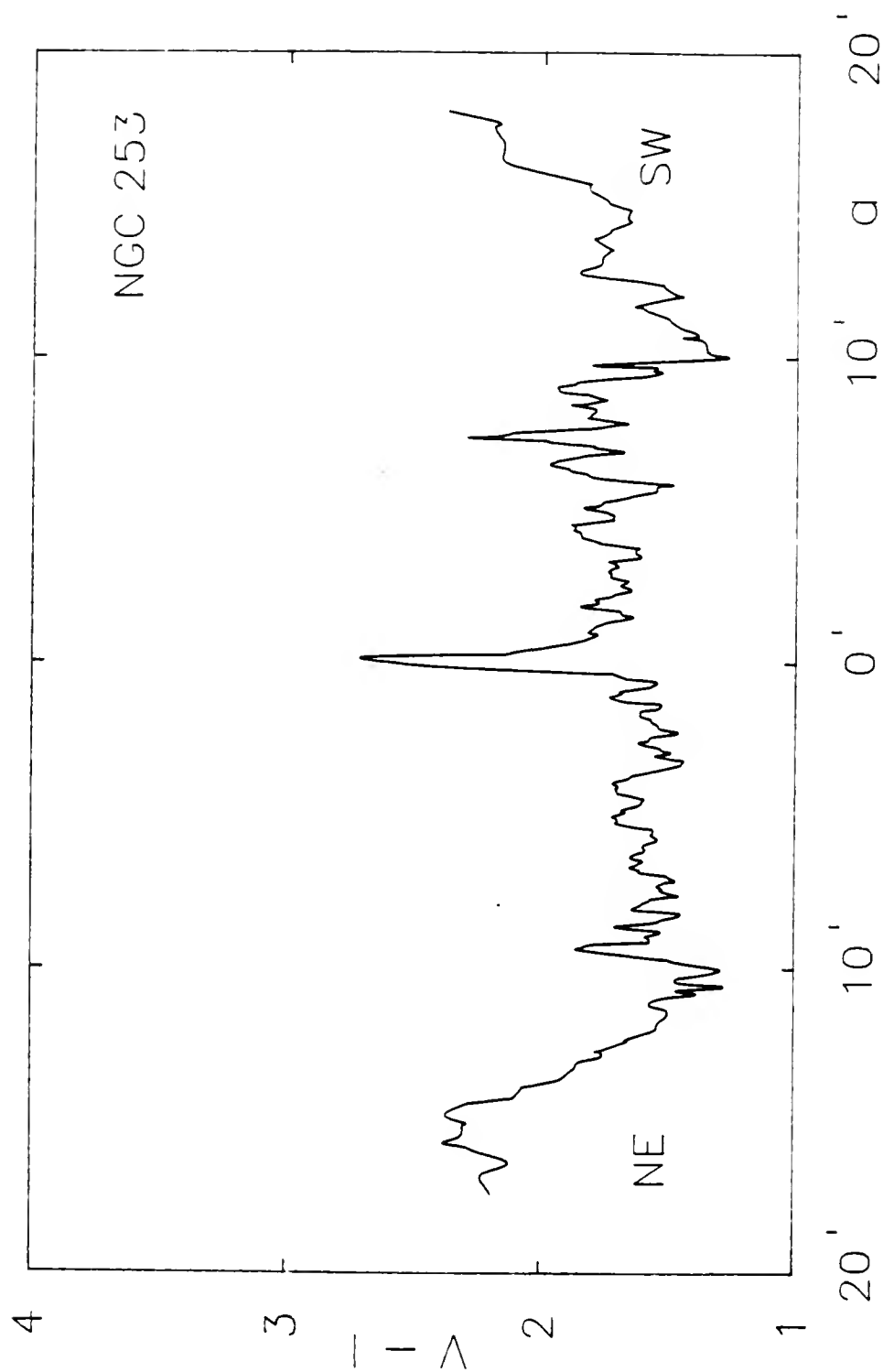


Figure 51. Major axis (V - I) color profile for NGC 253.

The nuclear region has colors $V-R = 1.34$, $R-I = 1.27$ and $V-I = 2.61$, but the area $0'.2$ southwest has the reddest colors: $V-R = 1.57$, $R-I = 1.18$ and $V-I = 2.69$. Pence has $B_J-V_J = 1.3$ near the nucleus which gives $B_J-I \approx 3.9$, and Scoville et al. give the nuclear colors as $J_J-H_J \approx 1.0$, $H_J-K_J \approx 0.78$. Using a much larger aperture than used for the above measurements, Spinrad et al. measured the nuclear region to have $r-i = 0.84$. Obscuring dust is responsible for the redness of these colors. As noted by Pence and Scoville et al., the bar shows the effect of the dust lane that cuts into it on the southwest, reddening the light there more than on the northeast side.

Nearly constant colors characterize the plateau between about $1'$ and $10'$ either side of the nucleus: $V-R \approx 0.9$, $R-I \approx 0.7$, and $V-I \approx 1.7$. However, there is a slight tendency for the color indices to increase with radial distance on the southwest side of the profile. In comparison, Scoville et al. give $J_J-H_J = 0.7$, $H_J-K_J = 0.4$ for the major axis out to $\pm 3'.3$, as far as their color measurements extend. Pence finds $B-V \approx 0.75$ for $2'.5 \leq |r| \leq 7'$, and Spinrad et al. give $r-i$ values constantly decreasing as a function of distance from the nucleus which has a value of $r-i = 0.84$. Both of these latter sets of measurements were not made along the major axis but along an east-west direction, so direct comparison with major axis measurements is not possible. Also, the $r-i$ measurements beyond $3'$ (where $r-i = 0.50 \pm 0.2$) show large errors and may

not be inconsistent with a constant value of $r-i$. The hump on the R-I profile at $6'.5$ southwest of the nucleus is caused by the bright infrared feature visible on the I luminosity profile.

Beyond $10'$ the exponential disk is encountered. All three color profiles show a change in color where the bright plateau ends, a slight tendency to become bluer followed by an almost monotonic increase in the indices. This may result from a sudden decrease in the amount of dust at distances beyond a $\approx 10'$, where the outer "edge" of a dust lane may be reached. The increase in the indices at larger distances could come from a decreasing contribution of blue sources. However, because these changes occur near where the short exposure data ends and the long exposure data is joined to it, the decrease in the indices may result from a small mismatch of the profiles. By $a = \pm 15'$ the uncertainties in the data are too large to allow any conclusions to be drawn.

Minor Axis

Figures 52, 53 and 54 show the minor axis color profiles. These are characterized by a spike near the nucleus and a small region extending out to about $\pm 2'$ that has a somewhat constant color but with large variations caused by dust lanes. The outermost regions, $b > 4'$ are unreliable and will not be discussed.

As was the case for the major axis, the nuclear region is not the reddest feature. The spike has its maximum values, V-

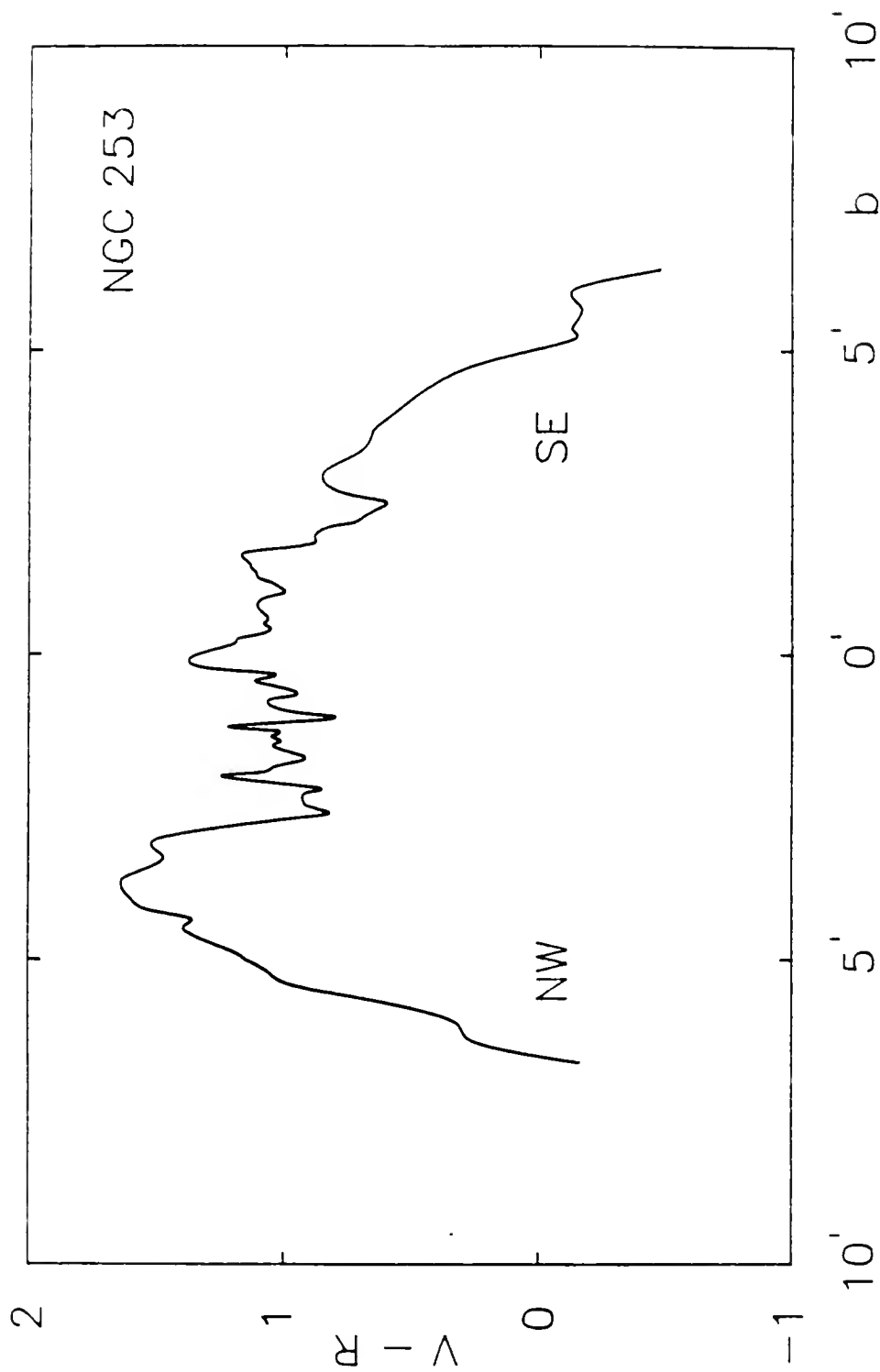


Figure 52. Minor axis (V - R) color profile for NGC 253.

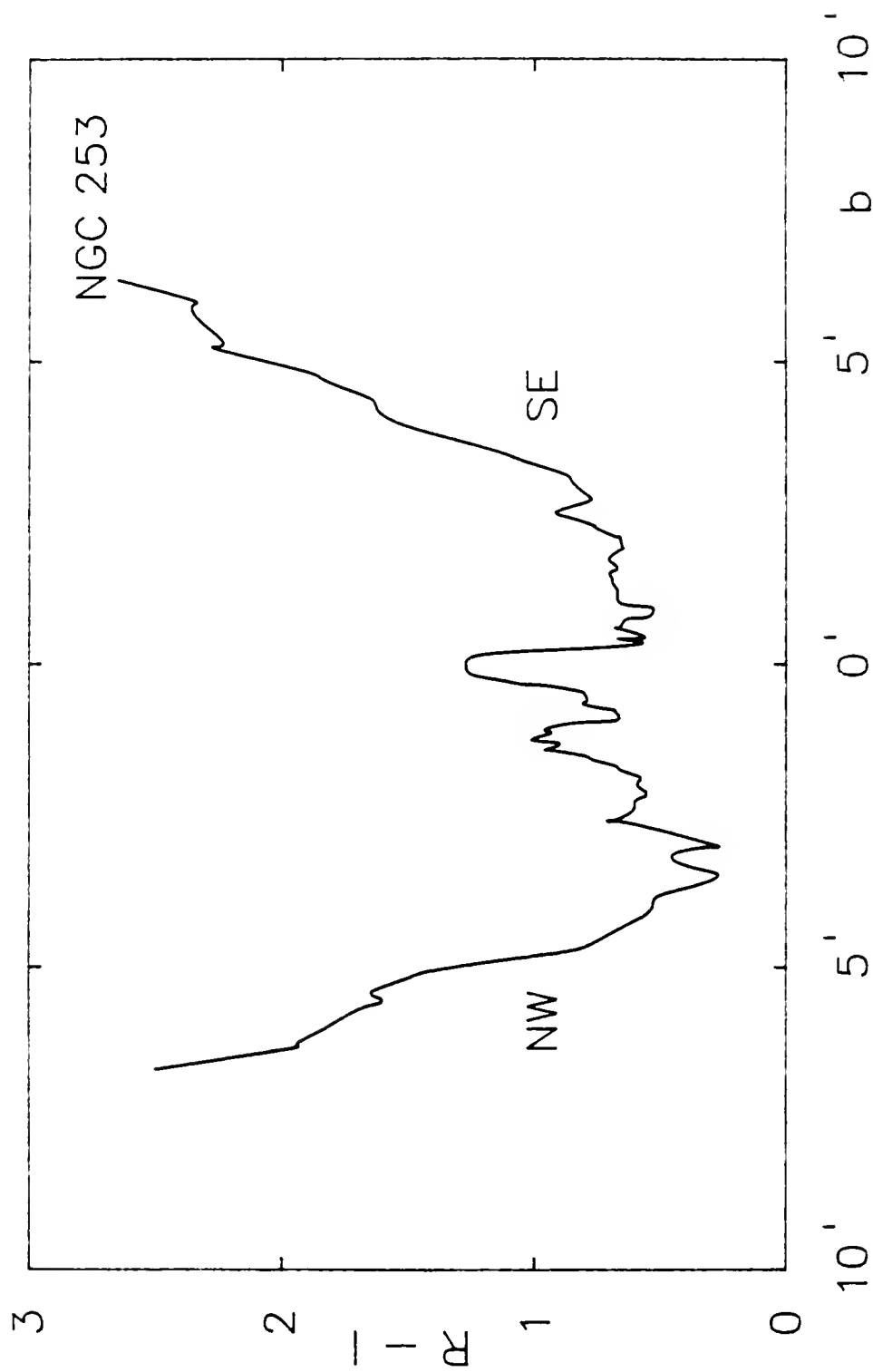


Figure 53. Minor axis (R - I) color profile for NGC 253.

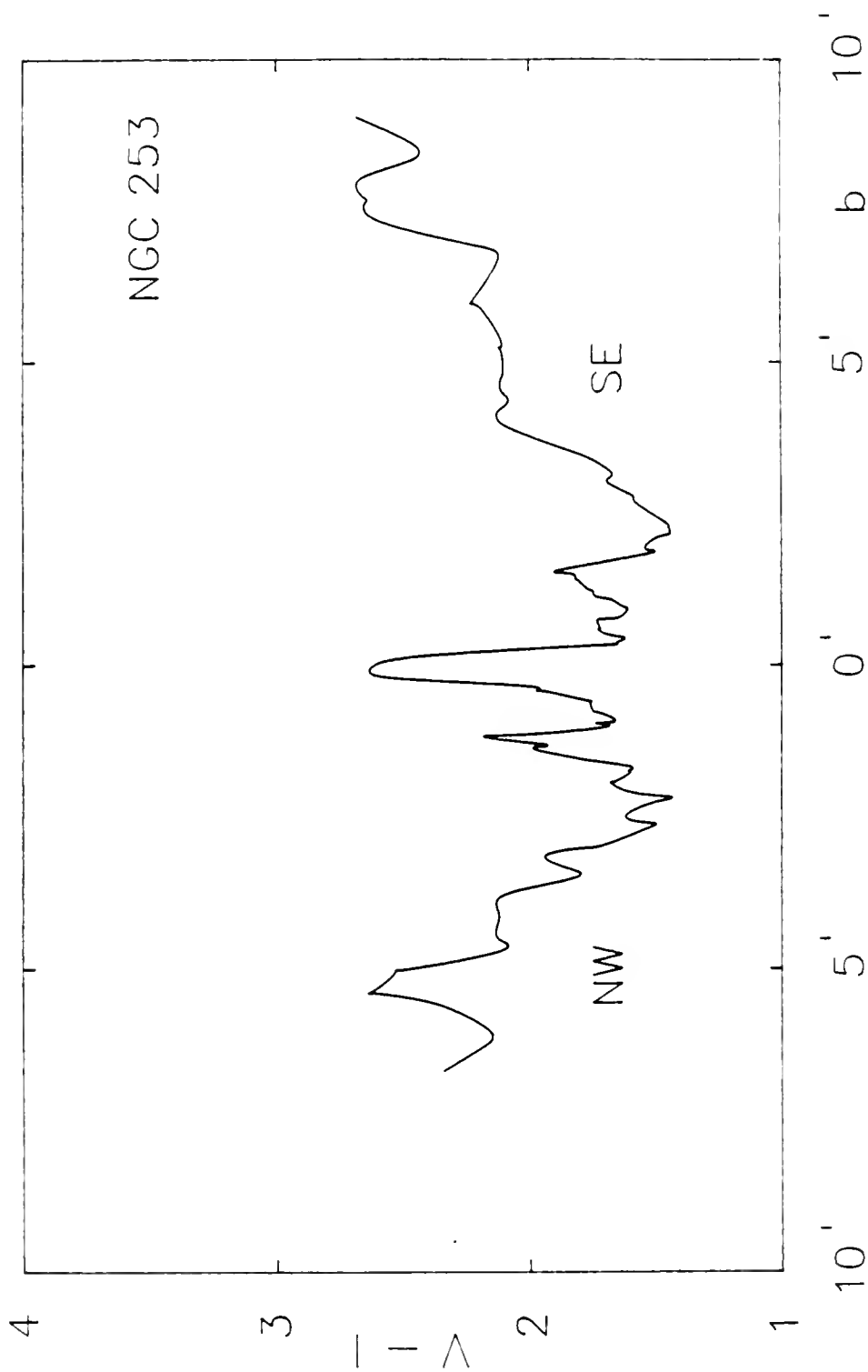


Figure 54. Minor axis (V - I) color profile for NGC 253.

$R = 1.36$, $R-I = 1.25$ and $V-I = 2.61$, about $10''$ to the northwest. Out to about $\pm 1'$ the colors become bluer as the bar is encountered. Between about $\pm 0'.5$ and $\pm 2'$ the bar and disk of NGC 253 have fairly constant colors: $V-R \approx 1.1$, $R-I \approx 0.6$ and $V-I \approx 1.6$ which compare favorably with the major axis values over the same part of the disk. Peaks of increased redness are found at about $\pm 1'.5$ where large dust lanes are visible on the photograph. Beyond about $\pm 2'$ the visible disk is left behind. Again, a slight decrease in the color is noticed after crossing the outer dust lane ($b > 2'$), similar to that noted for the major axis. The peculiar behavior of the $V-R$ and $R-I$ profiles at $b > \pm 3'$ is caused by the poorer quality of the R data at these fainter magnitudes. The $V-I$ profile shows a reddening of the light with increasing distance, just as observed for the major axis data beyond the plateau.

Integrated Parameters and Colors

The standard photometric parameters are calculated as was done for NGC 55. Again, the array of intensities in each color was numerically integrated within isophotes separated by 0.10 in $\log I$, and an equivalent radius, r' , computed for each intensity level. The resulting equivalent luminosity profiles are shown in Figures 55, 56 and 57.

Comparison of the three profiles shows all are approximately exponential over about a five magnitude range. The small rise that occurs in each profile at about $2'.5 \leq r'$

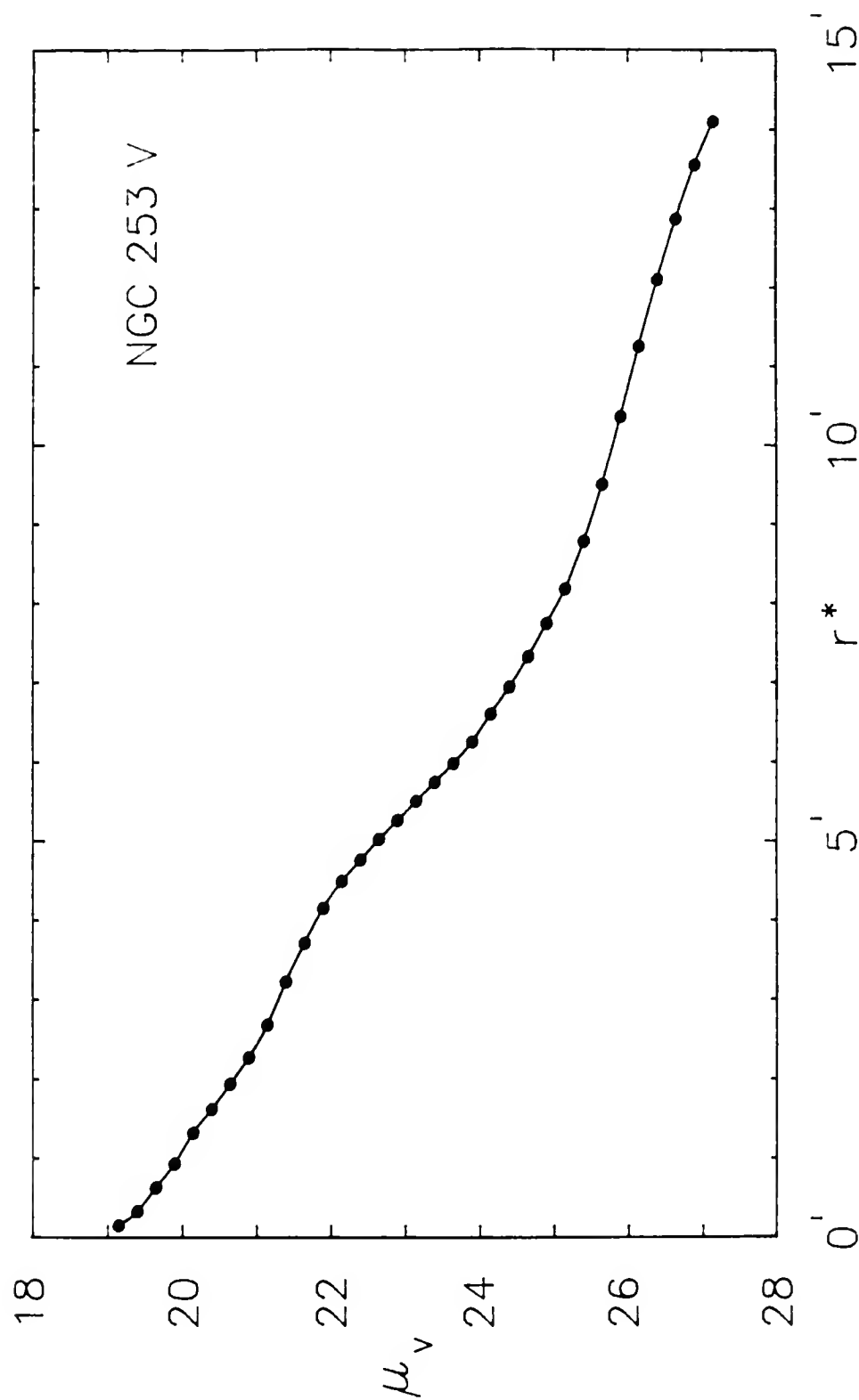
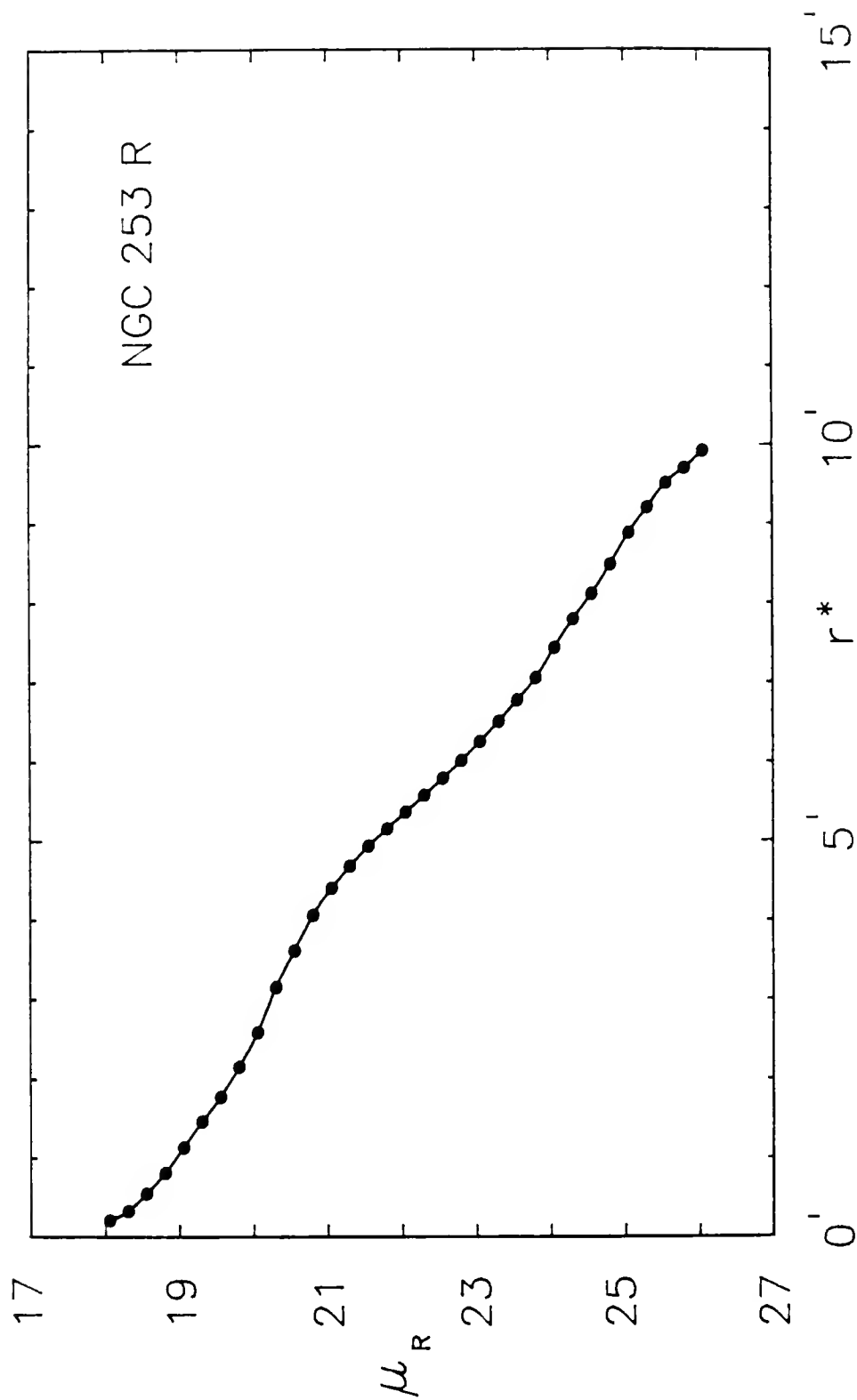


Figure 55. Equivalent mean V luminosity profile for NGC 253.



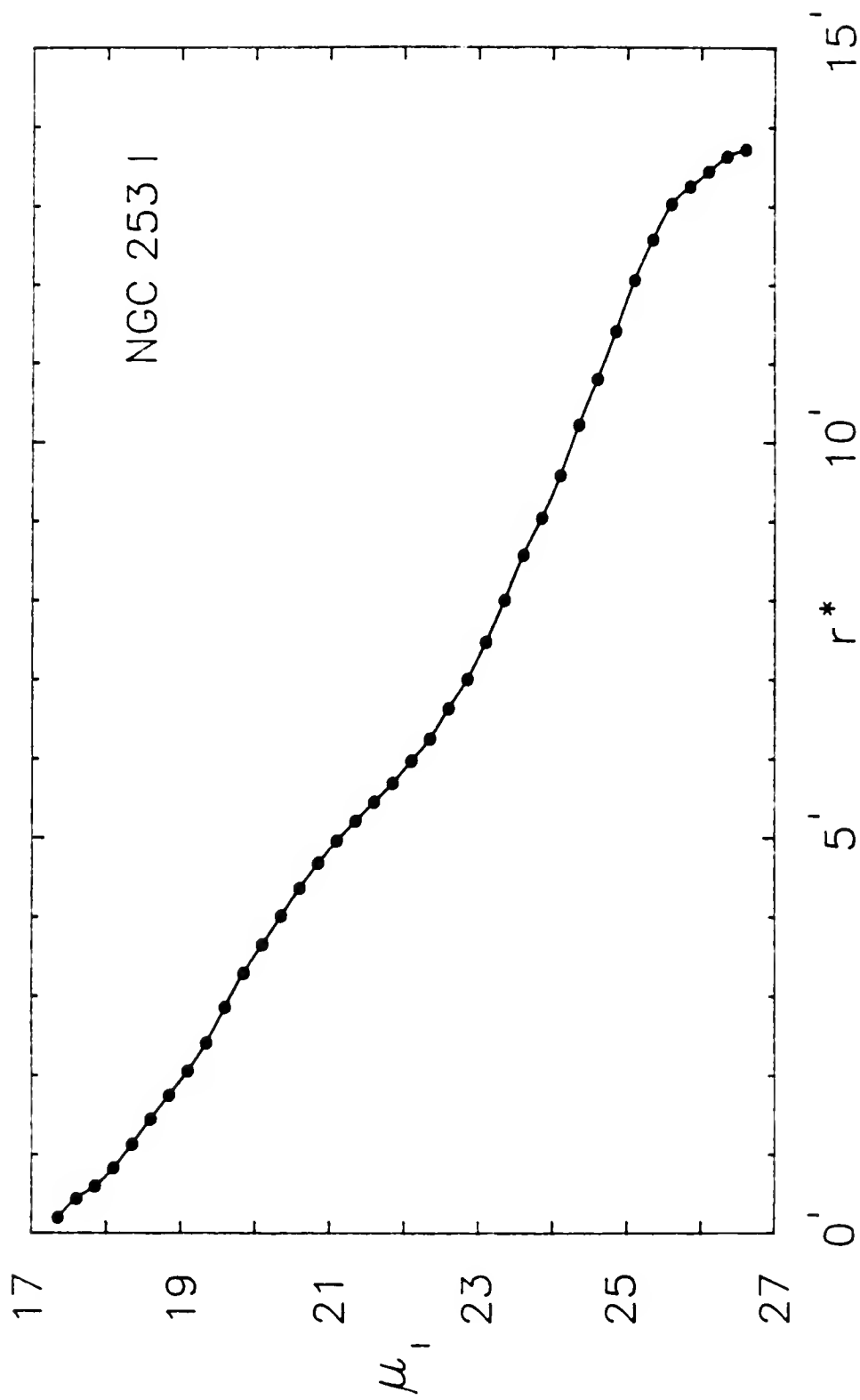


Figure 57. Equivalent mean I luminosity profile for NGC 253.

$\leq 6'$ is caused by the bright areas corresponding to the part of the disk containing the spiral arms. This rise, which is obvious on the V equivalent luminosity profile and Pence's (1978) blue profile, diminishes with increasing wavelength, as can be seen in the R and I profiles. Beyond about $7'$ the profiles all rise, due at least in part to the inclusion of the southern spur and the halo. As the progression is made from short to long wavelengths, each profile is brighter than its predecessor. Over the common range of r' , the V profile is $\approx 0.5 - 1.0$ magnitude brighter than Pence's B profile, the R is $\approx 0 - 1.0$ brighter than the V, and the I is $\approx 0.3 - 1.8$ magnitudes brighter than the V.

Tables 23, 24 and 25 give the mean luminosity distributions for the V, R and I data, based on the equivalent radius calculations. Column (1) lists the intensity level of each isophote step and column (2) gives the included area in square arc minutes. Column (3) gives the integrated luminosity, $L(r')$, at each equivalent radius r' . Column (4) lists the integrated luminosity at each level as the running sum of column (3). The total luminosity, L_T , is given by adding a small correction to the integrated luminosity within the last value of r' , using a small extrapolation from the last reliable data points to $I = 0$. Column (5) gives the equivalent radius at each brightness level and column (6) gives the fraction of the total luminosity contained within each successive level. Columns (7) and (8) list the sizes of

TABLE 23

MEAN V LUMINOSITY DISTRIBUTION IN NGC 253

log I	Area	Power	Sum P	r*	k(r*)	2a	2b	Mag
0.4	0.071	0.178	0.178	0.15	0.005	0.50	0.25	19.15
0.3	.342	.541	.719	.33	.020	0.97	0.40	19.40
0.2	1.25	1.574	2.29	.63	.063	1.29	0.54	19.65
0.1	2.72	2.017	4.31	.93	.118	3.02	1.08	19.90
0.0	5.47	3.027	7.34	1.32	.201	4.68:	1.62	20.15
-0.1	8.24	2.437	9.77	1.62	.268	5.18	1.94	20.40
-0.2	11.82	2.517	12.29	1.94	.337	6.44	2.09	20.65
-0.3	16.19	2.461	14.75	2.27	.405	7.52	2.23	20.90
-0.4	22.56	2.828	17.58	2.68	.482	12.73:	2.30	21.15
-0.5	32.64	3.579	21.16	3.22	.580	15.58:	2.52	21.40
-0.6	43.19	2.965	24.12	3.71	.662	16.65:	3.17	21.65
-0.7	54.23	2.490	26.61	4.15	.730	18.60:	3.45	21.90
-0.8	63.23	1.609	28.22	4.49	.774	20.76:	3.96	22.15
-0.9	71.18	1.129	29.35	4.76	.805	21.58	4.46	22.40
-1.0	79.25	0.912	30.27	5.02	.830	22.01	4.75	22.65
-1.1	86.76	.673	30.94	5.26	.849	22.45	5.00	22.90
-1.2	94.93	.578	31.52	5.50	.865	23.06	5.32	23.15
-1.3	103.5	.479	32.00	5.74	.878	24.10	5.54	23.40
-1.4	112.2	.388	32.38	5.98	.888	24.68	5.83	23.65
-1.5	122.9	.380	32.76	6.25	.899	25.18	6.19	23.90
-1.6	137.0	.396	33.16	6.60	.910	26.04	6.65	24.15
-1.7	151.3	.320	33.48	6.94	.919	26.65	7.05	24.40
-1.8	168.3	.302	33.78	7.32	.927	27.70	7.52	24.65
-1.9	188.4	.285	34.07	7.74	.935	28.92	8.09	24.90
-2.0	210.4	.245	34.31	8.18	.941	29.93	9.06	25.15
-2.1	242.2	.284	34.60	8.78	.949	31.08	10.00	25.40
-2.2	283.5	.291	34.89	9.50	.957	31.98	10.72	25.65
-2.3	336.9	.300	35.19	10.36	.965	32.88	11.80	25.90
-2.4	397.8	.272	35.46	11.25	.973	34.3:	13.2	26.15
-2.5	459.6	.220	35.68	12.10	.979	34.9	13.8	26.40
-2.6	520.2	.172	35.85	12.87	.984			26.65
-2.7	576.4	.127	35.98	13.55	.987			26.90
-2.8	624.2	.086	36.06	14.10	.989			27.15
			36.45:		(1)			

TABLE 24

MEAN R LUMINOSITY DISTRIBUTION IN NGC 253

log I	Area	Power	Sum P	r*	k(r*)	2a	2b	Mag
0.8	0.139	0.823	0.823	0.21	0.010	0.46	0.46	18.06
0.7	.342	1.113	1.94	.33	.024	.89	.60	18.31
0.6	.950	2.674	4.61	.55	.057	1.18	.75	18.56
0.5	2.06	3.850	8.46	.81	.105	3.02:	1.06	18.81
0.4	4.01	5.474	13.93	1.13	.174	4.32:	1.73	19.06
0.3	6.70	6.041	19.98	1.46	.249	5.01	1.93	19.31
0.2	9.88	5.600	25.58	1.77	.319	6.22	2.01	19.56
0.1	14.47	6.491	32.07	2.15	.400	6.94	2.19	19.81
0.0	20.88	7.116	39.18	2.58	.488	7.91	2.36	20.06
-0.1	31.15	9.091	48.27	3.15	.601	13.18:	2.53	20.31
-0.2	40.87	6.871	55.14	3.61	.687	15.77	3.05:	20.56
-0.3	51.80	6.169	61.31	4.06	.764	20.06	3.45	20.81
-0.4	60.80	4.069	65.38	4.40	.815	20.81	3.74	21.06
-0.5	68.92	2.910	68.29	4.68	.851	21.47	4.20	21.31
-0.6	76.32	2.101	70.39	4.93	.877	21.96	4.52	21.56
-0.7	83.22	1.552	71.94	5.15	.896	22.65	4.72	21.81
-0.8	90.40	1.283	73.23	5.36	.912	23.17	4.92	22.06
-0.9	97.36	0.988	74.22	5.57	.925	24.20	5.61	22.31
-1.0	105.2	.883	75.10	5.79	.936	24.89	6.07	22.56
-1.1	113.4	.733	75.83	6.01	.945	26.07	6.39	22.81
-1.2	122.7	.654	76.49	6.25	.953	27.08	6.88	23.06
-1.3	132.9	.572	77.06	6.50	.960	28.09	7.25	23.31
-1.4	144.2	.506	77.56	6.77	.966	28.98	7.68	23.56
-1.5	156.3	.431	78.00	7.05	.972	30.07	8.06	23.81
-1.6	173.2	.476	78.47	7.43	.978	31.83	8.46	24.06
-1.7	190.5	.387	78.86	7.79	.982	32.52	8.92	24.31
-1.8	206.4	.285	79.14	8.11	.986	33.04	9.44	24.56
-1.9	226.0	.276	79.42	8.48	.989	33.58	9.93	24.81
-2.0	247.6	.243	79.66	8.88	.992	34.1	10.4	25.06
-2.1	266.0	.165	79.83	9.20	.995	34.4	10.9	25.31
-2.2	284.1	.128	79.96	9.51	.996	34.7	11.5	25.56
-2.3	295.7	.065	80.02	9.70	.997	35.0	12.2	25.81
-2.4	309.0	.060	80.08	9.92	.998			26.06
			80.27:		(1)			

TABLE 25

MEAN I LUMINOSITY DISTRIBUTION IN NGC 253

log I	Area	Power	Sum P	r*	k(r*)	2a	2b	Mag
0.7	0.120	0.619	0.619	0.20	0.010	0.58	0.54	17.35
0.6	.600	2.066	2.685	.44	.044	.72	.61	17.60
0.5	1.14	1.868	4.553	.60	.075	1.22	.72	17.85
0.4	2.16	2.825	7.378	.83	.121	1.83	1.04	18.10
0.3	4.01	4.109	11.487	1.13	.187	3.45	1.44	18.35
0.2	6.59	4.574	16.061	1.45	.264	4.96	1.83	18.60
0.1	9.66	4.278	20.339	1.75	.334	6.15	2.01	18.85
0.0	13.34	4.137	24.476	2.06	.402	6.83	2.19	19.10
-0.1	18.23	4.382	28.858	2.41	.474	7.81	2.37	19.35
-0.2	25.76	5.245	34.103	2.86	.560	12.99	2.63	19.60
-0.3	34.00	4.588	38.691	3.29	.636	15.50	3.02	19.85
-0.4	41.81	3.491	42.182	3.65	.693	17.16	3.27	20.10
-0.5	50.45	3.064	45.246	4.01	.743	18.85	3.60	20.35
-0.6	59.60	2.838	48.084	4.36	.790	20.14	3.96	20.60
-0.7	68.79	2.057	50.141	4.68	.824	21.15	4.39	20.85
-0.8	77.37	1.522	51.663	4.96	.849	21.76	4.64	21.10
-0.9	85.30	1.120	52.783	5.21	.867	22.45	4.96	21.35
-1.0	93.40	0.911	53.694	5.45	.882	23.06	5.25	21.60
-1.1	101.6	.736	54.430	5.69	.894	23.78	5.61	21.85
-1.2	111.8	.722	55.152	5.97	.906	25.11	6.19	22.10
-1.3	122.8	.613	55.765	6.25	.916	25.94	6.58	22.35
-1.4	137.9	.677	56.442	6.63	.927	26.55	7.27	22.60
-1.5	154.0	.573	57.015	7.00	.937	28.06	8.27	22.85
-1.6	175.3	.596	57.611	7.47	.946	29.39	9.46	23.10
-1.7	200.9	.572	58.183	8.00	.956	31.29	10.90:	23.35
-1.8	230.6	.528	58.711	8.57	.964	32.55	11.65	23.60
-1.9	256.6	.369	59.080	9.04	.970	33.67	12.55	23.85
-2.0	288.6	.359	59.439	9.58	.976	34.71	14.82:	24.10
-2.1	328.0	.352	59.791	10.22	.982	35.65	22.48:	24.35
-2.2	366.6	.273	60.064	10.80	.987	36.76	23.60:	24.60
-2.3	408.6	.236	60.300	11.41	.990	37.48	25.25	24.85
-2.4	457.1	.217	60.517	12.06	.994	38.3	26.0	25.10
-2.5	497.0	.144	60.661	12.58	.996			25.35
-2.6	533.7	.105	60.766	13.03	.998			25.60
-2.7	551.6	.040	60.806	13.25	.999			25.85
-2.8	567.7	.030	60.836	13.44	(1)			26.10
-2.9	583.9	.024	60.860	13.63	(1)			26.35
-3.0	591.5	.009	60.869	13.72	(1)			26.60
			60.88:		(1)			

the major and minor axes at each level and column (9) gives the surface brightness in magnitudes per square arc second. The total magnitudes are: $V_T = 7.35 \pm 0.05$, $R_T = 6.41 \pm 0.08$ and $I_T = 5.75 \pm 0.11$ where the error is that of the sky determination, which is by far the dominant source of error. Converting the V_T magnitude to the Johnson system by the relation given in Chapter II yields a total $V_J = 7.43 \pm 0.10$. This compares reasonably well to Pence's value of $V_J = 7.20 \pm 0.06$ estimated from his B-V measurements.

The relative integrated luminosity, $k(r^*) = L(r^*)/L_T$, is plotted in Figures 58, 59 and 60 for the V, R and I data, respectively. The quantities r_1^* , r_2^* , r_3^* and μ_1 , μ_2 , and μ_3 , corresponding to $k = 1/4$, $1/2$ and $3/4$ are also shown. The equivalent effective radius, defined by $k(r_2^*) = 1/2$ is $r_2^* = 2'.77$, $2'.63$ and $2'.54$ for V, R and I. These correspond to 2.30, 2.18 and 2.11 kpc at 2.85 Mpc. Quartiles, defined by $k(r_1^*) = 1/4$ and $k(r_3^*) = 3/4$ occur at $r_1^* = 1'.53$, $1'.46$ and $1'.39$, or 1.27, 1.21 and 1.15 kpc, and $r_3^* = 4'.30$, $3'.97$ and $4'.06$, or 3.56, 3.29 and 3.37 kpc for V, R and I, respectively. The R r_3^* value is probably an underestimate caused by the lack of deep photometry in this color. By way of comparison, the B_J values of Pence are $r_2^* = 3'.16$, $r_1^* = 1'.85$ and $r_3^* = 4'.75$. His larger values indicate the blue light declines less rapidly with distance than does the longer wavelength V, R or I. This is to be expected since the longer wavelengths penetrate the dust more effectively, thus showing

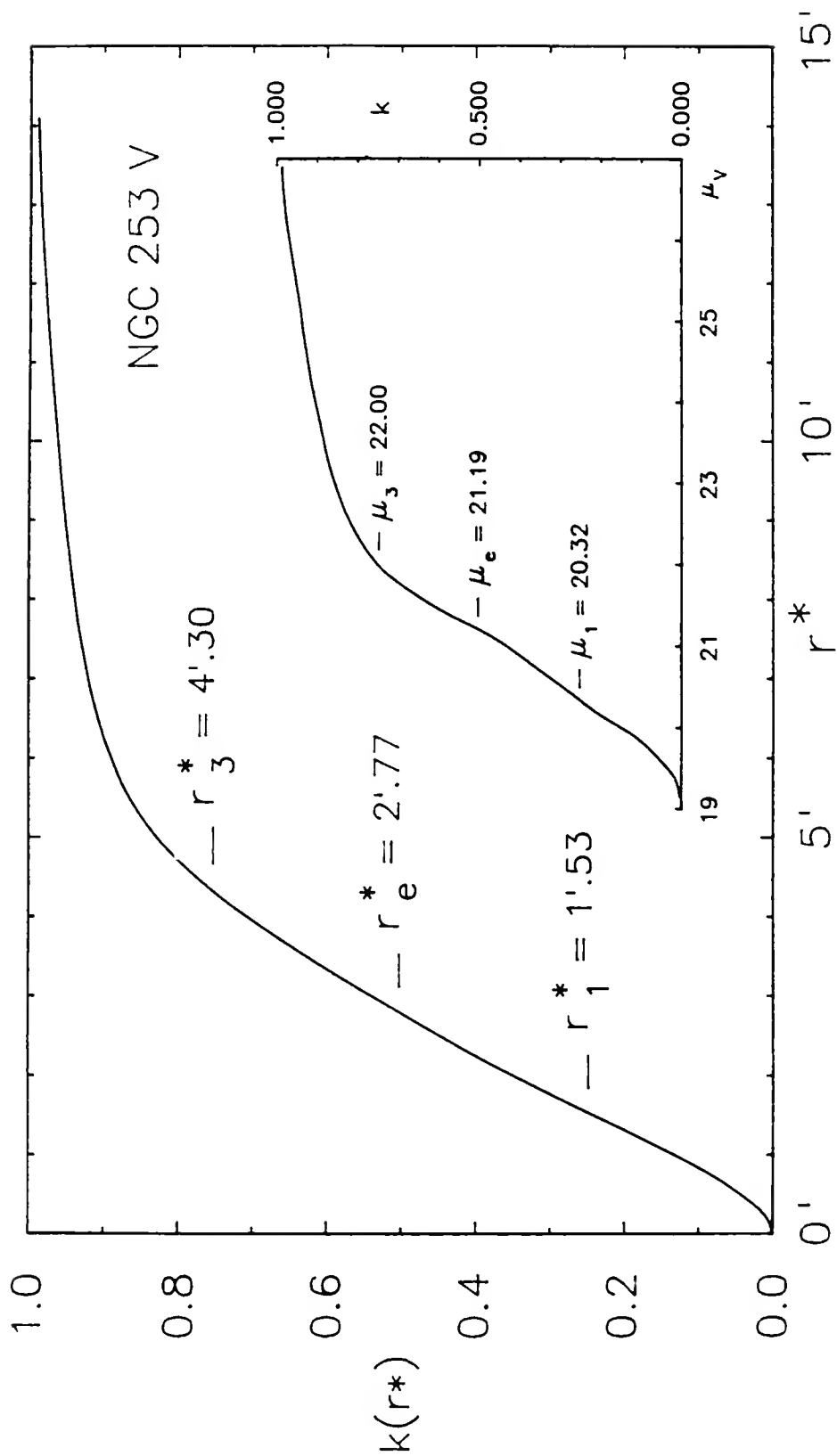


Figure 58. Relative V integrated luminosity curves for NGC 253 showing the fraction $k = L(r')/L_r$ of the total luminosity emitted within radius r^* . The insert shows the fraction of the total luminosity in regions brighter than μ_v .

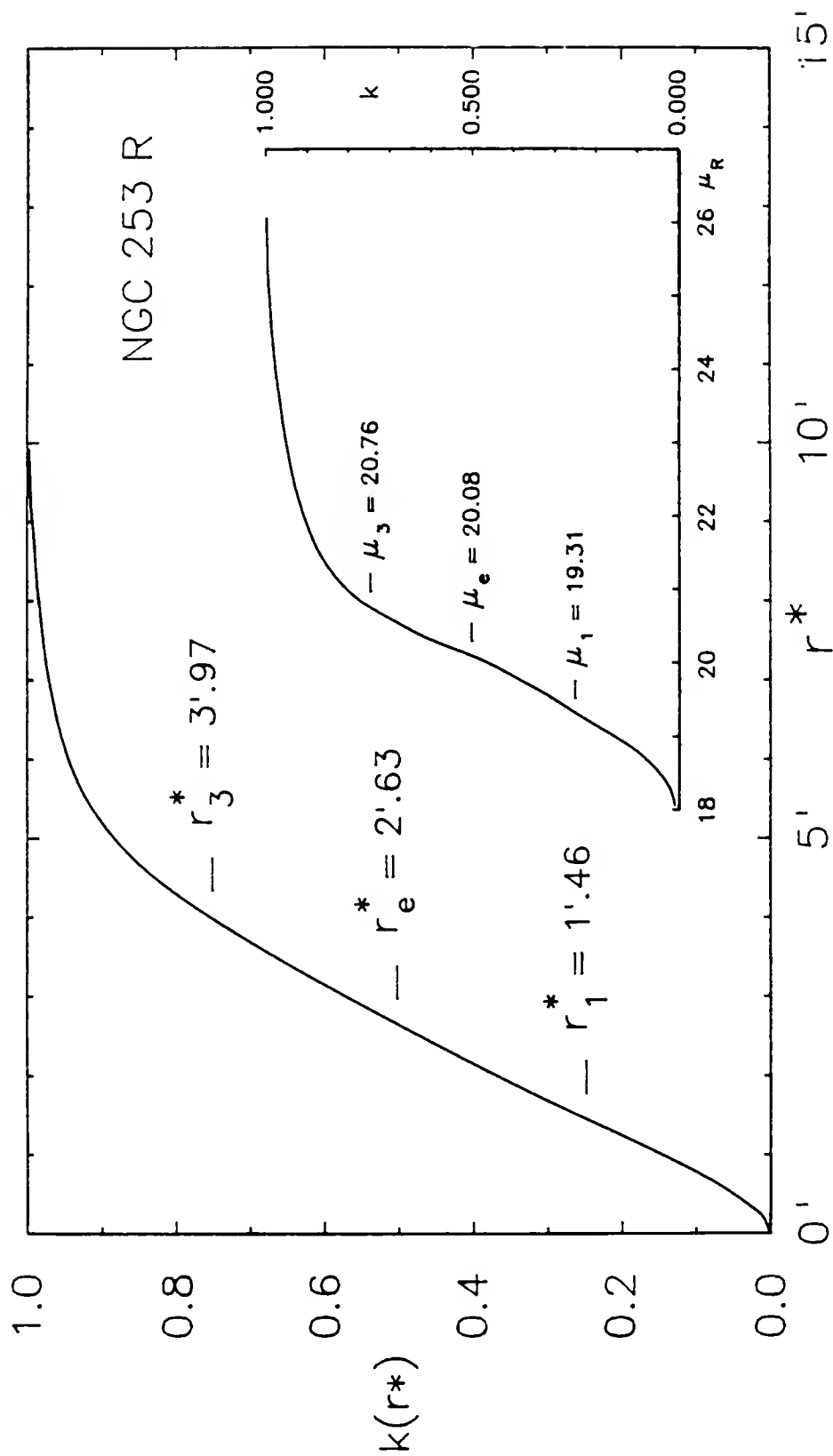


Figure 59. Relative R integrated luminosity curves for NGC 253 showing the fraction $k = L(r^*)/L_T$ of the total luminosity emitted within radius r^* . The insert shows the fraction of the total luminosity in regions brighter than μ_R .

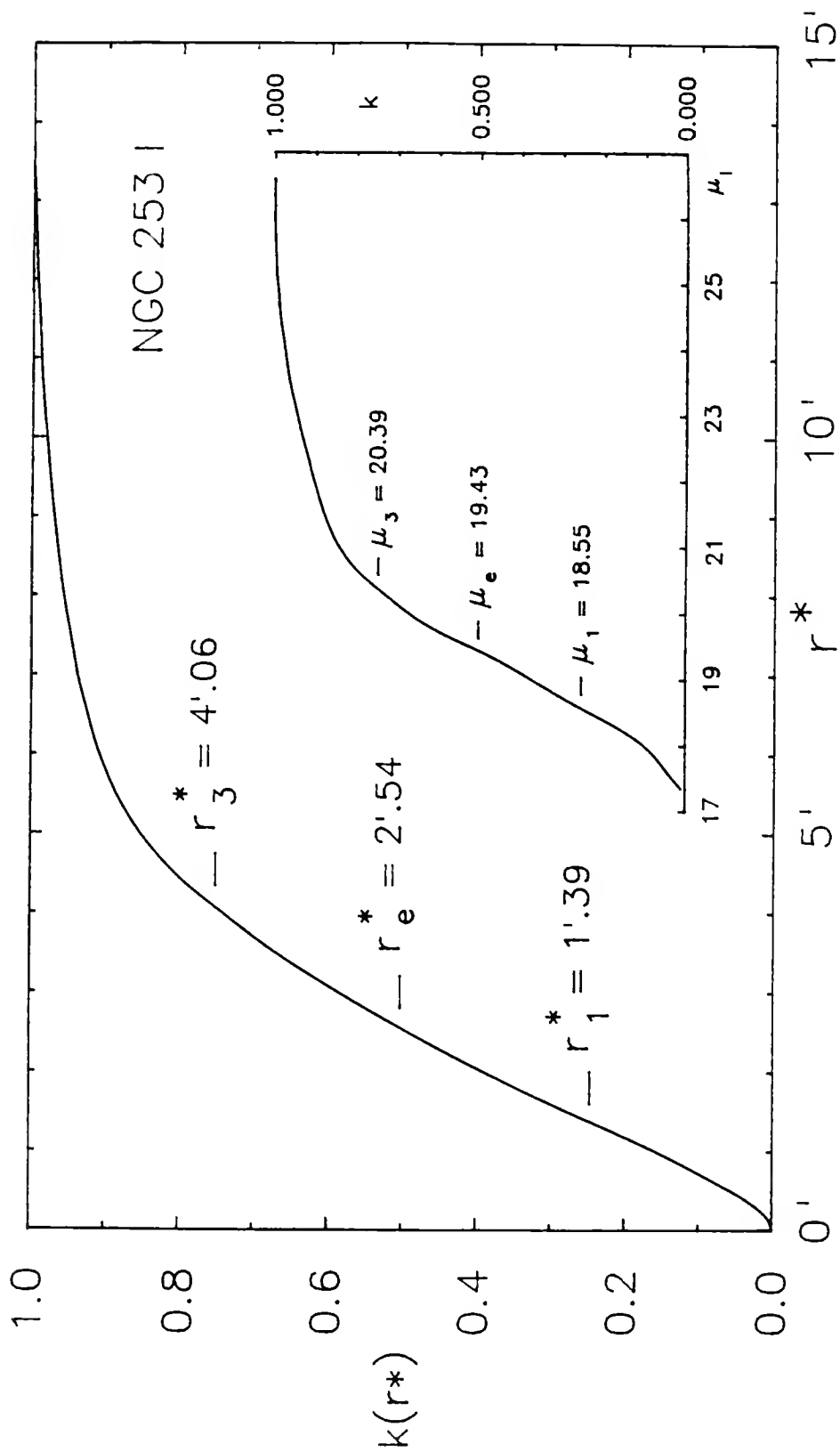


Figure 60. Relative I integrated luminosity curves for NGC 253 showing the fraction $k = L(r^*)/L_r$ of the total luminosity emitted within radius r^* . The insert shows the fraction of the total luminosity in regions brighter than μ_i .

the brighter inner regions that are more hidden in the blue passband.

Concentration indices, defined by $C_{21} = r_{\bullet}'/r_1'$ and $C_{32} = r_3'/r_{\bullet}'$ have values of 1.81, 1.80, 1.83, and 1.55, 1.51 and 1.60 for V, R and I, where the red C_{32} value is probably an underestimate. Pence finds $C_{21} = 1.71$ and $C_{32} = 1.50$ from his blue photometry. A pure exponential distribution would have $C_{21} = 1.75$ and $C_{32} = 1.60$; consequently, the C_{21} values of V, R and I show the light to be more centrally concentrated than would be the case for an exponential distribution, the B_J less concentrated. The C_{32} values indicate the light is less centrally concentrated in the B_J , V and R passbands, although the concentration increases with increasing wavelength. The I passband C_{32} index matches that expected for an exponential distribution, due, no doubt, to the infrared light penetrating the dust in the outer regions and more clearly showing the underlying stellar material. Hence, we conclude that the disk of NGC 253 does closely approximate an exponential distribution under the somewhat chaotic appearance caused by the dust and spiral arms.

Corrections to the apparent magnitudes to account for galactic extinction, internal extinction and redshift are made in much the same way as was done for NGC 55. Again, the redshift, or K correction, is less than 0.01 magnitude (Pence 1976) and will be neglected. The correction for galactic extinction is estimated to be $A_g = 0.21$ in the RC2. For the

effective wavelengths used here, values of $A_v = 0.15$, $A_r = 0.13$ and $A_i = 0.10$ are obtained using the data of Savage and Mathis (1979).

Internal extinction can be estimated in two ways. As was done for NGC 55, the internal differential absorption based on RC2 data can be calculated for blue light and then the corresponding V, R and I values can be estimated. The result for blue light is $A_0(i) = 0.49$, and for V, R and I, 0.35, 0.30 and 0.23. Then the face-on magnitude, not the absorption-free magnitude, is given by subtracting the above two corrections from the integrated total apparent magnitude, m_T , using equation (14) p. 101. The resulting total face-on magnitudes are $V_T^0 = 6.85 \pm 0.09$, $R_T^0 = 5.98 \pm 0.11$, and $I_T^0 = 5.42 \pm 0.12$. For blue light Pence (1978) found $B_T^0 = 7.35 \pm 0.11$.

Alternatively, the total extinction in the B_J band given by Pence can be used. His value of $(B_J - V_J)_T = 0.85 \pm 0.05$, coupled with the mean value of Sc galaxies in the RC2 (except those with strong line emission), de Vaucouleurs (1977), $\langle (B_J - V_J)_T^0 \rangle = 0.511 \pm 0.07$ (m.e.) gives a color excess of 0.34 ± 0.09 , assuming NGC 253 has normal colors. Then the formula in the RC2 gives $A_B = 4.4 E(B_J - V_J) = 1.50 \pm 0.4$. Converting this to the colors used here results in $A_v = 1.08 \pm 0.29$, $A_r = 0.93 \pm 0.25$, and $A_i = 0.70 \pm 0.19$. The integrated magnitudes, corrected for total extinction, internal and galactic, are $V_T^0 = 6.27 \pm 0.29$, $R_T^0 = 5.48 \pm 0.26$ and $I_T^0 = 5.05 \pm 0.22$. Pence gets $B_T^0 = 6.55 \pm 0.40$. Using the same tech-

nique but $(B_J - V_J)_T = 0.62 \pm 0.11$ obtained from Pence's B_T value and the V_T from this work put on the Johnson system, $E(B_J - V_J)_T = (B_J - V_J)_T - \langle (B_J - V_J)_T^0 \rangle = 0.11 \pm 0.14$. Now $A_B = 4.4 E(B_J - V_J) = 0.48 \pm 0.62$ and $A_V = 0.35 \pm 0.45$, $A_R = 0.30 \pm 0.38$ and $A_I = 0.23 \pm 0.29$. Then the integrated magnitudes, corrected for total extinction, are $V_T^0 = 7.00 \pm 0.45$, $R_T^0 = 6.11 \pm 0.39$ and $I_T^0 = 5.52 \pm 0.31$.

As Pence points out, these results are conservative estimates of A_B because the coefficient of the color excess was derived under the assumption that the absorbing material acts as a screen in front of the galaxy. For a mixture of absorbing and luminous material, the coefficient is larger. However, Pence's value of $(B_J - V_J)_T = 0.85$ is larger than that found here, 0.62, and therefore the first of the two sets of A_B corrections above may be too large. Therefore, the adopted values of the total magnitudes, corrected for extinction and absorption, will be taken as the mean of the above two values: $V_T^0 = 6.62 \pm 0.38$, $R_T^0 = 5.79 \pm 0.33$, and $I_T^0 = 5.28 \pm 0.27$.

At the assumed distance of 2.85 Mpc, the distance modulus of NGC 253 is 27.27 and the corrected face-on absolute magnitudes are: $M_T^0(V) = -20.65 \pm 0.4$., $M_T^0(R) = -21.48 \pm 0.3$., and $M_T^0(I) = -21.99 \pm 0.3$..

The colors of NGC 253 are $(B_J - V)_T = 0.70 \pm 0.06$, $(V-R)_T = 0.94 \pm 0.09$ and $(V-I)_T = 1.60 \pm 0.12$. As mentioned above, the value $(B_J - V_J)_T = 0.62 \pm 0.11$ when the V magnitude is put on the Johnson system, and is bluer than that derived by

Pence, 0.85 ± 0.05 from his drift scans of the inner disk. Following the precepts given in the RC2, the corrected face-on value of $(B_J - V_J)_T^0 = 0.46 \pm 0.16$, near the mean value for Sc galaxies mentioned above, but somewhat bluer than Pence's value of 0.69.

All of the basic photometric parameters for NGC 253 obtained from the V, R and I plate analyses are summarized in Tables 26, 27 and 28.

Decomposition of the Observed Profiles

The V and I mean luminosity profiles, Figures 40, 42, 43, and 45, show strong evidence of having both an exponential and a $r^{0.25}$ component. The exponential behavior is most easily seen in the mean major axis and the $r^{0.25}$ in the mean minor axis. Unfortunately, the R profiles, especially the mean minor axis, are not of sufficient extent and reliability to allow the two components to be distinguished, and therefore will not be considered.

The iterative fitting method proposed by Kormendy (1977) is used to separate the two components of the profiles. In the form used here, a least squares fit of a $r^{0.25}$ profile is made to the spheroidal component of the mean minor axis using equation (15),

$$\mu' = \mu'_0 + s' \cdot b^{0.25}. \quad (15)$$

This is extrapolated into the exponential range and subtracted from the observations to get a first estimate of the under-

TABLE 26

PHOTOMETRIC PARAMETERS OF NGC 253 V

Apparent distance modulus	$27.42 \pm 0.4:$
Corrected distance modulus	$27.27 \pm 0.4:$
Distance	2.85 ± 0.54 Mpc
Inclination*	$78^\circ.5$
Major axis position angle*	$51^\circ.0 \pm 0^\circ.4$
Ellipticity $23.0 < \mu < 25.5$	$0.23 - 0.33$
Total apparent magnitude	$V_T = 7.35 \pm 0.05$
Corrected magnitude	$V_T^0 = 6.62 \pm 0.38$
Absolute magnitude	$M_T^0 = -20.65 \pm 0.4:$
Threshold surface brightness	$\mu = 26.9$
Major axis at threshold	$2a = 36'.3, 30.1$ kpc
Minor axis at threshold	$2b = 16'.4, 13.6$ kpc
Major axis at $\mu = 25.0$	$2a = 29'.1, 24.2$ kpc
Minor axis at $\mu = 25.0$	$2b = 8'.4, 7.0$ kpc
Luminosity within $\mu = 25.0$	$k = 0.937$
Disk scale length	$1/\alpha = 2.12$ kpc
Parameters at $k = 1/4$	
Surface brightness	$\mu_1 = 20.32$
Equivalent radius	$r_1^* = 1'.53, 1.27$ kpc
Semi-major axis	$a_1 = 2'.52, 2.09$ kpc
Axis ratio	$b_1/a_1 = 0.38$
Parameters at $k = 1/2$	
Surface brightness	$\mu_2 = 21.19$
Equivalent radius	$r_2^* = 2'.77, 2.30$ kpc
Semi-major axis	$a_2 = 7'.15:, 5.93:$ kpc
Axis ratio	$b_2/a_2 = 0.16:$
Parameters at $k = 3/4$	
Surface brightness	$\mu_3 = 22.00$
Equivalent radius	$r_3^* = 4'.30, 3.56$ kpc
Semi-major axis	$a_3 = 10'.16, 8.42$ kpc
Axis ratio	$b_3/a_3 = 0.18$
Concentration indices	
C_{21}	$r_2^*/r_1^* = 1.81$
C_{32}	$r_3^*/r_2^* = 1.55$
Theoretical C_{21}	1.75
Theoretical C_{32}	1.60

Note: * Value adopted from Pence (1978).

TABLE 27

PHOTOMETRIC PARAMETERS OF NGC 253 R

Apparent distance modulus	$27.40 \pm 0.4:$
Corrected distance modulus	$27.27 \pm 0.4:$
Distance	2.85 ± 0.54
Inclination _a	$78^\circ.5$
Major axis position angle ^a	$51^\circ.0 \pm 0^\circ.4$
Ellipticity $22.1 < \mu < 24.6$	$0.21 - 0.29$
Total apparent magnitude	$R_T = 6.41 \pm 0.08$
Corrected magnitude	$R_T^0 = 5.79 \pm 0.33$
Absolute magnitude	$M_T^0 = -21.48 \pm 0.3:$
Threshold surface brightness	$\mu = 25.9$
Major axis at threshold	$2a = 35'.0, 29.0 \text{ kpc}$
Minor axis at threshold	$2b = 12'.3, 10.2 \text{ kpc}$
Major axis at $\mu = 25.0$	$2a = 33'.8, 28.0 \text{ kpc}$
Minor axis at $\mu = 25.0$	$2b = 10'.2, 8.4 \text{ kpc}$
Luminosity within $\mu = 25.0$	$k = 0.991:$
Parameters at $k = 1/4$	
Surface brightness	$\mu_1 = 19.31$
Equivalent radius	$r_1^* = 1'.46, 1.21 \text{ kpc}$
Semi-major axis	$a_1 = 2'.45, 2.03 \text{ kpc}$
Axis ratio	$b_1/a_1 = 0.38$
Parameters at $k = 1/2$	
Surface brightness	$\mu_2 = 20.08$
Equivalent radius	$r_2^* = 2'.63, 2.18 \text{ kpc}$
Semi-major axis	$a_2 = 3'.96, 3.28 \text{ kpc}$
Axis ratio	$b_2/a_2 = 0.34$
Parameters at $k = 3/4$	
Surface brightness	$\mu_3 = 20.76$
Equivalent radius	$r_3^* = 3'.97, 3.29 \text{ kpc}$
Semi-major axis	$a_3 = 9'.86:, 8.17:\text{kpc}$
Axis ratio	$b_3/a_3 = 0.16$
Concentration Indices	
C_{21}	$r_2^*/r_1^* = 1.80$
C_{32}	$r_3^*/r_2^* = 1.51$
Theoretical C_{21}	1.75
Theoretical C_{32}	1.60

Note: ^a Value adopted from Pence (1978).

TABLE 28

PHOTOMETRIC PARAMETERS OF NGC 253 I

Apparent distance modulus	$27.37 \pm 0.4:$
Corrected distance modulus	$27.27 \pm 0.4:$
Distance	2.85 ± 0.54 Mpc
Inclination*	$78^\circ.5$
Major axis position angle*	$51^\circ.0 \pm 0^\circ.4$
Ellipticity $21.4 < \mu < 23.9$	$0.22 - 0.40$
Total apparent magnitude	$I_T = 5.75 \pm 0.11$
Corrected magnitude	$I_T^0 = 5.28 \pm 0.27$
Absolute magnitude	$M_T^0 = -21.99 \pm 0.3:$
Threshold surface brightness	$\mu = 26.4$
Major axis at threshold	$2a = 42'.8, 35.5$ kpc
Minor axis at threshold	$2b = 21'.7:, 18.0$ kpc $31'.4:, 26.0:$ kpc
Major axis at $\mu = 25.0$	$2a = 37'.9, 31.4$ kpc
Minor axis at $\mu = 25.0$	$2b = 25'.6:, 21.2:$ kpc
Luminosity within $\mu = 25.0$	$k = 0.993$
Disk scale length	$1/\alpha = 2.67$ kpc
Parameters at $k = 1/4$	
Surface brightness	$\mu_1 = 18.55$
Equivalent radius	$r_1^* = 1'.39, 1.15$ kpc
Semi-major axis	$a_1 = 2'.35, 1.95$ kpc
Axis ratio	$b_1/a_1 = 0.26$
Parameters at $k = 1/2$	
Surface brightness	$\mu_2 = 19.43$
Equivalent radius	$r_2^* = 2'.54, 2.11$ kpc
Semi-major axis	$a_2 = 5'.51:, 4.57:$ kpc
Axis ratio	$b_2/a_2 = 0.22:$
Parameters at $k = 3/4$	
Surface brightness	$\mu_3 = 20.39$
Equivalent radius	$r_3^* = 4'.06, 3.37$ kpc
Semi-major axis	$a_3 = 9'.48:, 7.86:$ kpc
Axis ratio	$b_3/a_3 = 0.19:$
Concentration indices	
C_{21}	$r_2^*/r_1^* = 1.83$
C_{32}	$r_3^*/r_2^* = 1.60$
Theoretical C_{21}	1.75
Theoretical C_{32}	1.60

Note: * Value adopted from Pence (1978).

lying exponential distribution. Fitting this with an exponential, equation (16), it is extrapolated back into the spheroidal range and subtracted from the observations to get the $r^{0.25}$ distribution.

$$\mu'' = \mu_0'' + s'' \cdot b. \quad (16)$$

The notation follows that of Pence (1978). The iterative process is continued until two successive iterations agree within some specified threshold, taken here to be 0.02 magnitude. By judicious choices of the starting guesses, convergence was usually achieved in about four iterations although the number could reach as many as ten. A fit starting with the exponential component was tried and found to give almost identical results but required more iterations. Numerous trials were run, using different ranges for both components and the sums of the two components were then compared to the actual profile. The fit judged to be the best was selected and used to decompose the mean major axis profile.

Because the spheroidal component of the major axis is almost completely hidden by the stronger exponential component, no attempt is made to fit it by the method described above. Rather, following Pence, the major axis spheroidal distribution is determined from the minor axis distribution assuming his value of the intrinsic axis ratio of $c/a = 0.50$.

For an inclination of $78^\circ.5$, equation (13) gives the apparent axis ratio $b/a = 0.529$. This then allows the spheroidal component along the major axis to be calculated. To get the exponential distribution along the major axis, the calculated spheroidal component is subtracted from the observed mean major axis profile and an exponential is fit to the remaining luminosity curve at $a \geq 14'$ in V and $a \geq 12'.5$ in I, forcing the fit to meet the minor axis fit at $a = 0$.

The results for the V data spheroid are:

$$\mu'_V(a) = 17.35 + 4.70 \cdot a^{0.25},$$

$$\mu'_V(b) = 17.35 + 5.50 \cdot b^{0.25},$$

and,

$$\mu'_V(r) = 17.35 + 5.08 \cdot r^{0.25}.$$

For the disk solution, the equations are:

$$\mu''_V(a) = 19.29 + 0.425 \cdot a,$$

$$\mu''_V(b) = 19.29 + 1.77 \cdot b,$$

and,

$$\mu''_V(r) = 19.29 + 0.868 \cdot r.$$

In all the above, a and b are in arc minutes and $r = (ab)^{0.5}$. The solutions are plotted on the mean profiles in Figures 61 and 62.

For the I data, the spheroid equations are:

$$\mu'_I(a) = 15.34 + 4.58 \cdot a^{0.25},$$

$$\mu'_I(b) = 15.34 + 5.37 \cdot b^{0.25},$$

and,

$$\mu'_I(r) = 15.34 + 4.96 \cdot r^{0.25}.$$

The I disk solution is:

$$\mu''_I(a) = 17.53 + 0.406 \cdot a,$$

$$\mu''_I(b) = 17.53 + 1.80 \cdot b,$$

and,

$$\mu''_I(r) = 17.53 + 0.854 \cdot r.$$

These solutions are plotted on the mean profiles in Figures 63 and 64. The units are the same as for the V solution.

For the V data, the total power from each of the components is given by $L' = 19.90 I_{\bullet}' r_{\bullet}'^2$ and $L'' = 11.93 I_{\bullet}'' r_{\bullet}''^2$,

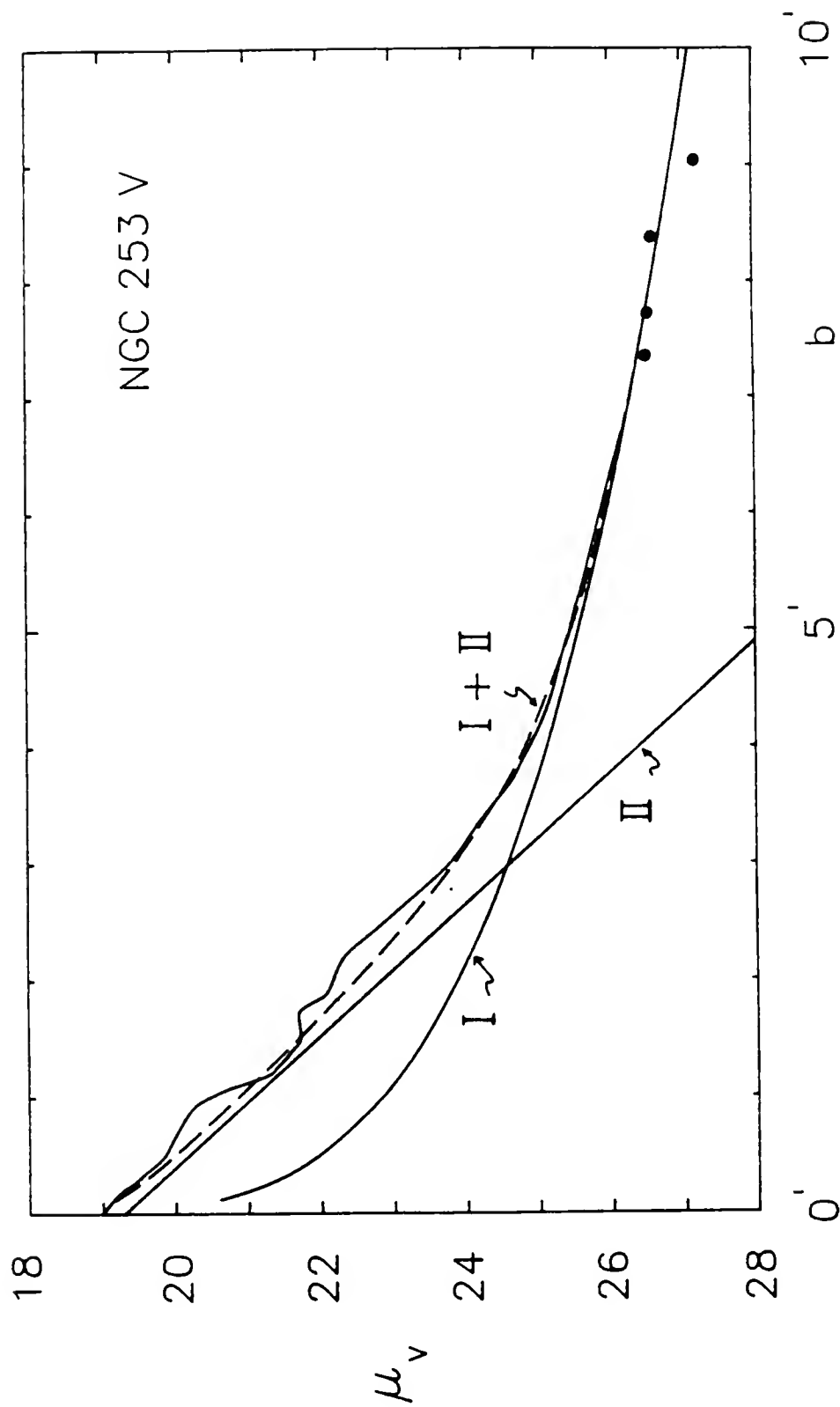


Figure 61. Decomposition of the V mean minor axis. The solid curve I is the $r^{0.25}$ component, the solid line II is the exponential component and the dashed curve, I+II is the sum.

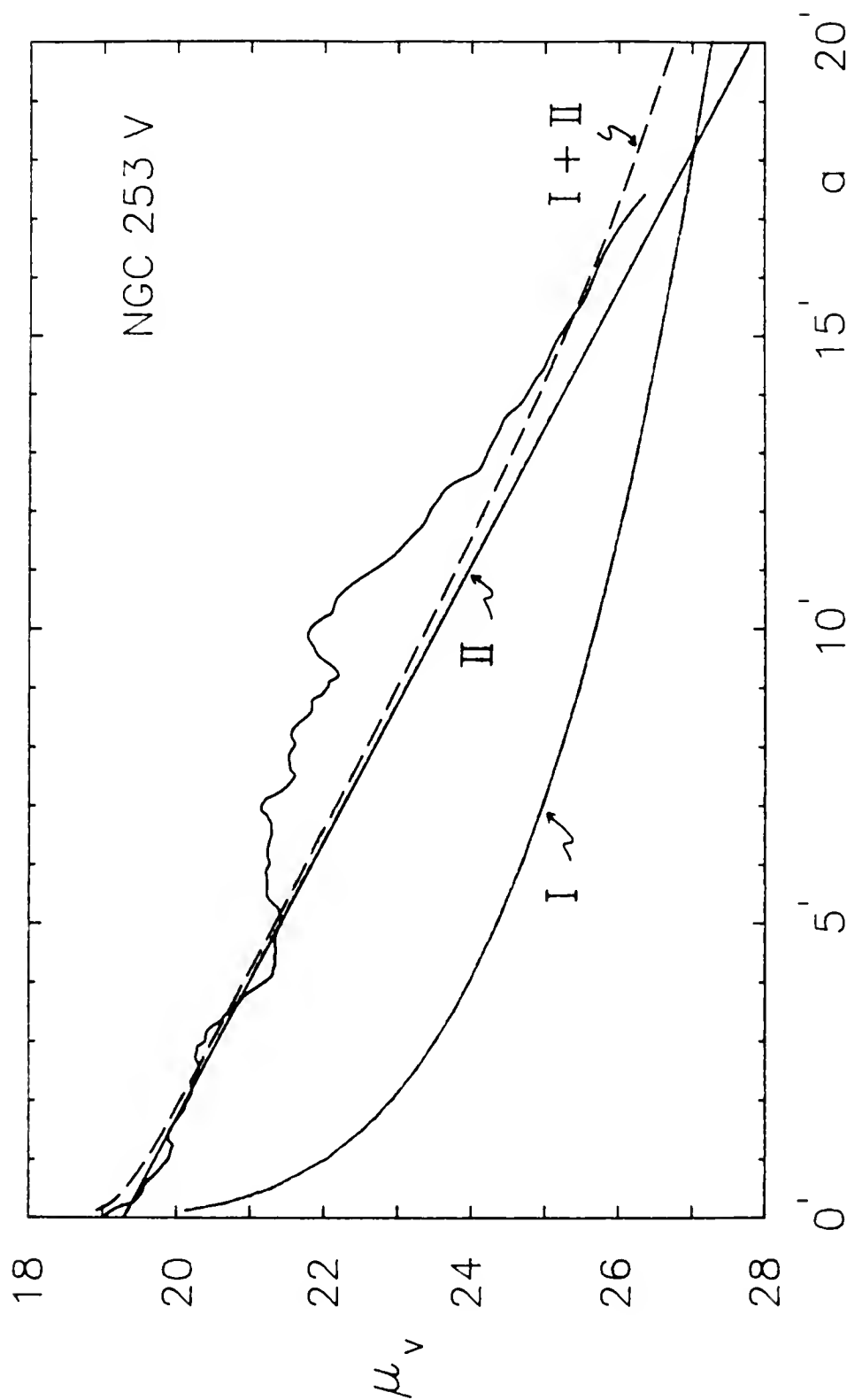


Figure 62. Decomposition of the V mean major axis. The solid curve I is the $r^{0.25}$ component, the solid line II is the exponential component, and the dashed curve I+II is the sum.

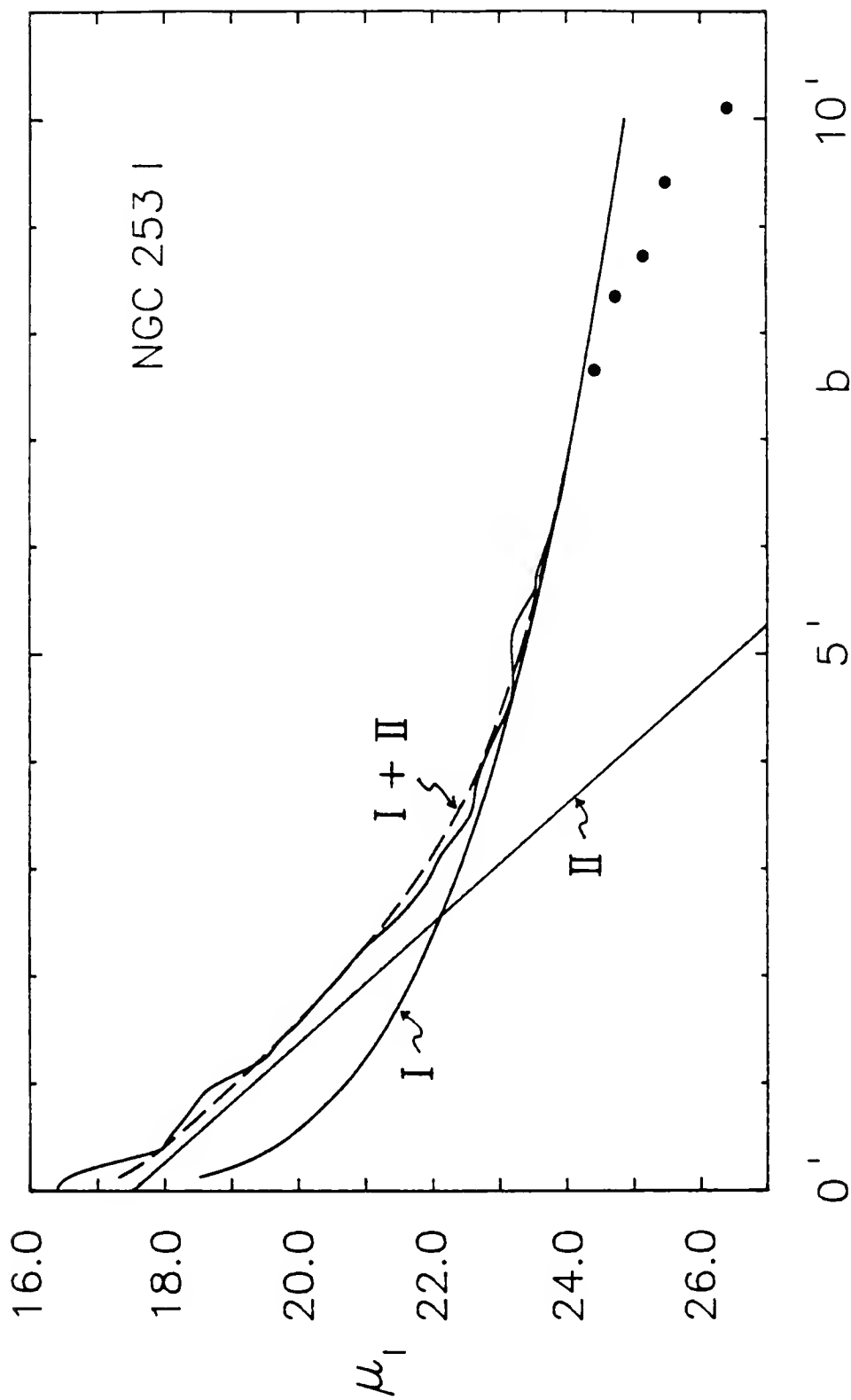


Figure 63. Decomposition of the I mean minor axis. The solid curve I is the $r^{0.25}$ component, the solid line II is the exponential component, and the dashed curve I+II is the sum.

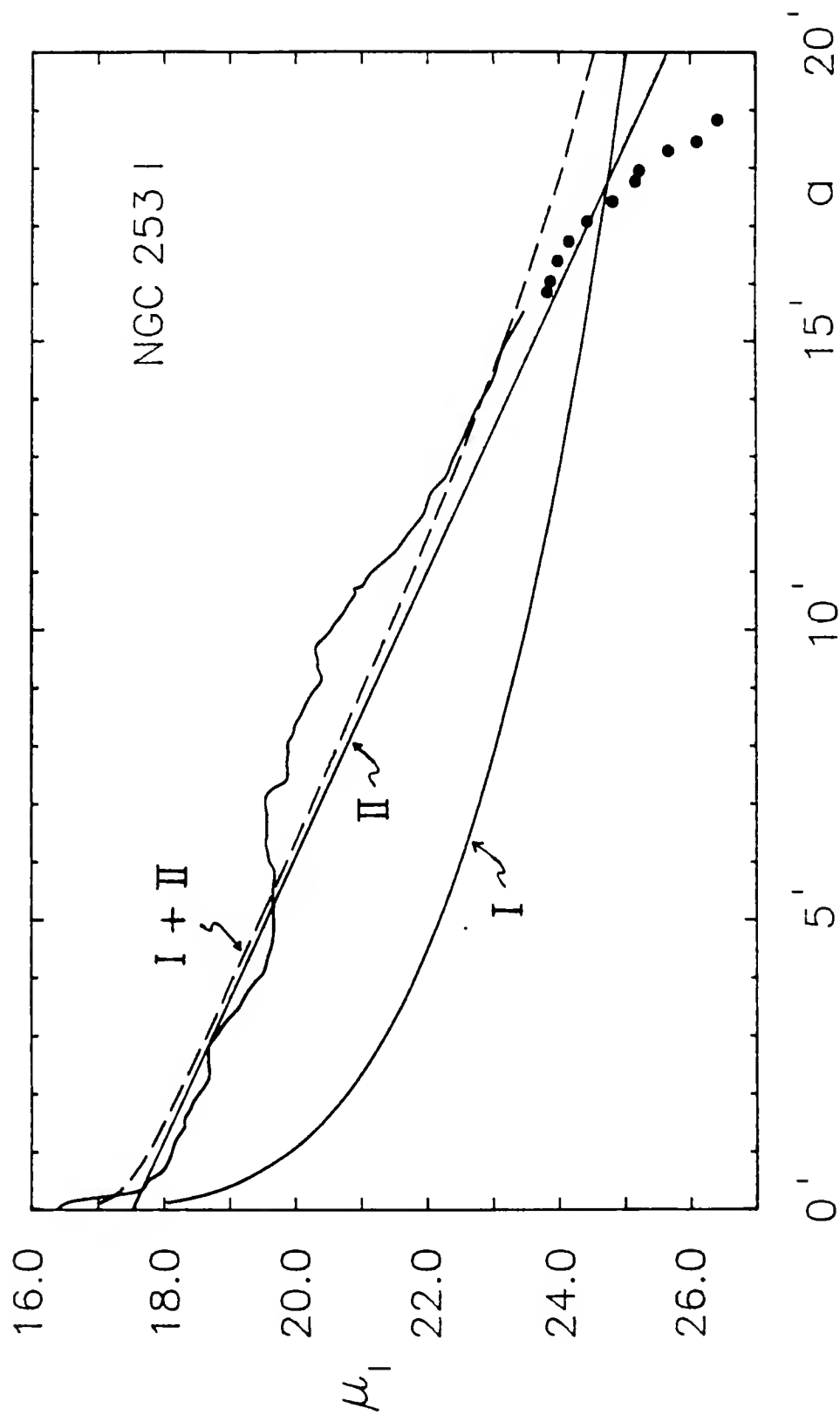


Figure 64. Decomposition of the I mean major axis. The solid curve is the $r^{0.25}$ component, the solid line II is the exponential component, and the dashed curve I+II is the sum.

where $r_{\bullet}' = 4'.47$, $\mu_{\bullet}' = 24.74$, $r_{\bullet}'' = 2'.10$, and $\mu_{\bullet}'' = 21.11$. Here $\mu_{\bullet} = -2.5 \log(I_{\bullet})$ is the surface brightness at $r = r_{\bullet}$. With $V_T = 7.35$, we get $L'/L_T = 0.16 \pm .05$ and $L''/L_T = 0.60 \pm .15$ as the ratios of the spheroid luminosity and the disk luminosity to the total luminosity. Then the remainder of the luminosity is ascribed to the spiral arms, $L'''/L_T = 0.24 \pm 0.16$, where $L''' = L_T - (L' + L'')$. The errors are estimates based on the spread in the values of the various models tried. Models that gave $L' + L'' > L_T$ were not considered. The resulting scale length of the V disk is 2.12 kpc.

In the case of the infrared data, the total power from each of the components is: $L' = 19.35 I_{\bullet}' r_{\bullet}'^2$ for the spheroid, and $L'' = 11.94 I_{\bullet}'' r_{\bullet}''^2$ for the disk, where $r_{\bullet}' = 4'.74$, $\mu_{\bullet}' = 22.66$, and $r_{\bullet}'' = 2'.11$, $\mu_{\bullet}'' = 19.35$. For $I_T = 5.75$, $L'/L_T = 0.27 \pm .05$, and $L''/L_T = 0.71 \pm .10$. Then the spiral arm component, $L'''/L_T = 0.02 \pm .11$. The scale length of the I disk is 2.67 kpc.

Comparing the above results, the model predicts that the spheroid light becomes more important at longer wavelengths, dominating the light from the disk in the infrared. In comparison, Pence's (1980) results for blue light gave $L'/L_T = 0.15 \pm 0.05$, $L''/L_T = 0.59 \pm 0.10$, and $L'''/L_T = 0.26 \pm 0.05$, showing the increased importance of the disk and spiral arms to the blue light.

CHAPTER V SUMMARY AND CONCLUSIONS

Surface photometry in any color other than blue light is available for few galaxies. Even less is available that covers an entire galaxy, and is of a quantitative nature. This work is intended to help fill this void by providing detailed photographic surface photometry of two nearby galaxies, NGC 55 and NGC 253 in visual (V), red (R) and near-infrared (I) light. Both galaxies are late-type spirals in the Sculptor Group and are seen at high inclination. Thus, both the disks and spheroids, or halos, can be examined. Long and short exposure plates are used to record the bright inner regions as well as the faint outer regions of these galaxies. The reductions are based, in part, on the Numerical Mapping Technique of Jones et al. (1968).

Photometric results for NGC 55 include isophote maps of the bright inner regions, as well as the faint outer regions which show the asymmetric nature of this galaxy. Measurements of the isophotes and major and minor axis profiles yield an inclination of $\approx 85^\circ$ and a position angle of the major axis of $107^\circ.8$. Major axis profiles and asymmetry profiles show a significant difference in brightness between the east and west sides, even though both sides decline exponentially in the

outer regions. Beyond the asymmetric arm, the east side of the major axis declines in brightness more rapidly than the west side. The two sides of the minor axis show a small discrepancy with the north side being fainter than the south. The minor axis profiles exhibit little or no departure from an exponential fall-off of brightness with distance. The scale length of the minor axis is 0.33 kpc - 0.37 kpc.

The size of NGC 55 in V is $35'.9 \times 9'.5 = 18.6 \text{ kpc} \times 4.9 \text{ kpc}$ at 27.6 magnitude per square arc second. In R, the size is $42'.6 \times 10'.2 = 22.1 \text{ kpc} \times 5.3 \text{ kpc}$ at 27.8 magnitude per square arc second. In I, the size is $35'.8 \times 12'.8 = 18.5 \text{ kpc} \times 6.6 \text{ kpc}$ at 27.0 magnitude per square arc second. Some evidence is apparent for a thickening of the disk with increasing wavelength, indicating a faint, red halo.

Color profiles of V-R, R-I, and V-I are presented for the major and minor axes. Along the major axis, the bar region is red, peaking near the nucleus at $V-R = 0.52$, $V-I = 1.00$. The bright inner disk, $2' < |a| < 5'$, is somewhat bluer, with $V-R \approx 0.2$, $V-I \approx 0.6$, and the outer disk, $|a| > 5'$ is red again, with the east side at $V-I \approx 0.9$ and the west side at $V-I \approx 0.8$. The dust and gas rich asymmetric arm on the east side obviously has some influence on its redder color. The minor axis data are only reliable for the innermost region, $|b| < 2'$, where the color is fairly uniform at $V-R \approx 0.2$ and $V-I \approx 0.6$. Because of difficulties in obtaining sky bright-

ness measurements, there may be large (on the order of a few tenths of a magnitude) errors in the measurements.

The total magnitudes found for NGC 55 are: $V_T = 8.17 \pm 0.04$, $R_T = 7.94 \pm 0.03$, and $I_T = 7.30 \pm 0.02$. The face-on magnitudes, corrected for galactic absorption and inclination are: $V_T^0 = 7.51 \pm 0.06$, $R_T^0 = 7.38 \pm 0.05$, and $I_T^0 = 6.87 \pm 0.04$. Integrated colors are $(V-R)_T = 0.23 \pm 0.05$, and $(V-I)_T = 0.87 \pm 0.04$. Converting the V magnitude used here to the Johnson system gives a $(B_J - V_J)_T = 0.31$, bluer than that of de Vaucouleurs and Freeman (1970), 0.55, or that of Puche Carignan and Wainscoat (1990), 0.47. The corrected face-on color is $(B_J - V_J)_T^0 = 0.04$.

For NGC 253, the isophote maps of the bright inner disk show the bar and the spiral arms. The bar is estimated to be $5.9 \text{ kpc} \times 4.3 \text{ kpc} \pm 0.4 \text{ kpc}$, and to lie at position angle $\approx 70^\circ$. On the isophote maps of the faint outer regions a large spur is visible to the south, with a smaller spur in the north-northwest. These are most readily visible on the infrared map. Major and minor axis profiles are shown for each color as well as mean profiles formed by averaging the data for each axis about the nucleus. The outer disk shows an exponential decline in brightness while the minor axis shows evidence of a $r^{0.25}$ spheroid.

The size of NGC 253 in V is $36'.3 \times 16'.4 = 30.1 \text{ kpc} \times 13.6 \text{ kpc}$ at 26.9 magnitude per square arc second. For R, the size is $35'.0 \times 12'.3 = 29.0 \text{ kpc} \times 10.2 \text{ kpc}$ at 25.9 magnitude

per square arc second. In I, the size is $42'.8 \times 24'.2 = 35.5$ kpc \times 20.1 kpc at 26.4 magnitude per square arc second, and $42'.8 \times 31'.4 = 35.5$ kpc \times 26.0 kpc if the spur is included.

The ellipticity, b/a , is given as a function of the semi-major axis distance for all three colors. In the R and I, the nuclear region shows an elongation along the minor axis, a trait not seen in the V or in Pence's (1978) blue photometry. The ellipticity reaches a minimum at about $a = 10'$, where $b/a \approx 0.18$, then increases for larger a . In particular, the I curve shows a large increase in b/a to ≈ 0.56 at $a = 19'$, not including the effect of the spur. The disk shows a thickening with decreasing brightness and increasing wavelength, indicative of a faint, red halo.

Color profiles of V-R, R-I and V-I are presented for the major and minor axes of NGC 253. The region containing the nucleus and bar is quite red, peaking at $0'.2$ southwest of the nucleus with $V-R = 1.57$, and $V-I = 2.69$. Nearly constant colors characterize the disk between $1'$ and $10'$ where $V-R \approx 0.9$ and $V-I \approx 1.7$, although there is a slight tendency for the colors to increase with radial distance on the southwest side of the disk. Where the exponential disk is encountered at the "edge" of the spiral arms, a small drop in the color indices of a few tenths of a magnitude is seen, followed by a monotonic increase at larger distances. Along the minor axis the bar and disk have fairly constant colors, $V-R \approx 1.1$ and $V-I \approx 1.6$. Beyond the visible disk, the colors increase with

increasing distance. The color of the halo is uncertain but it appears to be quite red. Comparing Pence's decomposition model for blue light with the infrared model presented here, the minor axis ($B_J - I$) is predicted to be ≥ 3 for $b \geq 5'$.

The total magnitudes found for NGC 253 are: $V_T = 7.35 \pm 0.05$, $R_T = 6.41 \pm 0.08$ and $I_T = 5.75 \pm 0.11$. Corrected for galactic and internal extinction, the face-on magnitudes are $V_T^0 = 6.62 \pm 0.38$, $R_T^0 = 5.79 \pm 0.33$ and $I_T^0 = 5.28 \pm 0.27$. Integrated colors are: $(V-R)_T = 0.94 \pm 0.09$ and $(V-I)_T = 1.60 \pm 0.12$. Converting the V magnitude to the Johnson system, $(B_J - V_J)_T = 0.62 \pm 0.11$, bluer than that derived by Pence, 0.85 ± 0.05 from B and V drift scans of the inner disk. Corrected for extinction, $(B_J - V_J)_T^0 = 0.46 \pm 0.16$, near the mean value of 0.51 ± 0.07 (m.e.) for Sc galaxies found by de Vaucouleurs (1979).

When viewed in infrared light, NGC 253 is seen to have the concentration index C_{32} of a pure exponential distribution. Decomposition of the V and I mean profiles into a spheroidal and an exponential component was done by an iterative method. The resulting fits for the V data indicate that the spheroid contributes $0.16 \pm .05$ of the total light, the disk contributes $0.60 \pm .15$, and the spiral arms contribute the remaining $0.24 \pm .16$. For the I data, the decomposition resulted in the spheroid contributing $0.27 \pm .05$ of the total light, the disk $0.71 \pm .10$, and the spiral arms, $0.02 \pm .11$.

On the basis of this photometric study, the following conclusions are derived for NGC 55:

From the isophote maps and axis ratios, the inclination is $\approx 85^\circ$ in good agreement with the optical appearance. No structure is apparent that would indicate a lower value. The position angle of the major axis is $107^\circ.8$.

The measured disk thickness increases with the wavelength of the observation. This is interpreted as indicating a red halo, or spheroid for this galaxy.

The east and west sides of the major axis are significantly different in structure. There is no single underlying symmetric exponential disk. Simply adding an arm onto such a disk gives too much light for the east side, in disagreement with the observations.

There is little or no $r^{0.25}$ spheroidal bulge for this galaxy, in keeping with the expected form for a late-type galaxy. The infrared observations show a profile that appears to be something between an exponential decline and a $r^{0.25}$ decline, however. A faint red halo does exist but declines quickly (probably exponentially) along the minor axis. The luminous part of this halo cannot contribute much mass to the system as a whole, however.

At the adopted distance of 1.78 Mpc the absolute visual magnitude (corrected for galactic absorption and viewed face-on) is - 18.74. This is slightly fainter than the LMC value

of - 19.06 based on RC2 data and an assumed distance of 50 kpc.

The color of NGC 55 is somewhat peculiar. The corrected face-on value $(B_J - V_J) = 0.04$ is bluer than the typical SBm galaxy and may indicate line emission. Variations in color along the major axis indicate that the M/L of the luminous material may not be constant throughout the galaxy.

For NGC 253 we find agreement with Pence's (1978) values of the inclination ($78^\circ.5$) and the position angle of the major axis (51°). The position angle of the bar is not well determined and decreases with increasing wavelength of observation. The infrared data yield a position angle of $\approx 70^\circ$, but it may be less than this.

NGC 253 shows optical evidence of a disturbance in the form of a large "spur" to the south, and a smaller one to the northeast. These features are most readily visible in the infrared and may indicate a tidal interaction occurred in the past.

The galaxy is well approximated by an exponential disk, especially in the infrared, where the outer concentration index, C_{32} indicates the disk is a perfect exponential disk. The agreement between observation and theory decreases as one observes at shorter wavelengths.

The galaxy is very red, no doubt due to the large amount of dust present. An almost constant color characterizes the

major axis out to the "edge" of the spiral arms indicating a constant M/L for the luminous material in the disk.

At the adopted distance of 2.85 Mpc, the corrected face-on absolute visual magnitude is -20.65. Thus NGC 253 is the brightest member of the Sculptor group, and among the brighter spirals. In the infrared, the absolute magnitude increases to about - 22.

Decomposition of the galaxy into a $r^{0.25}$ spheroid and an exponential disk shows that it possesses a substantial red halo, or spheroid. For $b > 5'$ the color index $(B_J - I) \geq 3$. Measurements indicate this spheroid contributes some 1/4 of the total light in the infrared, so it must provide a non-trivial amount of mass to the system if it has a M/L equal to that of the disk. If the halo has a M/L greater than that for the disk, it is possible that the halo detected here may contain roughly as much mass as the disk. Halo-to-disk mass ratios of ≈ 1 have been discussed and modeled for spirals by Bahcall and Casertano (1985), Carignan and Freeman (1985) and van Albada et al. (1985), using dark halos and exponential disks. A mixture of dark matter with the luminous material found here for NGC 253 could result in such a mass ratio.

REFERENCES

- Antonucci, R. R. J., and Ulvestad, J. S. 1988, *Ap. J.* (Letters), 330, L97.
- Bahcall, J. N., and Casertano, S. 1985, *Ap. J.*, (Letters), 293, L7.
- Barbon, R., Benacchio, L., and Capaccioli, M. 1976, *Mem. Soc. Astron. Ital.*, 47, 263.
- Beck, R., Biermann, P., Emerson, D. T., and Wielebinski, R. 1979, *Astr. Ap.*, 77, 25.
- Beck, R., Hutschenreiter, G., and Wielebinski, R. 1982, *Astr. Ap.*, 106, 112.
- Bessell, M. S. 1979, *Pub. A. S. P.*, 91, 589.
- Blecha, A. 1986, *Astr. Ap.*, 154, 321.
- Bottinelli, L., Gouguenheim, L., Paturel, G., and de Jaucouleurs, G. 1983, *Astr. Ap.*, 118, 4.
- Burbidge, E. M., Burbidge, G. R., and Prendergast, K. H. 1962, *Ap. J.*, 136, 339.
- Canzian, B., Mundy, L. G., and Scoville, N. Z. 1988, *Ap. J.*, 333, 157.
- Carignan, C., and Freeman, K. C. 1985, *Ap. J.*, 294, 494.
- Combes, F., Gottesman, S. T., and Weliachew, L. 1977, *Astr. Ap.*, 59, 181.
- Comte, G. 1985, in New Aspects of Galaxy Photometry, ed. J.-L. Nieto (Berlin: Springer), p. 169.
- Condon, J. J. 1983, *Ap. J. Suppl.*, 53, 459.
- _____. 1987, *Ap. J. Suppl.*, 65, 485.

- Condon, J. J., Condon, M. A., Gisler, G., and Puschell, J. J. 1982, *Ap. J.*, 252, 102.
- Da Costa, G. S., and Graham, J. A. 1982, *Ap. J.*, 261, 70.
- Davoust, E., and Pence, W. D. 1982, *Astr. Ap. Suppl.*, 49, 631
- Dawe, J. A. 1984, in Astronomy with Schmidt-Type Telescopes, ed. M. Capaccioli (Dordrecht: Reidel), p. 193.
- Demoulin, M. H., and Burbidge, E. M. 1970, *Ap. J.*, 159, 799.
- de Vaucouleurs, G. 1948, *Ann. d'Ap.*, 11, 247.
- _____. 1960, *Ap. J.*, 131, 574.
- _____. 1961, *Ap. J.*, 133, 405.
- _____. 1962, in Problems of Extra-Galactic Research, ed. G. C. McVittie (New York: Macmillan), p. 3.
- _____. 1977, in The Evolution of Galaxies and Stellar Populations, ed. B. Tinsley and R. Larson (New Haven: Yale Univ. Obs.), p. 43.
- _____. 1979a, *Ap. J.*, 227, 380.
- _____. 1979b, *Ap. J.*, 227, 729.
- _____. 1981, *Sky and Tel.*, 62, 406.
- _____. 1986, in Galaxy Distances and Deviation from Universal Expansion, ed. B. F. Madore and R. B. Tully (Dordrecht: Reidel), p. 1.
- de Vaucouleurs, G., and Agüero, E. 1973, *Pub. A. S. P.*, 85, 150.
- de Vaucouleurs, G., and Davoust, E. 1980, *Ap. J.* 239, 783.
- de Vaucouleurs, G., de Vaucouleurs, A., and Corwin, H. 1976, Second Reference Catalogue of Bright Galaxies, (Austin: Univ. of Texas Press) (RC2).
- de Vaucouleurs, G., and Freeman, K. C. 1972, *Vistas in Astronomy*, 14, 163.
- Diffley, J. A. 1968, *A. J.*, 73, 762.
- Donas, J., and Deharveng, J. M. 1984, *Astr. Ap.*, 140, 325.
- Elmegreen, D. M. 1981, *Ap. J. Suppl.*, 47, 229.

- Fabbiano, G. 1988, Ap. J., 330, 672.
- Fitzgibbons, G. L. 1981, M. S. thesis, Univ. of Florida.
- Freeman, K. C., Carrick, D. W., and Craft, J. L. 1975, Ap. J., (Letters), 198, L93.
- Furenlid, I. 1978, in Modern Techniques in Astronomical Photography, ed. R. M. West and J. L. Heudier (Geneva: European Southern Obs.), p. 153.
- Gottesman, S. T., Lucas, R., Weliachew, L., and Wright, M. C. H. 1976, Ap. J., 204, 699.
- Graham, J. A. 1982, Ap. J., 252, 474.
- Harnett, J. I., and Reynolds, J. E. 1985, M. N. R. A. S., 215, 247.
- Hoag, A. A., Furenlid, I., and Schoening, W. E. 1978, AAS Phot. Bull., No. 19, 3.
- Huchtmeier, W. K. 1972, Astr. Ap., 17, 207.
- _____. 1975, Astr. Ap., 45, 259.
- Hummel, E., Dettmar, R-J., and Wielebinski, R. 1986, Astr. Ap., 166, 97.
- Hummel, E., Smith, P., and van der Hulst, J. M. 1984, Astr. Ap., 137, 138.
- Jones, W. B., Obitts, D. L., Gallet, R. M., and de Vaucouleurs, G. 1967, Astronomical Surface Photometry by Numerical Mapping Techniques, Univ. of Texas Publ. in Ast., 1, Series II, No. 8.
- Keel, W. C. 1984, Ap. J., 282, 75.
- Kiszkurno-Koziej, E. 1988, Astr. Ap., 196, 26.
- Koo, D. C. 1985, A. J., 90, 418.
- Kormendy, J. 1977, Ap. J., 217, 406.
- Lang, K. R. 1980 in Astrophysical Formulae (Berlin: Springer), p. 559.
- Latham, D. W. 1978, in Modern Techniques in Astronomical Photography, ed. R. M. West and J. L. Heudier (Geneva: European Southern Obs.), p. 141.


- Lewis, B. M. 1969, *Proc. Astr. Soc. Aust.*, 1, 289.
- Lewis, B. M., and Robinson, B. J. 1973, *Astr. Ap.*, 23, 295.
- Longo, G., and de Vaucouleurs, A. 1983, A General Catalogue of Photoelectric Magnitudes and Colors in the U, B, V System of 3,578 Galaxies Brighter than the 16th V-Magnitude (1936 - 1982), Univ. of Texas Monographs in Ast., No. 3.
- McCarty, P. J., Heckman, T., and van Breugel, W. 1987, *A. J.*, 92, 265.
- Pence, W. 1976, *Ap. J.*, 203, 39.
- _____. 1978, A Photometric and Kinematic Study of the Barred Spiral Galaxy NGC 253, Univ. of Texas Publ. in Ast., No. 14.
- _____. 1980, *Ap. J.*, 239, 54.
- Pence, W. D., and Davoust, E. 1985, *Astr. Ap. Suppl.*, 60, 517.
- Pritchett, C. J., Richer, H. B., Schade, D., Crabtree, D., and Yee, H. K. C. 1987, *Ap. J.*, 323, 79.
- Puche, D., and Carignan, C. 1988, *A. J.*, 95, 1025.
- Puche, D., Carignan, C., and Wainscoat, R. J. 1990, preprint.
- Rieke, G. H., Lebofsky, M. J., Thompson, R. I., Low, F. J., and Tokunaga, A. T. 1980, *Ap. J.*, 238, 24.
- Rieke, G. H., Lebofsky, M. J., and Walker, C. E. 1988, *Ap. J.*, 325, 679.
- Rieke, G. H., and Low, F. J. 1975, *Ap. J.*, 197, 17.
- Robinson, B. J., and van Damme, K. J. 1966, *Aust. J. Phys.*, 19, 111.
- Sandage, A. 1961, The Hubble Atlas of Galaxies, (Washington, D. C.: Carnegie Institution of Washington).
- Sandage, A., and Bedke, J. 1988, Atlas of Galaxies Useful for Measuring the Cosmological Distance Scale, NASA SP-496, (Washington, D. C.: NASA).
- Sandage, A., and Tammann, G. A. 1981, A Revised Shapley - Ames Catalog of Bright Galaxies, (Washington, D. C.: Carnegie Institution of Washington).

- Savage, B. D., and Mathis, J. S. 1979, *Ann. Rev. Astr. Ap.*, 17, 73.
- Schoening, W. E. 1978, *AAS Phot. Bull.*, No. 17, 12.
- Schweizer, F. 1976, *Ap. J. Suppl.*, 31, 313.
- Scoville, N. Z., Soifer, B. T., Neugebauer, G., Young, J. S., Matthews, K., and Yerka, J. 1985, *Ap. J.*, 289, 129.
- Sersic, J. 1968, *Galaxias Australes*, (Cordoba: Univ. Nac. de Cordoba).
- Seielstad, G. A., and Whiteoak, J. B. 1965, *Ap. J.*, 142, 616.
- Smith, A. G., and Hoag, A. A. 1979, *Ann. Rev. Astr. Ap.*, 17, 43.
- Spinrad, H., Ostriker, J. P., Stone, R. P. S., Chiu, L-T. G., and Bruzual A., G. 1978, *Ap. J.*, 225, 56.
- Telesco, C. M., and Harper, D. A. 1980, *Ap. J.*, 235, 392.
- Tsikoudi, V. 1977, *Photometric Study of the Structure of Lenticular Galaxies*, Univ. of Texas Publ. in Ast., No. 10.
- Turner, B. E. 1985, *Ap. J.*, 299, 312.
- Turner, J. L., and Ho, P. T. P. 1983, *Ap. J. (Letters)*, 268, L79.
- Ulrich, M.-H. 1978, *Ap. J.*, 219, 424.
- Uyama, K., Matsumoto, T., and Thomas, J. A. 1984, *Pub. Astr. Soc. Japan*, 36, 477.
- van Aldaba, T. S., Bahcall, J. N., Begeman, K., and Sanscisi, R. 1985, *Ap. J.*, 295, 305.
- Walker, G. 1987, *Astronomical Observations: an Optical Perspective*, (Cambridge: Cambridge Univ. Press), p. 14.
- Wevers, B. M. H. R. 1984, Ph. D. thesis, Groningen Univ.
- Whiteoak, J. B., and Gardner, F. F. 1977, *Aust. J. Phys.*, 30, 187.
- Young, J. S., Xie, S., Kenney, J. D. P., and Rice, W. L. 1989, *Ap. J. Suppl.*, 70, 699.

BIOGRAPHICAL SKETCH

Gregory Lynn Fitzgibbons was born on June 17, 1950, in Indianapolis, Indiana. He graduated from Emmerich Manual High School in 1968 and enrolled at Indiana University where he received the degree Bachelor of Arts in Astronomy in 1973. He later attended the University of Florida, receiving a Master of Science degree in Astronomy in 1981. While in graduate school he was a teaching assistant for physics, astronomy and mathematics, and was named an Outstanding Teaching Assistant by the University in 1981. He was also a research assistant, working on the quasar monitoring program and then on an investigation of the response of commercial Kodak films to hypersensitization methods commonly used by astronomers. On May 18, 1986, he married Berna Rose Lowenstein of Kissimmee, Florida.

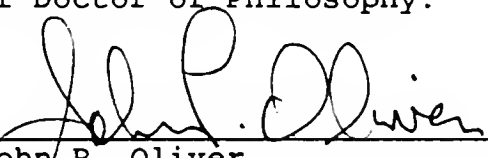
I certify that I have read this study and that in my opinion it conforms to acceptable standards of scholarly presentation and is fully adequate, in scope and quality, as a dissertation for the degree of Doctor of Philosophy.


Stephen T. Gottesman, Chairman
Professor of Astronomy

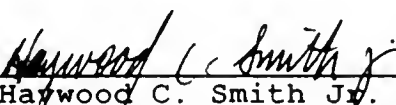
I certify that I have read this study and that in my opinion it conforms to acceptable standards of scholarly presentation and is fully adequate, in scope and quality, as a dissertation for the degree of Doctor of Philosophy.


Alex. G. Smith
Distinguished Service Professor
of Astronomy

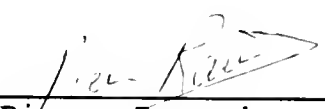
I certify that I have read this study and that in my opinion it conforms to acceptable standards of scholarly presentation and is fully adequate, in scope and quality, as a dissertation for the degree of Doctor of Philosophy.


John P. Oliver
Associate Professor of Astronomy

I certify that I have read this study and that in my opinion it conforms to acceptable standards of scholarly presentation and is fully adequate, in scope and quality, as a dissertation for the degree of Doctor of Philosophy.


Haywood C. Smith Jr.
Associate Professor of Astronomy

I certify that I have read this study and that in my opinion it conforms to acceptable standards of scholarly presentation and is fully adequate, in scope and quality, as a dissertation for the degree of Doctor of Philosophy.



Pierre Ramond
Professor of Physics

This dissertation was submitted to the Graduate Faculty of the Department of Astronomy in the College of Liberal Arts and Sciences and to the Graduate School and was accepted as partial fulfillment of the requirements for the degree of Doctor of Philosophy.

August 1990

Dean, Graduate School

